SYNTHESIS, FABRICATION, AND CHARACTERIZATION OF 2D LAYERED NANOMATERIALS AND POLYMER BASED FLEXIBLE PIEZOELECTRIC AND TRIBOELECTRIC NANOGENERATORS FOR ENERGY HARVESTING APPLICATIONS

THESIS

Submitted to

Delhi Technological University

in fulfilment of the requirements for the degree of

DOCTOR OF PHILOSOPHY
in
PHYSICS

by

VISHAL SINGH
(2K18/PhD/AP/19)

Under the supervision of

DR. BHARTI SINGH
Assistant Professor

DEPARTMENT OF APPLIED PHYSICS
DELHI TECHNOLOGICAL UNIVERSITY
DELHI-110042, INDIA

NOVEMBER 2023

Dedication

This dissertation is dedicated to my family and my supervisor.

DELHI TECHNOLOGICAL UNIVERSITY

(Govt. of National Capital Territory of Delhi)
Shahbad Daulatpur, Bawana Road, Delhi-110042

CERTIFICATE

This is to certify that the thesis entitled **"*Synthesis, Fabrication, and Characterization of 2D Layered Nanomaterials and Polymer Based Flexible Piezoelectric and Triboelectric Nanogenerators for Energy Harvesting Applications*"** submitted by **Mr. Vishal Singh (2K18/PhD/AP/19)** to Delhi Technological University (DTU), Delhi, India for the degree of Doctor of Philosophy, is a bonafide record of the research work carried out by him under my supervision and guidance. The work embodied in this thesis has been carried out in the Computational & Functional Materials Research Laboratory (CFMRL), Department of Applied Physics, Delhi Technological University (DTU), Delhi, India. The work of this thesis is original and has not been submitted in parts or fully to any other Institute or University for the award of any other degree or diploma.

Dr. Bharti Singh
Supervisor
Delhi Technological University
Delhi-110042, India

Prof. A.S. Rao
Head of the Department
Department of Applied Physics
Delhi Technological University

DELHI TECHNOLOGICAL UNIVERSITY

(Govt. of National Capital Territory of Delhi)
Shahbad Daulatpur, Bawana Road, Delhi-110042

CANDIDATE'S DECLARATION

I, **Mr. Vishal Singh**, hereby certify that the thesis entitled **"*Synthesis, Fabrication, and Characterization of 2D Layered Nanomaterials and Polymer Based Flexible Piezoelectric and Triboelectric Nanogenerators for Energy Harvesting Applications*"** submitted in the fulfilment of the requirements for the award of the degree of Doctor of Philosophy is an authentic record of my research work carried out under the supervision of **Dr. Bharti Singh**. This work in the same form or any other form has not been submitted by me or anyone else earlier for any purpose. Any material borrowed or referred to is duly acknowledged.

Vishal Singh
(2K18/PhD/AP/19)
Department of Applied Physics
Delhi Technological University
Delhi – 110042, India

ACKNOWLEDGEMENT

Above all, I extend my heartfelt gratitude to the almighty for providing me with the strength and patience needed to persevere throughout these years of hard work.

I hope this acknowledgement serves as a little token of my sincere appreciation to everyone who helped me in this journey.

I wholeheartedly want to thank my supervisor, **Dr. Bharti Singh**, for her excellent mentorship, patience, motivation, enthusiasm, immense knowledge, and continuous support through all these years. Her persistent commitment and rich reservoir of knowledge have not only made the journey easier but have also been instrumental in shaping the core of my thesis. I would also look to her for consolation during my Ph.D. journey at times of uncertainty and tiredness, and her insightful advice and consoling words never ceased to lift my mood. Her mentorship is a rare gem and I consider myself extraordinarily fortunate to have had the privilege of being nurtured under her unparalleled guidance. She is not just an advisor; she is a beacon of inspiration and mentorship that is truly one of a kind, a rare gem in the realm of academia.

My sincere thanks also go to **Prof. Yogesh Singh and Prof. J. P. Saini,** Ex-Hon'ble Vice-Chancellors, DTU, **Prof. S. Indu**, Hon'ble Vice-Chancellor, DTU and other officials for their valuable support and for providing ample facilities to conduct this research. I would also like to acknowledge the DTU's financial support to attend the 11th International Conference on Materials for Advanced Technologies (IUMRS-ICAM & ICMAT 2023) held during 26-30 June 2023.

I would also thank **Prof. Rinku Sharma**, Dean (Academic-PG), DTU, and **Prof. A.S. Rao**, Head of the Department of Applied Physics, DTU and all other faculty and staff members for their help and cooperation throughout my research. Thanks to the Department of Applied Physics, Delhi Technological University (DTU), for providing the required facilities so that I can work voraciously, barring the time limit.

I am also thankful to **Prof. Nitin K. Puri and Dr. Amrish Panwar**, for providing me the research environment and research facilities. I am grateful for the insightful discussion, valuable advice and trust they showed during the research work.

I express my heartfelt gratitude to my fellow lab mates **Km. Komal** and **Shilpa Rana** in the Computational & Functional Materials Research Laboratory (CFMRL) for the stimulating

discussions, selfless support, and all the fun we had, that kept me going in this challenging yet beautiful journey.

A special thanks to all my friends within and outside DTU for keeping me sane. To my college companions: **Anshu, Bhavya, Megha, Ankita, Rajat, Jasveer**, **Sunil**, **Sandeep, Yakshansh** and **Anshul**, you know how much you all mean to me and I can't imagine my life at DTU without you guys! I extend a special appreciation to **Anshu** for consistently being there and assisting me at every possible step throughout these years. To **Dr. Parveen Kumar, Rajkumar,** and **Ankit** you guys are always there to support me! To **Priya**, **Shivani**, **Vinay** and **Sharad,** I extend my heartfelt gratitude for your constant warmth and endearing presence as juniors. The moments shared with them will forever be cherished as golden memories in my life.

I want to pay high regard to my father, **Mr. Mahavir Singh** and my mother, **Mrs. Laj Wanti Devi** for their love, constant care, and emotional support throughout my life. My father has been the most significant pillar of support during these years. Both of them has invested all of their time in trying to make me a successful person. They have always taught me to work beyond my limits. My parents have always supported me in everything and provided me with the best facilities for me to reach here. The encouragement and support from my younger brother **Mr. Ajay Singh** always motivated me to accomplish this thesis work. His faith, trust and confidence in me always pushed me towards my goal. His contagious laughter and light hearted presence, which lightened my challenging Ph.D. journey and offered a welcome feeling of joy and innocence. The support, compassion, tolerance, and encouragement from my family got me through this challenging journey. I sincerely appreciate all that you have done for me over the years.

Vishal Singh

Date: 06-11-2023

Place: New Delhi

ABSTRACT

With increasing demand of energy, the emission of carbon is increasing in our environment and also the limited resources of fossil fuels have brought the green and renewable energy generation on high demand. Most of the electronic gadgets use batteries that also requires to be recharged after some time. The advances in low powered electronics, wireless sensors and micro electromechanical systems have tremendously raised the power requirement in the existing digital world. In the present scenario, we are completely surrounded with several electronics devices, such as, cell phones, tablets, I-pods, smart watches etc., which collectively require huge amount of power for their operation. A green energy generating device, which can harvest the energy from ambient sources present in our surroundings to fulfill the energy needs of future technologies without polluting our surrounding is becoming more in demand. The development of nanogenerators offers the best hope for the current global energy crisis rises due to social globalization. Piezoelectric nanogenerators (PENGs) and triboelectric nanogenerators (TENGs) are currently gaining a lot of attention for harvesting mechanical energy from the ambient environment to serve as the power source for powering electronic devices. When a piezoelectric material is used as one of the two components in the triboelectric nanogenerator, these two effects can be coupled. It is possible to further improve the output efficiency of the nanogenerator by integrating these two effects to form a hybrid nanogenerator. The present thesis involves the synthesis of nanocomposite films based on PVDF and 2D layered nanomaterials and the subsequent investigation of their applications within energy harvesting devices, primarily through the utilization of piezoelectric and triboelectric effects.

With this aim, PVDF films with different nanocomposites have been synthesized, where the systematic effect of the chalcogen atom of the Transition metal dichalcogenides (TMDCs) (MoS_2, MoSSe, $MoSe_2$) and polyvinylidene fluoride (PVDF) based composites on the piezoelectric performance of the fabricated piezoelectric nanogenerator has been investigated. Raman and FTIR spectroscopy revealed the enhancement of piezoelectric behaviour due to increase in the polar β-phase content of PVDF after addition of TMDCs in PVDF. Out of all the fabricated piezonanogenerator, the PVDF/MoSSe based nanogenerator showed the maximum peak to peak open circuit voltage of 31.2 V and short circuit current of 1.26 μA. This enhancement was achieved just by adding TMDCs without any further treatment. The enhanced piezoelectric performance is attributed to the synergistic contributions from inherent piezoelectricity of synthesized TMDCs and intensified β-phase for the PVDF/TMDCs

composites. The highest output voltage for the PVDF/MoSSe device is ascribed to the lack of reflection symmetry in MoSSe structure. The generated voltage was also used for lightning a commercial LED and for charging of a capacitor of 4.7 uF.

After studying the effect of different TMDCs on the piezoelectric properties of PVDF, we have checked the effect of different percentages of MoS_2 as a nanofiller in the PVDF matrix. The concentration of nanofiller in the PVDF also contributes to the device output performance. To check the ideal concentration of nanofiller, we have fabricated the different piezoelectric energy harvesters based on PVDF-MoS_2 materials by varying the weight percentage (0 %, 2%, 5 % and 7 wt %) of MoS_2. The piezoelectric output of the PVDF was found to be increased due to the incorporation of MoS_2. In comparison to bare PVDF film, the piezoelectric nanogenerator based on 7 wt% of MoS_2 as filler in PVDF shows nearly 2-fold increase in peak-to-peak output voltage from 9.4 V to 18.0 V. After that, we have also investigated the impact of MoS_2 weight percentage on the triboelectric performance of PDMS/PVDF-MoS_2 based nanogenerator. The results show that 7 wt% of MoS_2 is the optimum amount of doping for triboelectric energy harvesting similar to the case of piezoelectric energy harvesting; above this level, the energy harvesting performance of the nanogenerator abruptly decreased due to MoS_2 agglomeration in the PVDF matrix. Therefore, the triboelectric nanogenerator with 7 wt% of MoS_2 exhibits maximum output voltage of 189 V and a short circuit current of 1.61 μA. The TENG with 7 wt% MoS_2 produced a power density of 104.5 μWcm^{-2} which is ~2.7 times of the power density produced by the bare PVDF based TENG. Further, a piezo-tribo based hybrid nanogenerator (HNG) is fabricated by integrating the MoS_2-PVDF film having 7 wt% of MoS_2 with PDMS thin film as two layers required for the HNG device. Our study reveals that inclusion of MoS_2 in the PVDF matrix stimulates the generation of β-phase and also the intrinsic piezoelectric properties which contributes in the overall enhancement of the piezoelectric output of PVDF. In addition to enhanced β-phase, the distribution of MoS_2 increase the surface roughness which increases the contact area and also boosts the surface potential and dielectric constant thereby increasing the triboelectric output of the device. Each of these factors combine to significantly increase the performance of the hybrid nanogenerator. The fabricated TENG demonstrated the practical application, by powering electronic stopwatch and scientific calculator.

After the analysis of the effect of filler concentration, to further improve the efficiency of the PENG and TENG, the PVDF-$MoSe_2$ nanofibers were synthesized via electrospinning technique with different wt% of $MoSe_2$ (0 wt%, 3 wt%, 5 wt%, 7 wt% and 10 wt%). In this work, hybrid triboelectric nanogenerator coupling both the piezoelectric and triboelectric effects have been

fabricated to drive the environment friendly approach of splitting the water for hydrogen production. Here, electrospun PVDF-$MoSe_2$ fiber deposited over aluminium foil, and Nylon fiber based triboelectric negative and positive material, respectively have been used for fabricating the hybrid nanogenerator. The PVDF-$MoSe_2$/Nylon based TENG exhibits remarkable peak to peak open circuit voltage of 113.6 V and 26.5 μA of short-circuit current. Moreover, it exhibits a high power density of 230.4 μWcm^{-2} under piezo-tribo coupling, which is even superior than the majority of previously fabricated similar type of devices. This TENG, which has great output performance, can also capture energy from a variety of mechanical and biological motions, and the device versatility has also been shown by its use in hydrogen evolution.

It has been observed that material selection is critical for TENGs since the triboelectric properties of the materials have significant effect on the performance of TENGs. Therefore, after fabricating a high performance PVDF-$MoSe_2$ nanofiber based TENG, in the last part, we have studied the effect of triboelectric layer material on the output performance of the TENG device. In this study, the PVDF-$MoSe_2$ nanofiber film has been fixed as one of the triboelectric layers, whereas the second layer material has been varied including PTFE, PDMS, PET, Paper and Nylon. The TENG consisting of Nylon as second triboelectric material demonstrates the maximum power density of ~231 μWcm^{-2}. The effect of tapping frequency and force on the triboelectric output of PVDF-$MoSe_2$/Nylon was also studied and an increasing trend of output voltage and current is observed with increasing force and frequency thereby producing a maximum voltage of ~206 V. The increase in output performance of the TENG with increase in frequency is attributed to faster charge transfers process, when the contact frequency is higher. With the rise in contact force, the effective area and capacitance of the TENG also increases which further results in the enhancement of triboelectric output of the nanogenerator. This study proposes an effective approach for enhancing the performance of triboelectric nanogenerator just by selecting the suitable material.

LIST OF PUBLICATIONS

Publications in Peer Reviewed Journals:

1. **V. Singh** and B. Singh, "*PDMS/PVDF-MoS_2 based flexible triboelectric nanogenerator for mechanical energy harvesting*", Polymer, (2023), 274, 125910.
2. **V. Singh** and B. Singh, "*MoS_2-PVDF/PDMS Based Flexible Hybrid Piezo-Triboelectric Nanogenerator for Harvesting Mechanical Energy*", Journal of Alloys and Compounds, (2023),168850.
3. **V. Singh**, D. Meena, H. Sharma, A. Trivedi and B. Singh, "*Investigating the role of chalcogen atom in the piezoelectric performance of PVDF/TMDCs based flexible nanogenerator*", Energy, (2022), 239, 122125.

Communicated:

1. **V. Singh,** S. Rana, R. Bokolia, A. K. Panwar, R. Meena and B. Singh, "*Electrospun PVDF-$MoSe_2$ Nanofibers based Hybrid Triboelectric Nanogenerator for Self-Powered Water Splitting System*".
2. **V. Singh** and B. Singh, "*Effect of variation of triboelectric layer material on output performance of the PVDF-MoSe2 based flexible triboelectric nanogenerator*".

Publications not included in this thesis:

1. Bhatt, **V. Singh**, P. Bamola, D. Aswal, S. Rawat, S. Rana, C. Dwivedi, B. Singh, H. Sharma, "*Enhanced Piezoelectric Response Using TiO_2/MoS_2 Heterostructure Nanofillers in PVDF Based Nanogenerators*", Journal of Alloys and Compounds, (2023), 170664.
2. S. Rana, **V. Singh** and B. Singh, "*Tailoring the Output Performance of PVDF-Based Piezo–Tribo Hybridized Nanogenerators via B, N-Codoped Reduced Graphene Oxide*", ACS Applied Electronic Materials, (2022), 4(12), 5893-904.
3. S. Rana, **V. Singh** and B. Singh, "*Recent trends in 2D materials and their polymer composites for effectively harnessing mechanical energy*", iScience, (2022), 103748.

Publications in Conferences:

1. **V. Singh** and B. Singh, "*Fabrication of PVDF-transition metal dichalcogenides based flexible piezoelectric Nanogenerator for energy harvesting applications*", Materials Today: Proceedings, (2020), 28, 282-285.

Book Chapters:

1. **V. Singh,** I. Rayal, H. Sharma, C. Dwivedi and B. Singh, "*Solar radiation and light materials interaction*", Energy Saving Coating Materials (2020), 1-32.
2. S. Rana, **V. Singh,** H. Sharma and B. Singh (2022) Chapter titled: "*Fluoropolymer Nanocomposites for Piezoelectric Energy Harvesting Application*", In Advanced Fluoropolymer Nanocomposites Woodhead Publishing (2023), 317-358.

Conference Contributions-Poster and Oral Presentations:

1. **V. Singh** and B. Singh, "*Self-Powered Water Splitting System triggered by Electrospun PVDF-$MoSe_2$ Nanofibers based Piezo-Tribo Hybrid Nanogenerator*", ICMAT 2023, at SUNTEC, Singapore, 26^{th} - 30^{th} June, 2023. **(POSTER) (Received Best Poster Award)**
2. **V. Singh** and B. Singh, "*Improved Piezoelectric Performance of MoS_2 Filled PVDF for Harvesting Mechanical Energy from the Environment*", ICMAT 2023, at SUNTEC, Singapore, 26^{th} - 30^{th} June, 2023. **(POSTER)**
3. **V. Singh** and B. Singh, "*PVDF-MoS_2 Composite Based Flexible High Performance Triboelectric Nanogenerator for Mechanical Energy Harvesting*", IUMRS-ICA 2022, Indian Institute of Technology Jodhpur, India, 19^{th} -23^{rd} December, 2022. **(POSTER)**
4. **V. Singh** and B. Singh, "*Enhanced Piezoelectric Performance of MoS_2 Filled PVDF for Harvesting Ambient Mechanical Energy*", International Conference on Nanotechnology: opportunities and challenges (ICNOC-2022), Department of Applied Sciences & Humanities, Faculty of Engineering & Technology, Jamia Millia Islamia, New Delhi, India, 28^{th}-30^{th} November, 2022. **(POSTER)**
5. **V. Singh** and B. Singh, "*Flexible PVDF-$MoSe_2$/PDMS based Piezo-Tribo Hybrid Nanogenerators*", International Conference: Thin films and nanotechnology-knowledge, leadership and commercialization (ICTN-KLC), Indian Institute of Technology, Delhi, India, 24^{th}-26^{th} August, 2021. **(ORAL TALK)**

6. **V. Singh** and B. Singh, "*Fabrication of PVDF-transition metal dichalcogenides based flexible piezoelectric Nanogenerator for energy harvesting applications*", International Conference on Advanced Materials and Nanotechnology (AMN-2020), Jaypee Institute of Information Technology, Noida (INDIA), 20th-22nd February 2020. **(POSTER)**
7. **V. Singh,** D. Meena and B. Singh, "*Enhanced β Phase of a PVDF-TMD Based Nanocomposite for Energy Harvesting Applications*", International Conference on Atomic, molecular, optical and nanophysics with applications CAMNP-2019, Delhi Technological University, India, 18th-20th December, 2019. **(POSTER) (Received Best Poster Award)**

CONTENTS

Chapter 2

Chapter 3

Chapter 4

LIST OF FIGURES

Figure No. **Page No.**

Chapter 1

Chapter 2

Chapter 3

Chapter 4

Chapter 5

Chapter 6

LIST OF TABLES

LIST OF ABBREVIATIONS

Acronyms	Meaning
TMDC	Transition metal dichalcogenides
MoS_2	Molybdenum disulfide
$MoSe_2$	Molybdenum diselenide
MoSSe	Molybdenum sulphoselenide
PVDF	Polyvinylidene fluoride
PENG	Piezoelectric nanogenerator
TENG	Triboelectric nanogenerator
HNG	Hybrid nanogenerator
V_{oc}	Open circuit voltage
I_{sc}	Short circuit current
PDMS	Polydimethylsiloxane
PTFE	Polytetrafluoroethylene
PET	Polyethylene terephthalate
DMF	N, N di-methyl formamide
rpm	Revolutions per minute
wt%	Weight percentage

CHAPTER 1

Introduction

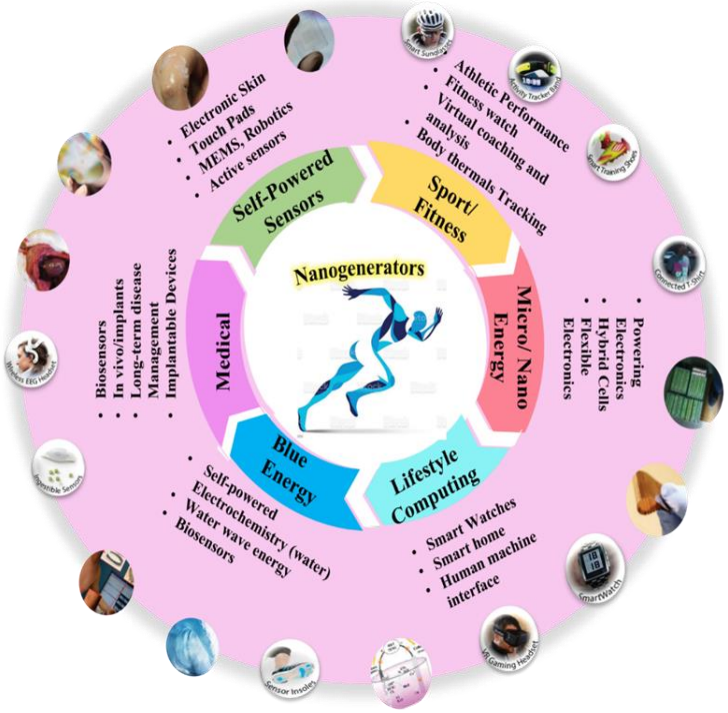

Chapter 1 gives the brief introduction about the need and the different ways to produce sustainable energy supplies using mechanical energy harvesters in order to complete the increasing demand of energy. This chapter deals with the significance of green energy and ideas to enhance the efficiency of mechanical energy harvesters. The increasing demands for power have posed serious obstacles to the development of wireless and wearable devices. A renewable power source for wearable technology is highly desired to address this issue. For harvesting energy, numerous principles have been established over the years based on diverse mechanisms, such as piezoelectric, electromagnetic, thermoelectric and triboelectric phenomenon. Due to their wide range of potential uses, including energy harvesting from human motion, mechanical motion, wind, and flowing water, as well as self-powered sensors in various sensing applications, piezoelectric nanogenerators (PENG) and triboelectric nanogenerators (TENGs), which convert mechanical energy into electricity, have drawn significant attention.

1.1 Overview

Energy harvesting is a transformative process involving the conversion of ambient energy, traditionally dissipated and wasted, into a valuable alternate energy form, primarily in the electrical energy. This harnessed energy reservoir holds the potential to enhance the efficacy of pre-existing systems, furnish power to wireless sensors, or drive miniature electronic devices. The importance of energy harvesting technology has grown as a result of the combination of declining fossil fuel supplies and the rising ecological consequences. Furthermore, the spike in technical advances over the last decade has resulted in a trend of device size reduction, resulting in portability, efficiency, and manageability advantages, but frequently at the price of reduced battery dimensions. As the traditional external power source for modern electronic gadgets, lithium-ion batteries are primarily used. Nonetheless, these batteries are constrained by their short operating lifespan and accompanying environmental issues [1, 2]. As a result, there is an urgent need for energy solutions that are both efficient and ecologically friendly, while still having a long operating lifespan. Simultaneously, the progress of nanotechnology has resulted in significant decreases in power consumption for microelectronics, with power utilisation shifting from milliwatts (mW) to microwatts (μW) [3, 4]. These advancements underpin various applications like wireless sensor networks, implantable biodevices, and beyond [5].

Previously, these small wireless sensors were powered by small batteries that required cyclic recharging. However, the current situation necessitates the pursuit of alternative energy sources with minimum to no negative environmental consequences. Solar and wind energy are commonly harvested energy types. Solar energy is a plentiful resource that manifests as light and heat. Solar light may be converted to electrical energy by using solar cells, however, the amount of solar radiation absorbed at a given location is determined by the sun's angle. Environmental conditions also exert influence; instances include diminished solar panel efficiency during cloud cover or night-time, potentially leading to electricity generation reduction. Despite its high energy production, this energy harvesting technology is inappropriate for powering small wearable and portable electronic gadgets. This technology is designed to collect immobilised energy [6]. There are several options, including solar thermal collectors and solar heat concentrators. These devices collect solar heat to power various applications directly or via later energy conversion. Wind energy is another option; through turbine spinning, electricity is generated. Wind turbines properly placed in agricultural regions or rocky terrains of remote locations provide economic viability without polluting the environment [7]. Wind and solar energy sources are both very unpredictable due to their high

dependency to environmental conditions. Consequently, solely relying on them to directly power critical electronic apparatus becomes unfeasible [8]. Mechanical vibrations, on the other hand, are a separate energy category distinguished by their plentiful presence within the ambient environment and are independent of external conditions.

Mechanical vibrations are a plentiful and underutilised reservoir that has yet to be explored. This collection of mechanical vibrations has a wide range of amplitudes and frequencies [9, 10]. Human or biological vibrations normally have a frequency range of 1-10 Hz, whereas machine vibrations have a frequency range of 10-100 Hz [11]. Exploiting mechanical vibration energy, which may be derived from irregular airflow, ultrasonic waves, tidal motions, and even human movements, is an attractive way owing to its ease of access and ecologically friendly nature.

The current thesis, within this framework, elucidates novel approaches for capturing mechanical energy by using piezoelectric and triboelectric phenomena. The primary focus is on thoroughly unravelling the operational mechanisms while simultaneously developing hybrid devices designed to improve energy harvesting performance. The primary goals are to provide a simplified, resilient, and financially feasible method that prioritises ecological compatibility.

1.2 Nanogenerators for Mechanical Energy Harvesting

Nanogenerators are a ground-breaking approach of converting mechanical energy into useful electrical power. This topic is a continuously expanding field of study, with advances in nanotechnology accelerating its expansion even further. Notably, Professor Zhong Lin Wang and his research team established the manufacturing of a piezoelectric nanogenerator based on ZnO nanowires in 2006 [12, 13]. Their approach included using a conductive AFM tip to apply mechanical pressure on the nanowire and then measuring the resulting voltage output. This key study pioneered a new paradigm for power production based on piezoelectric nanomaterials. Following this watershed moment, the area has seen a slew of investigations aimed at improving efficiency and deeper understanding of the different ways of power production principles. After inventing the piezoelectric nanogenerator, Professor Zhong Lin Wang and his research team proposed a unique way to harnessing electrical energy by utilising the triboelectric effect in 2012 [14]. Following this pioneering work, significant advances in both the design and uses of this technology have occurred. The advantages of nanogenerators are their ease of production, low cost, and resilience [15]. A broad range of nanogenerator designs

have developed in light of the various forms of mechanical energy, ranging from wind energy [16-20] water waves [21-23] biological motions [24-26] and machine vibrations [11, 27]. These designs capture otherwise wasted mechanical energy, which would normally be lost to forms like as sound, heat, and other mechanical motions. Beyond their role in generating electricity for small-scale electronic devices, nanogenerators possess the capability to serve as a sensor device. Motion tracking [28], touch sensors [29], pressure [30], temperature [31], and wind speed sensor [32] are among the array of sensing functions wherein the nanogenerators find direct application. The forthcoming chapter provides an elaborate exposition of piezoelectric and triboelectric nanogenerators, and their operational mechanisms.

1.3 Piezoelectric Nanogenerators

Piezoelectric nanogenerator (PENG) uses the piezoelectric phenomena to convert mechanical energy into electrical power. When an external force acts upon a piezoelectric material, a piezo potential is created. This potential gradient drives the movement of electrons between the two opposing metal electrodes that are affixed to either surface of the films. Material refinement and design optimisation have dominated research efforts in the piezoelectric nanogenerator area. This aims to improve system flexibility and utility in a variety of applications, notably in the field of flexible electronics. The next section looks into the materials used in PENG fabrication, as well as the associated design structures.

1.3.1 Piezoelectric Materials

The invention of piezoelectric materials may be traced back to 1880, attributed to the pioneering work of Pierre and Jacques Curie. Within the realm of naturally occurring substances, several materials display inherent piezoelectric characteristics. Examples include topaz, Rochelle salts, quartz, and cane sugar. Understanding the fundamental principles requires an understanding of the crystal structures of inherent piezoelectric materials, as well as the underlying physics regulating the piezo potential production. Mechanical pressure causes polarisation in piezoelectric materials, and voltage causes material deformation, an distinctive property of some materials. This characteristic demands the lack of a centre of symmetry within the crystal structure. Figure 1.1 shows an excellent example of a hexagonal crystal structure that exhibits piezo potential in response to mechanical pressure. As shown in Figure 1.1(a), when a line is drawn in any direction, the charge distribution at a particular place is not equal to that at an equidistant point in the opposite direction. Prior to the imposition of mechanical strain causing structural deformation, the aggregate positive and negative charge centers coincide, symbolized by point 'O', which serves as the net charge center. When mechanical

stress is applied along the Y-axis, the locations of positive and negative charges along the deformed axis change. This divergence prevents the negative and positive charge centres from overlapping, causing polarisation along the applied force vector. Subsequently, when a force is exerted along the X-axis, polarization occurs along the Y-axis, as depicted in Figure 1.1(c). This illustrates the mechanism of generating polarization in different directions corresponding to the applied forces.

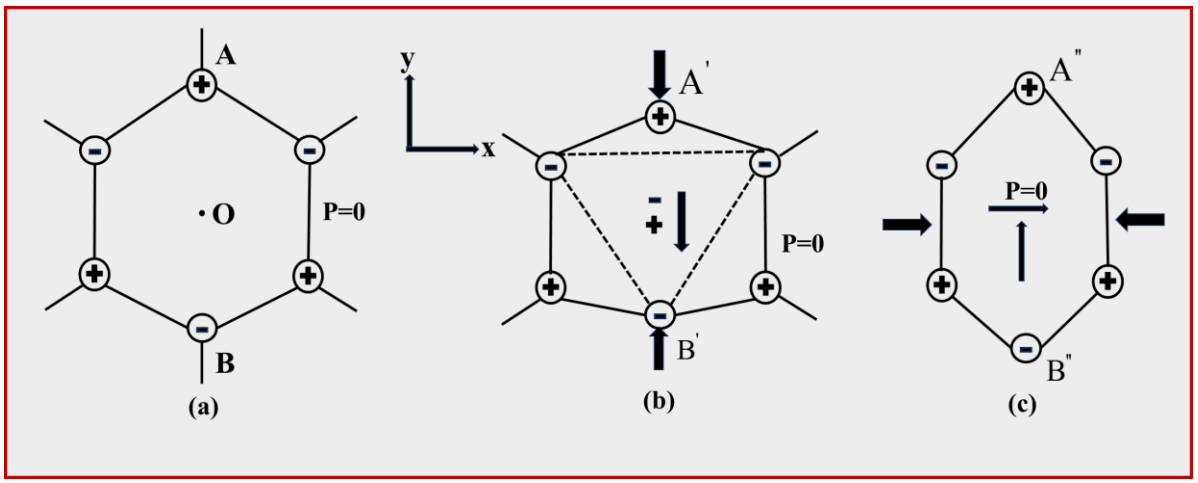

Figure 1.1 Hexagonal structure of crystal (a) without stress, (b) when stress is applied along Y-axis, and (c) when stress is applied across X-axis.

The linear correlation between the applied stress, denoted as T_j, and the resultant polarization, P_i, is mathematically represented as:

$$P_i = d_{ij}T_j \tag{1.1}$$

Here, d_{ij} signifies the piezoelectric coefficients, with i and j denoting specific directions. Analogously, the deformation elicited within the material, represented as S_j, in response to an applied electric field, denoted as E_i, is expressed as:

$$S_j = d_{ij}E_i \tag{1.2}$$

Lead zirconate titanate (PZT) has the highest piezoelectric coefficient (d_{33} = 480 pm/V) among the different available piezoelectric materials. Nevertheless, the presence of toxic Pb^{+} within PZT raises environmental concerns. In response, scientists have directed their efforts toward identifying lead-free piezoceramics, such as KNaNbO3 (KNN), $BiNaTiO_3$, $BaTiO_3$, etc.

1.3.2 Evolution of Piezoelectric Nanogenerators

The evolution of PENG design has been a progressive journey, in its initial stages, the fundamental configuration of PENG involved the synthesis of nanowires and nanorods, subsequently linking them individually to metal electrodes. This connection was established using either interconnecting electrodes or through the design of interdigital electrodes, as depicted in Figure 1.2. For device manufacturing, a wide range of nanowires were used, including CdS [33], ZnS [34], PZT [35], ZnO [36], and others.

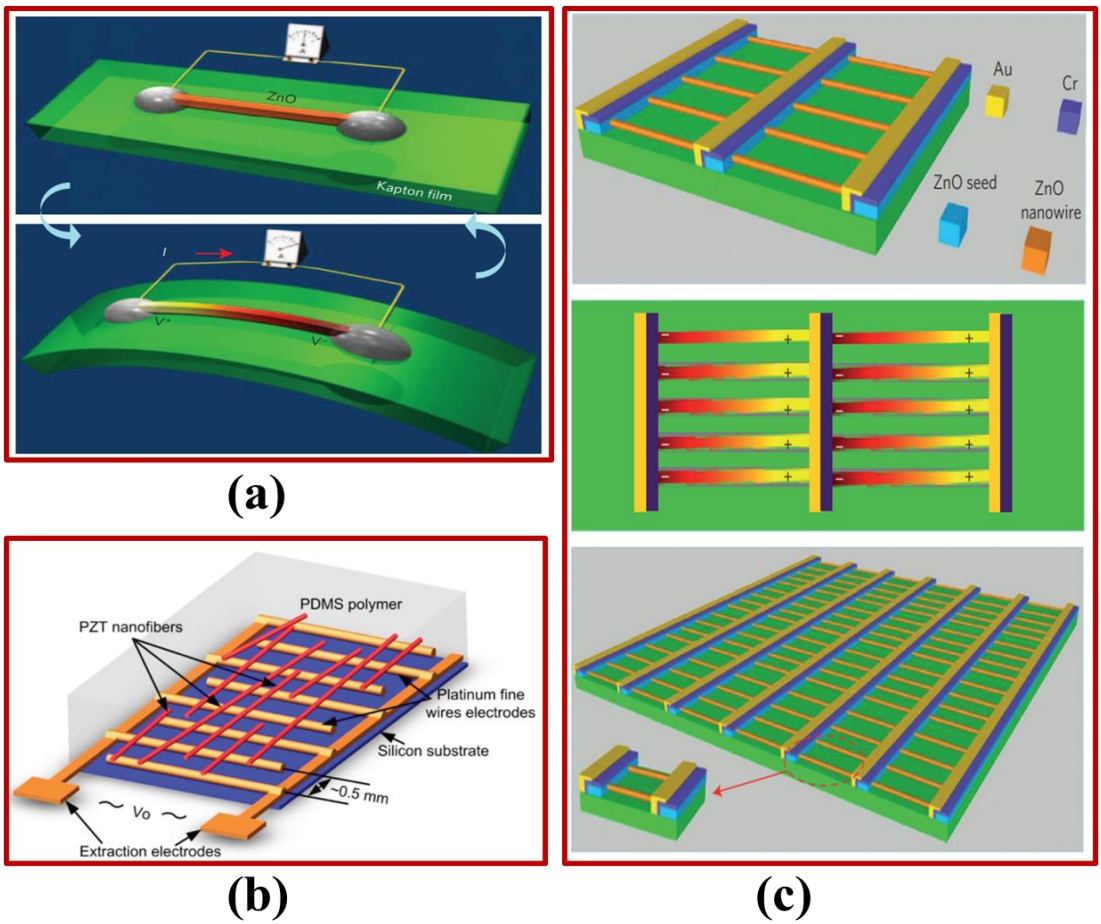

Figure 1.2 (a) The construction of a PENG device involves the utilization of a Kapton film with integrated ZnO nanowires [38], (b) PZT nanofibers are interconnected and linked by interdigital electrodes, which are supported by a flexible PDMS layer [39] and (c) The configuration comprises a side-by-side alignment of ZnO nanowire arrays [37].

Nanofibers and nanowires structured as single units exhibit remarkable pressure sensitivity, even a modest strain of 0.19% can yield a substantial voltage output of 1.26 V, sufficient to recharge an AA battery [37]. Nevertheless, the fabrication process for these structures demands intricate methodologies. Additionally, when these devices encounter

repetitive mechanical stresses, there exists a risk of early breakdown. As a result, a new research path has evolved in pursuit of flexible, freestanding film based PENGs. A fundamental polymer matrix is developed in this design paradigm, into which piezoelectric nanostructures are inserted, while flexible films serve as electrode deposition substrates. Polyvinylidene fluoride (PVDF) is a well known polymer due to its high piezoelectric coefficient. The integration of piezoelectric contributions from both the polymer and the incorporated nanostructures holds the potential to enhance output power. In later sections the structure of PVDF and several methods for increasing its piezoelectric coefficient will be discussed.

1.4 Triboelectric Nanogenerators

Triboelectric nanogenerators (TENGs) work on the basic idea of triboelectrification. This phenomenon arises when two materials make contact, leading to the generation of charges on their surfaces. This effect has been recognized for an extended duration, with a notable illustration being the occurrence of negative charges on a plastic comb when it is used to comb dry hair. This process is known scientifically as "contact electrification," and it emphasises the generation of charges through the contact of two different materials. Triboelectrification occurs in solids, liquids, and gases, encompassing a wide range of materials. This phenomenon gained substantial attention subsequent to the introduction of the triboelectric nanogenerator by Professor Zhong Lin Wang in 2012 [14]. The operation of a Triboelectric Nanogenerator (TENG) is based on the interaction of triboelectrification and electrostatic induction. TENGs are versatile in design, allowing fabrication in various configurations to capture mechanical energies originating from diverse sources, such as body movements (e.g., bending, walking, tapping, clapping) [1, 40], ocean waves [41], interactions with objects like keyboard pads [42] and backpacks [43], rotational motions [44], and wind energy [16]. The generated electricity can be either stored for alternative applications or utilized directly within the device, which can also serve as a sensor.

1.4.1 Triboelectric Materials and Triboelectrification

Several ideas have been proposed to explain the mechanics underlying charge creation via triboelectrification. The Kelvin probe microscope has evolved as a powerful method for inspecting and analysing surface charges. Among the several ideas that explain the charge transfer process, the electron transfer hypothesis is widely accepted as the explanation for the beginnings of triboelectrification. According to this theory, when two materials make contact, the electron clouds enveloping the atoms of these materials intersect. This intersection results in the migration of electrons from one atom to another, a phenomenon depicted in Figure 1.3.

Electrons stay firmly connected to their respective atoms when materials A and B are separated by a distance 'd'. Mechanically reducing the separation distance to the point where electron clouds overlap or atomic bonding length reduces on the other hand, results in a decreased potential between the atoms. This transition causes contact electrification, which is characterised by the transfer of electrons from one atom to the other. When two atoms separated (as seen in Figure 1.3(c)), one gains an electron while the other loses one. These resulting charges persist on the surfaces of the interacting materials. The mechanical forces sole function is to facilitate intimate contact at the atomic level, but only in specified locations, despite the fact that the whole surface of the material does not achieve such closeness [45]. Thus, to augment contact electrification, an effective strategy involves employing a soft material to rub against a hard or tightly-bound material. This action ensures increased points of contact, resulting in the transfer of more charges.

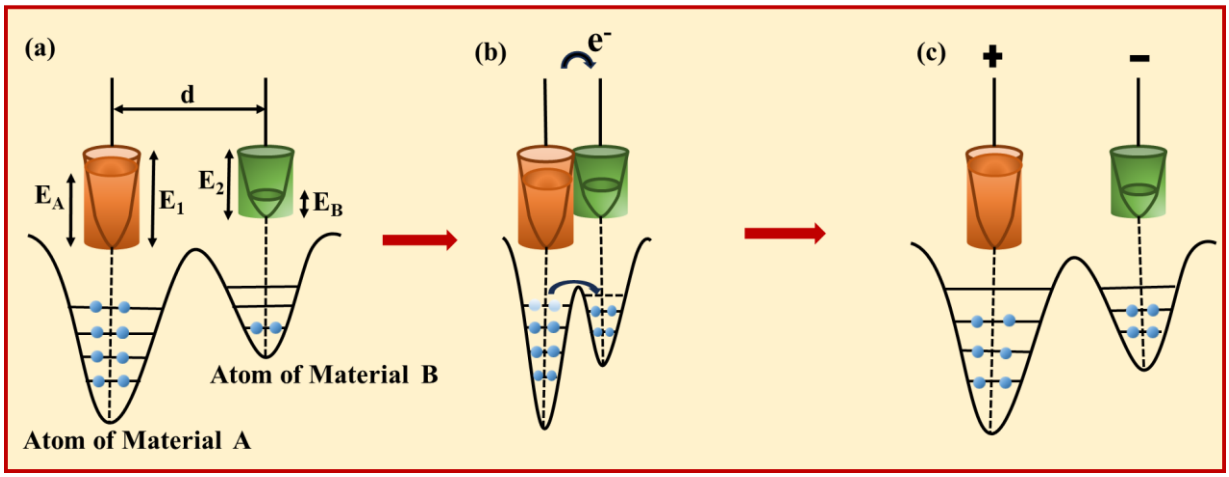

Figure 1.3 A schematic diagram illustrates the process of contact electrification. The diagrams depict the electron cloud and potential energy profile of two distinct materials, labelled as A and B. In the initial state (a), before these materials come into contact, as they make contact (b), their electron clouds begin to overlap, leading to the transfer of electrons between the two materials. After separation (c), it becomes evident that the atom of material B has gained electrons, resulting in a negative charge, while the atom of material A has lost electrons, leading to a positive charge.

Given that triboelectrification occurs between two distinct materials, a smart selection strategy comprises selecting one material from the lower positions of the triboelectric series and the other material from its higher position. The triboelectric series categorises materials according to their tendency to gain or lose electrons. Elements near the top of the series are more likely to quickly surrender electrons when they come into touch with elements at the

bottom of the series. When two contacting materials have significant differences within the triboelectric series, higher electron transport discrepancies are expected. Surface modification of materials has been identified as a means to augment the triboelectric effect. In the pursuit of flexibility, the selection of flexible polymer materials like polyethylene terephthalate (PET), Kapton (Polyimide), Polydimethylsiloxane (PDMS), Nylons, and Polytetrafluoroethylene (PTFE) films given preference over other materials. Numerous devices have been engineered wherein human skin is incorporated as one of the contacting materials, coupled with a material from the negative (lower) position of the triboelectric series.

1.4.2 Design and Operating Mechanism of TENG

As previously indicated, the phenomenon of contact electrification manifests across solids, liquids, and gases. Devices based on solid-solid triboelectrification (the interaction of two solid or rigid materials) and solid-liquid triboelectrification (where one material is solid or rigid and the other is a liquid (such as water) have been developed in the context of Triboelectric Nanogenerator (TENG) construction. Categorized by their operational principles, four distinctive modes of TENG have emerged: (i) vertical contact-separation mode, (ii) lateral sliding mode, (iii) freestanding triboelectric layer mode, and (iv) single electrode mode [46-49]. These modes are illustrated in Figure 1.4.

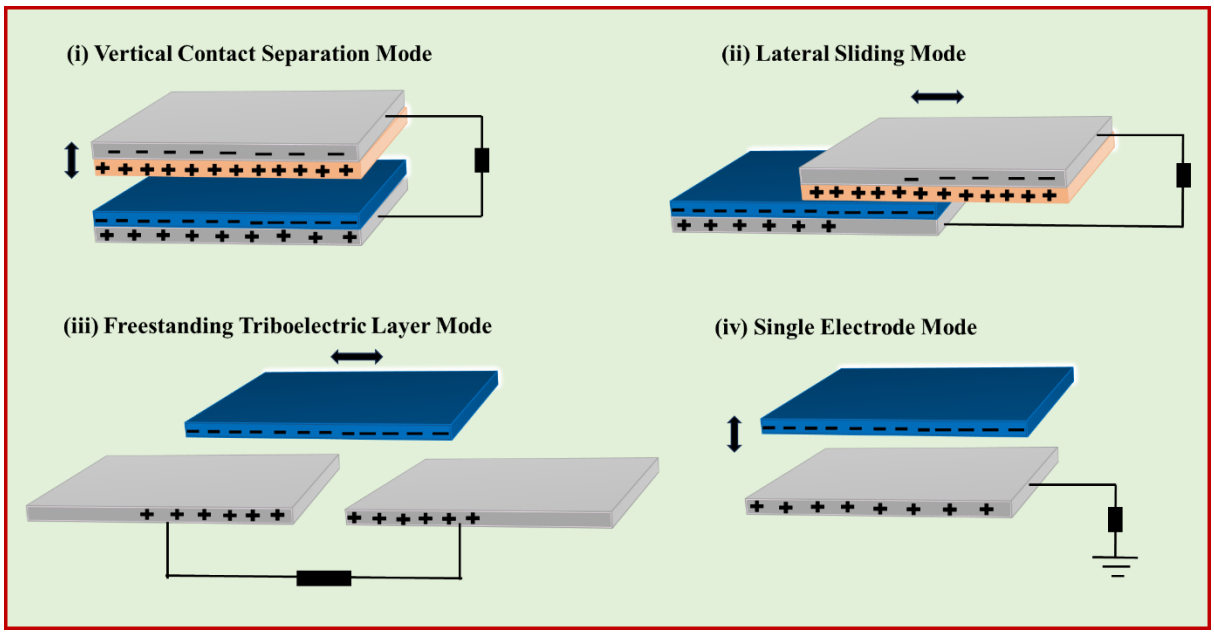

Figure 1.4 The distinct operational modes of TENG encompass: (i) the vertical contact-separation mode, (ii) the horizontal sliding mode, (iii) the freestanding triboelectric layer mode and (iv) the single-electrode mode.

In the vertical contact-separation mode, the two dielectric materials involved move exclusively in the vertical direction. Conversely, the lateral sliding mode entails the sliding motion of the two contacting materials over each other. The only difference between these modes is the method of causing contact and separation via mechanical force application. Metal electrodes are placed on the non-contacting surfaces of the interacting materials in both cases, with both materials interconnected. However, the latter two modes-the single electrode mode and the freestanding triboelectric layer mode-deviate from the preceding pair. In these modes, solely one dielectric material and one metallic material are employed. In this case, the metallic or conducting material that makes contact also serves as the electrode.

The operating mechanism of TENG is depicted in Figure 1.5 by taking the example PVDF-$MoSe_2$ and Nylon. Since no charge exists prior to the contact between the layers of TENG, resulting in zero potential difference between the layers (Figure 1.5(a)).

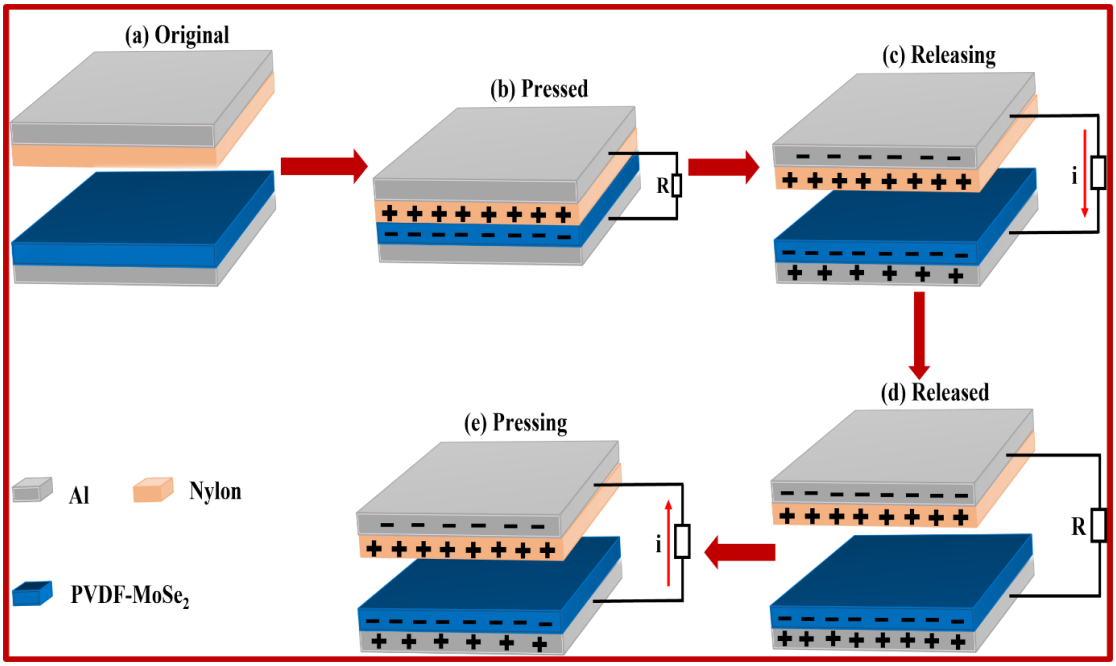

Figure 1.5 Schematic illustrating the working of PVDF-$MoSe_2$/Nylon based TENG in vertical contact-separation mode.

Using a dynamic shaker, both triboelectric layers are pushed into contact, leading to electrons movement from Nylon surface towards the PVDF-$MoSe_2$ surface via contact electrification. As a result, the Nylon surface charges positively, whereas the PVDF-$MoSe_2$ surface charges negatively. (Figure 1.5(b)). Because of the polymer films insulating nature, these charges will not flow away or be neutralised quickly. When these layers are separated, an electrical potential difference among their associated electrodes is created, causing electrons to

travel via an external circuit, leading to an electrical signal (Figure 1.5(c)). Once the separation distance is maximised, the electric potential difference between the electrodes is entirely neutralised by electron transfer, and in the external circuit no electrical signal is produced (Figure 1.5(d)). When the TENG is compressed again, an opposite electrical signal is produced due to back-flow of electron (Figure 1.5(e)). As a result, despite being repeatedly driven by an external force, TENG could generate a continuous alternating electrical output.

Figure1.6 depicts two contacting dielectric materials, indicated as 1 and 2, with thicknesses d_1 and d_2, respectively. Following contact, these materials subsequently separate, resulting in charges accumulation on their surfaces due to triboelectrification. Under the assumption that equivalent yet opposite charges accumulate on both surfaces, the charge density on material 1's surface is '+σ', while material 2's surface bears '-σ'. This charge creation causes the induction of an electric potential, which results in the transfer of a charge quantity 'Q' between the two electrodes. In the framework of Gauss theorem, we can think of each material as an infinite number of dielectric plates. The electric field contained within dielectric material 1 (E_1), dielectric material 2 (E_2), and the intervening air space (E_3) may be calculated using this theorem [50].

$$E_1 = \frac{-Q}{S\varepsilon_0\varepsilon_{r1}} \tag{1.3}$$

$$E_2 = \frac{-Q}{S\varepsilon_0\varepsilon_{r2}} \tag{1.4}$$

$$E_3 = -\frac{-\frac{Q}{S}+\sigma(t)}{\varepsilon_0} \tag{1.5}$$

Here, S denotes the surface area of the plates, ε_0 represents the absolute permittivity, and ε_{r1} and ε_{r2} correspond to the relative permittivity of material 1 and 2, respectively.

The resulting electric potential between the two electrodes may be calculated as follows:

$$V = E_1 d_1 + E_2 d_2 + E_3 x(t) \tag{1.6}$$

Using the previous equations, we get:

$$V = -\frac{Q}{S}\left(\frac{d_1}{\varepsilon_{r1}} + \frac{d_2}{\varepsilon_{r2}} + x(t)\right) + \frac{\sigma x(t)}{\varepsilon_0} \tag{1.7}$$

This equation can be simplified further by incorporating d_0 as the effective thickness constant, which is equal to the sum of ($d_1/\varepsilon_{r1} + d_2/\varepsilon_{r2}$). As a result, the ultimate expression describing the

voltage created between the two electrodes is:

$$V = -\frac{Q}{S}\left(d_0 + x(t)\right) + \frac{\sigma x(t)}{\varepsilon_0} \tag{1.8}$$

This equation, often known as the V-Q-x relation, summarises the relationship describing the voltage generated between the two electrodes.

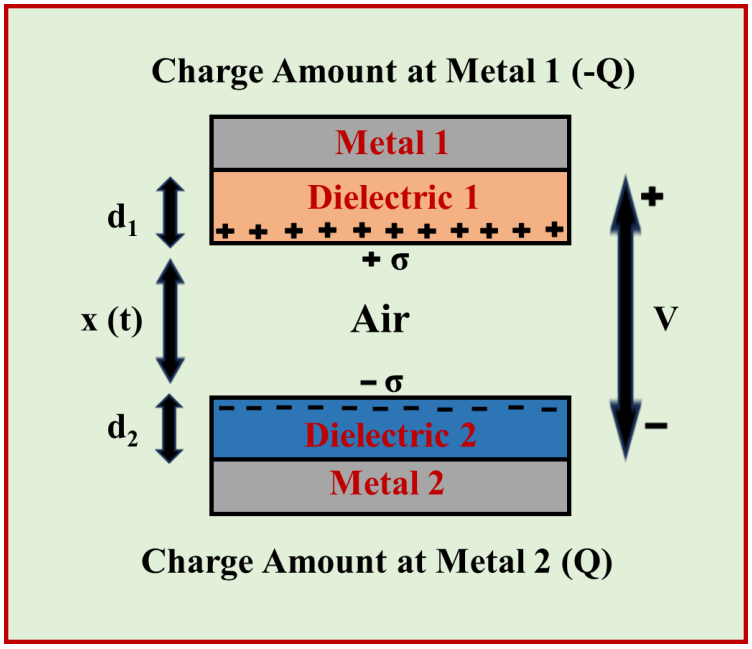

Figure 1.6 Illustration depicting the separation of the two interacting materials subsequent to the creation of equally opposing charge densities (σ) on their respective surfaces.

1.5 Design of Hybrid Device for Mechanical Energy Harvesting

A single device cannot capture many types of energy, therefore by combining two or more devices is a proficient and inventive technique for increasing energy harvesting efficiency. Within this context, the present study has realized the creation of hybrid systems by integrating both piezoelectric and triboelectric effects within a single nanogenerator.

Piezoelectric and triboelectric nanogenerators are both excellent at producing power from mechanical vibrations or motions. As a result, using two nanogenerators to generate electricity from a common mechanical force is a simple and effective technique. To attain this purpose, several techniques have been tried. Yang et al., for example, initiated the construction of a hybrid device in which vertically oriented ZnO nanorods serve as both the piezoelectric material and the contact material for the triboelectric effect [51]. A prevalent technique for device fabrication involves employing a piezoelectric polymer such as Polyvinylidene fluoride (PVDF) and its copolymers as the designated piezoelectric material [52-54]. Nonetheless,

despite several approaches developed to enhance piezoelectric properties of PVDF, researchers have yet to thoroughly study its optimisation to serve as an adept triboelectric material in its own right.

1.6 Polymers for Piezoelectric Nanogenerators and Applications

Flexible polymers have emerged as particularly favourable materials in the development of nanogenerators, whether they are piezoelectric or triboelectric in nature. Their ability to properly absorb vibrations, along with their eco-friendly composition and durability, makes them an excellent choice. This has attracted the interest of researchers towards electroactive polymers, which have found utility in a variety of applications, including actuators, sensors, and energy harvesting. Because of their diversified characteristics, they have acquired the label of smart materials [55]. Previously, it was thought that the concept of piezoelectric capabilities was limited to ceramic materials, however the discovery of piezoelectric characteristics in polymers began in 1963, when such qualities were discovered in two particular polymers: poly(vinyl chloride) (PVC) and poly(methyl methacrylate) (PMMA) [56]. Kepler was the first to notice the piezoelectric property of polyvinylidene fluoride (PVDF) [57]. Following that, Kepler and Anderson discovered the ferroelectric properties of PVDF in 1978 [56]. Other polymers with piezoelectric capabilities include parylene-C, Nylon-11, polyamide, poly(lactic-co-glycolic acid) (PLGA), and polylactic acid (PLLA) [55]. Among the many piezoelectric polymers, the ones containing PVDF and its copolymers have the greatest piezoelectric coefficients. Nonetheless, when compared to piezoceramics, their piezoelectric characteristics are low. The fundamental limitation of piezoceramics is their inability to be shaped to meet a variety of applications [58]. Furthermore, repetitive stress exposure frequently results in the formation of cracks over time, leaving them non-functional. As a result, current research efforts are primarily focused on the development of flexible piezoelectric polymers. These materials have an outstanding capacity to absorb mechanical vibrations and have the added benefit in fabrication of nanogenerator into a variety of shapes while remaining stable. Polyvinylidene fluoride (PVDF) has received a lot of attention in this field because of its biocompatibility, environmental stability, and most importantly its intrinsic piezoelectricity. Higher piezoelectric qualities are seen accompanying strong mechanical features among the range of piezoelectric nanostructures of 2D transition metal dichalcogenides (TMDCs) [59-61]. As a result, they are sustainable and attractive alternative for creating devices that capture mechanical energy. Furthermore, the high surface-to-volume ratio of these nanostructures allows them to easily integrate with polymeric chains in the formation of composite films, such as those created with

PVDF and PDMS [62, 63]. As a result, these composite films have outstanding mechanical properties. In the following part, we will devote our attention to exploring into the structure and characteristics of PVDF and 2D nanostructures, a crucial investigation within the scope of this thesis.

1.6.1 PVDF: A Ferroelectric Polymer

The polymer chain of polyvinylidene fluoride is composed of recurring CH_2-CF_2 monomer units. Predicated on the arrangement of these monomers, PVDF exhibits various crystalline phases (β, α, γ and δ), predominantly the β and α phases. In the β-phase, an all-trans conformation (TTTT) gives rise to its formation, while an alternate trans and gauche conformation (TGTG) leads to the α-phase [55]. The schematic depictions of the β and α phases of PVDF are depicted in Figure 1.7 (a) and (b), respectively. The substantial difference in electronegativity between hydrogen and carbon atoms compared to fluorine atoms engenders a pronounced dipole moment within each PVDF monomer unit. This dipole moment attains its highest value per unit cell due to the parallel alignment of monomer units in the β-phase. Conversely, the α-phase, characterized by an antiparallel monomer unit arrangement, results in a nullification of dipole moments, thus yielding no net dipole moment. As γ-phase is the intermediate stage between α, and β-phase, therefore, it also exhibit a dipole moment but less than that of β-phase [55, 64]. As a result, ensuring a sufficient fraction of β-phase content in PVDF becomes critical for maximising its viability for applications involving piezoelectric capabilities. The piezoelectric properties of PVDF are primarily determined by the presence of the electroactive polar β-phase [65-68].

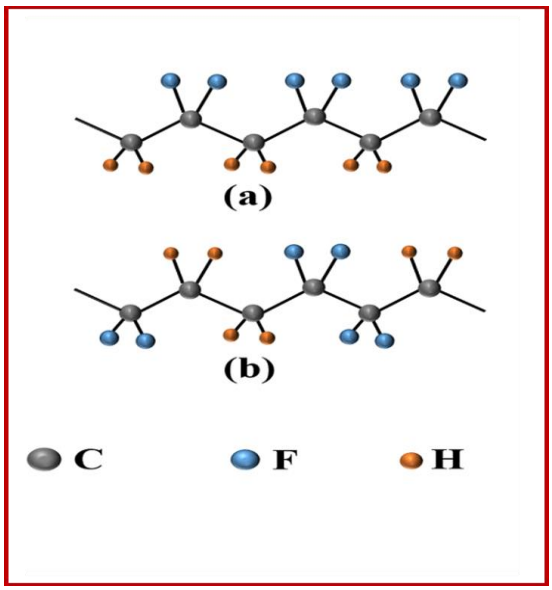

Figure 1.7 A schematic illustrating the orientation of (a) β-phase, (b) α –phase of PVDF

1.6.1.1 Methods for Enhancing the Piezoelectric Properties of PVDF

In order to efficiently utilise PVDF in energy harvesting systems, nucleation of β-phase is important. The β-phase in PVDF may be grown via sophisticated film preparation processes such as melt annealing [69], rapid cooling [70], low supercooling melt crystallisation [71], mechanical stretching [72], and the insertion of external fillers [73-75]. Among these strategies, the incorporation of external fillers offers significant advantages, owing to its ability to control the β-phase nucleation process. The introduction of nanofillers is well recognised to disturb PVDF ordered crystal structure, promoting the formation of crystalline electroactive β-phase. External nanofillers such as TiO_2 [76], $BiVO_4$ [77], Fe_3O_4 [74], CuS [73], and others have been incorporated into PVDF matrices to efficiently convert vibrational energy into electrical energy. The goal of this selective inclusion is to control the formation of the polar β-phase inside PVDF. In addition, nanofillers having inherent piezoelectric properties, such as rGo [78], MoS_2 [79], $(Na_{0.5}K_{0.5})NbO_3$ (NKN) [80], $PbZr_{0.52}Ti_{0.48}O_3$ (PZT) [81], $BaTiO_3$ [82], and, have been included. This purposeful addition intends to improve the piezoresponse of PVDF nanocomposites by utilising the piezoelectric capabilities of these nanofillers. Furthermore, critical nanoparticles with strong piezoelectric properties, such as PZT, have been easily integrated into the PVDF matrix to boost the overall piezoresponse. This enhancement includes both the β-phase contribution and the intrinsic piezoelectric properties of the material [81]. However, the toxicity and complicated production techniques, the use of PZT as a nanofiller in PVDF remains limited. Our method in this thesis focused on the introduction of piezoelectric 2D TMDC nanostructures into PVDF. Our research looks at the fundamental factors which are responsible for the enhancement in piezoelectric properties of PVDF. We have also investigated its ability as an active material within the context of the triboelectric nanogenerator.

1.6.2 2D TMDCs

Recently, 2D layered transition metal dichalcogenides (TMDCs) such as MoS_2, $MoSe_2$, $MoTe_2$, WS_2, WSe_2, etc. have been attracting attention of materials scientist due to their favourable electronic, optical, mechanical properties and non-toxic nature [83, 84]. Furthermore, 2D nanomaterials with an extraordinarily thin layer of crystalline structure are employed as fillers to improve the β-phase and dielectric characteristics of PVDF [83, 84]. The inherent piezoelectric properties of 2D materials is responsible for the enhanced piezoelectric output of the nanogenerator [59, 85]. The density functional theory (DFT) at the generalized gradient approximation level has been used for evaluating the piezoelectric properties in terms of the piezoelectric and stiffness coefficient for the 2D TMDCs [86]. It has been observed that

piezoelectric coefficient d_{11} for the flat 2D monolayer materials, which relates the polarization induced as a function of applied stress increases while moving downward until $MoTe_2$ across the group 16 (chalcogenides) of the periodic table. Duerloo et al. calculated the piezoelectric coefficients based on DFT results and is found to be 3.65, 4.55 and 7.39 pm/V for MoS_2, $MoSe_2$ and $MoTe_2$, respectively [59]. While, TENGs output performance is improved by the maximising surface charges generated by high surface to volume ratio and the ultrathin structure of 2D nanomaterials [87, 88]. To improve the output performance of PVDF based PENGs and TENGs, recent works have referenced 2D materials as fillers, such as MoS_2, $MoSe_2$, black phosphorus [89-91]. Therefore, these combined effect of addition of the nanofiller in the PVDF have opened the potential of fabricating flexible, low cost piezoelectric and triboelectric nanogenerator to enhance the nanogenerator performance for powering wide range of electronic devices. As a result, the present study suggests a feasible, economical approach to fabricate a high-performance piezoelectric and triboelectric hybrid nanogenerator by combining both the piezoelectric and triboelectric effects which may be utilized to drive the wearable electronic devices.

1.7 Primary Challenges and Strategies

Despite significant advances in the design and fabrication of nanogenerators for mechanical energy harvesting, there is still a significant gap in research concerning the comprehensive understanding of material properties that have a significant impact on the operational efficiency of both piezoelectric and triboelectric nanogenerators. Furthermore, the need to scale up energy generation from these devices is obvious in order to widen their scope of applicability for powering other devices. A path for efficiently improving material piezoelectric qualities occurs as a result of the rapid advances in nanotechnology, which allows us to carefully modify material properties through size manipulation. Among the alternatives, producing lead-free piezoelectric nano materials such as $NaNbO_3$, $BaTiO_3$, rGo, MoS_2, $MoSe_2$, etc. is a feasible choice. After combining these nanomaterials with PVDF, a nanocomposite is formed that enhances the piezoelectric properties of PVDF. Given that the effectiveness of a triboelectric nanogenerator is dependent on the surface features and material qualities of the contacting substance, research into optimising a piezoelectric polymer to produce a stronger triboelectric effect offers promise. The choice of a piezoelectric polymer over other polymers for the triboelectric nanogenerator is based on its ability to enable the combined effort of piezoelectric and triboelectric phenomena in a single device. Given that both devices require mechanical input for electricity generation, this combination offers the possibility of extracting more power from a single mechanical force. Given the wide range of mechanical movements spanning over various frequencies, it becomes critical

to combine devices in a manner that enables the simultaneous harnessing of higher and lower frequency mechanical vibrations within a singular apparatus for electricity generation.

1.8 Thesis Problem

The primary goal of present thesis is to improve the output efficiency of PVDF based nanogenerators while also investigating the impact of TMDCs as nanofillers on the overall performance of nanogenerators. The research also includes the use of PVDF nanocomposite films as the active component of triboelectric nanogenerators, as well as a thorough examination of the TENGs operational principles. Furthermore, a significant portion of the thesis highlights the advantages of developing hybrid devices with the goal of increasing output power and as a result, expanding the scope of nanogenerator applications.

1.8.1 Thesis Objectives

The central focus of this thesis involves the synthesis of nanocomposite films based on PVDF and 2D TMDCs and the subsequent investigation of their applications within energy harvesting devices, primarily through the utilization of piezoelectric and triboelectric effects.

The following are the key objectives of the thesis:

1. To study the effect of the different chalcogens (S, Se, SSe) in the output performance of the PVDF-TMDCs based flexible piezoelectric nanogenerator.
2. To study the effect of wt.% of MoS_2 on the piezo response of PVDF-MoS_2 composite based flexible piezoelectric nanogenerator.
3. To study the effect of MoS_2 wt% in the output performance of PDMS/PVDF-MoS_2 composite based flexible piezo-triboelectric hybrid nanogenerator.
4. To study the improved performance of composite flexible thin film based on Nylon/PVDF-$MoSe_2$ hybrid triboelectric nanogenerator with $MoSe_2$ wt.% variation.
5. To study the effect of variation of different polymers as second layer in the enhancement of triboelectric performance of the PVDF based triboelectric nanogenerator.

1.8.2 Thesis Layout

A thorough set of experiments and detailed analyses have been methodically carried out inside this thesis, all in accordance with the previously mentioned objectives.

The findings of current thesis are described in the subsequent chapters:

Chapter 1. Introduction

Chapter 1 gives the brief introduction about the need and the different ways to produce sustainable energy supplies using mechanical energy harvesters in order to complete the increasing demand of energy. This chapter deals with the significance of green energy and ideas to enhance the efficiency of mechanical energy harvesters. In the past few years, portable electronic gadgets have become more and more popular in a variety of fields, including wireless sensor networks, smart homes, health monitoring, artificial intelligence, human-machine interface, and the Internet of Things. The increasing demands for power have posed serious obstacles to the development of wireless and wearable devices. Because of their short lifespans, conventional batteries are subject to numerous constraints in wearable and wireless electronics. A renewable power source for wearable technology is highly desired to address this issue. For harvesting energy, numerous principles have been established over the years based on diverse mechanisms, such as piezoelectric, electromagnetic, and triboelectric phenomenon. Due to their wide range of potential uses, including energy harvesting from human motion, mechanical motion, wind, and flowing water, as well as self-powered sensors in various sensing applications, piezoelectric nanogenerators (PENG) and triboelectric nanogenerators (TENGs), which convert mechanical energy into electricity via triboelectric charging and electrostatic induction, have drawn significant attention. Thorough literature review of the mechanical energy harvesting has been composed in chapter 1.

Chapter 2. Synthesis and Characterization Techniques

Chapter 2 outlines various experimental methods which have been employed to synthesize and analyse the prepared samples, along with the pertinent theoretical underpinnings using COMSOL software. 2D Transition metal dichalcogenides (TMDCs) have attracted researchers attention because of their unique electronic, optical, mechanical properties and non-toxic nature. PVDF and its copolymers are also of great interest in the fabrication of PENG and TENG because of their lightweight, high flexibility, cost effective and simple processing. In the present chapter, hydrothermal technique used for the synthesis of TMDCs has been discussed first, after then methods used for the fabrication of PVDF and PVDF-TMDCs nanocomposite films by using drop casting and electrospinning have also discussed briefly.
Characterization methods used to examine prepared samples, such as powder X-ray diffraction (XRD), scanning electron microscope (SEM), Fourier transform infrared spectroscopy (FTIR), Raman, atomic force microscopy (AFM), kelvin probe force microscopy (KPFM), polarization-electric field (PE) loop tracer, dielectric analyser etc., are presented in depth.

Chapter 3. Effect of the different chalcogen atoms (S, Se, SSe) of transition metal dichalcogenides (TMDCs) on the output performance of the PVDF-TMDCs based flexible piezoelectric nanogenerator.

In this chapter, we have demonstrated a high performance piezoelectric nanogenerator based on PVDF/(TMDCs) for generating electrical power. The addition of 2D nanosheets of MoS_2, $MoSe_2$ and MoSSe in the PVDF matrix for studying flexible nanogenerators has been carried out. It was found that the piezoresponse of PVDF/TMDCs based nanogenerators was greatly enhanced in comparison to pristine PVDF as a function of chalcogen atoms (S, Se, SSe) of TMDCs. The effect of variable vibrating frequency applied is also investigated for all the nanogenerators and is found that all the devices shows the maximum response at a vibrating frequency of 7 Hz. The maximum output voltage, short circuit current of PVDF/TMDCs composite based devices reaches up to 31 V, 1.26 uA for PVDF/MoSSe which is 3.3 times higher than those of pure PVDF films. The excellent performances of PENG are ascribed to the synergistic contribution due to the nucleation of the electroactive polar β-phase content of the PVDF in the composite films, contribution of inherent piezoelectric property of TMDC (MoS_2, $MoSe_2$) due to in-plane asymmetry, and finally addition of piezoelectric contribution due to the breaking of out-of-plane symmetry in PVDF/MoSSe based PENG. The current study promises the usage of 2D TMDCs, which are ultrathin, mechanically stronger in the field of energy harvesting for self-powering wearable electronics.

Chapter 4. Effect of variation of weight percentage of MoS_2 in PVDF-MoS_2 drop casted films for flexible piezoelectric and triboelectric nanogenerator for powering electronic devices.

In the chapter 3, we have studied that the addition of TMDCs enhances the piezoelectric properties of PVDF, however, the concentration of nanofiller in the PVDF also contributes to the device output performance. To check the ideal concentration of nanofiller, we have fabricated different piezoelectric and triboelectric nanogenerators based on PVDF-MoS_2 by varying the weight percentage (0 %, 3%, 5 %, 7 wt %and 10 wt%) of MoS_2. The piezoelectric output of the PVDF was found to be increased due to the incorporation of MoS_2. In comparison to bare PVDF film, the piezoelectric nanogenerator based on 7 wt% of MoS_2 as filler in PVDF shows nearly 2-fold increase in output voltage from 9.4 V to 18.0 V. The triboelectric nanogenerator with 7 wt% of MoS_2 also exhibits maximum output voltage of 189 V and a short circuit current of 1.61 μA. The TENG with 7 wt% MoS_2 also produced a power density of

104.5 μWcm-^{2} which is ~2.7 times of the power density produced by the bare PVDF based TENG. The results show that 7 wt% of MoS_2 is the optimum amount of doping for both piezoelectric and triboelectric energy harvesting; above this level, the performance of the nanogenerator abruptly decreased due to MoS_2 agglomeration in the PVDF matrix. Further, PVDF-MoS_2/PDMS based piezo-tribo based hybrid nanogenerator (HNG) is fabricated which generated the power density of ~220 μWcm^{-2}. Our study reveals that inclusion of MoS_2 in the PVDF matrix stimulates the generation of β-phase and also the intrinsic piezoelectric properties which contributes in the overall enhancement of the piezoelectric output of PVDF. In addition to enhanced β-phase, the distribution of MoS_2 increase the surface roughness which increases the contact area and also boosts the surface potential and dielectric constant thereby increasing the triboelectric output of the device. Each of these factors combine to significantly increase the performance of the hybrid nanogenerator. The generated output power was used for powering of electronic stopwatch and scientific calculator.

Chapter 5. Energy harvesting performance of PVDF-$MoSe_2$ electrospun fiber based flexible nanogenerator for generating green hydrogen.

After the analysis of the effect of filler concentration, to further improve the efficiency of the PENG and TENG, in this chapter, the PVDF-$MoSe_2$ nanofibers were synthesized via electrospinning technique with different wt% of $MoSe_2$ (0 wt%, 3 wt%, 5 wt%, 7 wt% and 10 wt%) in PVDF fibre matrix. It has been reported that fabrication technique also plays an important role in the structural and morphological properties of thin films. As a result, the electrospun PVDF films exhibit increased piezoelectric characteristics without the post-poling step commonly utilised in other fabrication processes. In this chapter, we have developed a self-powered water splitting system for generation of H_2 as a source of green energy by capturing mechanical energy using fabricated triboelectric nanogenerator. We have shown that incorporation of $MoSe_2$ nanosheets can considerably improve the piezoelectric and triboelectric performance of PVDF. The PENG with 7 wt% of $MoSe_2$ has generated maximum output voltage of 64.8 V and a short circuit current of 13.4 μA. Furthermore, a high performance PVDF-$MoSe_2$/Nylon TENG based on this improved negative triboelectric material has been successfully produced. The TENG with 7 wt% of $MoSe_2$ exhibits excellent triboelectric performance by generating an output voltage of 113.6 V and a short-circuit current of 26.5 μA. TENG with $MoSe_2$ also generated a power density of 230.4 μW/cm2 that is 2.9 times more than the maximum power density produced by bare PVDF based TENG. The impact of tapping frequency, and impact force on the triboelectric performance of the TENG

has been also examined. Finally, a self-sustaining water splitting system for generation of hydrogen was presented by employing TENG as a power supply resource. As a result, the current study proposes a feasible, low-cost way for creating a high-performance triboelectric nanogenerator for the application of clean and sustainable energy.

Chapter 6. Effect of variation of triboelectric layer material on output performance of the PVDF-$MoSe_2$ based flexible triboelectric nanogenerator.

Therefore, after fabricating a high performance PVDF-$MoSe_2$ nanofiber based TENG, in the last part, we have studied the effect of triboelectric layer material on the output performance of the TENG device. In this study, the PVDF-$MoSe_2$ nanofiber film has been fixed as one of the triboelectric layers, whereas the second layer material has been varied including PTFE, PDMS, PET, Paper and Nylon. The TENG consisting of Nylon as second triboelectric material demonstrates the maximum power density of ~231 μWcm^{-2}. The effect of tapping frequency and force on the triboelectric output of PVDF-$MoSe_2$/Nylon was also studied and an increasing trend of output voltage and current is observed with increasing force and frequency thereby producing a maximum voltage of ~206 V. The increase in output performance of the TENG with increase in frequency is attributed to faster charge transfers process, when the contact frequency is higher. With the rise in contact force, the effective area and capacitance of the TENG also increases which further results in the enhancement of triboelectric output of the nanogenerator. This study proposes an effective approach for enhancing the performance of triboelectric nanogenerator just by selecting the suitable material.

Chapter 7. Conclusions and scope for future work

This chapter provides a summary of all findings in this work and comparison with available literature on different mechanical energy harvesters. This chapter also include the future scope of this research work and challenges.

References

[1] Z.L. Wang, Triboelectric nanogenerators as new energy technology for self-powered systems and as active mechanical and chemical sensors, ACS nano, 7,(2013), 9533-9557

[2] S.K. Ghosh, T.K. Sinha, B. Mahanty, D. Mandal, Self-poled efficient flexible “Ferroelectretic” nanogenerator: a new class of piezoelectric energy harvester, Energy Technology, 3,(2015), 1190-1197

[3] X. Zhang, X. Huang, C. Li, H. Jiang, Dye-sensitized solar cell with energy storage function through PVDF/ZnO nanocomposite counter electrode, Advanced Materials, 25,(2013), 4093-4096

[4] Z. Zhang, J. He, T. Wen, C. Zhai, J. Han, J. Mu, W. Jia, B. Zhang, W. Zhang, X. Chou, Magnetically levitated-triboelectric nanogenerator as a self-powered vibration monitoring sensor, Nano Energy, 33,(2017), 88-97

[5] B. Kumar, S.-W. Kim, Recent advances in power generation through piezoelectric nanogenerators, Journal of Materials Chemistry, 21,(2011), 18946-18958

[6] M.D.P. Emilio, Microelectronic circuit design for energy harvesting systems, Springer2017.

[7] R. Saidur, N.A. Rahim, M.R. Islam, K.H. Solangi, Environmental impact of wind energy, Renewable and sustainable energy reviews, 15,(2011), 2423-2430

[8] R. Tiwari, N.R. Babu, Recent developments of control strategies for wind energy conversion system, Renewable and Sustainable Energy Reviews, 66,(2016), 268-285

[9] T. Quan, Y. Wu, Y. Yang, Hybrid electromagnetic–triboelectric nanogenerator for harvesting vibration energy, Nano Research, 8,(2015), 3272-3280

[10] H. Liu, Y. Xia, T. Chen, Z. Yang, W. Liu, P. Wang, L. Sun, Study of a hybrid generator based on triboelectric and electromagnetic mechanisms, IEEE Sensors Journal, 17,(2017), 3853-3860

[11] J. Chen, G. Zhu, W. Yang, Q. Jing, P. Bai, Y. Yang, T.C. Hou, Z.L. Wang, Harmonic-resonator-based triboelectric nanogenerator as a sustainable power source and a self-powered active vibration sensor, Advanced materials, 25,(2013), 6094-6099

[12] Z.L. Wang, G. Zhu, Y. Yang, S. Wang, C. Pan, Progress in nanogenerators for portable electronics, Materials today, 15,(2012), 532-543

[13] J. Song, J. Zhou, Z.L. Wang, Piezoelectric and semiconducting coupled power generating process of a single ZnO belt/wire. A technology for harvesting electricity from the environment, Nano letters, 6,(2006), 1656-1662

[14] F.-R. Fan, Z.-Q. Tian, Z.L. Wang, Flexible triboelectric generator, Nano energy, 1,(2012), 328-334

[15] J. Wang, H. Zhang, Y. Xie, Z. Yan, Y. Yuan, L. Huang, X. Cui, M. Gao, Y. Su, W. Yang, Smart network node based on hybrid nanogenerator for self-powered multifunctional sensing, Nano Energy, 33,(2017), 418-426

[16] Y. Yang, G. Zhu, H. Zhang, J. Chen, X. Zhong, Z.-H. Lin, Y. Su, P. Bai, X. Wen, Z.L. Wang, Triboelectric nanogenerator for harvesting wind energy and as self-powered wind vector sensor system, ACS nano, 7,(2013), 9461-9468

[17] X. Fan, J. He, J. Mu, J. Qian, N. Zhang, C. Yang, X. Hou, W. Geng, X. Wang, X. Chou, Triboelectric-electromagnetic hybrid nanogenerator driven by wind for self-powered wireless transmission in Internet of Things and self-powered wind speed sensor, Nano Energy, 68,(2020), 104319

[18] X. Wang, S. Wang, Y. Yang, Z.L. Wang, Hybridized electromagnetic–triboelectric nanogenerator for scavenging air-flow energy to sustainably power temperature sensors, ACS nano, 9,(2015), 4553-4562

[19] W. Li, H. Guo, Y. Xi, C. Wang, M.S. Javed, X. Xia, C. Hu, WGUs sensor based on integrated wind-induced generating units for 360° wind energy harvesting and self-powered wind velocity sensing, RSC advances, 7,(2017), 23208-23214

[20] Y. Xie, S. Wang, L. Lin, Q. Jing, Z.-H. Lin, S. Niu, Z. Wu, Z.L. Wang, Rotary triboelectric nanogenerator based on a hybridized mechanism for harvesting wind energy, ACS nano, 7,(2013), 7119-7125

[21] G. Zhu, Y. Su, P. Bai, J. Chen, Q. Jing, W. Yang, Z.L. Wang, Harvesting water wave energy by asymmetric screening of electrostatic charges on a nanostructured hydrophobic thin-film surface, ACS nano, 8,(2014), 6031-6037

[22] X. Yang, S. Chan, L. Wang, W.A. Daoud, Water tank triboelectric nanogenerator for efficient harvesting of water wave energy over a broad frequency range, Nano Energy, 44,(2018), 388-398

[23] A. Ahmed, Z. Saadatnia, I. Hassan, Y. Zi, Y. Xi, X. He, J. Zu, Z.L. Wang, Self-powered wireless sensor node enabled by a duck-shaped triboelectric nanogenerator for harvesting water wave energy, Advanced Energy Materials, 7,(2017), 1601705

[24] X. Wang, B. Yang, J. Liu, C. Yang, A transparent and biocompatible single-friction-surface triboelectric and piezoelectric generator and body movement sensor, Journal of Materials Chemistry A, 5,(2017), 1176-1183

[25] C. Cui, X. Wang, Z. Yi, B. Yang, X. Wang, X. Chen, J. Liu, C. Yang, Flexible single-electrode triboelectric nanogenerator and body moving sensor based on porous Na2CO3/polydimethylsiloxane film, ACS applied materials & interfaces, 10,(2018), 3652-3659

[26] S.L. Zhang, Y.C. Lai, X. He, R. Liu, Y. Zi, Z.L. Wang, Auxetic foam-based contact-mode triboelectric nanogenerator with highly sensitive self-powered strain sensing capabilities to monitor human body movement, Advanced functional materials, 27,(2017), 1606695

[27] J. Qian, X. Wu, D.-S. Kim, D.-W. Lee, Seesaw-structured triboelectric nanogenerator for scavenging electrical energy from rotational motion of mechanical systems, Sensors and Actuators A: Physical, 263,(2017), 600-609

[28] J. Chen, P. Ding, R. Pan, W. Xuan, D. Guo, Z. Ye, W. Yin, H. Jin, X. Wang, S. Dong, Self-powered transparent glass-based single electrode triboelectric motion tracking sensor array, Nano Energy, 34,(2017), 442-448

[29] Z. Li, X. Zhang, G. Li, In situ ZnO nanowire growth to promote the PVDF piezo phase and the ZnO–PVDF hybrid self-rectified nanogenerator as a touch sensor, Physical Chemistry Chemical Physics, 16,(2014), 5475-5479

[30] Z.L. Wang, J. Song, Piezoelectric nanogenerators based on zinc oxide nanowire arrays, Science, 312,(2006), 242-246

[31] K. Xia, Z. Zhu, H. Zhang, Z. Xu, A triboelectric nanogenerator as self-powered temperature sensor based on PVDF and PTFE, Applied Physics A, 124,(2018), 1-7

[32] S.-J. Park, S. Lee, M.-L. Seol, S.-B. Jeon, H. Bae, D. Kim, G.-H. Cho, Y.-K. Choi, Self-sustainable wind speed sensor system with omni-directional wind based triboelectric generator, Nano Energy, 55,(2019), 115-122

[33] Y.-F. Lin, J. Song, Y. Ding, S.-Y. Lu, Z.L. Wang, Piezoelectric nanogenerator using CdS nanowires, Applied Physics Letters, 92,(2008),

[34] J.M. Wu, C.C. Kao, Self-powered pendulum and micro-force active sensors based on a ZnS nanogenerator, RSC Advances, 4,(2014), 13882-13887

[35] M.-G. Kang, W.-S. Jung, C.-Y. Kang, S.-J. Yoon, MDPI, pp. 5.

[36] G. Poulin-Vittrant, C. Oshman, C. Opoku, A.S. Dahiya, N. Camara, D. Alquier, L.P.T.H. Hue, M. Lethiecq, Fabrication and characterization of ZnO nanowire-based piezoelectric nanogenerators for low frequency mechanical energy harvesting, Physics Procedia, 70,(2015), 909-913

[37] S. Xu, Y. Qin, C. Xu, Y. Wei, R. Yang, Z.L. Wang, Self-powered nanowire devices, Nature nanotechnology, 5,(2010), 366-373

[38] R. Yang, Y. Qin, L. Dai, Z.L. Wang, Power generation with laterally packaged piezoelectric fine wires, Nature nanotechnology, 4,(2009), 34-39

[39] X. Chen, S. Xu, N. Yao, Y. Shi, 1.6 V nanogenerator for mechanical energy harvesting using PZT nanofibers, Nano letters, 10,(2010), 2133-2137

[40] J. Gong, B. Xu, X. Tao, Breath figure micromolding approach for regulating the microstructures of polymeric films for triboelectric nanogenerators, ACS applied materials & interfaces, 9,(2017), 4988-4997

[41] R. Li, Y. Li, Y. Zhao, Y. Li, Y. Li, Harvest of ocean energy by triboelectric generator technology, Applied Physics Reviews, 5,(2018),

[42] S. Li, W. Peng, J. Wang, L. Lin, Y. Zi, G. Zhang, Z.L. Wang, All-elastomer-based triboelectric nanogenerator as a keyboard cover to harvest typing energy, ACS nano, 10,(2016), 7973-7981

[43] A. Chandrasekhar, N.R. Alluri, V. Vivekananthan, Y. Purusothaman, S.-J. Kim, A sustainable freestanding biomechanical energy harvesting smart backpack as a portable-wearable power source, Journal of Materials Chemistry C, 5,(2017), 1488-1493

[44] M. Febbo, S.P. Machado, C.D. Gatti, J.M. Ramirez, An out-of-plane rotational energy harvesting system for low frequency environments, Energy conversion and management, 152,(2017), 166-175

[45] Z.L. Wang, A.C. Wang, On the origin of contact-electrification, Materials Today, 30,(2019), 34-51

[46] H. Feng, C. Zhao, P. Tan, R. Liu, X. Chen, Z. Li, Nanogenerator for biomedical applications, Advanced Healthcare Materials, 7,(2018), 1701298

[47] Z.L. Wang, L. Lin, J. Chen, S. Niu, Y. Zi, Z.L. Wang, L. Lin, J. Chen, S. Niu, Y. Zi, Triboelectric nanogenerator: single-electrode mode, Springer2016.

[48] Z.L. Wang, L. Lin, J. Chen, S. Niu, Y. Zi, Z.L. Wang, L. Lin, J. Chen, S. Niu, Y. Zi, Triboelectrification, Triboelectric Nanogenerators,(2016), 1-19

[49] Z.L. Wang, L. Lin, J. Chen, S. Niu, Y. Zi, Z.L. Wang, L. Lin, J. Chen, S. Niu, Y. Zi, Triboelectric nanogenerator: Vertical contact-separation mode, Triboelectric nanogenerators,(2016), 23-47

[50] S. Niu, S. Wang, L. Lin, Y. Liu, Y.S. Zhou, Y. Hu, Z.L. Wang, Theoretical study of contact-mode triboelectric nanogenerators as an effective power source, Energy & Environmental Science, 6,(2013), 3576-3583

[51] X. Yang, W.A. Daoud, Triboelectric and piezoelectric effects in a combined tribo-piezoelectric nanogenerator based on an interfacial ZnO nanostructure, Advanced Functional Materials, 26,(2016), 8194-8201

[52] W.-S. Jung, M.-G. Kang, H.G. Moon, S.-H. Baek, S.-J. Yoon, Z.-L. Wang, S.-W. Kim, C.-Y. Kang, High output piezo/triboelectric hybrid generator, Sci Rep, 5,(2015), 9309

[53] X. Chen, M. Han, H. Chen, X. Cheng, Y. Song, Z. Su, Y. Jiang, H. Zhang, A wave-shaped hybrid piezoelectric and triboelectric nanogenerator based on P (VDF-TrFE) nanofibers, Nanoscale, 9,(2017), 1263-1270

[54] X. Wang, B. Yang, J. Liu, Y. Zhu, C. Yang, Q. He, A flexible triboelectric-piezoelectric hybrid nanogenerator based on P (VDF-TrFE) nanofibers and PDMS/MWCNT for wearable devices, Sci Rep, 6,(2016), 36409

[55] P. Martins, A.C. Lopes, S. Lanceros-Mendez, Electroactive phases of poly (vinylidene fluoride): Determination, processing and applications, Progress in polymer science, 39,(2014), 683-706

[56] H.S. Nalwa, Ferroelectric polymers: chemistry: physics, and applications, CRC Press1995.

[57] P. Costa, J. Nunes-Pereira, N. Pereira, N. Castro, S. Gonçalves, S. Lanceros-Mendez, Recent progress on piezoelectric, pyroelectric, and magnetoelectric polymer-based energy-harvesting devices, Energy technology, 7,(2019), 1800852

[58] J. Nunes-Pereira, V. Sencadas, V. Correia, V.F. Cardoso, W. Han, J.G. Rocha, S. Lanceros-Méndez, Energy harvesting performance of BaTiO3/poly (vinylidene fluoride–trifluoroethylene) spin coated nanocomposites, Composites Part B: Engineering, 72,(2015), 130-136

[59] K.-A.N. Duerloo, M.T. Ong, E.J. Reed, Intrinsic piezoelectricity in two-dimensional materials, The Journal of Physical Chemistry Letters, 3,(2012), 2871-2876

[60] S. Manzeli, D. Ovchinnikov, D. Pasquier, O.V. Yazyev, A. Kis, 2D transition metal dichalcogenides, Nature Reviews Materials, 2,(2017), 1-15

[61] S.J. McDonnell, R.M. Wallace, Atomically-thin layered films for device applications based upon 2D TMDC materials, Thin Solid Films, 616,(2016), 482-501

[62] A.P. Guo, X.J. Zhang, S.W. Wang, J.Q. Zhu, L. Yang, G.S. Wang, Excellent microwave absorption and electromagnetic interference shielding based on reduced graphene oxide@ MoS2/poly (vinylidene fluoride) composites, ChemPlusChem, 81,(2016), 1305-1311

[63] J.-H. Lin, Y.-H. Tsao, M.-H. Wu, T.-M. Chou, Z.-H. Lin, J.M. Wu, Single-and few-layers MoS2 nanocomposite as piezo-catalyst in dark and self-powered active sensor, Nano Energy, 31,(2017), 575-581

[64] J.P. Lee, J.W. Lee, J.M. Baik, The progress of PVDF as a functional material for triboelectric nanogenerators and self-powered sensors, Micromachines, 9,(2018), 532

[65] H.H. Singh, S. Singh, N. Khare, Design of flexible PVDF/NaNbO3/RGO nanogenerator and understanding the role of nanofillers in the output voltage signal, Composites Science and Technology, 149,(2017), 127-133

[66] B. Dutta, E. Kar, N. Bose, S. Mukherjee, Significant enhancement of the electroactive β-phase of PVDF by incorporating hydrothermally synthesized copper oxide nanoparticles, RSC advances, 5,(2015), 105422-105434

[67] L. Jin, S. Ma, W. Deng, C. Yan, T. Yang, X. Chu, G. Tian, D. Xiong, J. Lu, W. Yang, Polarization-free high-crystallization β-PVDF piezoelectric nanogenerator toward self-powered 3D acceleration sensor, Nano Energy, 50,(2018), 632-638

[68] B. Bera, M.D. Sarkar, Piezoelectricity in PVDF and PVDF based piezoelectric nanogenerator: a concept, IOSR J. Appl. Phys, 9,(2017), 95-99

[69] H. Pan, B. Na, R. Lv, C. Li, J. Zhu, Z. Yu, Polar phase formation in poly (vinylidene fluoride) induced by melt annealing, Journal of Polymer Science Part B: Polymer Physics, 50,(2012), 1433-1437

[70] A. Gradys, P. Sajkiewicz, S. Adamovsky, A. Minakov, C. Schick, Crystallization of poly (vinylidene fluoride) during ultra-fast cooling, Thermochimica Acta, 461,(2007), 153-157

[71] B.S. Ince-Gunduz, R. Alpern, D. Amare, J. Crawford, B. Dolan, S. Jones, R. Kobylarz, M. Reveley, P. Cebe, Impact of nanosilicates on poly (vinylidene fluoride) crystal polymorphism: Part 1. Melt-crystallization at high supercooling, Polymer, 51,(2010), 1485-1493

[72] A. Salimi, A.A. Yousefi, Analysis method: FTIR studies of β-phase crystal formation in stretched PVDF films, Polymer Testing, 22,(2003), 699-704

[73] X.-J. Zhang, G.-S. Wang, Y.-Z. Wei, L. Guo, M.-S. Cao, Polymer-composite with high dielectric constant and enhanced absorption properties based on graphene–CuS nanocomposites and polyvinylidene fluoride, Journal of Materials Chemistry A, 1,(2013), 12115-12122

[74] O.D. Jayakumar, B.P. Mandal, J. Majeed, G. Lawes, R. Naik, A.K. Tyagi, Inorganic–organic multiferroic hybrid films of Fe 3 O 4 and PVDF with significant magneto-dielectric coupling, Journal of Materials Chemistry C, 1,(2013), 3710-3715

[75] S.K. Karan, R. Bera, S. Paria, A.K. Das, S. Maiti, A. Maitra, B.B. Khatua, An approach to design highly durable piezoelectric nanogenerator based on self-poled PVDF/AlO-rGO flexible nanocomposite with high power density and energy conversion efficiency, Advanced Energy Materials, 6,(2016), 1601016

[76] X. Cao, J. Ma, X. Shi, Z. Ren, Effect of TiO2 nanoparticle size on the performance of PVDF membrane, Applied Surface Science, 253,(2006), 2003-2010

[77] S. Sarkar, S. Garain, D. Mandal, K.K. Chattopadhyay, Electro-active phase formation in PVDF–BiVO 4 flexible nanocomposite films for high energy density storage application, RSC Advances, 4,(2014), 48220-48227

[78] M. Zeyrek Ongun, S. Oguzlar, E.C. Doluel, U. Kartal, M. Yurddaskal, Enhancement of piezoelectric energy-harvesting capacity of electrospun β-PVDF nanogenerators by adding GO and rGO, Journal of Materials Science: Materials in Electronics, 31,(2020), 1960-1968

[79] S.S. Nardekar, K. Krishnamoorthy, P. Pazhamalai, S. Sahoo, S.J. Kim, MoS2 quantum sheets-PVDF nanocomposite film based self-poled piezoelectric nanogenerators and photovoltaically self-charging power cell, Nano Energy, 93,(2022), 106869

[80] H.B. Kang, C.S. Han, J.C. Pyun, W.H. Ryu, C.-Y. Kang, Y.S. Cho, (Na, K) NbO3 nanoparticle-embedded piezoelectric nanofiber composites for flexible nanogenerators, Composites Science and Technology, 111,(2015), 1-8

[81] X. Guan, Y. Zhang, H. Li, J. Ou, PZT/PVDF composites doped with carbon nanotubes, Sensors and Actuators A: Physical, 194,(2013), 228-231

[82] Y. Niu, K. Yu, Y. Bai, H. Wang, Enhanced dielectric performance of BaTiO 3/PVDF composites prepared by modified process for energy storage applications, IEEE transactions on ultrasonics, ferroelectrics, and frequency control, 62,(2015), 108-115

[83] L. Lu, W. Ding, J. Liu, B. Yang, Flexible PVDF based piezoelectric nanogenerators, Nano Energy, 78,(2020), 105251

[84] S.K. Ghosh, D. Mandal, Piezoelectricity of 2D materials and its applications toward mechanical energy harvesting, 2D Nanomaterials for Energy Applications, Elsevier2020, pp. 1-38.

[85] M.N. Blonsky, H.L. Zhuang, A.K. Singh, R.G. Hennig, Ab initio prediction of piezoelectricity in two-dimensional materials, ACS nano, 9,(2015), 9885-9891

[86] R. Hinchet, U. Khan, C. Falconi, S.-W. Kim, Piezoelectric properties in two-dimensional materials: Simulations and experiments, Materials Today, 21,(2018), 611-630

[87] L. Shi, H. Jin, S. Dong, S. Huang, H. Kuang, H. Xu, J. Chen, W. Xuan, S. Zhang, S. Li, High-performance triboelectric nanogenerator based on electrospun PVDF-graphene nanosheet composite nanofibers for energy harvesting, Nano Energy, 80,(2021), 105599

[88] S. Tu, Q. Jiang, X. Zhang, H.N. Alshareef, Large Dielectric Constant Enhancement in MXene Percolative Polymer Composites, ACS Nano, 12,(2018), 3369-3377

[89] V. Singh, D. Meena, H. Sharma, A. Trivedi, B. Singh, Investigating the role of chalcogen atom in the piezoelectric performance of PVDF/TMDCs based flexible nanogenerator, Energy, 239,(2022), 122125

[90] P. Cui, K. Parida, M.-F. Lin, J. Xiong, G. Cai, P.S. Lee, Transparent, Flexible Cellulose Nanofibril–Phosphorene Hybrid Paper as Triboelectric Nanogenerator, Advanced Materials Interfaces, 4,(2017), 1700651

[91] C. Wu, T.W. Kim, J.H. Park, H. An, J. Shao, X. Chen, Z.L. Wang, Enhanced Triboelectric Nanogenerators Based on MoS2 Monolayer Nanocomposites Acting as Electron-Acceptor Layers, ACS Nano, 11,(2017), 8356-8363

[92] R. Zhang, H. Olin, Material choices for triboelectric nanogenerators: A critical review, EcoMat, 2,(2020), e12062

CHAPTER 2

Synthesis and Characterization Techniques

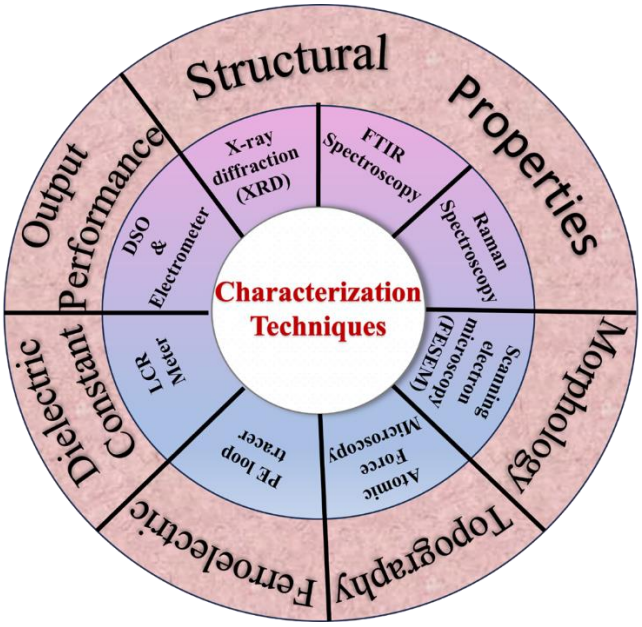

This chapter provides comprehensive insights into the synthesis of nanostructured materials, the preparation of nanocomposite films, and the variety of characterization techniques employed in the scope of this research. Additionally, it delves into the fabrication process of nanogenerators and instruments used for the electrical characterization of the fabricated devices. The hydrothermal approach is used to synthesize nanostructured materials, whereas the drop-casting process and electrospinning technique is used to fabricate nanocomposite films. X-ray diffraction (XRD) is used to examine the crystal structure of the synthesized nanostructures and films. Quantification of distinct phases within the films is conducted using Fourier transform infrared spectroscopy (FTIR). The surface morphology is explored through scanning electron microscopy (SEM) and transmission electron microscopy (TEM). Atomic force microscopy (AFM) is used to thoroughly evaluate surface topography. Polarisation versus electric field (P-E) loop measurements and Kelvin probe force microscopy (KPFM) are used to determine the ferroelectric properties and surface potential distribution of nanocomposite films. Thermal evaporation is used to deposit metal electrodes on the synthesized thin films in order to fabricate nanogenerators. This chapter also encompasses the determination of the dielectric constant, as well as voltage and current measurements of the fabricated devices. All of these approaches are briefly summarized in this chapter.

2.1 Synthesis of Transition Metal Dichalcogenides (MoS_2, $MoSe_2$ and MoSSe)

Various techniques are available for the synthesis and modification of TMDCs, enabling the tailoring of structures and properties to meet diverse applications. These approaches may be divided into two categories: 1) Top down, and 2) Bottom up. The Top-down strategy involves exfoliating bulk material into layers by overcoming interlayer forces such as Van der Waals interactions using methods such as mechanical, chemical, or ultrasonic means. The Bottom-up approach, on the other hand, comprises the building of nanosheets from individual atoms, in which precursor materials comprising Molybdenum (Mo), Sulphur (S) and Selenium (Se) atoms are first dissolved, then assembled into MoS_2, $MoSe_2$ and MoSSe structures. The selection of an appropriate synthesis route is crucial before delving into property investigation and targeted applications. Achieving successful commercialization and industrialization necessitates the synthesis of high yields of quality 2D nanomaterials [1]. Thus, for the synthesis of TMDCs nanostructures in our work, we used a simple and ecologically hydrothermal approach.

2.1.1 Hydrothermal Synthesis Route

Karl Emil von Schafhäutl, a German geologist, published the first report of crystal formation by hydrothermal techniques in 1845. Subsequently, a collaborative effort of researchers and scientists worldwide has contributed to the advancement of this technique. Hydrothermal synthesis is the process of creating nanomaterials by chemical reactions that occur within a sealed stainless-steel autoclave lined with Teflon and loaded with reagents dissolved in water, all under particular temperature and pressure conditions. A precise volume of aqueous reagents is poured in the Teflon liner to provide the pressure required to produce nanomaterials with desired properties and morphology. Also, it is essential to prevent overflow of Teflon during the reaction. A significant yield of well-crystallized nanomaterials may be obtained by optimising temperature, pressure, and reaction time in a high-temperature oven [2]. Figure 2.1 depicts the hydrothermal autoclave arrangement used for this purpose.

The constituents involved in the hydrothermal reaction are detailed as follows:

1. Reactant Precursors: These compounds are the initial reactants that engage in chemical reactions within appropriate solvents, ultimately resulting in the formation of the intended final product.

2. Mineralizing Agents and Supplementary Additives: Throughout the reaction, diverse acids and bases are incorporated to achieve a specific pH level. These compounds, referred to

as mineralizers, play a crucial role in the process. Additionally, there are supplementary additives like reducing agents, chelating agents, capping agents, and stabilizers. These additives are essential for shaping the desired morphology of the resultant nanomaterial.

The Hydrothermal method offers several advantages, including:

1. This technique is well-suited for the economical and large-scale production of nanomaterials.

2. The method enables precise control over the size and morphology of the resulting nanomaterials, contributing to tailored material properties.

3. Hydrothermal synthesis can be seamlessly integrated with other techniques such as sonochemical and electrochemical microwave synthesis, thereby expanding the possibilities for creating novel nanomaterials.

4. The setup for hydrothermal synthesis is straightforward, facilitating its repeated use for multiple cycles of nanomaterial synthesis.

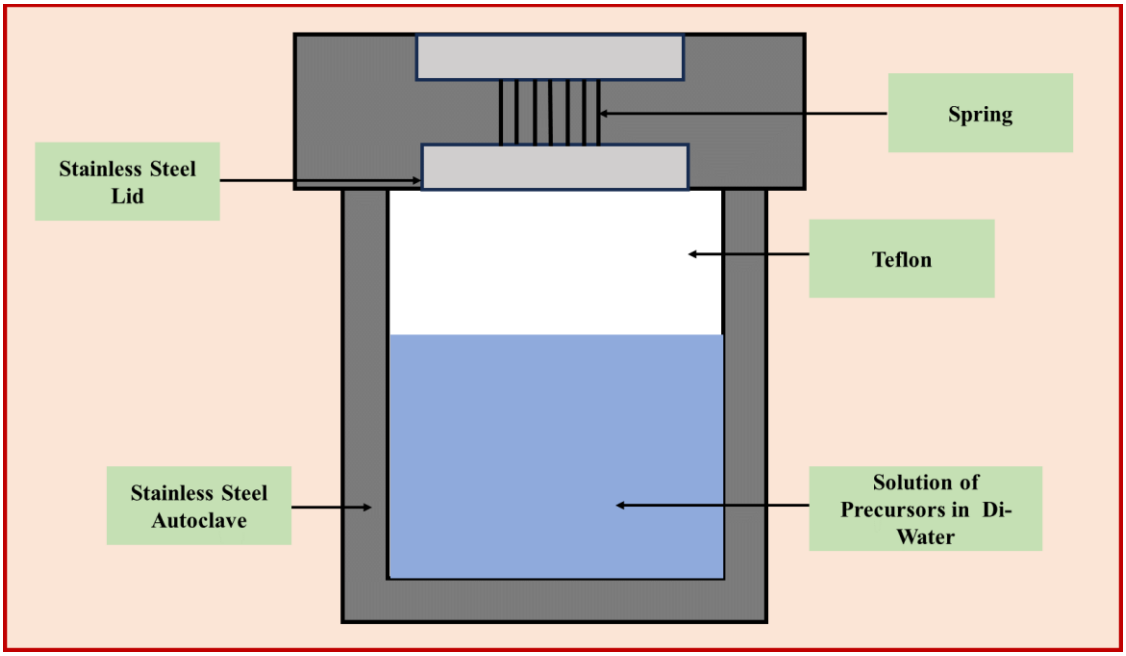

Figure 2.1 Schematic of autoclave used for hydrothermal synthesis

2.2 Deposition of Thin Films

Drop casting and Electrospinning techniques were used for the fabrication of thin films.

2.2.1 Drop Casting Method

The drop-casting approach was used to create flexible nanocomposite films in this work, which is a simple procedure that includes dissolving solutes in specified solvents at a constant

concentration. The drop-casting method is a widely used technique for depositing thin films onto various substrates. It offers a straightforward and cost-effective approach to create thin films with controlled thickness and composition. This method is particularly suitable for research and development purposes, where precise control over film properties is essential. The concentration of the solutes in the solution can be adjusted to achieve the desired properties of the thin film. The solution is then mixed thoroughly through magnetic stirring to ensure homogeneity. A predetermined volume of the solution is drawn into a micropipette and deposited onto a flat substrate, such as a glass substrate as shown in Figure 2.2. By carefully controlling the volume of the solution and the rate of deposition, a uniform film can be achieved on the substrate. The coated substrate was subsequently dried within a temperature-controlled oven.

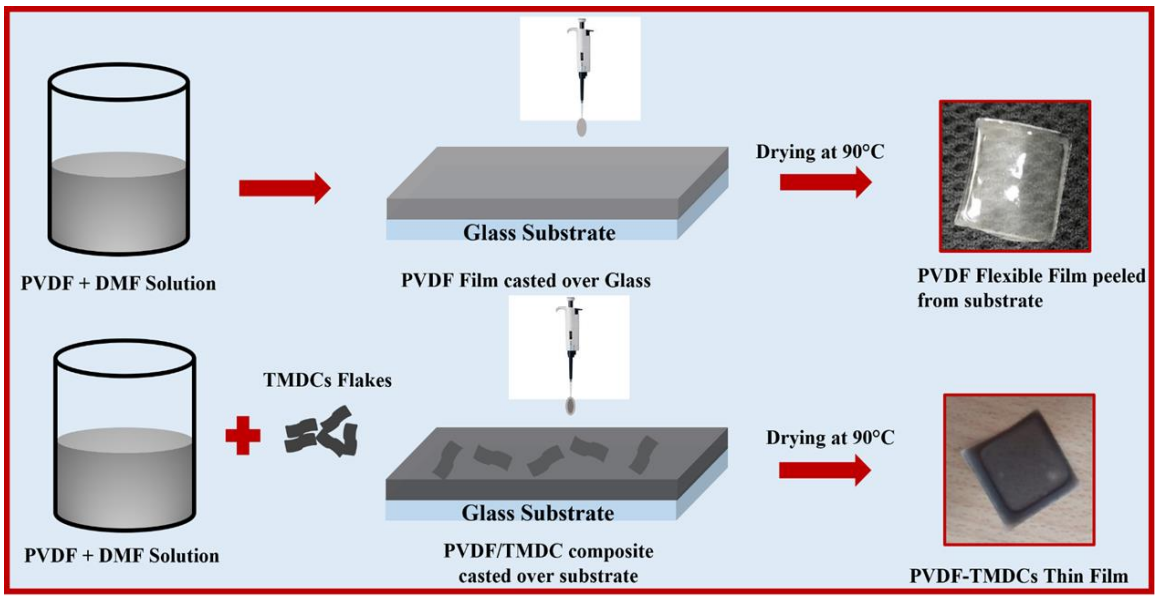

Figure 2.2 Schematic showing the synthesis of thin films via drop casting technique

One of the benefits of the drop-casting method is its simplicity and versatility. It enables researchers to quickly investigate the effects of different solute concentrations, solvent selections, and deposition circumstances on the resultant thin film characteristics. However, it's important to note that the method may result in some degree of film thickness variation, and the final film characteristics can be influenced by factors like solvent evaporation rate and substrate surface properties.

2.2.2 Electrospinning Technique

The electrospinning method is a versatile and widely employed technique for fabricating nanofiber-based thin films. It offers a precise control over the morphology, structure, and

properties of nanofibers, making it a valuable approach in various fields such as materials science, tissue engineering, and electronics. The electrospinning process involves the use of an electric field to create a thin continuous jet of polymer solution or melt from a charged needle or nozzle. This jet undergoes elongation and thinning due to electrostatic repulsion, resulting in the formation of ultrafine fibers that are collected onto a grounded substrate, typically in the form of a rotating drum or a stationary collector.

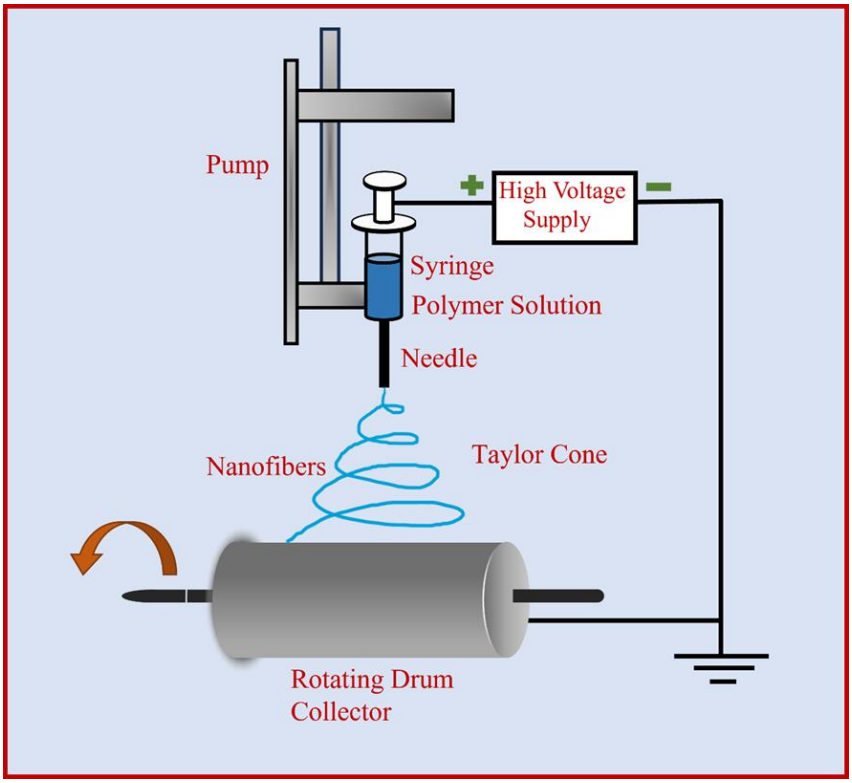

Figure 2.3 Schematic illustration of electrospinning system showing the fabrication of nanofibers.

The basic setup consists of a high-voltage power supply connected to the needle or nozzle, a syringe or reservoir containing the polymer solution, and a grounded collector as shown in the Figure 2.3. As the polymer solution is ejected from the needle, the electric field induces charge separation in the solution, causing the solvent to evaporate rapidly and leaving behind solid polymer fibers. Several factors influence the electrospinning process, including solution viscosity, electrical field intensity, distance between the needle and collector, flow rate, and surrounding factors. These variables together determine fibre diameter, alignment, and uniformity. Researchers may modify the final nanofiber shape to match specific requirements by altering these factors. Furthermore, electrospinning enables the fabrication of continuous

and porous nanofiber networks with high surface area-to-volume ratios, making them useful for a variety of applications.

2.3 Characterization Techniques

Various characterization techniques are employed to confirm the successful formation of TMDCs nanostructures and PVDF-TMDCs based thin films. X-ray diffraction (XRD) is used to begin the structural study, which is then followed by morphological analyses using scanning electron microscopy (SEM), field emission scanning electron microscopy (FESEM), and transmission electron microscopy (TEM). Raman spectroscopy is also used to confirm the presence of multilayer structures. To investigate the attachment of desirable functional groups, Fourier transform infrared spectroscopy (FTIR) is used. Additionally, atomic force microscopy (AFM) is used to analyse the topography and surface potential of the thin films were measured using KPFM. This section that follows offers a brief review of the operating principles of each of these characterisation approaches that we have used in our work.

2.3.1 X-ray Diffraction (XRD)

X-ray Diffraction (XRD) is utilized for a wide range of applications including crystallography, the identification of compounds, measurement of strain, determination of crystallite size, assessment of coefficients of expansion and densities, investigation of crystal texture, quantification of sample crystallinity, evaluation of dislocation density, and various other analytical processes [3]. Almost a century has passed since the influential contributions of Debye, Scherrer, and Hull in 1916-17, which represented the first ventures into powder X-ray diffraction research [4, 5]. While these pioneers and others established the fundamental concepts of powder diffraction in the early years, the unanticipated advancement of computing technology and its computational powers in the twenty-first century could not have been predicted at the time. Hugo Rietveld brought a dramatic change in the field of powder diffraction around fifty years after the development of the first powder diffraction patterns. This shift was driven by the widespread availability of computational power, as demonstrated by his innovative concept of computer-assisted comprehensive fitting of entire powder patterns. This was a watershed moment in the history of powder diffraction analysis. In modern practise, sophisticated algorithms are used to analyse and recognise crystal structures inside powder samples. The goal of this historical overview is to highlight significant advances in the field of powder diffraction throughout the preceding century. These advances include the first transmission experiments and the identification of fundamental cubic crystal formations, which

culminated in modern approaches that allow for the detailed refining of thousands of atoms contained inside a single unit cell [6].

A vacuum tube is used to produce X-rays. These x-rays are type of electromagnetic waves with wavelengths ranging from 0.1 Å to 100 Å. Electromagnetic waves with wavelengths ranging from 0.5 Å to 2.5 Å are used during diffracting from crystals because of the same size of crystals. The schematic of x-ray generation setup is shown in Figure 2.4 which comprises of the x-ray tube, and a vacuum chamber with a cathode and anode. The cathode is tungsten filament, whereas the anode is copper metal. The tungsten filament emits high-energy electrons that rush towards the anode with a powerful accelerating force ranging from 30 to 60 kV. When these high-energy electrons collide with copper metal, they eject the electrons from the innermost shell. As a result, electrons from the L and M shells move to the K shell to fill the vacant electron positions. This process generates radiations known as CuK_{α} and CuK_{β}, with wavelengths of 1.54 Å (from L to K) and 1.39 Å (from M to K) respectively. To attain the desired monochromatic radiation of 1.54 Å, a filter made of nickel (Ni) is employed. This filter effectively eliminates the CuK_{β} radiation with a wavelength of 1.39 Å [7].

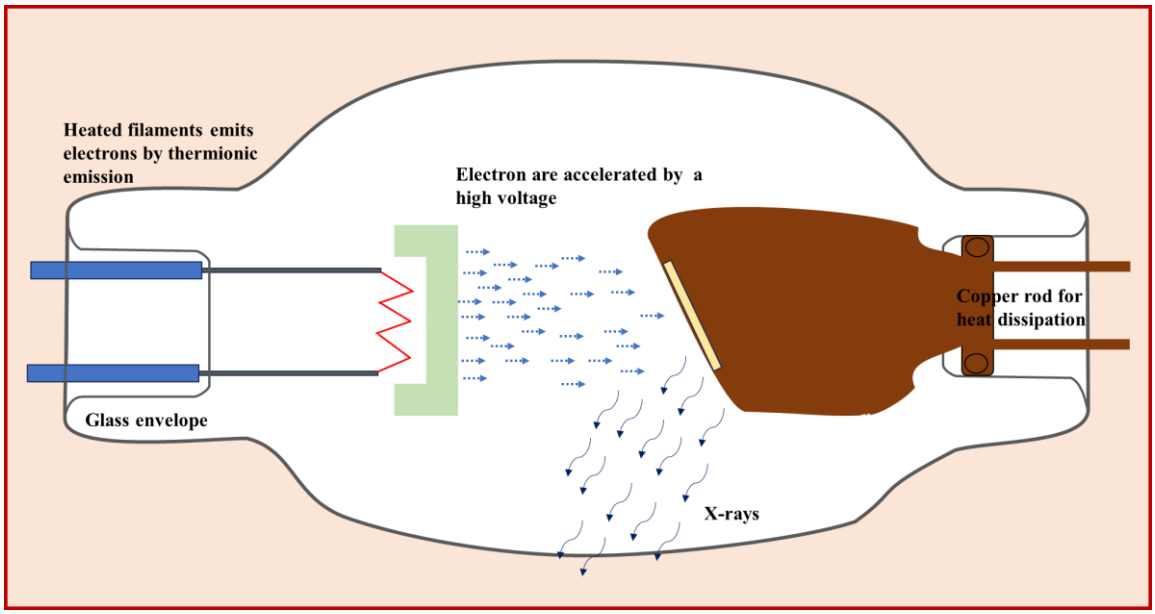

Figure 2.4 Schematic showing the generation of X-rays in X-ray tube.

W. H. Bragg and W. L. Bragg discovered in 1913 that crystalline materials reveal a characteristic pattern of X-rays being reflected. This phenomenon is identified by significant scattered radiation peaks at certain incidence angles and wavelengths. According to W. L. Bragg's postulation, a crystal can be regarded as a congregation of parallel planes, with a

specified spacing indicated as 'd'. When X-rays are reflected by ions inside these parallel planes, a distinct and sharp peak arises, and when these rays originate from successive parallel planes, they participate in constructive interference, as seen in Figure 2.5. To establish Bragg's condition, it's necessary for the path difference between these rays, represented as 2dsinθ, to be equivalent to an even integer multiple of half the wavelength, given by the equation:

$$2dsin\theta = n\lambda \tag{2.1}$$

Here, the integer "n" denotes the order of diffraction.

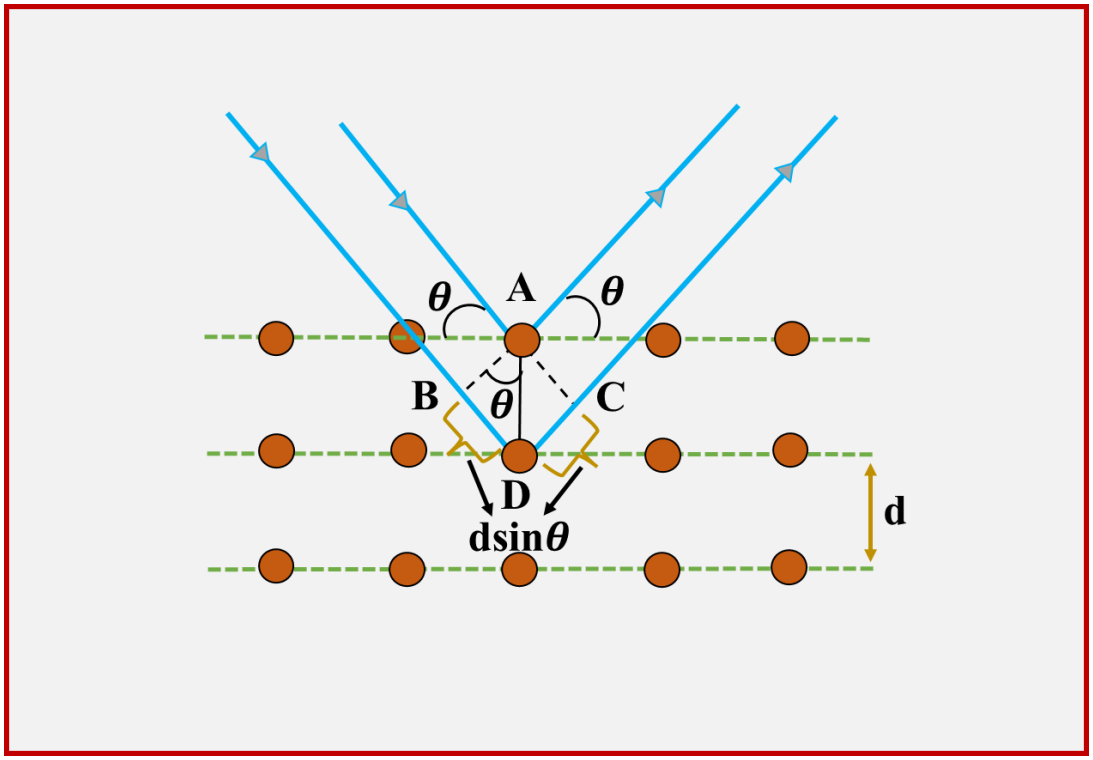

Figure 2.5 Schematic showing the diffraction of X-rays obeying Brags law

Bragg's reflection occurs within the X-ray range for wavelengths $\lambda \leq 2d$, making it the domain where crystalline diffraction occurs. The subsequent factors influencing peak positioning encompass the unit cell's size, space group symmetry, and crystal symmetry. This collective interaction determines the peak's intensity, as described by equation:

$$F_{hkl} = \Sigma f_n e^{2\pi i(hu_n kv_n lw_n)} \tag{2.2}$$

Here, the element coordinates are represented by uvw, the Miller indices by hkl, and the electron scattering density by fn. As this methodology is commonly applied to samples in a powdered state, the powder substance interacts with incident radiation, engaging with all feasible planes within the material, adhering to Bragg's law. Peaks appear for parallel planes

and at different angles, indicating constructive interference [8]. X-ray diffraction may be used to retrieve information on crystallite diameters by using the correlation shown in equation:

$$D = k\lambda/\beta cos\theta \quad (2.3)$$

The D8 Advance Bruker instrument (shown in Figure) X-ray diffractometer was utilized to generate the XRD pattern for this study with CuK_α radiation (λ = 1.5406 Å) a X-ray source. The patterns were recorded at room temperature, employing a step size of 0.02º and a scan speed of 2º per minute. The obtained patterns were subsequently compared using the JCPDS database and previously reported literatures. The presence of different phases in the PVDF and PVDF nanocomposite films is also confirmed using the XRD spectra.

2.3.2 Fourier Transform Infrared Spectroscopy

The vibrational properties of functional groups in organic and semi-organic molecules can be investigated using Fourier-transform infrared spectroscopy (FTIR). This analysis is carried out by exposing the compounds to the electromagnetic spectrum between 400 $cm^{-1}$and 4000 cm^{-1}. The energy levels of the molecule's vibrations change as it absorbs infrared light. These vibrations manifest in two distinct modes: stretching and bending. The absorbed energy facilitates adjustments in these energy levels. This method holds utmost significance in identifying organic molecules containing robust dipoles and polar chemical bonds (such as NH, OH, CH, etc.) [9-11]. The FTIR spectroscopy technique has several benefits, including its faster scanning capabilities as compared to other dispersive techniques and its adaptability in analysing solids, liquids, and gases. This method is based on the molecular bonds between the sample's components. The constituent atoms determine the nature of these molecular bonds. The molecules in the sample absorb energy and shift to higher energy levels when exposed to IR light. When these molecules return to their original (de-excited) states, they emit radiation defined by the energy difference between the excited and de-excited states. Various wavelengths are present in the incoming light, and each material absorbs a particular IR wavelength, adding to its individual spectral signature [12]. Infrared spectroscopy identifies molecules that vibrate or rotate at certain frequencies corresponding to different energy levels. Resonant frequencies are influenced by a variety of parameters such as atomic masses, molecule potential energy surfaces, and vibronic coupling. As a result, a relationship between binding kinds and vibration frequencies arises. Simple diatomic molecules have a single bond that can stretch, whereas complex compounds have numerous bonds that can stretch and conjugate vibrations. This interaction results in specific infrared absorption frequencies

connected to chemical groupings. Because each functional group has a specific vibrational energy, IR spectroscopy is similar to a unique fingerprint for each group. FTIR spectroscopy quantifies these assimilated wavelengths, allowing for the determination of material identification and bonding properties. The resulting graph can show "transmittance" or "absorption" of infrared light on the y-axis, with wavenumber on the x-axis. Depending on the chemical nature, the graph may include many peaks. The identification of functional groups within the sample is aided by thorough investigation and comparison of these peaks with collected IR signatures for various materials and bonds. The Michelson interferometer which is depicted in Figure 2.6 is a commonly used technique in FTIR spectroscopy. The schematic in Figure 2.7 depicts the several steps involved in the FTIR spectroscopy. In the interferometer arrangement, infrared radiation from the source is routed through a collimator to the beam splitter. The incident beam is then separated into two independent beams by the beam splitter. Both beams travel to the interferometer's mirrors, with one mirror moving at all times. This motion causes a path disparity between the beams, resulting in modulation of each wavelength in the incident beam at a different frequency. Following reflection from the mirrors, the beams combine to form a complicated interferogram.

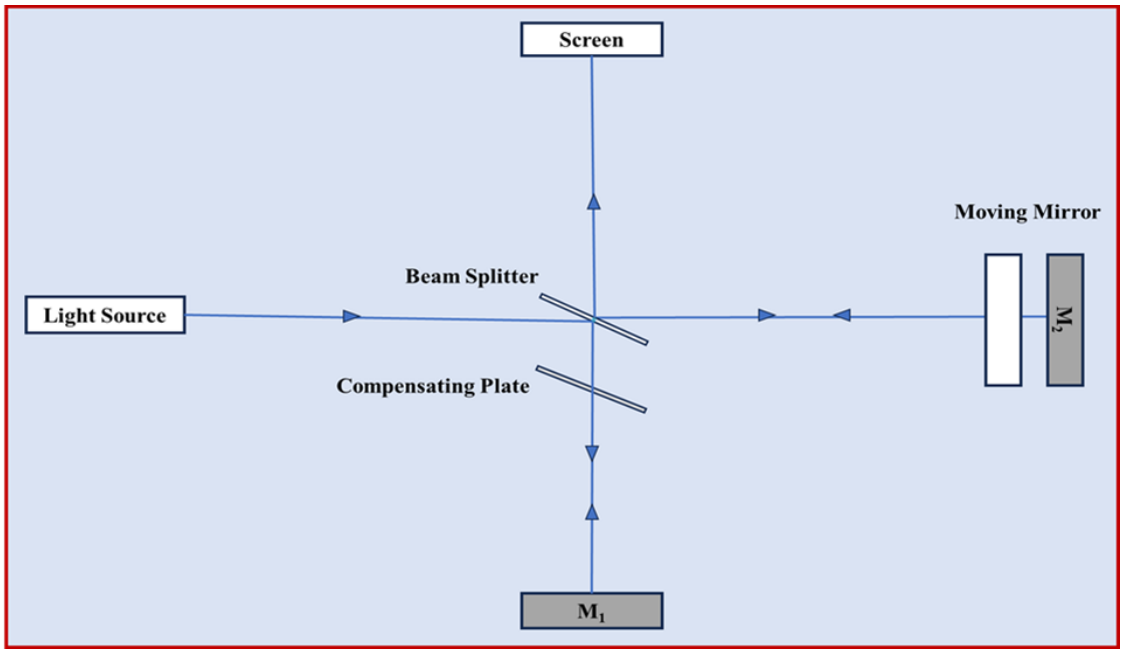

Figure 2.6 Schematic of Michelson Interferometer.

The generated interferogram is then projected onto the sample. As previously stated, the sample selectively absorbs various wavelengths of transmitted light from the incident spectrum. A detector measures the intensity of different wavelengths of transmitted light. Using

the "Fourier transform" approach, the incoming signal is processed and transformed into useful data. The final graph produced by utilising the Fourier transform approach assists in identifying several functional groupings within the analysed sample.

In the present study we have used the FTIR spectra to analyse the percentage of β-phase of PVDF in different PVDF based thin films.

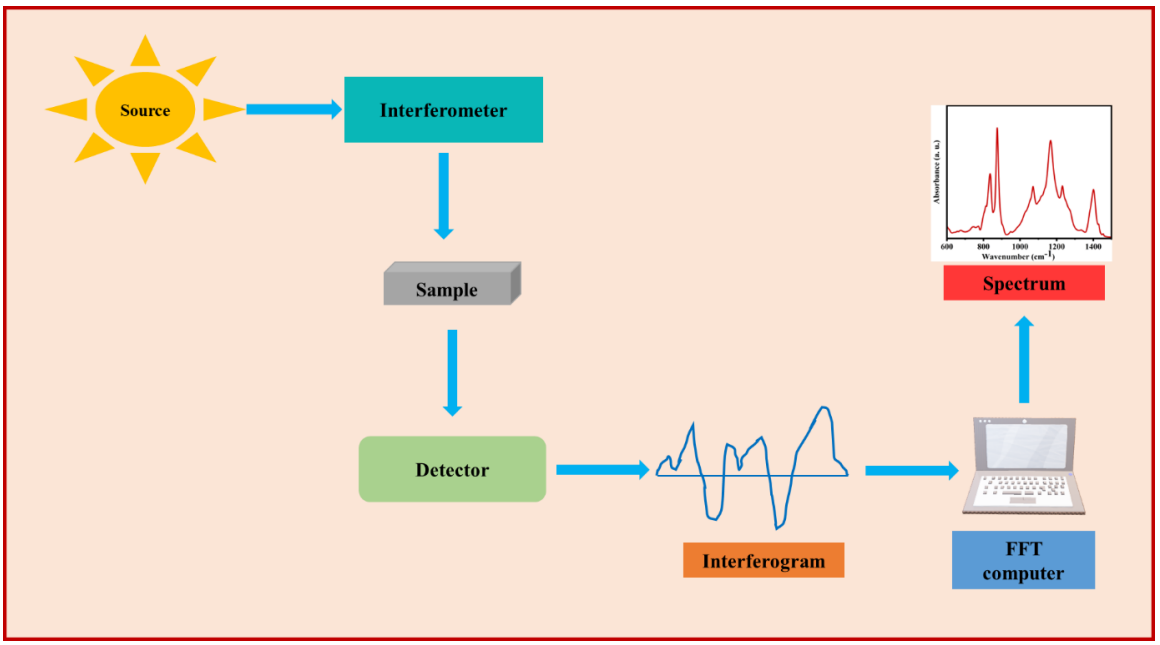

Figure 2.7 Schematic showing FTIR spectroscopy

2.3.3 Raman Spectroscopy

Raman spectroscopy is utilized to analyse the rotational, vibrational, and additional frequency modes exhibited by specimens. This approach provides information on molecule bonding and structure, resulting in a unique fingerprint for molecular identification. This spectroscopy, which is fundamentally based on the inelastic scattering of light known as the Raman Effect [13]. When monochromatic radiation interacts with a material, it might result in scattering, reflection, or absorption. Scattered radiation is useful for learning about molecular structure. A coherent source, frequently in the form of a laser, is widely used in Raman spectroscopy to analyse specimens [14]. The majority of incident radiation experiences elastic scattering, resulting in the emission of Rayleigh scattered light. A minute proportion, approximately 1 in 10^6, undergoes inelastic scattering, primarily manifesting as Stokes and anti-Stokes lines. Within this small subset, the Stokes lines are of primary interest for specimen analysis. In Rayleigh Raman scattering, the frequencies of incident and scattered light are identical. Contrastingly, in anti-Stokes Raman scattering, the scattered light exhibits a frequency higher

than the incident light, while in Stokes Raman scattering, the frequency of the scattered light is lower than that of the incident light [15]. A simplified design of the Raman spectrometer is shown in Figure 2.8.

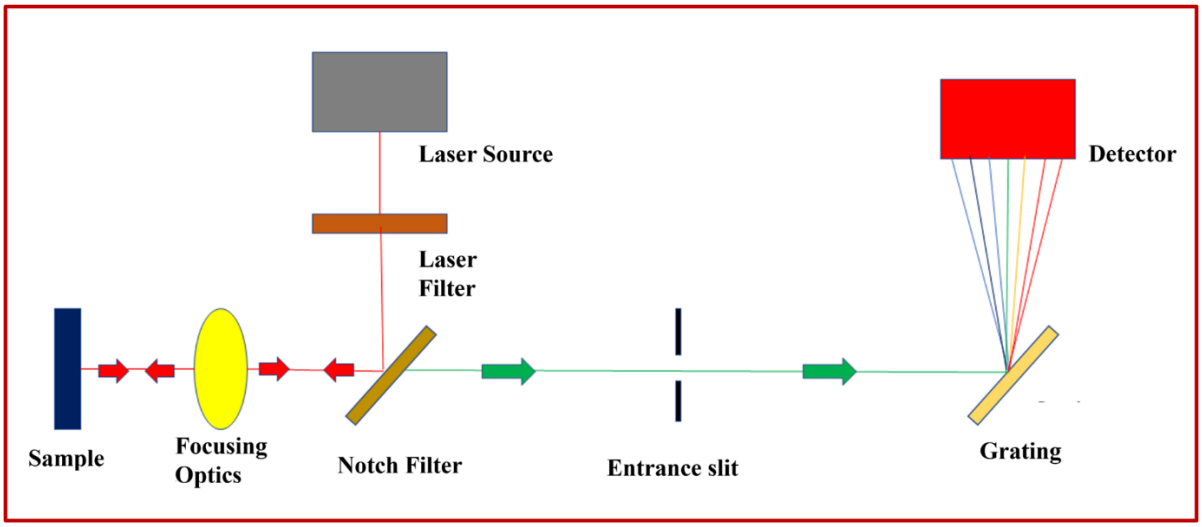

Figure 2.8 Schematic representation of Raman spectrometer

The Raman spectrum is plotted with scattered light intensity against the energy difference known as the Raman shift. Upon photon interaction with a molecule, the electric field 'E' induces a dipole moment 'P', as expressed by

$$P = \alpha E \tag{2.4}$$

where α signifies the proportionality constant indicative of the electron cloud's deformation around the molecule [16]. These molecular bonds, characterized by specific energy transitions linked to alterations in polarizability, give rise to Raman active modes. A contemporary Raman spectrometer comprises three essential components: a laser source, a sample illumination system, and a suitable spectrometer. Lasers are frequently chosen for studying Raman spectra due to their monochromatic nature and high-intensity beams, facilitating robust signal-to-noise (S/N) ratios. Raman spectrometers are categorized into two types: those employing charge-coupled devices (CCD) or those incorporating cooled germanium within Fourier-transform infrared (FTIR) setups. Raman spectroscopy often holds an advantage over IR spectroscopy due to its applicability in examining inorganic systems within aqueous solutions. It has shown to be extremely useful in the study of biological systems. Raman spectroscopy requires just a small sample volume, making it ideal for analysing liquid and film materials. The technique is adept at detecting molecular impurities and additives. In various scenarios, Raman

spectroscopy has emerged as a non-destructive method for both qualitative and quantitative analysis.

2.3.4 SEM and FESEM

Scanning Electron Microscopy (SEM) represents an advanced form of microscopy that investigates the three-dimensional structure of solid specimens using electrons instead of light. This technique proves invaluable for acquiring comprehensive insights about a sample, including its topography, composition, and morphology. At scales ranging from nanometers to micrometres, SEM stands as an optimal method for analysing both organic and inorganic materials. With magnification capabilities reaching up to 30,000x, and even up to 100,000x in modern models, SEM produces highly precise images of diverse materials. In a scanning electron microscope (SEM), electromagnetic "lenses" are employed to focus an electron beam onto a sample. This sample may comprise materials such as metals, metal oxides, ceramics, or biological specimens. Consequently, an image is generated by recording the interactions between the electron beam and the surface of the specimen. As the electron beam engages with the sample, it causes deflection in different types of electrons.

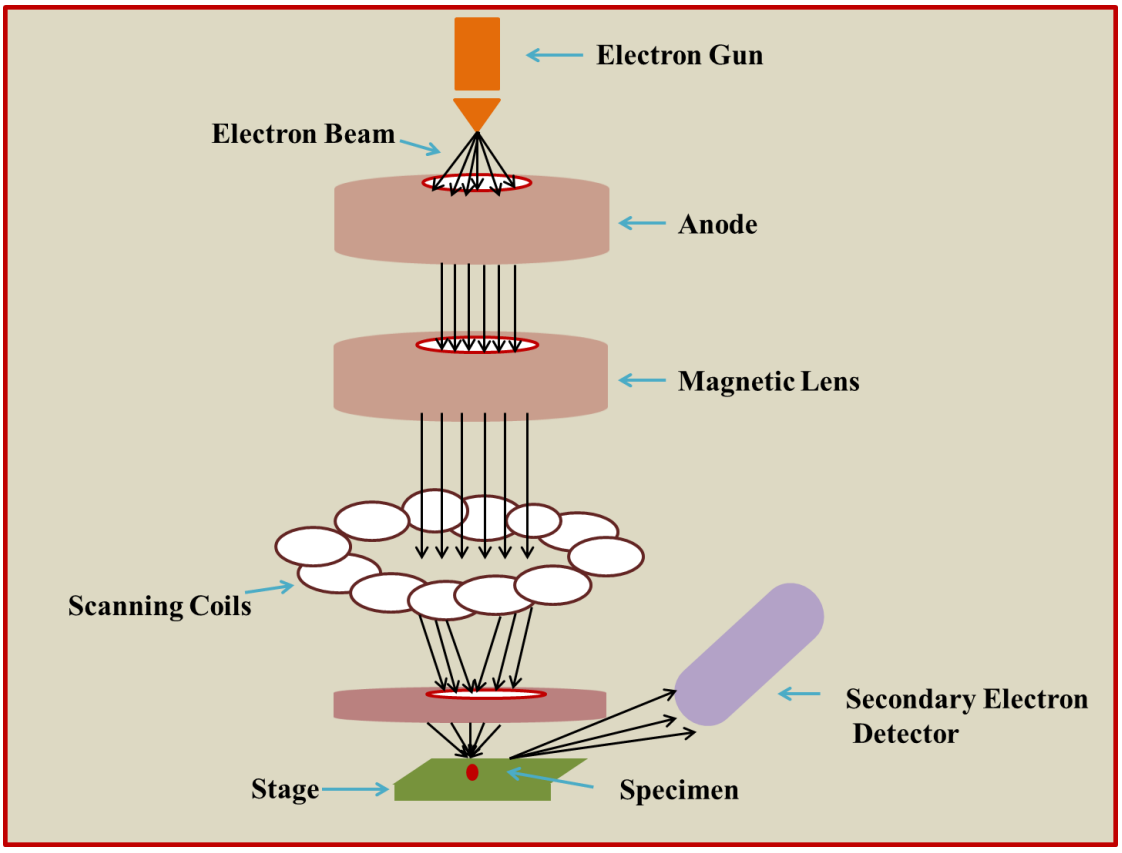

Figure 2.9 Schematic showing the components of a SEM

Preparing a sample for SEM analysis involves dispersing powder samples, applying thin films, or arranging pellets over conductive carbon tape, followed by coating them with conducting metals like gold (Au) or platinum (Pt) [17]. This metal coating prevents the accumulation of incident electrons at specific areas on the sample. Consequently, the electron beam is systematically directed across the sample, ensuring interaction with the specimen. During this interaction, electrons scatter from the surface, giving rise to secondary electrons and backscattered electrons (BSE). These electron types, along with their production, particularly secondary electrons emitted from a few surface layers with an energy of < 50 eV, offer insights into the sample's morphology. Conversely, BSE, characterized by energy > 50 eV, are elastically scattered from the surface and can penetrate more deeply compared to secondary electrons [18]. Elements with higher atomic numbers yield a greater quantity of backscattered electrons in comparison to those with lower atomic numbers. The appearance of brighter patches in SEM pictures demonstrates this difference. Thus, variations in chemical composition on the surface become discernible through the contrast within images produced by backscattered electrons. The interplay between bright and dark regions in these images reflects the density of backscattered electrons, while the signal intensity correlates with the concentration of secondary electrons [19]. A visual depiction of fundamental SEM components is illustrated in Figure 2.9.

2.3.4.1 Field Emission Scanning Electron Microscopy (FESEM) is an advanced microscopy technique that employs a field emission source to traverse the specimen in a zig-zag manner. The electron emitters within the field emission gun possess emission capabilities that can exceed those of a conventional tungsten filament by up to a factor of 1000 [20]. Furthermore, FESEM demands high vacuum levels. Following emission, electrons are concentrated into a narrow, monochromatic beam using metal apertures and magnetic lenses. Following that, data from several electron detectors are combined to provide a picture of the specimen. FESEM provides insights into topography and elemental composition across magnification scales spanning from 10x to 300,000x, coupled with an extensive depth of field. Its performance surpasses that of conventional Scanning Electron Microscopy (SEM) by a factor of three to six, yielding sharper images with spatial resolution down to half a nanometer. Notably, FESEM images exhibit reduced electrostatic distortions [21].

2.3.5 Atomic Force Microscopy (AFM)

Atomic Force Microscopy (AFM) was invented in 1986 at Stanford University by eminent scientists G. Binning, C. Quate, and C. F. Quate. Their invention involved affixing a tiny

diamond fragment to one end of a thin strip of gold foil. For a variety of applications, AFM is capable of inspecting the topography and surfaces of materials, including both uniform and uneven surfaces. The contact force between the specimen's surface and the probe, represented in Figure 2.10, is critical to AFM performance. This probe is made up of elastic cantilevers that end in an extremely small tip with a diameter of around 10 nanometers. The separation between the probe's tip and the sample is governed by the forces experienced between them. Two primary categories of forces operate between the tip and the sample surface: attractive (non-contact) and repulsive (contact) forces. Analysing the bending and deflection of the cantilever facilitates the assessment of the force exerted between the tip and the surface [22]. Consequently, three distinct methodologies can be employed within AFM.

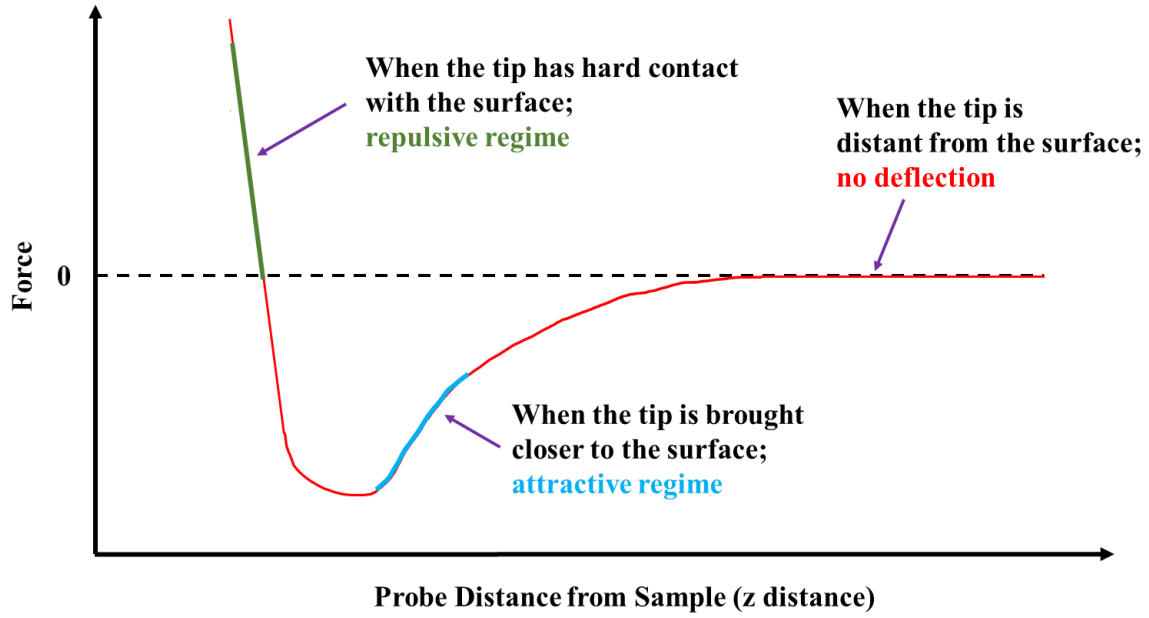

Figure 2.10 Graph showing the relation between force and probe distance of AFM tip

1. Contact Mode: The contact mode is examined under quasi-static conditions and functions within the repulsive region of the van der Waals curve. Within the contact measurement approach, the tip establishes direct contact with the sample's surface. The deflected cantilever, generating the elastic force, counteracts the force between the tip and the sample. For this mode, researchers should opt for a cantilever possessing low rigidity.

2. Non-Contact Mode: The oscillatory mode is another name for the non-contact mode. High sensitivity and reliable feedback are required for non-contact operation to be effective. This mode is sometimes used in a semi-contact mode to examine changes in phase and amplitude

of cantilever oscillations as the tip engages with the specimen via attractive van der Waals forces without establishing physical contact.

3. Tapping Mode: In this mode, it's common to employ a cantilever characterized by a substantial resonant frequency. The interaction between elastic and van der Waals forces between the tip and the specimen induces notable amplitude deflections during scanning. This technique is functionally similar to the non-contact mode, but the increased amplitude deflection improves feedback loop control for topography analysis.

The method known as beam deflection is often used in AFM to detect small cantilever variations. The Lennard-Jones potential, represented as an exponential function, approximates the van der Waals potential energy between two atoms separated by a distance 'r' [23]. Figure 2.11 depicts the main operating concept of AFM.

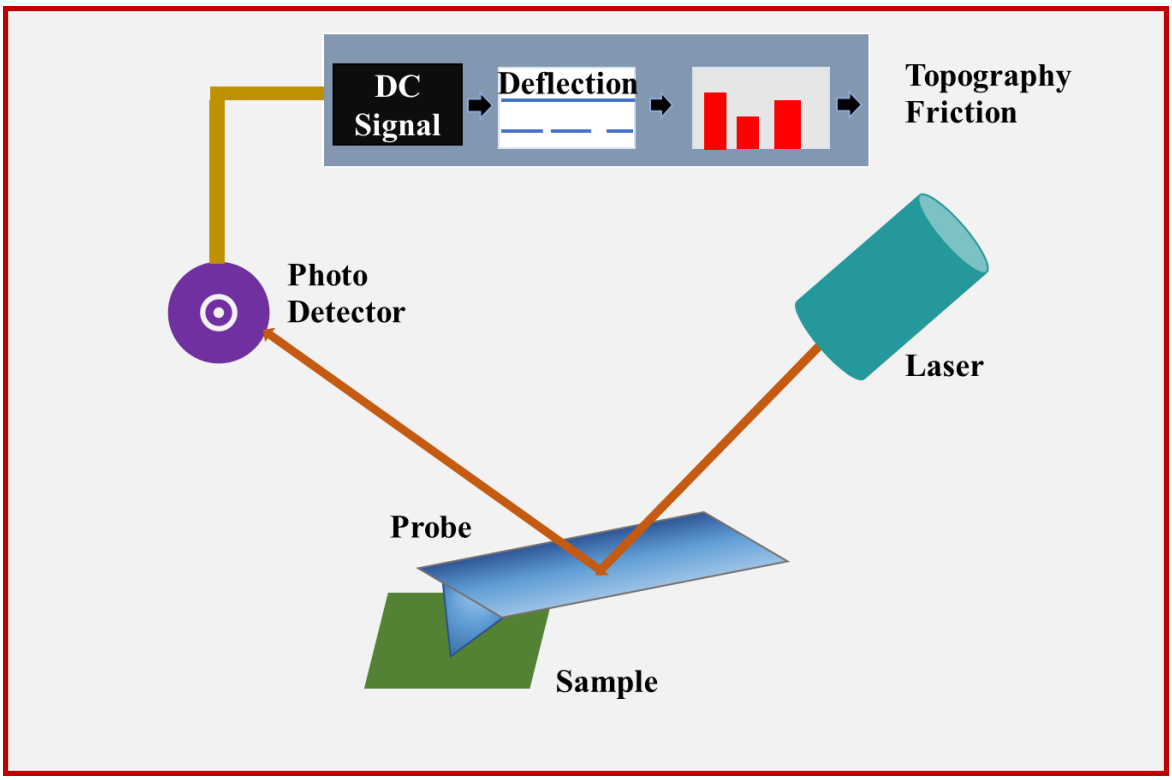

Figure 2.11 Schematic showing the working of AFM

2.3.5.1 Kelvin Probe Force Microscopy (KPFM):

Kelvin Probe Force Microscopy (KPFM) is a technique used to map the surface potentials of materials with nanoscale precision. It's a specialized form of Atomic Force Microscopy (AFM) (in non-contact mode) that provides insights into the local electric potentials across a sample's surface [24].

The working principle of KPFM involves the use of a conductive AFM probe, which functions as a sensing electrode. The probe is positioned at a small distance above the sample's surface, and a bias voltage is applied between the probe and the sample. This bias voltage generates an electric field between the probe and the surface, inducing a force on the cantilever of the AFM [25]. This force is detected and quantified using the deflection of the cantilever, providing information about the local surface potential. A feedback loop is used to measure the surface potential. The bias voltage applied is changed until the cantilever's deflection reaches a predefined set point, hence keeping a constant force on the cantilever. This bias voltage, also known as the contact potential difference, relates to the work function difference between the AFM probe and the surface of the sample [24]. A map of the local surface potentials is constructed by scanning the probe across the surface and recording the bias voltage at each spot.

KPFM is a useful approach in several domains, including materials science, nanotechnology, and electronics, since it allows researchers to learn about the electrical characteristics and charge distribution of materials at the nanoscale.

2.3.6 Transmission Electron Microscopy (TEM)

TEM is a microscopic methodology employing an electron beam that traverses an ultrathin specimen, initiating interactions that yield diverse insights about the sample. As the beam penetrates, it accumulates details regarding the specimen's morphology and crystallography. TEM uses a nanometer-scale electron to produce an electron beam with a shorter wavelength, resulting in much improved specimen resolution [26]. Interactions occur when the electron beam passes through the material, contributing to picture creation. Various imaging technologies, such as fluorescent screens, photographic film, or sensors such as charge-coupled devices (CCD), are used to achieve magnified images. The system may function in two modes: diffraction mode and image mode.

The TEM configuration encompasses an electron gun producing a high-energy electron beam that traverses a vacuum tube within the microscope setup. Following that are the condenser lenses, which are essential for electron focusing. A motorized specimen stage comes next, serving as a platform to hold a conducting copper grid that's coated with the sample. At the core of the TEM apparatus lie the objective lens and the specimen chamber, where the transmitted electron beam interacts with the thin specimen [27]. To obtain excellent TEM images, the sample thickness should be between 100 and 200 nm, as electrons struggle to

penetrate thicknesses greater than 200 nm. An imaging system that includes an objective lens and complementary lenses is required to generate high-resolution pictures and diffraction patterns. The electron intensity distribution is projected onto a fluorescent screen through a three-stage lens system after passing through the object [28]. Finally, a charged coupled device (CCD) camera is used to transform the electric charge into picture pixels. HR-TEM, SAED, and basic TEM are all modes of TEM that may be used to analyse particle size, morphology, lattice parameters, and material expansion direction. The TEM setup is depicted schematically in Figure 2.12.

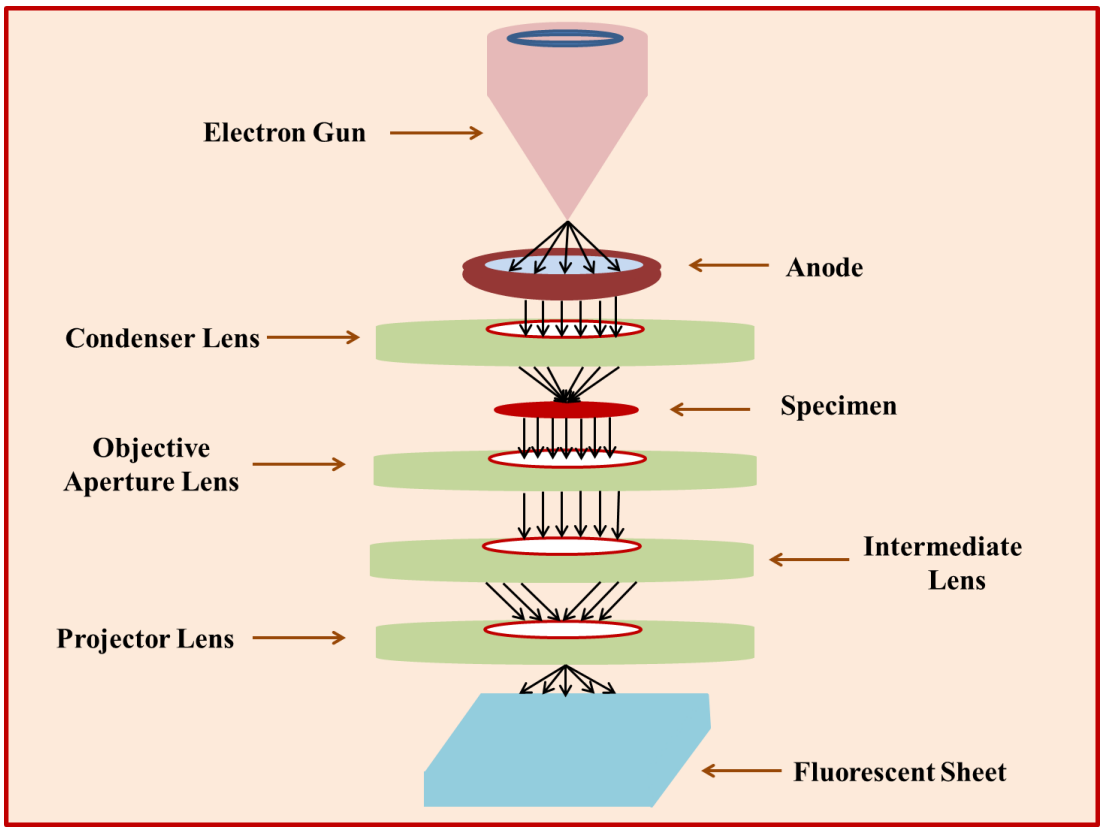

Fig 2.12 Schematic showing the setup of TEM

The complete TEM setup resides within a high vacuum chamber and is linked to a graphical user interface (GUI) data acquisition system. Electron beams emanating from electron guns interact with the sample, leading to beam scattering. Two categories of scattering occur: elastic and inelastic. Elastic scattering is a result of atomic arrangement within nanostructure crystals, manifesting as coherent electron beam scattering and generating spot patterns. In contrast, inelastic scattering gives rise to beam absorption or emission, a phenomenon specific to the compound or chemical structure of nanomaterials. The processes of Bright-field and Dark-field imaging are responsible for picture distinction. In the Bright-

field image, the entire specimen is uniformly illuminated, resulting in a dark image set against a bright background. Conversely, a Dark-field image is generated on the back focal plane of the objective lens, utilizing a diffracted wave through the objective aperture [29]. Based on the compatibility of the sample, the electron wavelength is reduced by increasing the accelerating voltage of the field emission gun to a maximum of 300 kV, which improves the image's point resolution. The outcome of this mode is referred to as High-Resolution TEM (HRTEM).

2.3.7 Thermal Evaporation Technique for Thin Film Electrode Fabrication

The thermal evaporation technique is a versatile and frequently used method for producing thin film electrodes. This technique relies on the controlled sublimation and condensation of material under vacuum conditions to produce uniform and precisely deposited films. It is used in a variety of disciplines like as electronics, optoelectronics, and energy conversion devices.

The thermal evaporation technique leverages the concept of vapor-phase deposition. The evaporation source is a solid substance that is heated within a vacuum chamber, causing it to sublimate or evaporate. The vaporised substance then condenses and forms a thin layer on a substrate. Condensation happens as a result of the interaction of vapour molecules with the substrate surface, resulting in the production of a film with characteristics similar to the source material.

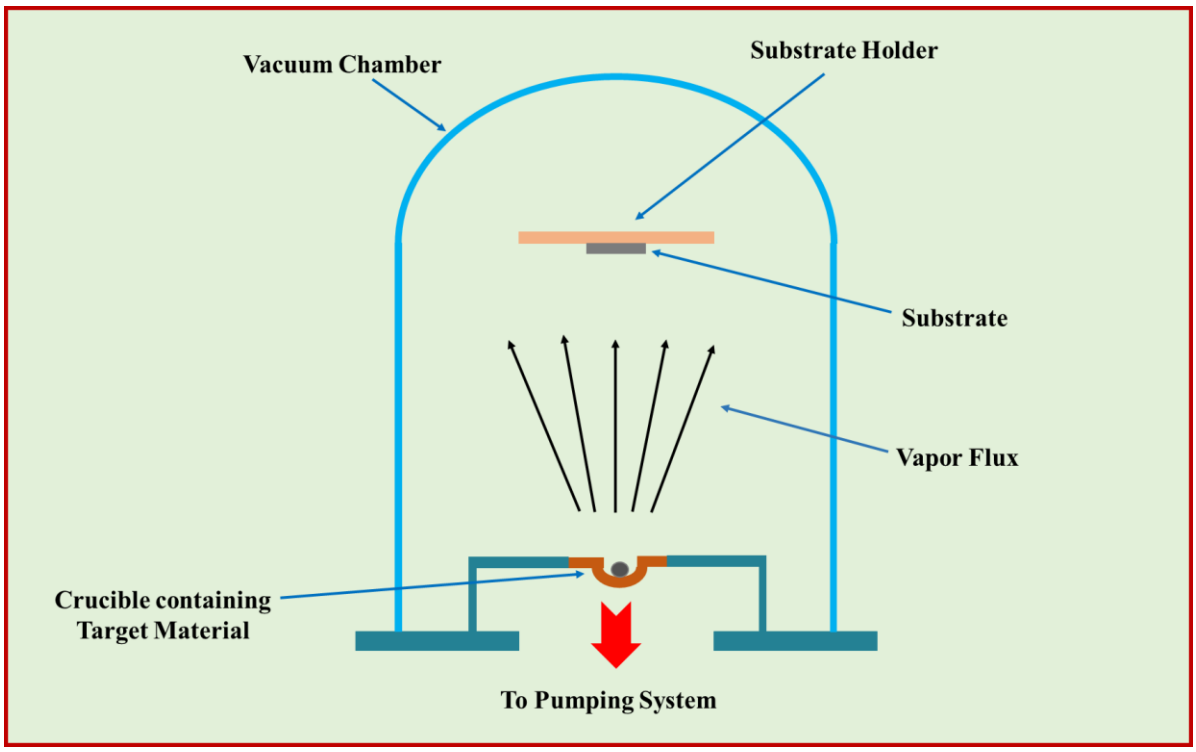

Figure 2.13 Schematic representation of thermal evaporation system

Thermal evaporation fabrication generally consists of the following steps:

1. Vacuum Chamber: A vacuum chamber contains the substrate and the evaporation source. It is critical to provide a low-pressure environment in order to avoid undesirable reactions and maintain regulated deposition.

2. Heating the evaporation source: Resistive or electron beam heating is used to heat the evaporation source, which is frequently in the form of pellets, wires, or rods. The source sublimates when it approaches its evaporation temperature, releasing vaporised atoms or molecules.

3. Deposition: The vaporized material travels within the vacuum chamber and comes into contact with the substrate's surface. Upon collision, the vapor condenses and adheres to the substrate, forming a thin film. The deposition rate is regulated by factors like the temperature of the evaporation source and the distance between the source and substrate.

4. Film Growth: The deposition time determines the thickness of the coating. The features of the resultant film, such as shape, crystallinity, and thickness uniformity, are determined by factors such as substrate temperature, pressure, and deposition rate.

In the present study, thermal evaporation (setup is shown in Figure 2.13) is utilized to deposit metal electrodes on PVDF based thin films in order to fabricate nanogenerators.

2.3.8 Dielectric/Impedance Analyser

The term "dielectric" was initially introduced by William Whewell. This approach is applicable for assessing fluctuations in parameters such as real and imaginary permittivity (ε' and ε'') and the loss factor (tanδ), in relation to either frequency or temperature changes. The fundamental interconnected electrical responses encompass impedance (Z*), admittance (Y*), relative permittivity (ε*), and electric modulus (M*).

The real and imaginary components of dielectric permittivity are related to the material's ability to store energy inside an electric field and electrical energy absorption, respectively. Equation 2.6 is used to compute the dielectric constant:

$$\varepsilon' = C_p d / \varepsilon_0 A \tag{2.5}$$

Here, d represents the pellet/thin film thickness, A denotes the cross-sectional pellet/thin film area, Cp stands for the measured capacitance of the sample, and ε_0 corresponds to the permittivity of free space, equivalent to $8.854*10^{-12}$ F/m. Determinations of the loss tangent

(tanδ) and the imaginary component of dielectric (ε'') for the samples are conducted employing the provided equation 2.7:

$$\varepsilon'' = \varepsilon' tan\delta \tag{2.6}$$

In this context, the "dielectric loss tangent" designates the energy dissipated from the applied field into the sample and is indicated by the tangent tanδ.

For dielectric analysis, the setup is encompassed of a temperature span from -196 °C to +300 °C and a frequency range spanning 1 Hz to 10^7 Hz. By altering the frequency and temperature, diverse physical parameters (L, C, and R) can be measured. AC voltage is the prevailing voltage source. Current and voltage are supervised through an analyser. The measurements encompass aspects such as the phase angle between voltage and current, inductance, impedance, and resistance of the sample. An impedance analyser connected to a computer enables the acquisition of data regarding inductance, AC conductance, capacitance, and dissipation factor as functions of frequency. The acquired parameters from the LCR meter can be converted into desired values utilizing various correlations. In the present study, the thin film based dielectric material was sandwiched between the brass electrodes to form a parallel plate capacitor and the dielectric performance was analysed as a function of frequency.

2.3.9 Polarisation vs Electric Field Measurements (P-E Loops)

P-E loops were initiated to understand the unique behaviour of ferroelectric materials, which exhibit spontaneous electric polarization that can be reversed by the application of an external electric field. The P-E loop measurement involves applying an electric field to the material and then measuring the induced polarisation. This process gives crucial information regarding the ferroelectric nature of the material, its polarisation saturation, and the occurrence of domain switching. P-E loops function by providing a rising electric field to a ferroelectric sample, measuring the polarisation response, and then decreasing the field to measure the depolarization. When the applied field is withdrawn, the polarisation does not entirely return to zero, resulting in a hysteresis loop. The shape and size of the loop reveal important information about ferroelectric features such as remnant polarisation, coercive field, and domain stability.

In the measurement of polarization-electric field (P-E), an electric field is imposed across the sample, and the resulting charges or polarization within the sample are quantified. The Sawyer-Tower circuit is used to measure the generated charge across the sample. The setup

encompasses a reference capacitor with a notably smaller value than the effective capacitance of the ferroelectric sample, linked in series. The reasoning behind selecting a lower value for the reference capacitor is to guarantee that it has the least voltage drop when compared to the sample's voltage drop. This setup ensures that nearly all the applied voltage is distributed across the sample, with the voltage across the reference capacitor indicative of the sample's polarization. PE loop tracer from Marine India was used to record the P-E loops of the samples in this investigation. Metal electrodes are placed onto flexible PVDF nanocomposite films to serve as measuring electrodes.

2.3.10 Electrical Measurements

To perform the electrical analysis of the piezoelectric nanogenerator and triboelectric nanogenerators, metal electrodes were deposited over different PVDF based thin films in order to make electrical connections. For examining the piezoelectric and triboelectric performance of devices, a dynamic shaker (Micron MEV-0025) was used to manage the continuous contact-separation motions between the triboelectric layers by adjusting its operating parameters, which included tapping frequency and contact force. Voltage measurements were conducted utilizing a digital storage oscilloscope (Tektronix MDO34). A Keithley digital multimeter (DMM7510) was used to measure current. An electrometer (Keysight B2985B) was used to monitor current and produced charges in the case of the triboelectric nanogenerator and other hybrid devices. Si diode-based bridge rectifier circuits were used to measure the rectified output voltage and current.

References

[1] H. Zhang, H.-M. Cheng, P. Ye, 2D nanomaterials: beyond graphene and transition metal dichalcogenides, Chemical Society Reviews, 47,(2018), 6009-6012

[2] J. Li, Q. Wu, J. Wu, Synthesis of Nanoparticles via Solvothermal and Hydrothermal Methods 12,(2016),

[3] P. Debye, P. Scherrer, Interferenzen an regellos orientierten Teilchen im Röntgenlicht. I, Nachrichten von der Gesellschaft der Wissenschaften zu Göttingen, Mathematisch-Physikalische Klasse, 1916,(1916), 1-15

[4] A.W. Hull, A new method of X-ray crystal analysis, Physical Review, 10,(1917), 661

[5] M. Etter, R.E. Dinnebier, A century of powder diffraction: a brief history, Zeitschrift für anorganische und allgemeine Chemie, 640,(2014), 3015-3028

[6] P. Klimanek, Wiley Online Library1977.

[7] C. Kittel, Introduction to solid state physics, John Wiley & sons, inc2005.

[8] B.E. Warren, X-ray Diffraction Dover publications, Inc, New York,(1990), 253

[9] W.M. Doyle, Principles and applications of Fourier transform infrared (FTIR) process analysis, Process Control Qual, 2,(1992), 11-41

[10] E. Knözinger, Wiley Online Library1986.

[11] G.C. Schatz, R.P. Van Duyne, J.M. Chalmers, P.R. Griffiths, Handbook of vibrational spectroscopy, New York: Wiley, 1,(2002), 759

[12] D. Titus, E.J.J. Samuel, S.M. Roopan, Nanoparticle characterization techniques, Green synthesis, characterization and applications of nanoparticles, Elsevier2019, pp. 303-319.

[13] M.J. Pelletier, Quantitative analysis using Raman spectrometry, Applied spectroscopy, 57,(2003), 20A-42A

[14] I.R. Lewis, H. Edwards, Handbook of Raman spectroscopy: from the research laboratory to the process line, CRC press2001.

[15] P. Graves, D. Gardiner, Practical raman spectroscopy, Springer, 10,(1989), 978-973

[16] J.R. Ferraro, Introductory raman spectroscopy, Elsevier2003.

[17] A. Mohammed, A. Abdullah, pp. 7-9.

[18] W. Zhou, R. Apkarian, Z.L. Wang, D. Joy, Fundamentals of scanning electron microscopy (SEM), Scanning Microscopy for Nanotechnology: Techniques and Applications,(2007), 1-40

[19] B.J. Inkson, Scanning electron microscopy (SEM) and transmission electron microscopy (TEM) for materials characterization, Materials characterization using nondestructive evaluation (NDE) methods, Elsevier2016, pp. 17-43.

[20] M.A. Sutton, N. Li, D.C. Joy, A.P. Reynolds, X. Li, Scanning electron microscopy for quantitative small and large deformation measurements part I: SEM imaging at magnifications from 200 to 10,000, Experimental mechanics, 47,(2007), 775-787

[21] A. Ul-Hamid, A beginners' guide to scanning electron microscopy, Springer2018.

[22] F.J. Giessibl, Advances in atomic force microscopy, Reviews of modern physics, 75,(2003), 949

[23] D. Rugar, P. Hansma, Atomic force microscopy, Physics today, 43,(1990), 23-30

[24] W. Melitz, J. Shen, A.C. Kummel, S. Lee, Kelvin probe force microscopy and its application, Surface science reports, 66,(2011), 1-27

[25] T. Glatzel, M.C. Lux-Steiner, E. Strassburg, A. Boag, Y. Rosenwaks, Principles of Kelvin probe force microscopy, Scanning Probe Microscopy: Electrical and Electromechanical Phenomena at the Nanoscale,(2007), 113-131

[26] L.H. Schwartz, J.B. Cohen, L.H. Schwartz, J.B. Cohen, The nature of diffraction, Diffraction from Materials,(1987), 46-76

[27] F. Lin, Preparation and characterization of polymer TiO 2 nanocomposites via in-situ polymerization,(2006),

[28] L.A. Bendersky, F.W. Gayle, Electron diffraction using transmission electron microscopy, Journal of research of the National Institute of Standards and Technology, 106,(2001), 997

[29] H.H. Willard, L.L. Merritt Jr, J.A. Dean, F.A. Settle Jr, Instrumental methods of analysis,(1988),

CHAPTER 3

Effect of the different chalcogen atoms (S, Se, SSe) of transition metal dichalcogenides (TMDCs) on the output performance of the PVDF-TMDCs based flexible piezoelectric nanogenerator.

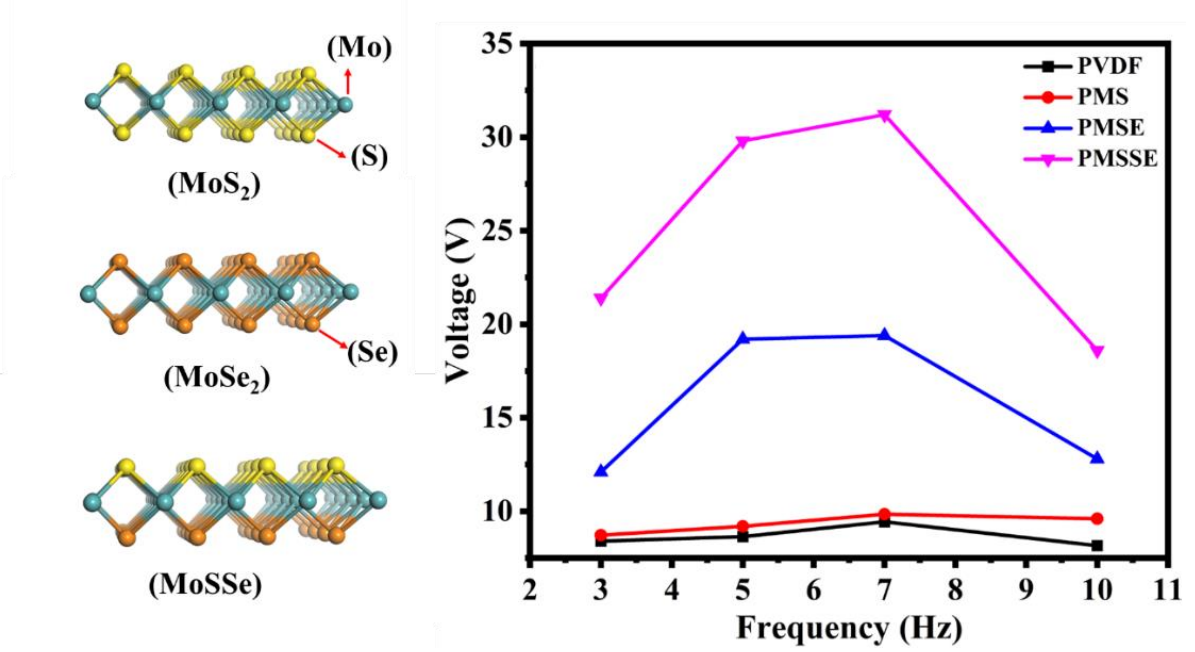

In this chapter, we have demonstrated a high performance piezoelectric nanogenerator based on polyvinylidene fluoride (PVDF) and transition metal dichalcogenides (TMDCs) for generating electrical power. The systematic effect of the chalcogen atoms (S, Se, Se) of the synthesized TMDCs (MoS_2, $MoSe_2$, MoSSe) and PVDF based composites on the piezoelectric performance of the fabricated piezonanogenerator has been investigated. Raman, Fourier-transform infrared spectroscopy, P-E hysteresis loop measurements confirmed the enhancement in the piezoelectric properties on changing the chalcogen atom from S, Se and SSe. Out of all the fabricated piezonanogenerator, the PVDF/MoSSe based nanogenerator showed the maximum peak to peak open circuit voltage of 31.2 V and short circuit current of 1.26 μA. The highest output voltage for the PVDF/MoSSe device is ascribed to the lack of reflection symmetry in MoSSe structure. The generated voltage was also used for glowing a commercial LED.

3.1 Introduction

The advances in low powered electronics, wireless sensors and micro electromechanical systems have tremendously raised the power requirement in the existing digital world. In the present scenario, we are completely surrounded with several electronics devices, such as, cell phones, tablets, I-pods, smart watches etc., which collectively require huge amount of power for their operation. According to the survey, carried out by "International Energy Agency" up to 2040, worldwide electricity demand is expected to expand at a pace of 2.1 percent per year, which is twice the rate of primary energy demand. Electricity percentage of total final energy consumption rises from 19 percent in 2018 to 24 percent in 2040 as a result of the advancement in these low powered devices. The growth of electricity demand is expected to be especially substantial in developing economies [1]. If the power demand of these household items could be satisfied by local powering devices or making them self-powered by harnessing the energy available in our environment, the existing power problem can be relieved. In this regard, different kinds of energy sources are present in the environment, such as, solar energy, wind energy, thermal energy, mechanical energy etc. Among them, mechanical energy is one of the most popular energy harvesting source because of its availability at all time and place. The devices which utilizes the ambient energy and convert into useful electrical energy are called energy harvesters. Further, the device which scavenge the electrical energy from wasted mechanical energy, by utilizing the intrinsic property (piezoelectricity) of certain smart materials, where a small external mechanical deformation may give rise to electrical potential is called as piezoelectric nanogenerator (PENG) and has attracted the tremendous research interests [2-4].

In the past few years, the scientific community has shifted their attention towards piezoelectric materials because of their excellent capability to transform the ambient mechanical energy into useful electrical energy. A large number of researchers have reported the PENG constructed by using nanostructures of various piezoelectric materials, such as, ZnO [5, 6], $ZnSnO_3$ [7], $BatiO_3$ [8], and PMN-PT [9] for flexible and wearable energy harvesting applications. However, the nanogenerators based on the inorganic materials given above have higher energy conversion efficiencies and large piezoelectric coefficients but still not suitable for practical implementation because of their brittle nature, cost-intensive processability and toxic lead (Pb) constituent in few cases [57]. In this regard, piezoelectric polymers, such as, poly (vinylidene fluoride) PVDF and its copolymers are of great interest in the fabrication of PENG because of their lightweight, high flexibility, cost effective and simple processing [10-13]. Being a ferroelectric polymer, PVDF mainly exist in four phases, which are α, β, γ and δ.

β-phase of the PVDF is highly crystalline and is also well known for its piezoelectric properties. PENGs based on PVDF has lower electric output efficiency when compared with PENGs made up of inorganic piezoelectric materials. To overcome this, we need to increase the content or nucleate more and more crystalline β-phase in the PVDF polymer matrix. Many methods are given in the literature to increase the nucleation of β-phase in the PVDF film, such as, thermal, mechanical or electrical treatment [14]. Addition to these treatments, β-phase of PVDF can also be enhanced by the addition of nano fillers having intrinsic piezoelectric property in the PVDF matrix to get a flexible nanocomposite with enhanced piezo-output without any compromise in their flexibility. Some of the nano fillers which are most commonly used to disrupt the symmetry of PVDF, to enhance its ferroelectric properties by nucleating the crystalline β-phase are ZnO [15], $BaTiO_3$ [16], RGO [17], transition metal dichalcogenides etc.

Recently, 2D layered transition metal dichalcogenides (TMDCs), such as, molybdenum disulfide (MoS_2), molybdenum diselenide ($MoSe_2$), molybdenum ditelluride ($MoTe_2$), tungsten disulfide (WS_2), tungsten diselenide (WSe_2), etc. have gained attention of materials scientist due to their favorable electronic, optical, mechanical properties and non-toxic nature [18]. Among them, MoS_2 has been widely used as a functional material in diverse fields, such as, lubrication, electronic transistors, batteries, photovoltaics, and catalysis [19-21]. It has been given in the literature that in the bulk form, no piezoelectricity is observed among the TMDCs, because of their centrosymmetric structure in bulk form, however, when thinned down to monolayer, they have different symmetries. Unlike graphene, TMDCs, monolayer hexagonal boron nitride (h-BN) and black phosphorous, shows strong piezoelectricity because of their broken inversion symmetry [22-24]. It has been reported in the literature, that TMDCs are an interesting material for harvesting energy because of their engineered piezoelectricity, implying that some materials which are non-piezoelectric by doing some structural modifications can be made piezoelectric. The density functional theory (DFT) at the generalized gradient approximation level has been used for evaluating the piezoelectric properties in terms of the piezoelectric and stiffness coefficient for the 2D TMDCs [25]. It has been observed that piezoelectric coefficient d_{11} for the flat 2D monolayer materials, which relates the polarization induced as a function of applied stress increases while moving downward until $MoTe_2$ across the group 16 (chalcogenides) of the periodic table. Duerloo et al. calculated the piezoelectric coefficients based on DFT results, which and are found to be 3.65, 4.55 and 7.39 pm/V for MoS_2, $MoSe_2$ and $MoTe_2$, respectively [22]. Further, it has been reported by several groups based on DFT theoretical calculations [46-47, 58], that Janus TMDCs MXY (M= Mo or W, X/Y= S, Se or Te) having different chalcogen atoms in monolayer and multilayer have enhanced

piezoelectric effect due to the combined effect of stronger in-plane and weaker out-of-plane piezoelectric polarization. The multilayer MXY has strong out-of-plane piezoelectric polarization in comparison to monolayer form. It has been observed that the above effect of enhanced piezoelectricity in Janus MXY monolayer and multilayer films have only been theoretically verified, without any experimental results, and therefore motivates the present thesis work.

In this work, we have reported the flexible piezoelectric nanogenerator based on few layers of MoS_2, $MoSe_2$, and MoSSe sheets incorporated into PVDF matrix. The effect of incorporation of various 2D TMDCs materials in the PVDF matrix have been obtained by doing the fourier-transform infrared spectroscopy (FTIR) analysis of the synthesized flexible composite films. The systematic effect of the chalcogen atoms (S and Se) in the various 2D TMDCs on the piezoelectric performance of the fabricated PENG has been studied. The piezo response of the fabricated flexible devices based on bare PVDF, PVDF/MoS_2, PVDF/$MoSe_2$ and PVDF/MoSSe have been obtained by giving periodic mechanical stimulation using an electro dynamic shaker. The obtained open circuit voltage and short circuit current results clearly indicates that piezoresponse of the nanogenerators increases as S atoms are replaced with Se atoms in the 2D TMDCs. Among all the fabricated PENG devices, the nanogenerator based on PVDF/MoSSe composites generates maximum peak to peak open circuit voltage of 31.2 V. The extraordinary performance of nanocomposites based on 2D semiconducting TMDCs and PVDF, and more importantly the composites based on MoSSe/PVDF with superior piezoelectric properties in terms of generated output power has laid the foundation of new and exciting area of sustainable energy generation for flexible and wearable electronic devices. Therefore, the present study opens new ways of improving the performance of the device by systematic tailoring the properties of nanocomposites.

3.2 Experimental Section

3.2.1 Materials

Sodium molybdate, Ammonium molybdate, Sulphur and Selenium were commercially purchased from Sigma Aldrich. N, N di-methyl formamide (DMF) was purchased from Fisher and PVDF powder (44080) was purchased from Alfa Aesar. All the chemicals were used as received without any further treatment.

3.2.2 Synthesis Procedure for MoS_2 Flakes

To synthesize MoS_2 a simple hydrothermal method was used in which, 2.48 g of ammonium molybdate tetrahydrate [$(NH_4)_6Mo_7O_{24}.4H_2O$] and 4.56 g of thiourea were dissolved in 72 mL

deionized water. After dissolving the precursors in deionized water, they were homogeneously mixed at room temperature with a continuous stirring by using a magnetic stirrer at 500 rpm for 30 minutes. Then this homogeneous mixture was poured into a teflon beaker of 100 mL, which was placed in a stainless-steel autoclave and was kept at 200 °C for 24 h inside the oven. Then, the autoclave was allowed to cool down naturally. The black precipitates from the resultant solution were collected by centrifugation and was washed several times to remove further impurities with deionized water and ethanol. At last, the MoS_2 powder was obtained by drying at 60 °C for 12 h in an oven.

3.2.3 Synthesis Procedure for $MoSe_2$ Flakes

$MoSe_2$ powder is also synthesized using hydrothermal technique, in which deionized water (20 mL) and ethanol (30 mL) were used to dissolve 0.48 g of sodium molybdate dihydrate [$Na_2MoO_4.2H_2O$] by stirring at 400 rpm using a magnetic stirrer for 30 minutes to obtain a clear solution. After mixing, a mixture containing of 0.32 g of selenium powder in 10 mL hydrazine hydrate (86%) was added into the above solution and stirred further at 400 rpm for next 30 minutes. Then, the final mixture was shifted into a teflon beaker of 100 mL, which was placed in an autoclave and was kept at 200 °C for 24 h inside the oven. The black precipitates from the resultant solution were collected by centrifugation and was washed several times to remove further impurities with deionized water and ethanol. After the centrifugation, $MoSe_2$ powder was obtained by drying for 12 h at 80 °C.

3.2.4 Synthesis Procedure for MoSSe Flakes

To synthesize MoSSe powder 50 mL of deionized water was used to dissolve 0.48 g of sodium molybdate dihydrate by stirring at 400 rpm for 30 minutes. After that, a solution containing 0.15 g and 0.06 g of each selenium powder and sulphur powder, respectively in 10 mL of hydrazine hydrate (86%) was mixed into the above prepared solution and was further stirred at 400 rpm for the next 30 minutes. Then, the final mixture was shifted into a teflon beaker of 100 mL, which was placed tightly in an autoclave and was kept inside the oven for 24 h at 200 °C. The black precipitates from the resultant solution were collected by centrifugation and was washed several times to remove further impurities with deionized water and ethanol. After the centrifugation, MoSSe powder was obtained by drying for 12 h at 80 °C.

3.2.5 Preparation of PVDF/TMDCs Flexible Films

Figure 3.1 represents the steps followed in the fabrication process of the PVDF and PVDF/TMDCs composite based flexible thin films. To prepare the thin films, 50 mg of synthesized TMDCs powder was added in the solution containing 1g PVDF dissolved in 10 mL of DMF. After that, the solution was homogeneously mixed for next 1 hour by using

magnetic stirrer. The obtained solution was drop casted on a glass plate, which was kept in oven at 90 ° C for 2 h. After this, the glass substrate was dipped into the deionized water to obtain the standalone flexible films of thickness ~40 µm. The synthesized composite thin films of PVDF/MoS_2, PVDF/$MoSe_2$ and PVDF/MoSSe are named as PMS, PMSE and PMSSE, respectively.

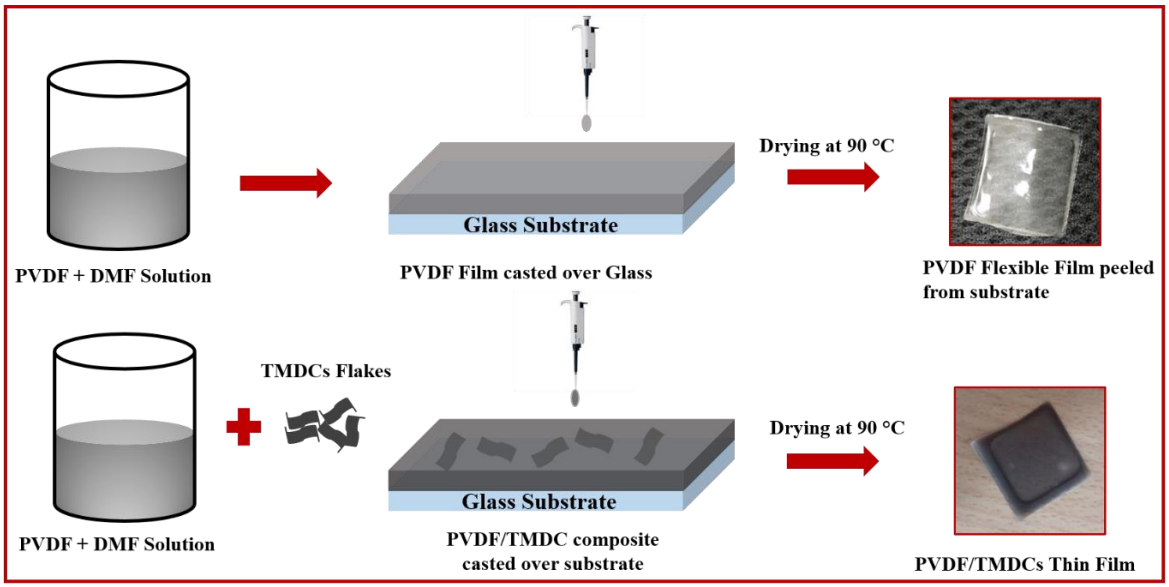

Figure 3.1 Schematic representation of various fabrication steps for different PVDF/TMDCs based nanocomposite thin films.

3.2.6 Fabrication of Nanogenerators

To check the utility of PVDF/TMDCs composite thin films in mechanical energy harvesting, we fabricated the different piezoelectric nanogenerators. The synthesized films were sandwiched between Al electrodes of thickness ~100 nm, deposited using thermal evaporation technique at a chamber pressure of $4x10^{-6}$ mbarr. Copper wires were attached to the top and bottom metal electrodes to conduct the different electrical measurements. The finally fabricated device was encapsulated with the help of insulating tape to ensure that the metal electrodes remain untouched during measurements.

3.2.7 Characterizations and Energy Harvesting Performance

Firstly, the synthesized TMDCs flakes have been characterized using Raman spectrometer (Renishaw plc, Micro Raman Spectrometer) with a laser source of wavelength 514 nm. X-ray diffractometer study has been used (Rigaku, Ultima-IV) to study the crystallinity of the PVDF/TMDCs films, with a Cu Kα radiation source (1.54 Å) in thin film mode. The β-phase content of thin films was studied by Raman Spectroscopy and Fourier Transform Infrared Spectroscopy (Perkin Elmer FTIR spectrum-II). Field Emission Scanning Electron Microscope

(Quanta 3D FEG, (FEI's) was used to study the morphological features of the PVDF and PVDF/TMDCs based flexible films. Finally, an external force at different frequencies was applied to the nanogenerator with the help of electrodynamic shaker (Micron 0020) to recorded the piezoresponse. All the electrical measurements were done with a digital storage oscilloscope (Tektronix, MDO500) and the digital Multimeter (Keithley DMM6500

3.3 Results and Discussion

3.3.1 Raman Spectroscopy of Synthesized TMDCs

Figure 3.2 shows the Raman spectra of as synthesized MoS_2, $MoSe_2$ and MoSSe nanoflakes. As shown in Figure 3.2(a), two Raman active peaks at around 407 cm^{-1} and 380 cm^{-1} are observed in the spectra which correspond to the out of plane (A_{1g}) mode and in-plane (E^1_{2g}) mode of MoS_2 nanostructure. As we know, the (E^1_{2g}) mode originates from the opposite vibration of two S atoms with respect to the Mo atom in the basal plane and represents the interlayer displacements of Mo and S atoms. The broad peaks indicate the existence of crystal defects in the basal planes of synthesized MoS_2. The (A_{1g}) mode corresponds to the out of plane vibrations of Mo-S bonds along c axis, providing information on the strength of the interaction between the adjacent layers [26]. Peak positions marked in the Raman spectra proves the synthesis of MoS_2 nanostructures. Figure 3.2(b) shows the spectra of the synthesized $MoSe_2$ nanostructure, where two typical peaks of $MoSe_2$ at around 239 cm^{-1} and 281 cm^{-1} are observed which corresponds to the out of plane (A_{1g}) mode and in-plane (E^1_{2g}) mode respectively. The out of plane (A_{1g}) mode appears at 242 cm^{-1} for bulk $MoSe_2$, however, in the present case, the downward red shift of (A_{1g}) mode indicates the formation of few layered $MoSe_2$ [27, 28]. In the Raman spectra of the sample synthesized as MoSSe, several changes appeared in the spectrum which is shown in Figure 3.2(c), the new strong peak around 285.4 cm^{-1} corresponds to the out of plane vibrations of Se-Mo-S. Another peak around 342.5 cm^{-1} is assigned for in-plane vibration mode of Se-Mo-S. The random composite nanostructure of $MoS_{2x}Se_{2(1-x)}$ will consist of all the Raman modes of MoS_2 and $MoSe_2$ in its Raman spectrum [29, 30]. But in our composite nanostructure none of the Raman peak is overlapping with the major representative peaks of MoS_2 and $MoSe_2$, which confirms the synthesis of uniformly distributed MoSSe Janus nanostructure.

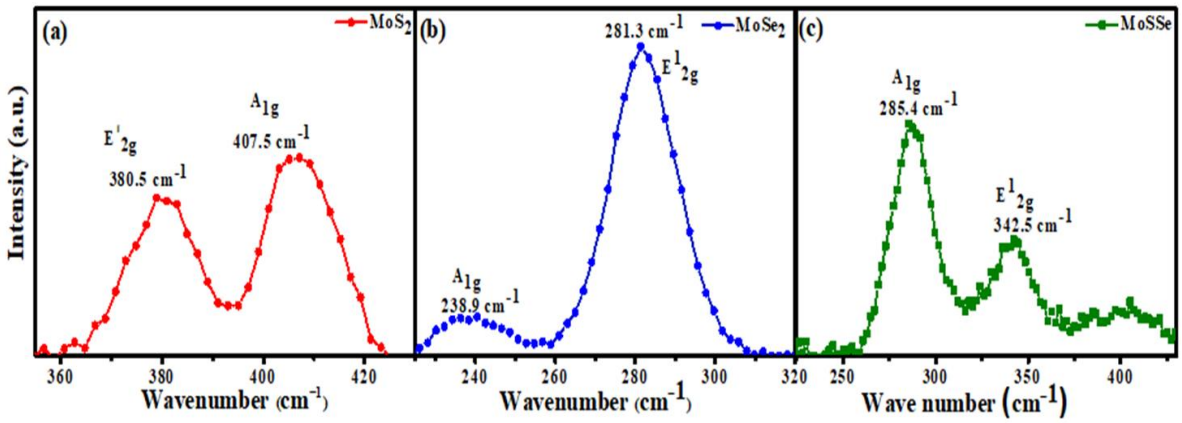

Figure 3.2 Raman spectra of synthesized TMDCs (a) MoS_2, (b) $MoSe_2$ and (c) MoSSe.

3.3.2 Structural and Morphological Analysis of PVDF/TMDCs Thin Films

XRD pattern for the bare PVDF and PVDF/TMDCs composite thin are shown in Figure 3.3(a). The XRD peak at 18.4° is corresponding to non-polar α-phase and the XRD peak at 20.2° corresponds to the polar β-phase of the PVDF [17, 31-33]. In the XRD pattern shown in Figure 3.3(a), the peaks corresponding to the PVDF are represented by *, #, whereas peaks correspond to MoS_2 and $MoSe_2$ are represented by $ [34-37]. XRD data confirm the coexistence of crystalline β-phase and transition metal dichalcogenides in the composite films. From the diffractograms, it can be observed that the crystalline polar β-phase is present in bare PVDF as well as in all the nanocomposite thin films. Figure 3.3(b) shows FTIR absorption spectra of the synthesized thin films and is mostly used to obtain the β-phase percentage of the PVDF based thin films [33, 38]. The β-phase of the PVDF contributes to the piezoelectric performance of the nanogenerator, and for largest β-phase content it has the largest dipole moment. From the FTIR absorption spectra, it can be observed that α and β phases are existing in all the fabricated thin films. The peaks corresponding to the polar β-phase of the PVDF are marked at 840, 1279 and 1400 cm^{-1}, whereas the peaks corresponding to 762, 795, 974, 1382 cm^{-1} are related to the α-phase [31, 33, 38, 39]. Determination of β-phase relative content can be done using Lambert-Beer law by using the equation (1) [38].

$$F(\beta) = \frac{A_\beta}{\left(\frac{K_\beta}{K_\alpha}\right)A_\alpha + A_\beta} * 100\% \qquad (3.1)$$

Where F(β) gives the content of β-phase in the respective nanocomposite film, $K_\beta = 7.7 \times 10^4$ cm^2/mol is the absorption coefficient at 840 cm^{-1} and $K_\alpha = 6.1 \times 10^4$ cm^2/mol is the absorption coefficient at 762 cm^{-1} [40]. Absorption at 762 cm^{-1} is denoted by A_α and for 840 cm^{-1} is denoted by A_β [31, 41]. The β-phase content was observed to be 54.26 % for bare PVDF thin film and increased up to ~80±2 % after the addition of TMDCs [17].

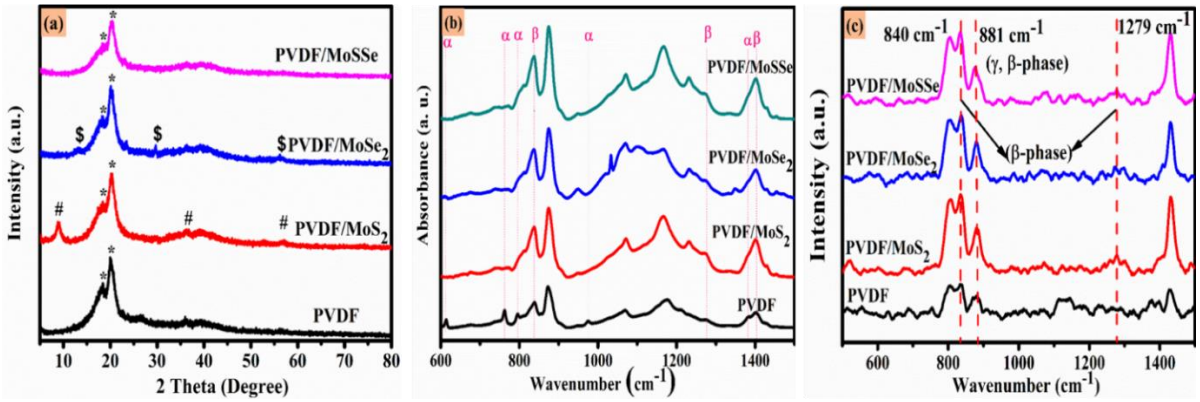

Figure 3.3 (a) XRD, (b) FTIR and (c) Raman spectra of all the fabricated thin films.

The Raman spectra of bare PVDF and PVDF/TMDCs nanocomposites based film is shown in Figure 3.3(c), which further strengthen the presence of polar β-phase with a peak at 840 cm^{-1} [42, 43]. Raman spectra also confirms the increase in the ferroelectric properties of PVDF after addition of transition metal dichalcogenides. Two new Raman bands, out of them one at 881 cm^{-1} is because of the γ and β-phases and one at 1279 cm^{-1} represents the β-phase of PVDF appeared, indicating the phase modification in PVDF [40, 42, 43]. Further the surface morphology of the fabricated thin films is also analyzed by using scanning electron microscopy (SEM) at a voltage of 10 kV. As shown in Figure 3.4 (b-d) the distribution of MoS_2, $MoSe_2$ and MoSSe is uniform over the PVDF matrix without any obvious agglomeration, suggesting that the fillers in the PVDF matrix were effectively dispersed.

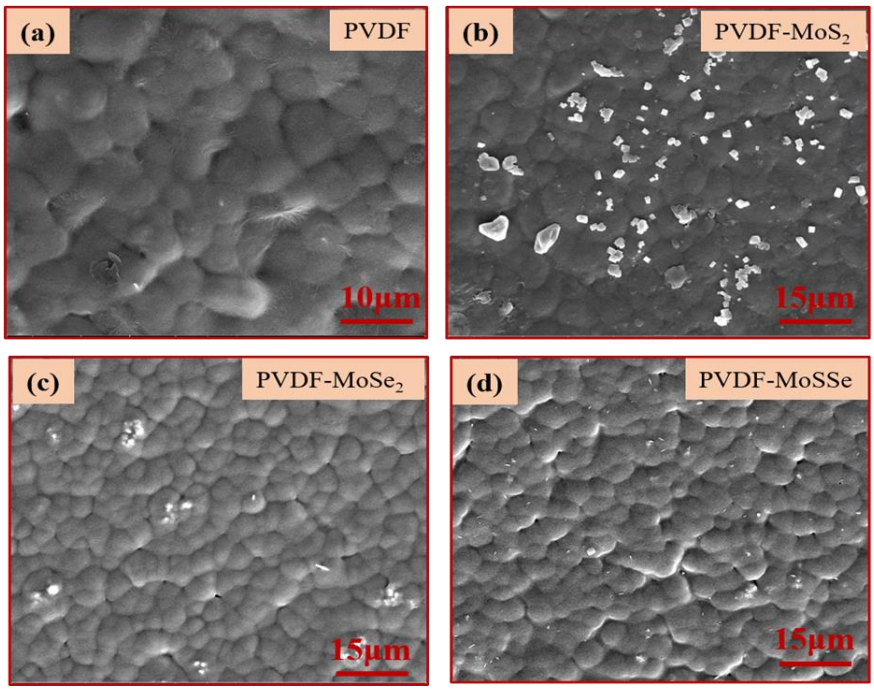

Figure 3.4 SEM image of thin films (a) PVDF; (b) PVDF/MoS_2, (c) PVDF/$MoSe_2$ and (d) PVDF/MoSSe.

3.3.3 Output Performance Analysis of Fabricated PENGs

The piezoresponse of the fabricated PENGs of dimensions of the order of 1.75 cm × 1.75 cm have been studied through continuous tapping on the PENGs with the help of an electro dynamic shaker unit with varying frequency from 3 Hz to 10 Hz (which is shown in Supplemental Video 1). The peak to peak open circuit voltage generated by the PVDF and PVDF/TMDCs composite films based nanogenerators at the tapping frequency of 7 Hz is shown in Figure 3.5. The observed results show that PVDF/TMDCs composite thin films based nanogenerators, generates more voltage than pristine PVDF based nanogenerator. We get the maximum peak to peak open circuit voltage for PVDF/MoSSe based nanogenerator, that is nearly 3.3 times more than the maximum peak to peak open circuit voltage (V_{OC}) generated by bare PVDF at a tapping frequency of 7 Hz. Table 3.1 gives the generated peak to peak open circuit voltage by various fabricated piezoelectric devices at tapping frequency of 7 Hz.

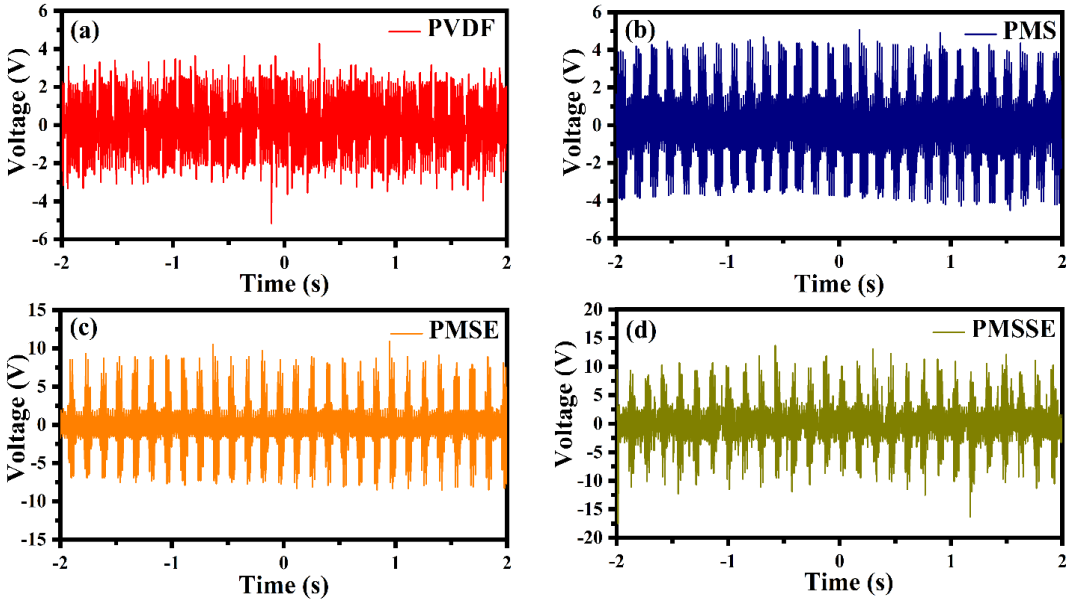

Figure 3.5 Open circuit voltage generation for (a) PVDF, (b) PVDF/MoS_2, (c) PVDF/$MoSe_2$, (d) PVDF/MoSSe thin film nanogenerators at a tapping frequency of 7 Hz.

Table 3.1. Peak to peak open circuit voltage generated by PENGs at a tapping frequency of 7 Hz.

S. No.	Nanogenerator	Peak to peak output voltage (V)
1.	PVDF	9.4
2.	PVDF/MoS_2	9.8
3.	PVDF/$MoSe_2$	19.4
4.	PVDF/MoSSe	31.2

Frequency dependent response of all the fabricated nanogenerators in terms of variation of peak to peak (V_{OC}) at different tapping frequencies is shown in Figure 3.6 (a). As shown in

Figure, all the nanogenerators follow the same trend, where the output voltage first increases up to the tapping frequency of 7 Hz and then the value starts decreasing with further increase in the tapping frequency beyond 7 Hz. Further, Figure 3.6 (b) shows the obtained open circuit voltages for the PVDF/MoSSe at different frequencies, which are 21.4, 29.8, 31.2 and 18.6 V at a tapping frequency of 3 Hz, 5 Hz, 7 Hz and 10 Hz, respectively. We have also generated voltage from the nanogenerators by tapping with finger. To conclude the excellency of the fabricated 2D TMDCs based piezoelectric device in the present study, its piezoresponse is compared in the Table 3.2. with the other reported results on the 2D materials. The table clearly signifies that the response of the PVDF/MoSSe based PENG is better than the other reported PENGs.

Table 3.2. Comparison between the performance of piezoelectric nanogenerator in terms of generated output voltage and current for different 2 D materials and their nanocomposites.

Device Structure	**Output Voltage**	**Output Current**	**Synthesis**	**Reference**
PVDF/RGO	1.915 V	-	Solution Casting	[48]
PVDF/RGO-Ag	18 V (peak to peak)		Solution Casting	[49]
PVDF/MoS_2	14 V		Salt intercalation, electrospinning	[44]
PVDF/RGO	~756 mv	0.114 μA	Solution Casting	[17]
PVDF/$NaNbO_3$/RGO	~2.16 V	0.383 μA	Solution Casting	[17]
Monolayer MoS_2	20 mV	30 pA	CVD	[50]
SnSe	~760 mV	~1 nA	mechanically exfoliated	[51]
PVDF-TrFE	7 V	58 nA	Spin coated	[52]
Graphene/P(VDF-TrfE)/graphene multilayers	~3 V	~0.37 μAcm^{-2}	CVD, spin coated	[53]
PVDF/Graphene	7.9 V	4.5 μA	Electrospinning	[54]
WSe_2	90 mV	100 pA	CVD, Turbostatic stacking	[55]
PVDF/Graphene, doped with Ce^{3+}	11V	6 nA/cm^2	Electrospinning	[56]
PVDF/MoSSe	31.2 V	1.26 μA	Solution Casting	**This work**

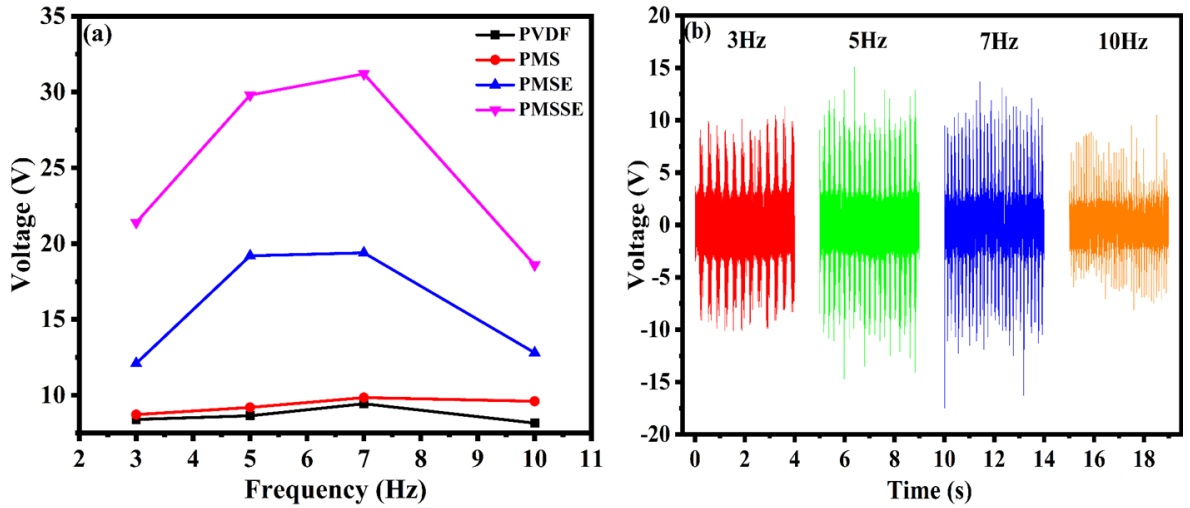

Figure 3.6 (a) Showing the variation in maximum peak to peak voltage by varying the tapping frequency from 3Hz to 10 Hz and (b) open circuit voltages for PVDF/MoSSe at different tapping frequencies.

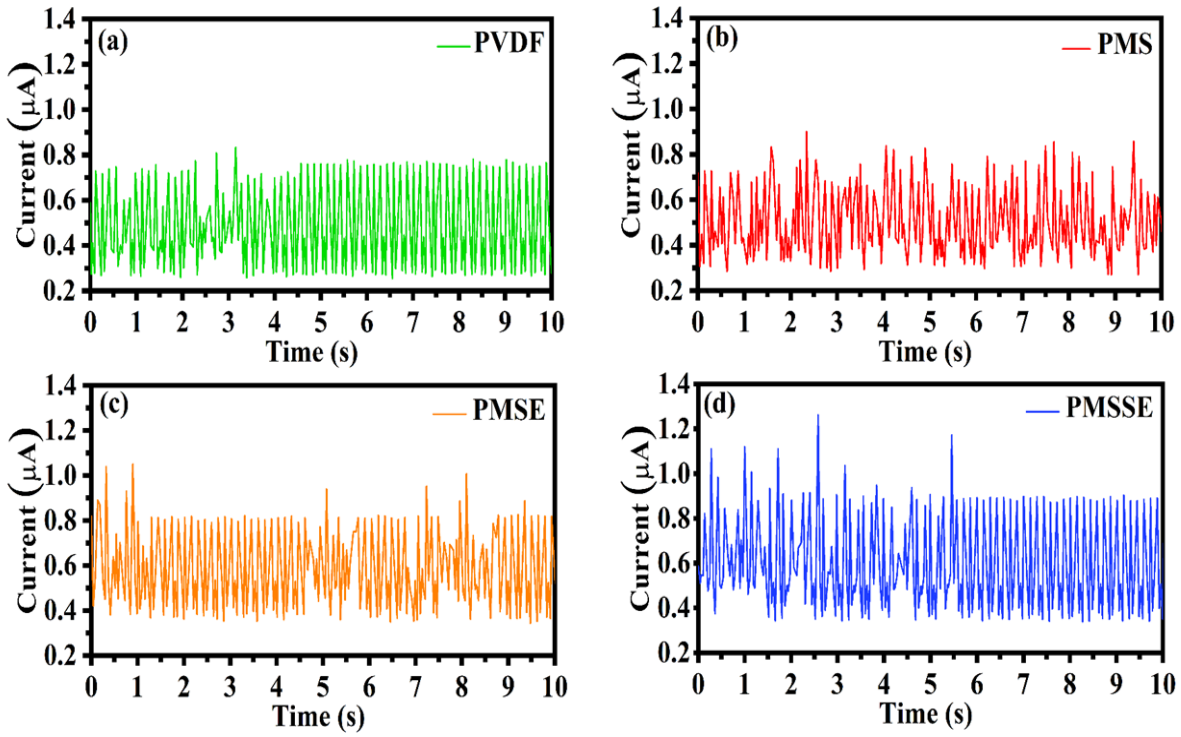

Figure 3.7 Short circuit current generation for (a) PVDF, (b) PVDF/MoS_2, (c) PVDF/$MoSe_2$ and (d) PVDF/MoSSe thin film nanogenerators by continuous tapping at 7Hz frequency.

The short circuit current for all the fabricated PENGs was also measured by applying the tapping frequency of 7 Hz, as shown in Figure 3.7. The short circuit current obtained is 0.8 μA, 0.9 μA, 1.05 μA and 1.26 μA for PVDF, PVDF/MoS_2, PVDF/$MoSe_2$ and PVDF/MoSSe, respectively. Further, we have also analyzed the output performance of all the nanogenerators

by applying different load resistance from 10 MΩ to 100 MΩ. It was observed that the voltage drop is increased as the load resistance was increased while the current is decreased with increasing load, which is shown in Figure 3.8 (a) and (b) respectively. The maximum output voltage of around 25 V is observed for PVDF/MoSSe nanogenerator at a load resistance of 100 MΩ.

To check the potential utility of the nanogenerators we used the output voltage generated by them to light up the commercially available LED without any storage device. The generated ac voltage is converted to dc by a full wave rectifier. A capacitor of 4.7μF is used to store the charge generated by PENGs, which is charged up to 2 V.

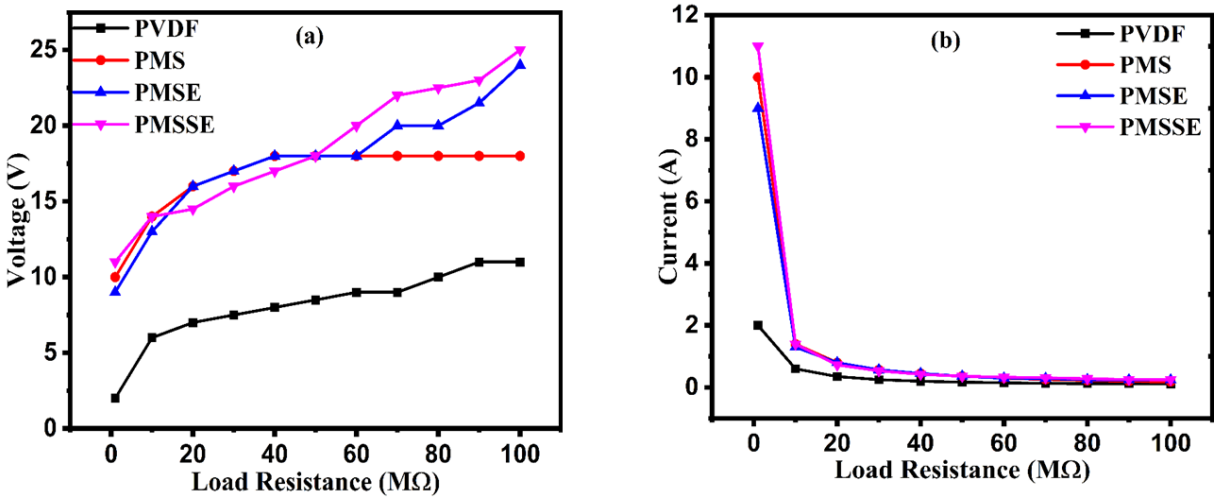

Figure 3.8 Variation in (a) Voltage and (b) Current by varying the load resistance from 10 MΩ to 100 MΩ.

3.3.4 Underlying Mechanism of the Fabricated PENGs

In the present study, the enhanced piezoresponse of the fabricated nanogenerators after the addition of TMDCs in the PVDF matrix is attributed to the following facts, which are: (i) increment in β-phase content after the addition of TMDCs and (ii) contribution of inherent piezoelectricity of TMDCs in the overall piezoresponse of nanogenerators. The polymer chain of polyvinylidene fluoride is consists of repeated units of CH_2-CF_2 monomers. Based on the sequence of these monomer units, PVDF exists in many crystalline phases, mainly two α and β-phases. The alternate trans and gauche conformation (TGTG) results in the α-phase and all trans conformation (TTTT) results in the formation of β-phase. Figure 3.9 (a) and (b) shows the schematic representation for the β and α-phases of the PVDF respectively. Because of the difference in the electronegativity of hydrogen and carbon atoms as compared to the fluorine atoms, a strong dipole moment exists in each monomer unit of PVDF. Due to the parallel

orientation of monomer units in the β-phase results in the highest dipole moment per unit cell. On the other hand, the α-phase which has the antiparallel arrangement of monomer units, results in no net dipole moment because all the dipoles cancel each other. Now, after the addition of TMDCs, chain of $–CH_2/CF_2$- dipoles present in PVDF, interacts with MoS_2, $MoSe_2$ and MoSSe. CH_2 interacts with negative charges present on the surface while the CF_2 interacts with the positive charges on the surface. Transition metal interacts with CF_2 and chalcogen atom interacts with CH_2. This interaction between the PVDF monomer units and TMDCs helps in the formation of all trans (TTTT) conformation, resulting into the enhancement of β-phase percentage in PVDF/TMDCs composites as compared to bare PVDF [44, 45]. TMDCs can also be helpful in the arrangement of the dipole moments which are previously present in the PVDF matrix [45]. As a result, piezo response of the composite thin films gets enhanced.

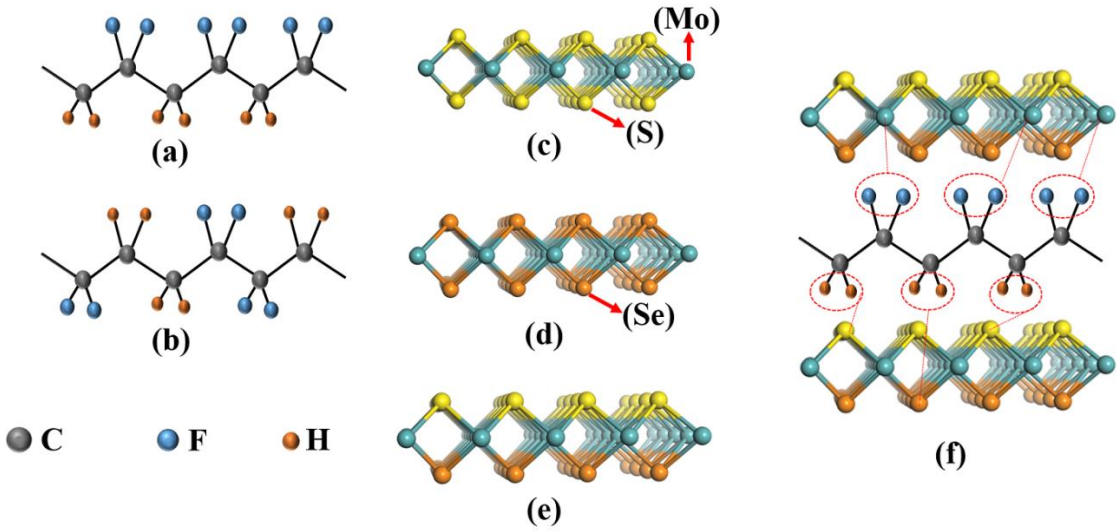

Figure 3.9 A schematic showing the orientation of (a) β-phase, (b) α –phase of PVDF, (c) MoS_2, (d) $MoSe_2$, (e) MoSSe and (f) shows the interaction of TMDCs with PVDF.

Further, the maximum piezoresponse for the PVDF/MoSSe based nanogenerators, can be explained on the basis of theoretical study carried out by J. Lou, et. al, in which the synthesized crystal has two dissimilar chalcogen atoms sandwiching a transition metal between them, such as, S-Mo-Se, S-W-Se etc. leading to enhanced piezoresponse because of the additional breaking of the out-of-plane mirror symmetry, in comparison to pure MoS_2 and $MoSe_2$, where piezoelectric effect is only due to the presence of in-plane asymmetry [30]. Further, it has also been reported, based on the DFT calculation, as we move downward in group 16 of the periodic table from sulphur (S) to tellurium (Te), the corresponding TMDC have higher piezoelectric coefficients, thereby supporting the higher piezoresponse for $MoSe_2$

in comparison to MoS_2 for the present study [22, 24]. The Piezoelectric coefficient (d_{11}) of TMDCs is calculated by using the relation

$$d_{11} = \frac{e_{11}}{C_{11}-C_{12}} \tag{3.2}$$

Where, coefficient d_{11} measures the mechanical to electrical energy conversion ratio of material, e_{11} is piezoelectric coefficient and C defines elastic stiffness parameters of the material. d_{11} coefficients in TMDCs follow a periodic trend, its magnitude increases while going downward in the chalcogenide group. This trend can also be related with the polarizability of chalcogenide atoms, because atoms are easily polarized while going down in a group in the periodic table. The chalcogenide atoms dominate the piezoelectric effect in TMDCs, chalcogenide atom has more effect on the d_{11} coefficient than transition metal atoms [22, 24]. Therefore, PVDF/$MoSe_2$ nanogenerator will generate higher voltage because of its higher piezoelectric property as compared to PVDF/MoS_2. However, the d_{11} of MoSSe is in between $MoSe_2$ and MoS_2 but the output voltage of PVDF/MoSSe is still maximum. As the MoS_2 and $MoSe_2$ both are regular MX_2 type transition metal dichalcogenides while the MoSSe is MXY type structure of transition metal dichalcogenides called as Janus TMDCs. Due to MXY type structure, the reflection symmetry with respect to Mo atom is broken in the MoSSe structure which results in the additional out of plane electric polarizations in addition to the already existing strong in-plane piezoelectric effects similar to the conventional MX_2 structure. Figure 3.9 (c), (d), (e) shows the schematic of the structures of MoS_2, $MoSe_2$ and MoSSe respectively and Figure 3.9 (f) shows the interaction of TMDCs with PVDF. Conventional MX_2 possesses a reflection symmetry around central M atom due to which their piezoelectric polarizations are confined along only in-plane direction. In MXY, the electronegativity of both X and Y are different which gives to unequal lengths of M-X and M-Y bonds [29, 30, 45, 47]. Due to which, the reflection symmetry in MoSSe is broken and therefore vertical piezoelectric polarizations were allowed only in MoSSe while it is zero in MoS_2 and $MoSe_2$, thereby enhancing the overall generated piezo-output voltage for PVDF/MoSSe as compared to PVDF/MoS_2 and PVDF/$MoSe_2$ based nanogenerators.

3.4 Conclusion

In summary, a piezoelectric nanogenerator based on PVDF/TMDCs with higher performance have been demonstrated for generating electrical power. The addition of MoS_2, $MoSe_2$ and MoSSe in the PVDF matrix for synthesizing composite thin film for fabricating flexible nanogenerators has been carried out. It was found that the piezoresponse of PVDF/TMDCs based nanogenerators was greatly enhanced in comparison to pristine PVDF. The effect of

variable vibrating frequency applied by an electro dynamic shaker is also investigated for all the nanogenerators, and is found that all the device shows the maximum response when tapped by 7 Hz frequency. PVDF/MoSSe based nanogenerator generates the maximum peak to peak output voltage and short circuit current of 31.2 V and 1.26 uA respectively, that is nearly 3.3 times more than generated by the pristine PVDF based nanogenerator. The excellent performances of PENG are attributed to the combined contribution due to the nucleation of the electroactive polar β-phase content of the PVDF in the composite films, contribution of inherent piezoelectric property of TMDC (MoS_2, $Mose_2$) due to in-plane asymmetry, and finally addition of piezoelectric contribution due to the breaking of out-of-plane symmetry in PVDF/MoSSe based PENG. In addition, the obtained PENG based on PVDF/MoSSe is shown to be a credible electric energy generator by harnessing mechanical energy generated by dynamic shaker which can mimic the ambient vibrations to glow the commercially available LED. The current study promises the usage of TMDC, which are ultrathin, mechanically stronger in the field of energy harvesting for self-powering wearable electronics. Hence, the present work will give a new approach to enhance the piezoelectric performance by systematically introducing the asymmetry across the out of plane crystal structure of 2D TMDCs in the PVDF matrix.

References

[1] IEA (2019), World Energy Outlook 2019, IEA, Paris https://www.iea.org/reports/world-energy-outlook-2019.

[2] S.P. Beeby, M.J. Tudor, N.M. White, Energy harvesting vibration sources for microsystems applications, Measurement Science and Technology 17(12) (2006) R175-R195.

[3] S.R. Anton, H.A. Sodano, A review of power harvesting using piezoelectric materials (2003-2006), Smart Materials and Structures 16(3) (2007) R1-R21.

[4] K.A. Cook-Chennault, N. Thambi, A.M. Sastry, Powering MEMS portable devices—a review

of non-regenerative and regenerative power supply systems with special emphasis on piezoelectric energy harvesting systems, Smart Materials and Structures 17(4) (2008) 043001.

[5] R. Yang, Y. Qin, L. Dai, Z.L. Wang, Power generation with laterally packaged piezoelectric fine wires, Nature Nanotechnology 4(1) (2009) 34-39.

[6] M.-Y. Choi, D. Choi, M.-J. Jin, I. Kim, S.-H. Kim, J.-Y. Choi, S.Y. Lee, J.M. Kim, S.-W. Kim, Mechanically Powered Transparent Flexible Charge-Generating Nanodevices with Piezoelectric ZnO Nanorods, Adv. Mat. 21(21) (2009) 2185-2189.

[7] J.M. Wu, C. Xu, Y. Zhang, Z.L. Wang, Lead-Free Nanogenerator Made from Single ZnSnO3 Microbelt, ACS Nano 6(5) (2012) 4335-4340.

[8] Z. Wang, J. Hu, A.P. Suryavanshi, K. Yum, M.-F. Yu, Voltage Generation from Individual BaTiO3 Nanowires under Periodic Tensile Mechanical Load, Nano Lett. 7(10) (2007) 2966-2969.

[9] B. Moorthy, C. Baek, J.E. Wang, C.K. Jeong, S. Moon, K.-I. Park, D.K. Kim, Piezoelectric energy harvesting from a PMN–PT single nanowire, RSC Advances 7(1) (2017) 260-265.

[10] A. Gheibi, R. Bagherzadeh, A.A. Merati, M. Latifi, Electrical power generation from piezoelectric electrospun nanofibers membranes: electrospinning parameters optimization and effect of membranes thickness on output electrical voltage, Journal of Polymer Research 21(11) (2014) 571.

[11] D. Zhang, P. Tian, X. Chen, J. Lu, Z. Zhou, X. Fan, R. Huang, Fullerene C60-induced growt of hollow piezoelectric nanowire arrays of poly (vinylidene fluoride) at high pressure, Composites Science and Technology 77 (2013) 29-36.

[12] V.V. Kochervinskii, Specifics of structural transformations in poly(vinylidene fluoride)-based ferroelectric polymers in high electric fields, Polymer Science Series C 50(1) (2008) 93-121.

[13] E. Fukada, History and recent progress in piezoelectric polymers, IEEE Transactions on Ultrasonics, Ferroelectrics, and Frequency Control 47(6) (2000) 1277-1290.

[14] H. Pan, B. Na, R. Lv, C. Li, J. Zhu, Z. Yu, Polar phase formation in poly(vinylidene fluoride) induced by melt annealing, J. Polym. Sci. B Ploym. Phys. 50 (2012) 1422-1437.

[15] H.H. Singh, S. Singh, N. Khare, Enhanced β-phase in PVDF polymer nanocomposite and its application for nanogenerator, 29(1) (2018) 143-150.

[16] Y. Niu, K. Yu, Y. Bai, H.J.I.t.o.u. Wang, ferroelectrics,, f. control, Enhanced dielectric performance of BaTiO 3/PVDF composites prepared by modified process for energy storage applications, 62(1) (2015) 108-115.

[17] H.H. Singh, S. Singh, N. Khare, Design of flexible PVDF/NaNbO3/RGO nanogenerator and understanding the role of nanofillers in the output voltage signal, Composites Science and Technology 149 (2017) 127-133.

[18] Y. Peng, M. Que, J. Tao, X. Wang, J. Lu, G. Hu, B. Wan, Q. Xu, C. Pan, Progress in piezotronic and piezo-phototronic effect of 2D materials, 2D Materials 5(4) (2018) 042003.

[19] S. Yu, Q. Rice, B. Tabibi, Q. Li, F.J. Seo, Piezoelectricity in WSe2/MoS2 heterostructure atomic layers, Nanoscale 10(26) (2018) 12472-12479.

[20] L.M. Malard, T.V. Alencar, A.P.M. Barboza, K.F. Mak, A.M. de Paula, Observation of intense second harmonic generation from MoS2 atomic crystals, Physical Review B 87(20) (2013) 201401.

[21] W. Wu, L. Wang, Y. Li, F. Zhang, L. Lin, S. Niu, D. Chenet, X. Zhang, Y. Hao, T.F. Heinz, J. Hone, Z.L. Wang, Piezoelectricity of single-atomic-layer MoS2 for energy conversion and piezotronics, Nature 514(7523) (2014) 470-474.

[22] K.-A.N. Duerloo, M.T. Ong, E.J. Reed, Intrinsic Piezoelectricity in Two-Dimensional Materials, The Journal of Physical Chemistry Letters 3(19) (2012) 2871-2876.

[23] X. Song, F. Hui, T. Knobloch, B. Wang, Z. Fan, T. Grasser, X. Jing, Y. Shi, M. Lanza, Piezoelectricity in two dimensions: Graphene vs. molybdenum disulfide, Appl. Phys. Lett. 111(8) (2017) 083107.

[24] M.N. Blonsky, H.L. Zhuang, A.K. Singh, R.G. Hennig, Ab Initio Prediction of Piezoelectricity in Two-Dimensional Materials, ACS Nano 9(10) (2015) 9885-9891.

[25] R. Hinchet, U. Khan, C. Falconi, S.-W. Kim, Piezoelectric properties in two-dimensiona materials: Simulations and experiments, Materials Today 21(6) (2018) 611-630.

[26] N. Chaudhary, M. Khanuja, Abid, S.S. Islam, Hydrothermal synthesis of MoS2 nanosheet for multiple wavelength optical sensing applications, Sensors and Actuators A: Physical 277 (2018) 190-198.

[27] Q. Gong, L. Cheng, C. Liu, M. Zhang, Q. Feng, H. Ye, M. Zeng, L. Xie, Z. Liu, Y. Li, Ultrathin MoS2(1–x)Se2x Alloy Nanoflakes For Electrocatalytic Hydrogen Evolution Reaction, ACS Catalysis 5(4) (2015) 2213-2219.

[28] H. Tang, K. Dou, C.-C. Kaun, Q. Kuang, S. Yang, MoSe2 nanosheets and their graphene hybrids: synthesis, characterization and hydrogen evolution reaction studies, Journal of Materials Chemistry A 2(2) (2014) 360-364.

[29] A.-Y. Lu, H. Zhu, J. Xiao, C.-P. Chuu, Y. Han, M.-H. Chiu, C.-C. Cheng, C.-W. Yang, K.H. Wei, Y. Yang, Y. Wang, D. Sokaras, D. Nordlund, P. Yang, D.A. Muller, M.-Y. Chou, X. Zhang, L.-J. Li, Janus monolayers of transition metal dichalcogenides, Nature Nanotechnology 12(8) (2017) 744-749.

[30] J. Zhang, S. Jia, I. Kholmanov, L. Dong, D. Er, W. Chen, H. Guo, Z. Jin, V.B. Shenoy, L. Shi, J. Lou, Janus Monolayer Transition-Metal Dichalcogenides, ACS Nano 11(8) (2017) 8192-8198.

[31] B. Jaleh, A. Jabbari, Evaluation of reduced graphene oxide/ZnO effect on properties of PVDF nanocomposite films, Appl. Surf. Sci. 320 (2014) 339-347.

[32] P. I. Devi, K. Ramachandran, Dielectric studies on hyberidised PVDF-ZnO nanocomposites, J. Exp. Nanosci. 6 (2011) 281-293.

[33] S. Sarkar, S. Garain, D. Mandal, K.K. Chattopadhyay, Electro-active phase formation in PVDF–BiVO4 flexible nanocomposite films for high energy density storage application, RSC Advances 4(89) (2014) 48220-48227.

[34] P. Yiya, M. Zhaoyu, Z. Chang, L. Jun, Y. Weichao, J. YunBo, Q. Yitai, Hydrothermal Synthesis and Characterization of Single-Molecular-Layer MoS2 and MoSe2, 30(8) (2001) 772-773.

[35] W. Ding, L. Hu, J. Dai, X. Tang, R. Wei, Z. Sheng, C. Liang, D. Shao, W. Song, Q. Liu, M. Chen, X. Zhu, S. Chou, X. Zhu, Q. Chen, Y. Sun, S.X. Dou, Highly Ambient-Stable 1T-MoS2 and 1T-WS2 by Hydrothermal Synthesis under High Magnetic Fields, ACS Nano 13(2) (2019) 1694-1702.

[36] Y. Zhang, W. Zeng, Y. Li, The hydrothermal synthesis of 3D hierarchical porous MoS2 microspheres assembled by nanosheets with excellent gas sensing properties, Journal of Alloys and Compounds 749 (2018) 355-362.

[37] Z. Wang, H.Y. Yue, Z.M. Yu, F. Yao, X. Gao, E.H. Guan, H.J. Zhang, W.Q. Wang, S.S. Song, One-pot hydrothermal synthesis of MoSe2 nanosheets spheres-reduced graphene oxide composites and application for high-performance supercapacitor, Journal of Materials Science: Materials in Electronics 30 (2019) 8537-8545.

[38] P. Martins, A.C. Lopes, S. Lanceros-Mendez, Electroactive phases of poly(vinylidene fluoride): Determination, processing and applications, Progress in Polymer Science 39(4) (2014) 683-706.

[39] N. Soin, D. Boyer, K. Prashanthi, S. Sharma, A.A. Narasimulu, J. Luo, T.H. Shah, E. Siores, T. Thundat, Exclusive self-aligned β-phase PVDF films with abnormal piezoelectric coefficient prepared via phase inversion, Chemical Communications 51(39) (2015) 8257-8260.

[40] D. Sengupta, A.G.P. Kottapalli, S.H. Chen, J.M. Miao, C.Y. Kwok, M.S. Triantafyllou, M.E. Warkiani, M. Asadnia, Characterization of single polyvinylidene fluoride (PVDF) nanofiber for flow sensing applications, AIP Advances 7(10) (2017) 105205.

[41] J.S. Lee, K.-Y. Shin, O.J. Cheong, J.H. Kim, J. Jang, Highly sensitive and multifunctional tactile sensor using free-standing ZnO/PVDF thin film with graphene electrodes for pressure and temperature monitoring, Scientific reports 5 (2015) 7887.

[42] P. Thakur, A. Kool, B. Bagchi, S. Das, P. Nandy, Enhancement of β phase crystallization and dielectric behavior of kaolinite/halloysite modified poly(vinylidene fluoride) thin films, Applied Clay Science 99 (2014) 149-159.

[43] A.P. Indolia, M.S. Gaur, Optical properties of solution grown PVDF-ZnO nanocomposite thin films, Journal of Polymer Research 20(1) (2012) 43.

[44] K. Maity, B. Mahanty, T.K. Sinha, S. Garain, A. Biswas, S.K. Ghosh, S. Manna, S.K. Ray, D. Mandal, Two-Dimensional Piezoelectric MoS2-Modulated Nanogenerator and Nanosensor Made of Poly(vinlydine Fluoride) Nanofiber Webs for Self-Powered Electronics and Robotics, 5(2) (2017) 234-243.

[45] V. Singh, B. Singh, Fabrication of PVDF-transition metal dichalcogenides based flexible piezoelectric Nanogenerator for energy harvesting applications, Materials Today: Proceedings 28 (2020) 282-285.

[46] L. Dong, J. Lou, V.B. Shenoy, Large In-Plane and Vertical Piezoelectricity in Janus Transition Metal Dichalchogenides, ACS Nano 11(8) (2017) 8242-8248.

[47] M.K. Mohanta, A. De Sarkar, Interfacial hybridization of Janus MoSSe and BX (X = P, As) monolayers for ultrathin excitonic solar cells, nanopiezotronics and low-power memory devices, Nanoscale (2020).

[48] A. Anand, D. Meena, K.K. Dey, M.C. Bhatnagar, Enhanced piezoelectricity properties of reduced graphene oxide (RGO) loaded polyvinylidene fluoride (PVDF) nanocomposite films for nanogenerator application, Journal of Polymer Research 27(12) (2020) 358.

[49] M. Pusty, L. Sinha, P.M.J.N.J.o.C. Shirage, A flexible self-poled piezoelectric nanogenerator based on a rGO–Ag/PVDF nanocomposite, 43(1) (2019) 284-294.

[50] S.K. Kim, R. Bhatia, T.-H. Kim, D. Seol, J.H. Kim, H. Kim, W. Seung, Y. Kim, Y.H. Lee, S.-W. Kim, Directional dependent piezoelectric effect in CVD grown monolayer MoS2 for flexible piezoelectric nanogenerators, Nano Energy 22 (2016) 483-489.

[51] P. Li, Z. Zhang, W. Shen, C. Hu, W. Shen, D. Zhang, A self-powered 2D-material sensor unit driven by a SnSe piezoelectric nanogenerator, Journal of Materials Chemistry A (2021).

[52] Z. Pi, J. Zhang, C. Wen, Z.-b. Zhang, D. Wu, Flexible piezoelectric nanogenerator made of poly(vinylidenefluoride-co-trifluoroethylene) (PVDF-TrFE) thin film, Nano Energy 7 (2014) 33-41.

[53] S.-H. Bae, O. Kahya, B.K. Sharma, J. Kwon, H.J. Cho, B. Özyilmaz, J.-H. Ahn, Graphene-P(VDF-TrFE) Multilayer Film for Flexible Applications, ACS Nano 7(4) (2013) 3130-3138.

[54] M.M. Abolhasani, K. Shirvanimoghaddam, M. Naebe, PVDF/graphene composite nanofibers with enhanced piezoelectric performance for development of robust nanogenerators, Composites Science and Technology 138 (2017) 49-56.

[55] J.H. Lee, J.Y. Park, E.B. Cho, T.Y. Kim, S.A. Han, T.H. Kim, Y. Liu, S.K. Kim, C.J. Roh, H.J.J.A.M. Yoon, Reliable piezoelectricity in bilayer WSe2 for piezoelectric nanogenerators, 29(29) (2017) 1606667.

[56] S. Garain, S. Jana, T.K. Sinha, D. Mandal, Design of In Situ Poled Ce3+-Doped Electrospun PVDF/Graphene Composite Nanofibers for Fabrication of Nanopressure Sensor and Ultrasensitive Acoustic Nanogenerator, ACS Applied Materials & Interfaces 8(7) (2016) 4532-4540.

[57] X. Guan, Y. Zhang, H. Li, J. Ou, PZT/PVDF composites doped with carbon nanotubes, Sens. Actuators, A 194 (2013) 228-231.

[58] R. Ahammed, N. Jena, A. Rawat, M. K. Mohanta, Dimple, A. D. Sarkar, Ultra Out-of-Plane Piezoelectricity Meets Giant Rashba Effect in 2D Janus Monolayers and Bilayers of Group IV Transition-Metal Trichalcogenides, The Journal of Physical Chemistry C, 124 (2021) 21250-21260.

CHAPTER 4

Effect of variation of weight percentage of MoS_2 in PVDF-MoS_2 drop casted films for flexible piezoelectric and triboelectric nanogenerator for powering electronic devices.

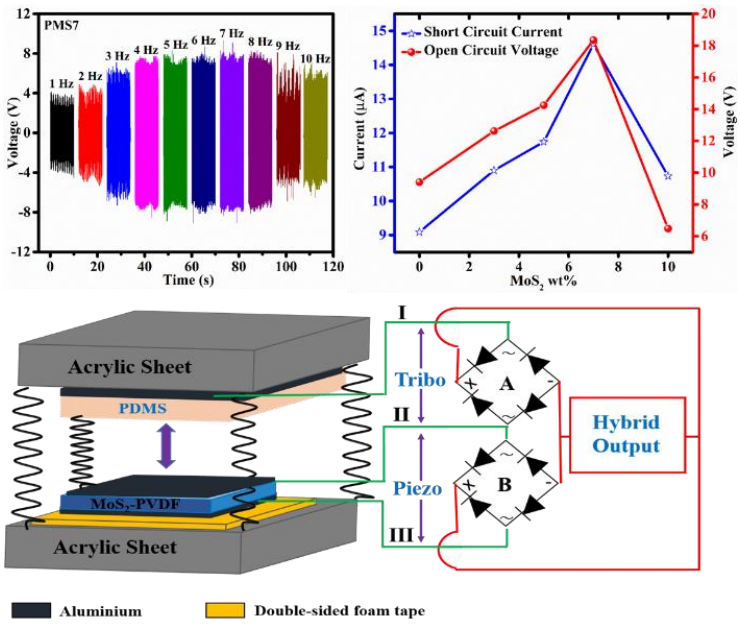

In the previous chapter, we have studied that the addition of TMDCs enhances the piezoelectric properties of PVDF, however, the concentration of nanofiller in the PVDF also contributes to the device output performance. To check the ideal concentration of nanofiller, here we have fabricated different piezoelectric and triboelectric nanogenerators based on PVDF-MoS_2 by varying the weight percentage (0 %, 3%, 5 %, 7 wt % and 10 wt%) of MoS_2. The results show that 7 wt% of MoS_2 is the optimum amount of doping for both piezoelectric and triboelectric energy harvesting, above this level the performance of the nanogenerator abruptly decreased due to MoS_2 agglomeration in the PVDF matrix. Further, PVDF-MoS_2/PDMS based piezo-tribo based hybrid nanogenerator (HNG) is fabricated which generated the power density of ~220 μWcm^{-2}. The generated output power was used for powering of electronic stopwatch and scientific calculator.

4.1 Introduction

With increasing demand of energy, the emission of carbon is increasing in our environment and also the limited resources of fossil fuels have brought the green and renewable energy generation on high demand. Most of the electronic gadgets use batteries that also requires to be recharged after some time [1]. Renewable energy harvesting is a wonderful approach to satisfy the future generations energy demand and to mitigate the climate changes. Recently, many energy harvesters, such as, mechanical energy harvesters [2-4], solar energy harvesting [5], thermoelectric nanogenerators [6] have gained great attention of scientific community because of their cost effectiveness and environment friendly nature. With the help of the piezoelectric and triboelectric effects, mechanical energy harvesting may turn lost mechanical energy into valuable electrical energy [7]. Piezoelectric nanogenerators can convert the small vibrations of our environment, human body motions, etc., into the useful electrical energy [8]. Poly(vinylidene fluoride) (PVDF) polymer is now a days mostly used to design the flexible nanogenerators because of its inherent piezoelectric properties and highly flexible nature [9, 10]. Instead of its piezoelectric nature and flexibility its piezoelectric output is still limited for many practical applications. The piezoelectric property of PVDF mainly depends on the β-phase content of PVDF, which can be enhanced with the addition of nanofillers into the PVDF matrix, such as $BaTiO_3$ [11], $NaNbO_3$ [12], ZnO [13], RGO [14], transition metal dichalcogenides [4]. This can make PVDF a promising polymer for mechanical energy harvesting mechanism. Because of their strong design, triboelectric nanogenerators can provide higher output and are also more cost effective [15-18]. Further one can also enhance the triboelectric output with the help of plasma treatment [19], surface etching [20, 21] although this is difficult to do on a big scale. In this direction, amalgamation of the piezoelectric and triboelectric effects to increase the output of a single nanogenerator has been found to a viable choice of the scientists, where two different operating mechanisms can work together for a common aim of enhancing the output power, allowing us to extract more electricity from a single device configuration [22-27]. As reported in literature to combine the different charge density generated by different mechanism no complex design or device design is required. One of the major requirements is that one material of the resulting hybrid nanogenerator should be a piezoelectric material layer and the other can be non-piezoelectric in the contact separation mode. So that, the piezoelectric material gives the piezoelectric output and the contact between both the materials will contribute to the triboelectric output in the most common vertical contact-separation approach for generating enhanced triboelectric output [27]. PVDF is a flexible piezoelectric polymer with good piezoelectric properties which can be further

enhanced, easy to process, low cost and nontoxic, therefore it will be a viable choice for the hybrid construction. [28-30]. Many transitions metal dichalcogenides (MoS_2, $MoSe_2$, etc) and other semiconducting materials (ZnO) have been used frequently as a nanofiller in the PVDF matrix because of dual benefits, where they not only enhance the electroactive phase of PVDF, their intrinsic piezoelectric property further enhance the piezoelectric output of the nanogenerator[4, 31, 32]. Further it has also been reported in the literature that semiconducting nanofillers not only enhance the piezoelectric output, their addition in the PVDF matrix also contribute in the enhancement of the dielectric properties as well as the surface roughness leading to increased triboelectric output of the nanogenerator [33-36]. For a triboelectric material, dielectric constant is crucial for improving triboelectric performances, and the same can be enhanced by adding dielectric additives, structure modifications or by enhancing polarizations such as dipolar polarization in case of PVDF or other ferroelectric polymers [37, 38].

In addition, 2D nanomaterials are having an incredibly thin layer of crystalline structure and are used as the fillers to enhance the dielectric properties of PVDF [30, 39, 40]. The TENGs output performance is enhanced by the maximum surface charge that is provided by the ultrathin structure, high surface to volume ratio of 2D nanomaterials [30, 41]. Recent reports for TENGs based on PVDF and its copolymers have mentioned 2D materials as a filler like reduced graphene oxide (rGO) [42], black phosphorus [43], MoS_2 [35] to enhance the output performance. But there are very few reports on the effect of wt% of filler added into the PVDF matrix [30]. As the amount of the additive filler also plays an important role in the enhancement of the output performance of the device. This motivates the present piece of work. Therefore, these combined effect of addition of the nanofiller in the PVDF have opened potential of fabricating hybrid nanogenerator, where both the piezo and triboelectric effect can be harnessed to magnify the nanogenerator performance for powering wide range of electronic devices.

In the present work, we have fabricated the PVDF-MoS_2 based piezoelectric and triboelectric nanogenerators with the different weight percentages (0%, 3%, 5%, 7% and 10%) of MoS_2 and have compared their piezoelectric and triboelectric outputs. With increase in the filler concentration in the PVDF film, an increase in the piezoelectric as well as triboelectric output has been observed. Further the device with maximum piezoelectric and triboelectric output have been used for fabricating hybrid piezo-tribo nanogenerator. For this MoS_2 filled PVDF as one layer and Polydimethylsiloxane (PDMS) films as second layer have been used for fabricating a triboelectric as well as HNG in vertical contact separation mode. The

triboelectric nanogenerator with 7 wt% of MoS_2 generates a power density of 104.5 μWcm^{-2}. Further, HNG combining both piezo-triboelectric phenomenon based on MoS_2 filled PVDF demonstrates the superior performance, with remarkable high-power density of 220 $\mu W/cm^2$ in comparison to pure PVDF based HNG. The addition of nanofillers to PVDF improves not only its piezoelectric properties, but also its triboelectric output, leads to an increase in the hybrid nanogenerator's overall output. To check the practical applicability of the fabricated nanogenerator, finger tapping test were performed and the resulting power was used to glow LEDS and for the powering of electronic stopwatch and scientific calculator.

4.2 Experimental Section

4.2.1 Synthesis of PVDF-MoS_2 Flexible Thin Films

The PVDF-MoS_2 composite thin films were synthesized using a two-step method. In the first step, hydrothermally method was used for the synthesis of MoS_2 powder, which has been previously described in chapter 3. Figure 4.1(a) shows the flow chart for the hydrothermal synthesis of MoS_2. The second stage involved dissolving of 1 gm PVDF powder in 10 ml of N, N di-methyl formamide (DMF) by stirring at room temperature on a magnetic hot plate for 30 minutes. Then the different wt % of the as prepared MoS_2 powder was added to the solution to get the PVDF-MoS_2 composite thin films. Finally, the resulting composite solution was poured on a glass slide and placed at 90°C in a hot air oven for 2 hours. The thin films were then detached from the glass slides by immersing them in di-water since they are hydrophobic in nature. Finally, we obtained PVDF-MoS_2 standalone flexible composite thin films of thickness ~50 μm with different MoS_2 weight percentages. The schematic in Figure 4.1(b) shows the steps for the thin film fabrication. The synthesized PVDF films with different MoS_2 weight percentage (0%, 3%, 5%, 7% and 10%), are named as PMS0, PMS3, PMS5, PMS7 and PMS10 respectively. Further to fabricate the triboelectric layer of the hybrid nanogenerator, PDMS films were prepared by mixing the base resin and curing agent (Sylgard 184, Dow Corning Co.) in a weight ratio of 10:1. Afterward, the resultant solution was vacuumed to remove the air bubbles. Then, the solution is spin-coated on the glass substrate followed by drying in the oven to remove any moisture contents.

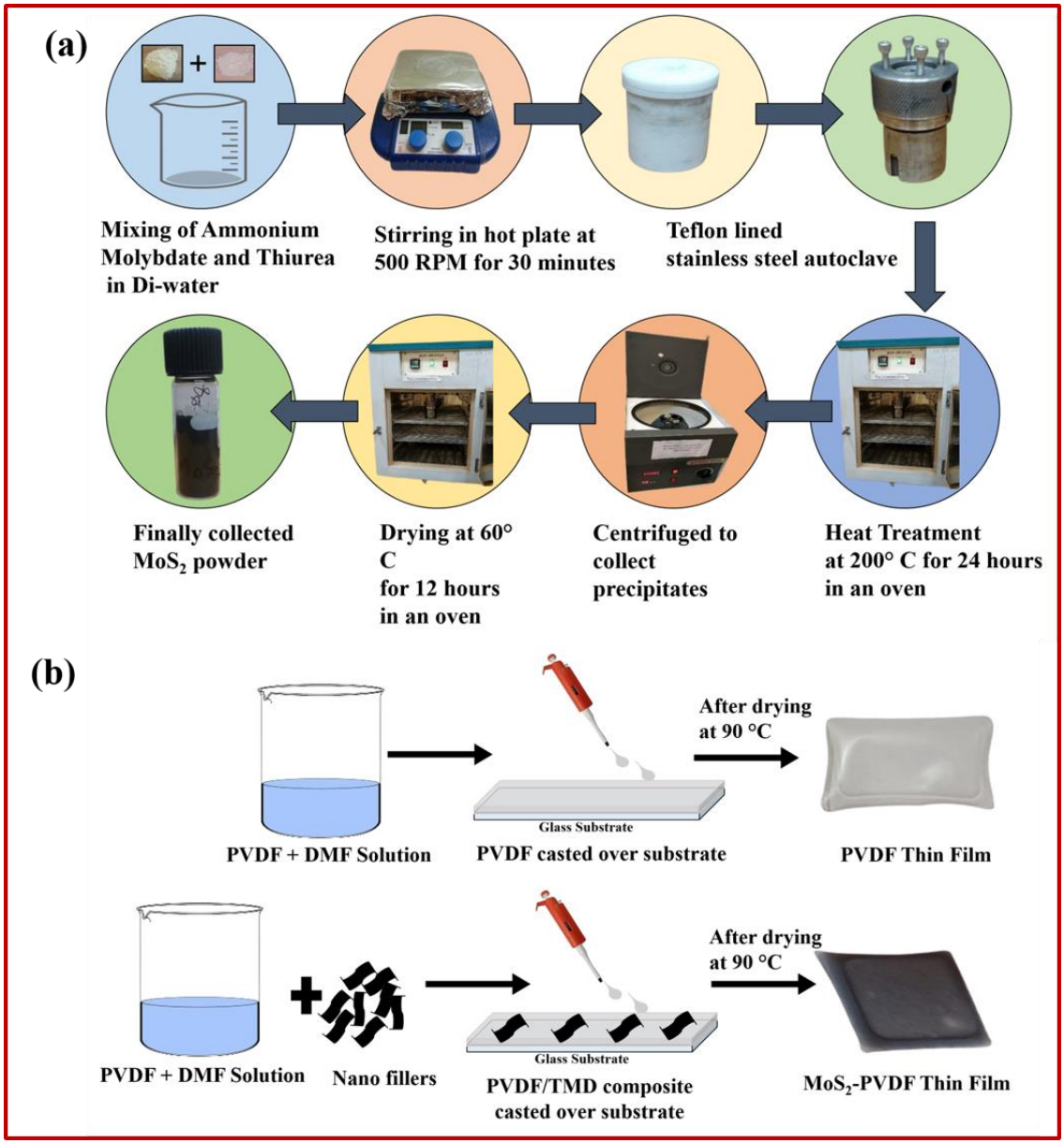

Figure 4.1 (a) Schematic diagram showing the synthesis steps for MoS_2 using hydrothermal technique and (b) step involved in the PVDF and PVDF-MoS_2 thin films fabrication using drop casting method.

4.2.2 Fabrication of Nanogenerators

To check the utility of different PVDF-MoS_2 composite thin films in mechanical energy harvesting, we fabricated the different piezoelectric nanogenerators. The synthesized films were sandwiched between Al electrodes of thickness ~100 nm, deposited using thermal evaporation technique at a chamber pressure of $4x10^{-6}$ mbarr. Copper wires were attached to the top and bottom metal electrodes to conduct the different electrical measurements. The

finally fabricated device was encapsulated with the help of insulating tap in order to ensure that the metal electrodes remain untouched during measurements.

Further, to study the effect of MoS_2 addition on the triboelectric performance of PVDF based TENG, we constructed the TENG in the vertical contact-separation geometry by coupling the PVDF and PVDF-MoS_2 thin film with the PDMS thin film as two triboelectric layers. To make the electrical connections, aluminium electrodes were deposited on the opposite side of both the thin films and the copper wires were attached to these electrodes to conduct different measurements.

4.2.3 Characterizations and Energy Harvesting Performance

Hydrothermally synthesized MoS_2 powder was characterized using X-ray diffraction (XRD) and Raman spectroscopy to confirm the successful synthesis of MoS_2. XRD characterization was carried out by Bruker D8 Advance X-ray diffractometer using X-ray source of Cu Kα (1.54 Å) and WiTec alpha 300 RA used to carry out Raman spectroscopy with a 532 nm laser source. Further, the as synthesized MoS_2 powder was examined using a high-resolution transmission electron microscope (HR-TEM). Further, to check the successful synthesis of thin films with different wt% of MoS_2 into PVDF matrix, X-ray diffractometer was used to examine the crystal structure of the films and β-phase of the films were calculated by using FTIR spectroscopy using Perkin Elmer Spectrum II. The surface morphology of all the thin films was studied using field emission scanning electron microscopy (FESEM). The surface topography and surface charge density of the thin films were investigated using Scanning Probe Microscope in AFM and KPFM modes. Then, to fabricate the piezoelectric nanogenerator, aluminum electrodes were coated on both sides of the films using thermal evaporation at $4x10^{-6}$ mbar chamber pressure. PE loop tracer was used to obtain the PE loops of the thin films at a maximum applied voltage of 80 kV/cm. The LCR meter was used to carry out the dielectric measurements in the frequency range 20 Hz to 10^4 Hz. Keithley DMM7510 digital multimeter and Tektronix MDO34 digital storage oscilloscope were used for the electrical measurements.

4.3 Results and Discussion

4.3.1 Structural and Morphological Analysis of MoS_2.

The X-ray diffraction pattern for MoS_2 powder is shown in Figure 4.2(a) confirming the synthesis of hexagonal 2H-MoS_2 phase. The peaks marked at 9.23°, 17.90°, 33.0°, 35.19°, 43.17°, and 57.62° correspond to (002), (004), (100), (101), (103) and (110) planes of MoS_2, respectively [44, 45]. Raman spectra of the synthesized MoS_2 is shown in Figure 4.2(b), where

two Raman active peaks are detected at 378.72 cm^{-1} and 405.27 cm^{-1} in the spectra. The peak that is present around 380 cm^{-1} in the spectra is due to in-plane E^1_{2g} mode of Mo-S atom in the layered structure where the peak at 405.27 cm^{-1} shows the out of plane vibrations of sulphur atoms and is assigned as A_{1g} mode. In the Raman spectra, presence of these peaks proves that MoS_2 nanostructure has been successfully synthesized and matches well with literature values [46]. Further, the morphology of the synthesized MoS_2 flakes is shown in Figure 4.2(c) through TEM images. The lower inset in the Figure 4.2 (c) shows the SAED pattern revealing the crystalline nature of the synthesized MoS_2 flakes as well as complementing the XRD results. The upper inset of Figure 4.2(c) depicts a high-resolution image, where a lattice distance was measured to be 0.6 nm corresponding to 002 plane of hexagonal MoS_2.

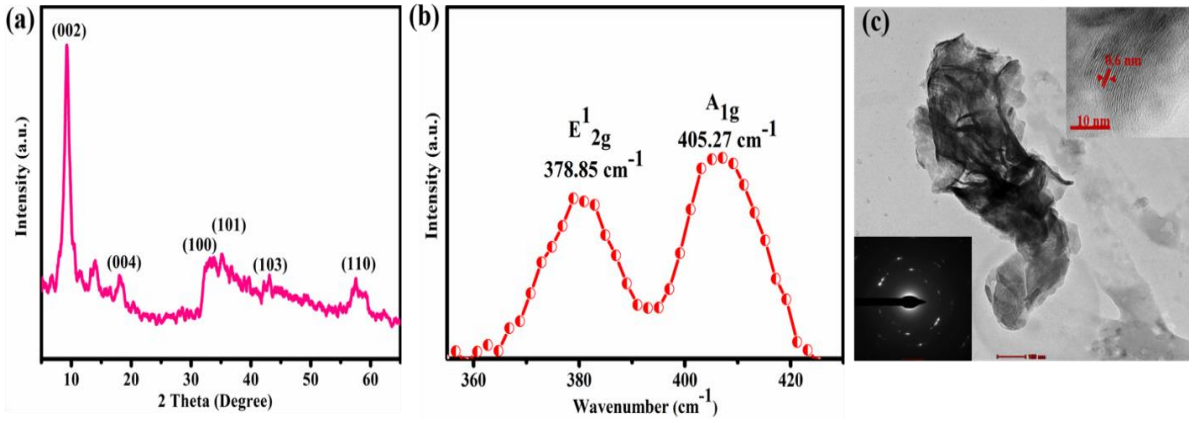

Figure 4.2 (a) XRD, (b) Raman spectra of synthesized MoS_2, and (c) TEM image of the MoS_2 nanosheets with in-plane lattice spacing and SAED pattern in upper and lower inset, respectively.

4.3.2 Structural, Morphological and Ferroelectric Analysis of PVDF-MoS_2 Thin Films.

To authenticate the distinct phases of PVDF, XRD and Fourier-transform infrared spectroscopy (FTIR) investigations were performed. The non-electroactive α-phase and electroactive β-phase can be distinguished using these techniques. Figure 4.3(a) depicts the XRD spectrum of the pure PVDF (PMS0) and MoS_2 filled PVDF thin films (PMS3, PMS5, PPMS7, PMS10) In the XRD spectra shown in Figure 4.3(a), the MoS_2 peaks are marked by '#' and PVDF peaks are marked as '*' for the given samples. The non-polar α-phase is mostly visible in the XRD pattern of pristine PVDF film, as shown by the diffraction peak labelled at 18.3° and the peak at 20.2° demonstrates the β-phase of the PVDF [4, 12, 47-49]. However, the spectra for films containing PVDF-MoS_2 composite reveals a significant increase in the electroactive β-phase, because nonpolar α-phase peaks are falling as the concentration of MoS_2 in the PVDF matrix

increases. It can be observed from the XRD spectra that after the addition of MoS_2, films reveal a remarkable rise in the electroactive β-phase as the peak intensity related to the α-phase falls whereas the intensity of the peak representing β-phase rises. The XRD spectra of thin films also confirms the successful synthesis of the composite thin films of PVDF-MoS_2 [4, 44].

Figure 4.3(b) depicts FTIR results of PVDF and PVDF-MoS_2 composite thin films. All the α and β-phases of the thin films are marked in the plot, it is observed that α and β phases are present in all the thin films [47, 49-51]. The content of β-phase plays a crucial role in determining the piezoelectric properties of PVDF. We have used FTIR spectroscopy to determine the β-phase for all the thin films using Lambert-Beer law with the equation [50, 52].

$$F(\beta) = \frac{A_\beta}{\left(\frac{k_\beta}{k_\alpha}\right)A_\alpha + A_\beta} \tag{4.1}$$

Where, K_β = 7.7 x 10^4 cm^2/mol and K_α =6.1 x 10^4 cm^2/mol are the absorption coefficients at 840 cm^{-1} and 762 cm^{-1} respectively [31, 53]. A_β and A_α are absorptions at 840 cm^{-1} and 762 cm^{-1} respectively [32, 52] and F(β) gives the β-phase content.

The existence of dominating α-phase content with trans-gauche-trans-gauche (TGTG) connection can be seen in the pristine PVDF film. When MoS_2 is added into the PVDF solution, the negative surface of the MoS_2 and the positive CH_2 dipoles of the PVDF chain interact strongly, resulting in the development of stable longer trans-trans-trans (TTTT) linkages β-phase [4, 29, 52, 54]. In these results, after calculation we find that the β-phase of bare PVDF thin film is 52.24% while β-phase is enhanced upto ~70% with the inclusion of MoS_2. So FTIR spectra confirms the presence of β-phase in all the thin films and also it is concluded that the addition of MoS_2 enhances β-phase, which means the overall piezoelectric properties of PVDF also gets enhanced. MoS_2 embedded PVDF film exhibits a progressive increase of intensity for the peak at 840 cm^{-1}, indicating a significant increase in the electroactive phase upto 7 wt %. Further on increasing the MoS_2 wt% from 7 to 10 wt %, the agglomeration of MoS_2 filler in the PVDF film may be responsible for the significant decrease in the electroactive β-phase [29, 54, 55]. To check the ferroelectric properties of the thin films, the PE loops were also performed which are shown in Figure 4.3(c). It is observed form the PE loops that the ferroelectric properties of the thin films were enhanced after the addition of MoS_2 into the PVDF matrix. Remnant polarization (D_R) calculated from the PE loops are 6.4, 8, 9.5, 11.6 and 7.7x10^{-2} μCcm^{-2} for PMS0, PMS3, PMS5, PMS7 and PMS10 thin films, respectively. The enhanced

remnant polarization depicts that the addition of MoS_2 helps in the dipole alignment of PVDF film, where PMS7 based thin film shows the maximum remnant polarization.

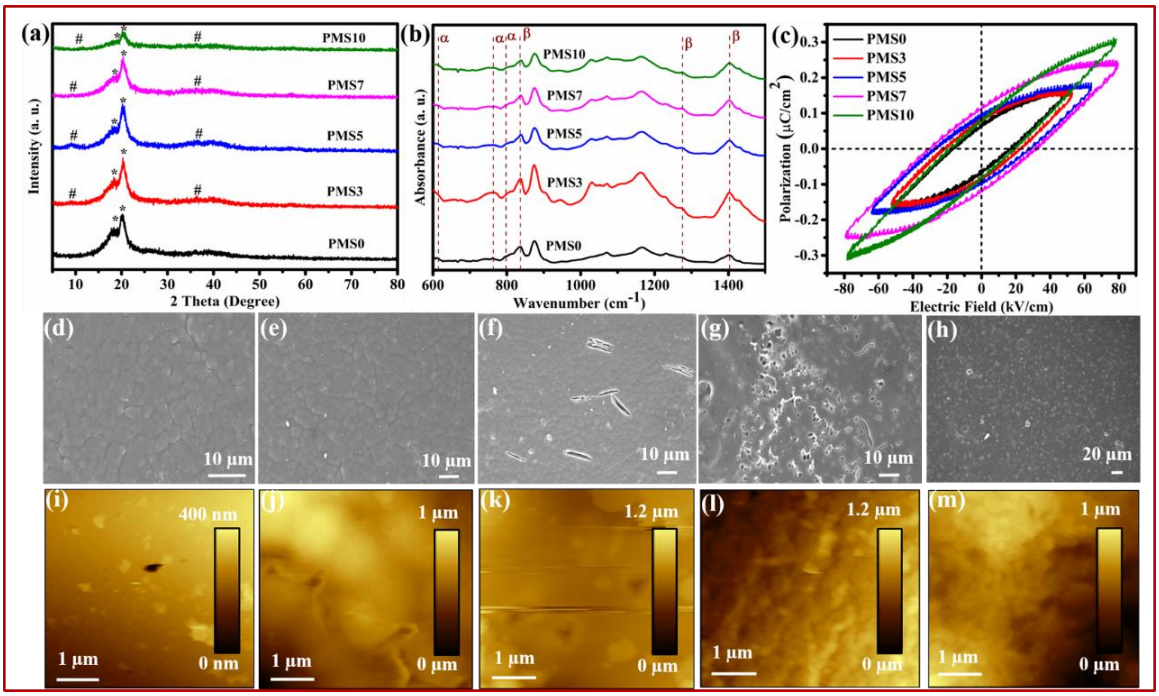

Figure 4.3 (a) Characterization of PVDF-MoS_2 composite thin films (a) XRD pattern (b) FTIR spectra, (c) PE loops, (d-h) FESEM images, and (i-m) AFM images of PMS0, PMS3, PMS5, PMS7 and PMS10, respectively.

In addition, FESEM measurements were also carried out to study the morphologies of the MoS_2-PVDF thin films. The FESEM image of the PVDF thin film is shown in Figure 4.3(d), which also demonstrates the uniformity of the PVDF matrix. Figure 4.3(e-h) shows the FESEM images of MoS_2 filled PVDF, which are named as PMS3, PMS5, PMS7 and PMS10, respectively showing the distribution of MoS_2 sheets into the PVDF matrix. Furthermore, aggregation of MoS_2 was seen with the rise in MoS_2 wt% in the PVDF matrix, suggesting that 7 wt % is the optimal doping level. This can also be observed from the PE loops that the remnant polarization is maximum for 7 wt% of MoS_2 and was decreased after 7 wt% of MoS_2 into the PVDF matrix. AFM images of PMS0, PMS3, PMS5, PMS7 and PMS10 films are shown in Figure 4.3(i-m), respectively. The root mean square roughness of all the thin films was calculated to be 4.92, 6.99, 8.23, 9.56 and 14.2 nm for PMS0, PMS3, PMS5, PMS7 and PMS10 films, respectively. Inclusion of MoS_2 into PVDF matrix augments surface roughness of PVDF-MoS_2 based composite thin films as compared to bare PVDF film. Further the addition of MoS_2 in PVDF matrix not only increases the surface roughness but also the effective area in which the charges can stay. It has also been reported in literature that when

PVDF interacts with other materials, it causes the surface charge density of the PVDF to increase [30, 33, 56]. The above enhancement in surface roughness is very helpful in enhancing the triboelectric output for the PVDF-MoS_2 composite films.

4.3.3 Output Performance Analysis of Fabricated PENGs

Now to study the effect of MoS_2 weight percentage (0 %, 3 %, 5 %, 7 %, 10 %) on the piezoelectric properties, the fabricated nanogenerators were put under continuous stress with the help of electrodynamic shaker. All the thin film nanogenerators were tapped with different frequencies from 1 Hz to 10 Hz, but it was found that at a tapping frequency of 7 Hz the nanogenerators are giving maximum output voltage.

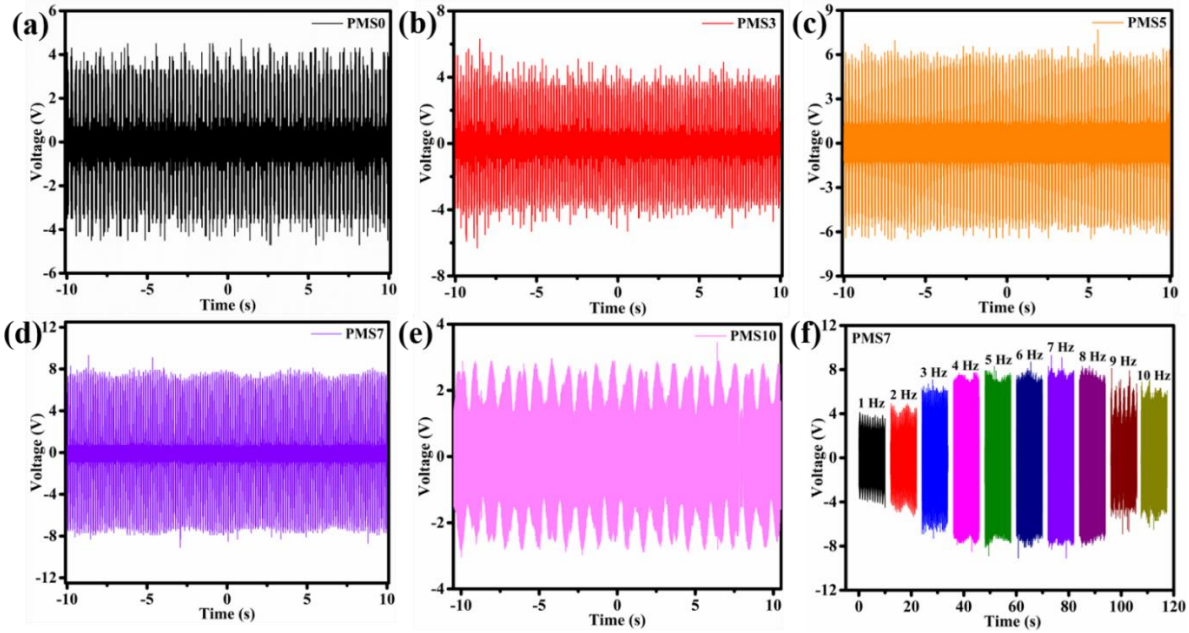

Figure 4.4 (a-e) Variation of piezoelectric open circuit output voltage with MoS_2 wt% at a tapping frequency of 7 Hz and (f) Piezoelectric open circuit voltage for PMS7 based piezoelectric nanogenerator generated at different tapping frequencies.

Hence to compare the piezoelectric energy harvesting capabilities of the MoS_2 integrated PVDF with bare PVDF, 7 Hz was used as optimum frequency for measuring the voltage and current outputs. The open circuit voltage of various fabricated devices is shown in Figure 4.4(a-e). The V_{OC} for PVDF is 9.4 V and for PVDF-MoS_2 the values are 12.6 V, 14.2 V, 18.0 V and 6.5 V for PMS3, PMS5, PMS7 and PMS10, respectively. With the increase in the MoS_2 wt %, the piezoelectric output of PVDF-MoS_2 composite thin film nanogenerators increases gradually. The highest output voltage is produced by PMS7 film based nanogenerator, which is roughly 2 times that of the bare PVDF open circuit voltage, showing the maximum

enhancement in the energy harvesting characteristics. The output voltage of the PMS7 based piezoelectric nanogenerator is compared in Figure 4.4(f) as a function of tapping frequency, when the applied tapping frequencies ranged from 1 Hz to 10 Hz, indicating their good energy harvesting capabilities. It has been shown in the Figure 4.4(f) that open circuit output voltage was increased upto 7 Hz tapping frequency and then starts decreasing with further increase in the frequency. Figure 4.5(a-e) shows the rectified current outputs of the piezoelectric nanogenerators at a tapping frequency of 7 Hz.

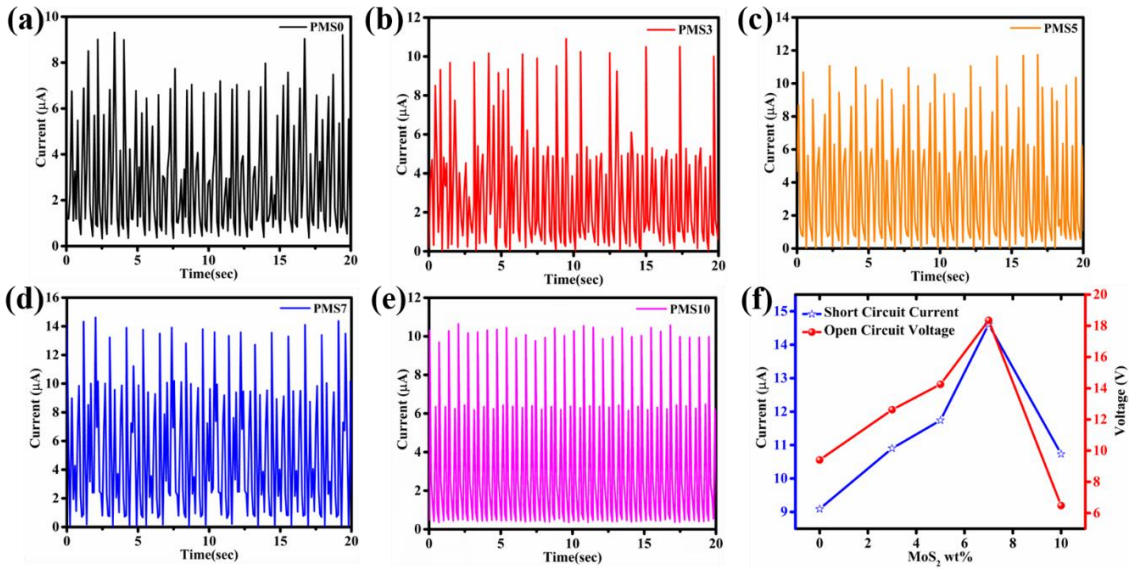

Figure 4.5 (a-e) Rectified short circuit piezoelectric current generated for different MoS_2 wt% at a 7 Hz tapping frequency (f) variation in output short circuit current and open circuit voltage as a function of MoS_2 wt%.

The bare PVDF (PMS0) based nanogenerator reveals an output current of 9.1 μA and for PVDF-MoS_2 based nanogenerators the current values are 10.9 μA, 11.7 μA, 14.6 μA and 10.7 μA for PMS3, PMS5, PMS7 and PMS10, respectively. The short circuit current also follows the same trend as the voltage output for different thin film nanogenerators. The variation of short circuit current and open circuit voltage with the MoS_2 wt% is also shown in Figure 4.5(f). The piezoelectric output results reveal that a loading of 7 wt% MoS_2 is optimal for efficient energy harvesting. The abrupt decline in output performance above 7 wt% MoS_2 was attributed to a number of issues, including low surface characteristics and MoS_2 agglomeration in the PVDF matrix as can be seen in the FESEM results shown in Figure 4.3(d-h). The enhancement in the piezoelectric output of nanogenerators after the addition of MoS_2 in the PVDF matrix can be attributed to two factors: (i) due to increase in the β-phase content of PVDF [31, 57] and (ii) additional contribution of the intrinsic piezoelectric capabilities of MoS_2 in the overall

output of the nanogenerator [4, 58, 59]. The above results are also consistent with studies available in literature where the piezoelectric properties of PVDF and its copolymers gets enhanced by the addition of nanofillers. [4, 60-63].

4.3.4 Dielectric Property Analysis of Different PVDF-MoS_2 Thin Films.

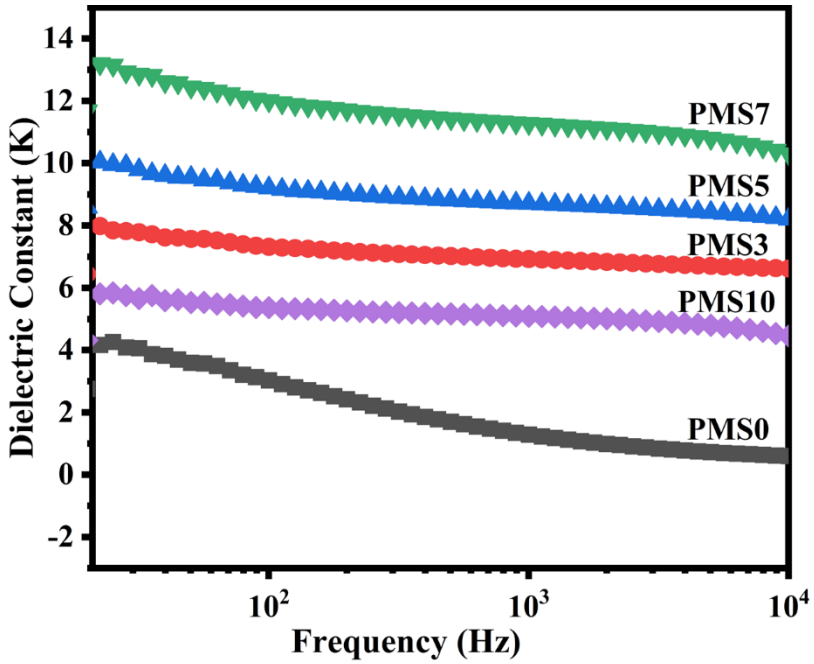

Figure 4.6 Graph showing the dielectric constant for PMS0, PMS3, PMS5, PMS7 and PMS10 thin films.

It has been reported in literature, that the triboelectric output performance might be improved by enhancing the dielectric constant of the triboelectric materials, which is one of the crucial properties of the TENG material [64]. Figure 4.6 displays the dielectric constant of the composite thin films for various filler concentrations as a function of frequency. The dielectric constant of the composite thin films was increased from 4.1 to 7.9, 10.0, 13.2, and 5.8, correspondingly, with increasing in MoS_2 wt percentage (0, 3, 5, 7, and 10%). Hence, the addition of 7 wt% MoS_2 into the PVDF matrix resulted in the film with highest dielectric constant. Due to the percolation limit for the PVDF-MoS_2 composite, as the MoS_2 content was increased further, up to 10 wt%, the dielectric constant gradually decreased [64, 65]. As a result of the dipolar contribution of the MoS_2 filling, which increased the value of the dielectric constant, PVDF became more polarizable [29, 64]. As it was also concluded from the FTIR spectra that addition of MoS_2 enhances the content of β-phase into the PVDF matrix, which means that the addition of MoS_2 into the PVDF matrix results in the dipolar polarization. This

dipolar polarization is responsible for the enhanced dielectric constant after MoS_2 addition [37, 38]. Triboelectric output efficiency of a TENG is significantly influenced by the transmitted charge density, which depends on the dielectric property of the thin film [64, 66]. As the dielectric constant increases with the addition of MoS_2, the surface charge density of the material also gets enhanced. The enhanced surface charges may be attributed to the increased capacitance C, which is directly dependent upon the dielectric constant of the synthesized triboelectric material [37]. Therefore, the triboelectric output performance of the thin films of PVDF-MoS_2 composite will be significantly increased as compared to bare PVDF thin films. The relation between surface charge density, output voltage and dielectric constant is shown through the equations given below [64, 67, 68]:

$$V_{oc} = \frac{\sigma_0 x(t)}{\varepsilon_0} \tag{4.2}$$

$$\sigma = \frac{C\Delta V}{S} = \frac{\varepsilon_0 \varepsilon_r \Delta V}{d} \tag{4.3}$$

Where the surface charge density is given by σ_0, x(t) represents the distance between the two layers, ε_0 is permittivity of the air. Dependence of the charge density on surface area (S), capacitance € of the thin film, film thickness (d), and relative dielectric constant (ε_r) is also given by these equations.

4.3.5 Output Performance Analysis of Fabricated TENGs

To study the effect of MoS_2 addition on the triboelectric performance of PVDF based TENG, we constructed the TENG in the vertical contact-separation geometry by coupling the PVDF and PVDF-MoS_2 thin film with the PDMS thin film as two triboelectric layers. To make the electrical connections, aluminium electrodes were deposited on the opposite side of both the thin films. To study the effect of MoS_2 wt% into the PVDF matrix, all the PVDF-MoS_2/PDMS based TENGs with varying wt% of MoS_2 were placed under continuous force in the contact separation mode with the help of an electrodynamic shaker. All the TENGs were pressed with a tapping frequency of 9 Hz and open circuit voltage and short circuit current were measured. The PVDF/PDMS based TENG generates an open circuit voltage of 107 V and the TENGs with PVDF-MoS_2/PDMS generates the voltage of 133 V, 164 V, 189 V, 106 V for 3, 5, 7 and 10 wt% of MoS_2, respectively which are illustrated in Figure 4.7(a).

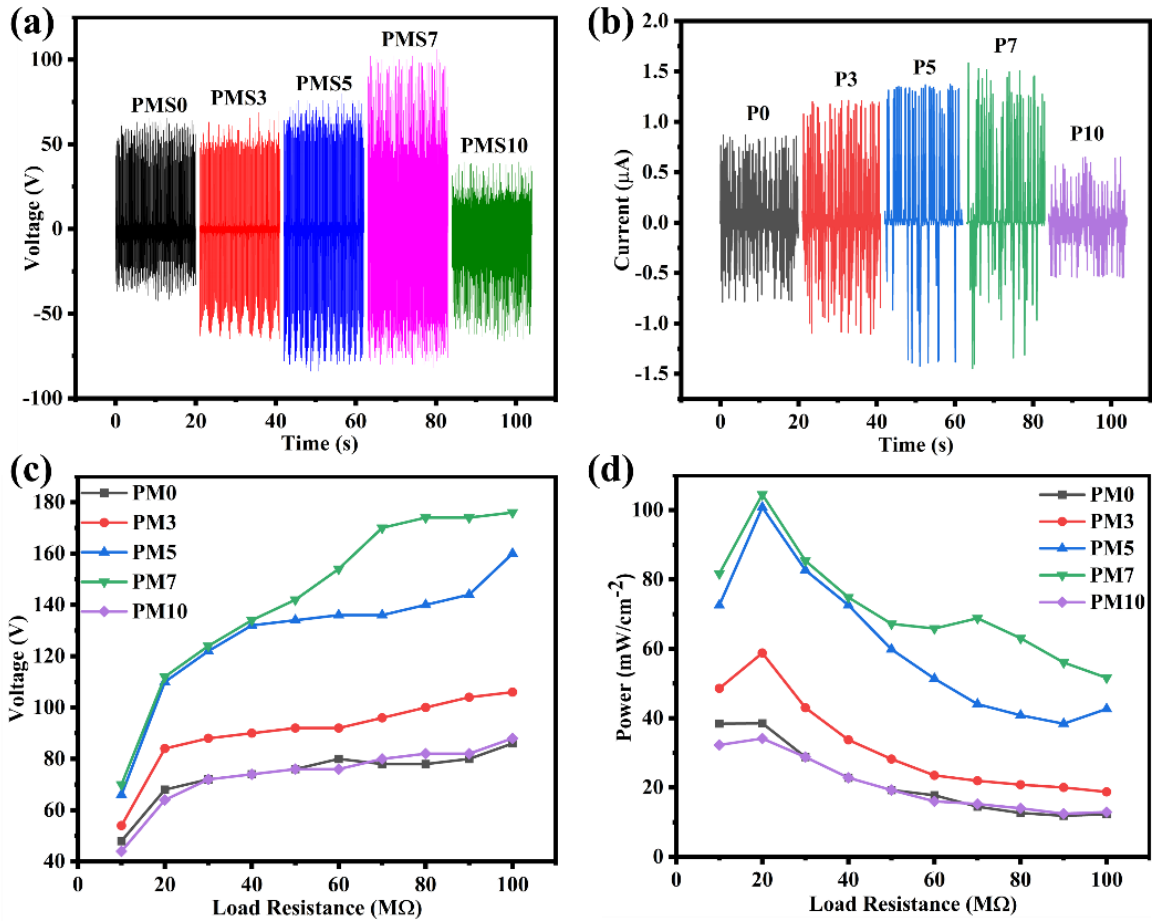

Figure 4.7 (a)Variation of triboelectric open circuit voltage, (b) short circuit current, (c) output voltage with different load resistance, and (d) power per unit area with different load resistance as a function of MoS_2 wt% at a tapping frequency of 9 Hz.

Figure 4.7(b) displays the short circuit current for the TENGs with varying wt% of MoS_2 under the same conditions. The value of short circuit current for PVDF/PDMS is 0.88 μA and for PVDF-MoS_2/PDMS are 1.21 μA, 1.37μ A, 1.61 μA and 0.70 μA for 3, 5, 7 and 10 wt% of MoS_2, respectively. The triboelectric output of PVDF-MoS_2 composite thin film based TENGs gradually increases with an increase in the MoS_2 weight percent. The maximum improvement in the energy harvesting properties is again shown by the PVDF-MoS_2 film-based TENG loaded with 7 wt% of MoS_2, which generates an output voltage that is about twice as high as the bare PVDF based TENG. Hence, 7 wt% is the optimal doping concentration for MoS_2, and the PVDF-MoS_2/PDMS TENG with 7 wt% of MoS_2 will only be used for further analysis. The enhanced output performance of TENGs after the MoS_2 incorporation is also supported by the above-mentioned dielectric, AFM and FTIR results. The effect of load resistance on the output voltage and power density (power per unit area) was also studied for

all the TENGs, which is illustrated in Figure 4.7(c) and 4.7(d), respectively. The output voltage and power density for PMS7/PDMS TENG is maximum for all the load resistances. The output voltages for all the TENGs first increases and the becomes nearly saturated. The PMS7/PDMS TENG generates maximum power density of 104.5 μWcm^{-2}, While the PMS0/PDMS TENG generates a power density of 38.5 μWcm^{-2}. The comparison of the output generated by different TENGs as a function of MoS_2 wt% is shown in table 4.1.

Table 4.1. Comparision of the β-phase, dielectric contant and generated output of the fabricated TENGs as a function of MoS_2 wt%.

Device Name	Weight % of MoS_2	β-phase (%)	Dielectric Constant	V_{oc} (V)	I_{sc} (μA)	Power Density ($\mu W/cm^2$)
PDMS/PMS0	0	71.9	4.1	107	0.88	38.5
PDMS/PMS3	3	76.5	7.9	133	1.21	58.8
PDMS/PMS5	5	80.5	10.0	164	1.37	100.8
PDMS/PMS7	7	82.7	13.2	189	1.61	104.5
PDMS/PMS10	10	66.7	5.8	106	0.70	34.1

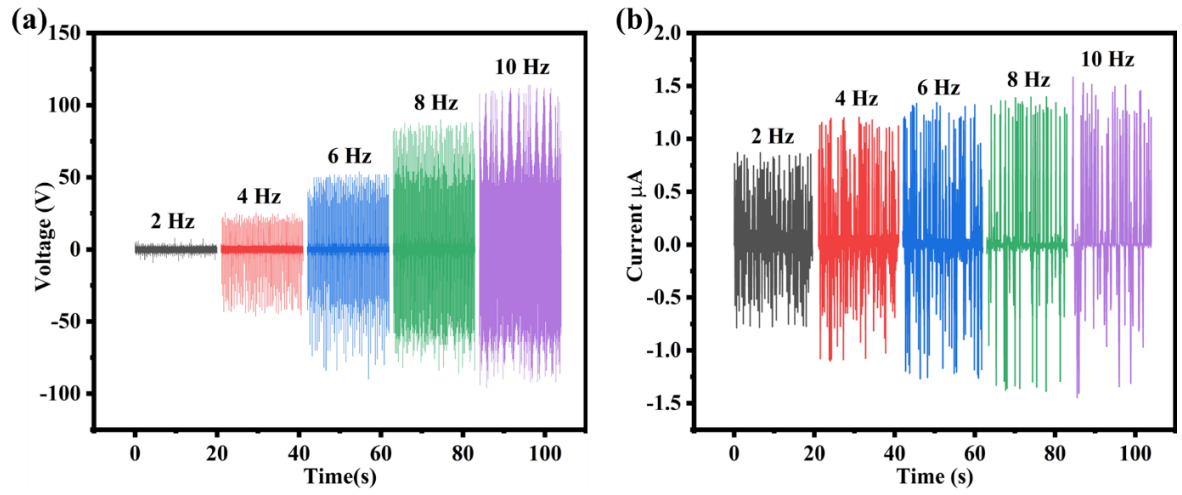

Figure 4.8 Effect of tapping frequency on the (a) open circuit output voltage and (b) short circuit current for PDMS/PMS7 based TENG.

Now, to check the effect of tapping frequency for contact-separation mode of TENG, the nanogenerator with 7 wt% of MoS_2 is tapped with different frequencies by electrodynamic shaker. Figure 4.8(a) shows the open circuit voltage for different tapping frequencies from 2 Hz to 10 Hz. Output voltage increases with the increase in frequency and at 10 Hz the generated

output voltage is ~211 V. The short circuit current also increases with the tapping frequency and is shown in Figure 4.8(b). The increased short-circuit current and open circuit voltage of PVDF-MoS_2/PDMS TENG with operating frequency may be attribute to faster charge transfer at higher tapping frequency [30]. Figure 4.9(a) and (b) shows the operation of the TENG at various impact forces ranging from 5 N to 20 N and at a constant tapping frequency of 9 Hz.

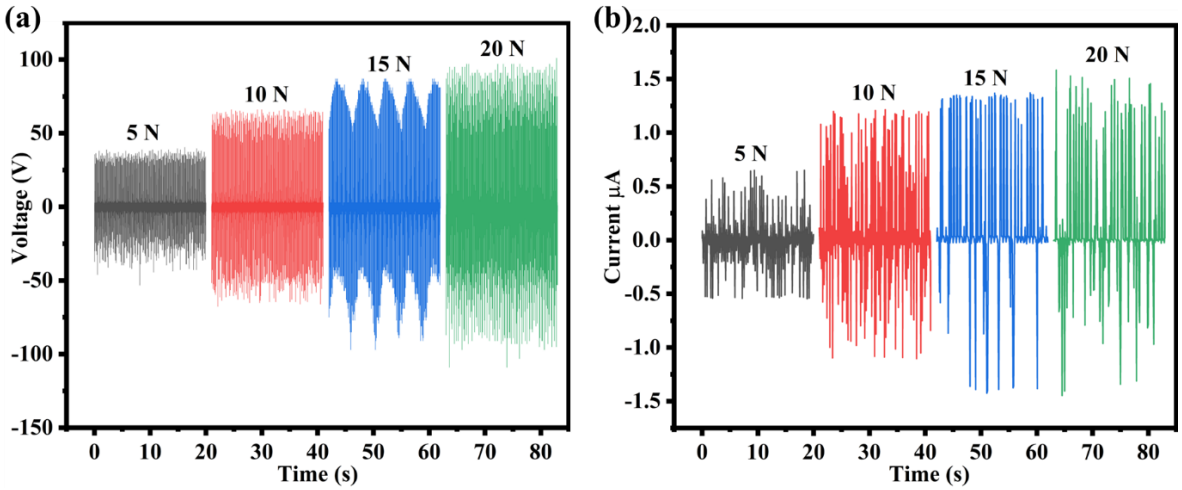

Figure 4.9. Effect of contact force on the (a) open circuit output voltage and (b) short circuit current for PDMS/PMS7 based TENG.

Following an increase in contact force from 5 N to 20 N, the output voltage continuously rises from 93 V to 211 V, the short circuit current also follows the same trend with the increase in contact force, which increases from 0.66 µA to 1.6 µA. Firstly, the enhanced triboelectric output with higher contact force may be attributed to the increased in effective contact area due to elastic properties of polymeric triboelectric materials, leading to more triboelectric charge generation which result into improved output voltage and current output. Secondly, when the contact force is increased, the elastic deformation of the PVDF film increases, causing a rise in TENG capacitance which may be helpful for storing triboelectric charges and increasing triboelectric performance [30].

4.3.6 Fabrication and Underlying Operating Mechanism of Hybrid Nanogenerator

To further enhance the mechanical to electrical energy conversion efficiency, we have fabricated the hybrid nanogenerator which will combine both the triboelectric and piezoelectric effects. For this we have coupled PMS7 nanocomposite film having highest piezoelectric and triboelectric output with PDMS as two triboelectric layers in the vertical contact-separation

mode. Figure 4.10(a) shows the electrical connections and schematic representation of hybrid nanogenerator based on the combined effect of piezoelectric and triboelectric phenomenon.

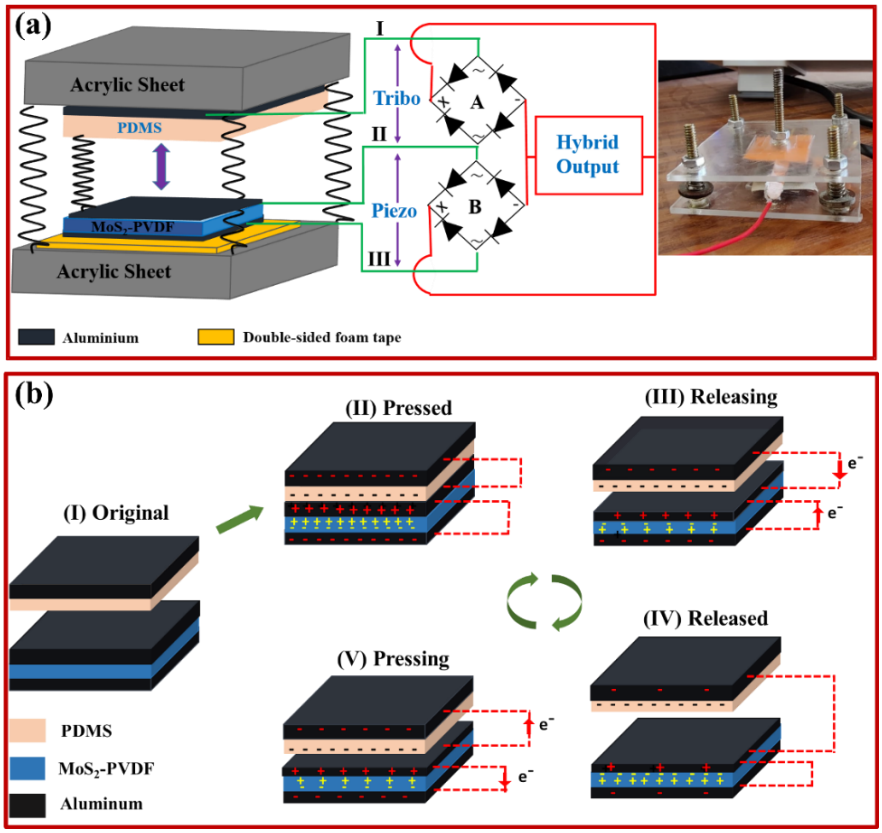

Figure 4.10. (a) Showing the electrical connections and schematic diagram of piezo-triboelectric HNG. Inset shows the image of the actual hybrid device, and (b) schematic showing the working mechanism of HNG.

For fabricating HNG, the PMS7 film was coated on both sides and PDMS layer on top side with Al coating of thickness ~ 100 nm using thermal evaporation technique. Further, double sided copper tape was used to connect the films with external circuit. After making the connections, double-sided foam tape was used to adhere the PDMS film and the composite films to the different acrylic sheets as shown in the schematic given in Figure 4.10(a). As the HNG is a combination of two different nanogenerators, the upper and bottom layer gives the triboelectric output while the bottom layer provides the piezoelectric output. The triboelectric output of the HNG depends on the contact velocity and distance between two layers, and the piezoelectric output depends upon the amount of stress applied to nanogenerator. When the force is applied on the HNG, the bottom layer generates the piezoelectric output due to the stress applied to it and the contact and separation of upper and bottom layer generates the triboelectric charges. The triboelectric output is provided by connections I and II from

aluminum coated above PDMS and PVDF based film, respectively, while the piezoelectric output from PVDF sandwiched between aluminum electrode is provided by connections II and III, as illustrated in Figure 4.10(a). Before measuring the hybrid output, triboelectric and piezoelectric outputs were independently measured using the rectifier A and B, respectively. Then to achieve the enhancement in the output because of the combined effect of triboelectric and piezoelectric part, the positive and negative ends of both the rectifiers were connected together and the final enhanced hybrid output was measured. The working mechanism of the hybrid nanogenerator is shown in Figure 4.10(b). There is initially no electric potential difference between the triboelectric layers since no charge is created prior to their contact and also no piezoelectric charges are present on the PVDF-MoS_2 film because no stress has been applied (Figure 4.10(b)(I)). Once, the mechanical stimulus is provided with the help of dynamic shaker to bring the two triboelectric layers into contact, contact electrification causes electrons from the PDMS to be transported to the aluminum electrode on PVDF-MoS_2 surface, and due to the applied stress on the PVDF-MoS_2 film, the dipoles got aligned inside the film which creates the potential difference inside the film and give rise to piezoelectric charges on the surface (Figure 4.10(b)(II)). Due to the insulating properties of the polymer films, these charges on the surfaces won't dissipate or be immediately neutralized. An electrical potential difference between the matching electrodes is then created when the two layers are separated, which causes electrons to flow between the different electrodes through an external circuit, producing an electric output signal (Figure 4.10(b)(III)). The electric potential difference is completely compensated by the transfer of electrons between the electrodes when the separation distance reaches its maximum value, and no current signal is produced in the external circuit (Figure 4.10(b)(IV)). Then, as the HNG is compressed again by an external force, an electrical signal in the opposite direction is produced as a result of the backflow of electrons (Figure 4.10(b)(V)). As a result, the PENG and TENG may produce an uninterrupted alternating electrical output while being continually stimulated by an external force which is further converted into DC signal with the help of a rectifier circuit as shown in Figure 4.10(a).

4.3.7 Output Performance Analysis of Hybrid Nanogenerator

Figure 4.11(a) and (b) depicts the rectified output voltages generated by finger tapping for bare PVDF (PMS0) and MoS_2-PVDF (PMS7) based HNGs, respectively. It can be seen clearly in both the Figures that by combining the piezo-tribo effects in HNG, the output voltage increases. Further to highlight the effect of nanofiller, it to be mentioned that not only the hybrid

output voltage got increased, the individual piezoelectric and triboelectric component shows the enhancement as we have already seen for above piezo and tribo results.

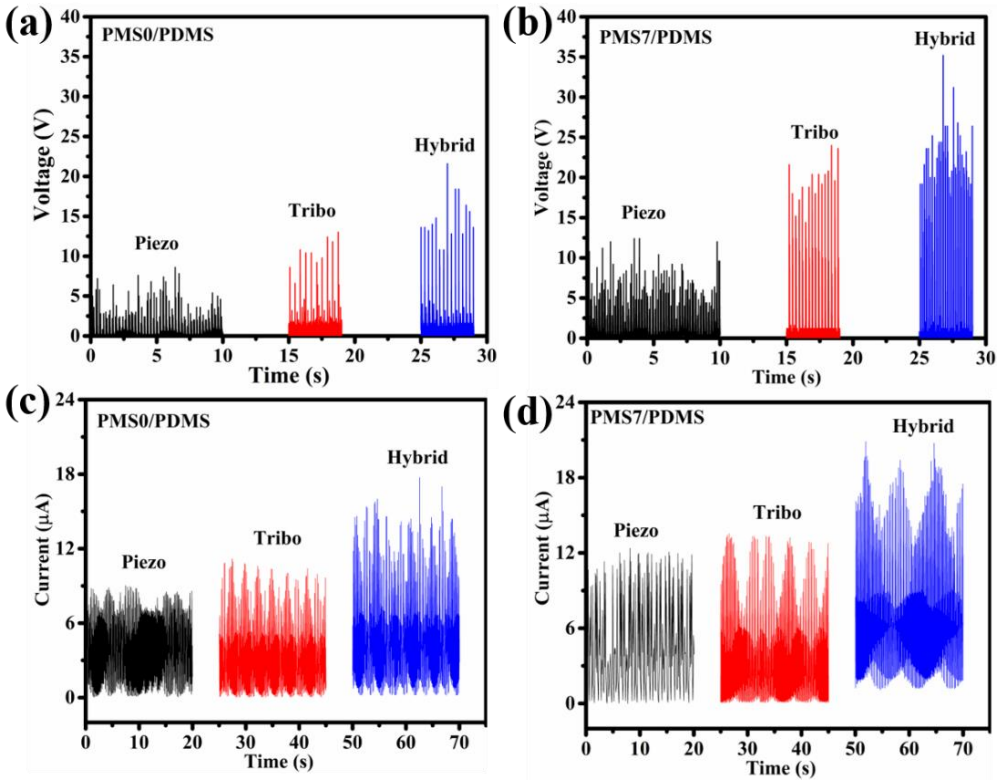

Figure 4.11. Rectified open circuit voltage for piezo tribo and hybrid operations of (a) PMS0/PDMS and (b) PMS7/PDMS nanogenerators. Rectified short circuit current for piezo tribo and hybrid operations of (c) PMS0/PDMS and (d) PMS7/PDMS nanogenerators generated by finger tapping.

The piezoelectric contribution after MoS_2 addition shows the increase from 8.7 V to 12.5 V, whereas, the triboelectric component shows the increase from 13.1 V to 24.1 V just by normal finger tapping. Further, after the integration of both the outputs, the hybrid output voltage was increased from 21.6 V for PVDF based hybrid nanogenerator to 35.3 V for MoS_2-PVDF based hybrid nanogenerator by finger tapping. The generated output of the current work is compared with the different previously reported mechanical energy harvesters based on PVDF-MoS_2 composite in the Table 4.2. As can be seen, the fabricated TENG in the present study exhibits a substantially increased instantaneous power density and voltage than other previously reported similar PENGs and TENGs, thus proving that MoS_2 an efficient filler for boosting PVDF's piezoelectric and triboelectric performance. The table makes it evident that the MoS_2-PVDF based nanogenerator in the current work responded more favorably than the other mechanical energy harvesters that were reported.

Table 4.2. Comparison of the nanogenerator's output voltage and current generation for various PVDF-MoS_2 based mechanical energy harvesters.

Device Structure	**V_{oc}**	**I_{sc}**	**Power Density ($\mu W/cm^2$)**	**Synthesis**	**Reference**
PVDF-rGO-MoS2	2.4 V	0.68 µA	-	Solution Casting	[69]
PVDF–MoS_2	9.8 V	0.9 µA	-	Drop Casting	[4]
PVDF/MoS_2	14 V	-	16 nW/cm^2	Electrospinning, salt intercalation	[60]
PVDF/MoS_2@ZnO	6.2 V	528 nA	10.85 µW (Only power)	Solution Casting	[70]
PVDF–$ZnSnO_3$–MoS_2	26 V	0.5 µA	28.9 mW/m^2	Electrospinning	[71]
ZnO-PVDF/PTFE	78 V	0.46 $\mu A/cm^2$	24.5 $\mu W/cm^2$	Drop Casting	[33]
Al-PVDF-Al/Silicon-Al	34.6	6.6 µA	-		[72]
MoS_2-PVDF **(Piezoelectric nanogenerator)**	18 V	14.6 µA	**53.4 $\mu W/cm^2$**	Drop Casting	This work
MoS_2-PVDF/PDMS **(Triboelectric nanogenerator)**	211 V	1.6 µA	**104.5 $\mu W/cm^2$**	Drop Casting	This work
MoS_2-PVDF/PDMS **(HNG)**	35.3 V (rectified)	20.8 µA	**~220 $\mu W/cm^2$**	Drop Casting	This work

The rectified short circuit current was also measured and after the incorporation of MoS_2, the piezoelectric short circuit current shows an enhancement from 8.9 μA to 12.5 μA, while the triboelectric current was increased from 11.1 μA to 13.5 μA. Furthermore, the total hybrid current was increased from 17.7 μA to 20.8 μA after the addition of MoS_2. The comparison of the output currents generated by PMS0 and PMS7 based hybrid nanogenerators is displayed in Figure 4.11(e) and (d), respectively. After inclusion of MoS_2, the efficiency of hybrid nanogenerator based on PVDF is improved not only in terms of piezoelectricity, but also in terms of triboelectricity. The increment in PVDF's polarizability following MoS_2 addition will affect the charge grabbing ability of aluminum layer when it interacts with PDMS film. Furthermore, with the inclusion of MoS_2 in PVDF matrix, surface roughness of PVDF rose from 4.9 nm to 9.6 nm for PMS7, as revealed in AFM imaging. Increased surface roughness provides more room for charges to live, resulting in a larger surface charge density and enhanced triboelectric output [33, 73]. Therefore, the increased polarizability and increased surface roughness of the composite thin film have a direct impact on the triboelectrification [42, 74].

To support the enhanced hybrid nanogenerator output Kelvin Probe Force Microscopy (KPFM) was carried out only on bare PVDF and highest output PVDF-MoS_2 (PMS7) nanocomposite film. The surface potentials maps for PMS0 and PMS7 are shown in Figure 4.12(a) and (b) respectively, which was obtained by scanning of 5 μm x 5 μm region of the films. Based on their triboelectric polarity, PDMS is used as a positive triboelectric layer while PVDF based composite thin films acts as negative triboelectric material [75]. As it can be seen from the KPFM results that after the inclusion of MoS_2 in PVDF, surface potential of the PMS7 composite thin film becomes more negative as compared to PMS0 thin film. This will increase the difference between the surface potentials of PDMS (positive layer) and PVDF composite (negative layer) after the incorporation of MoS_2 in comparison with bare PVDF film. Therefore, the overall enhancement in the hybrid output after the addition of MoS_2 is attributed to enhancement in the β-phase content, intrinsic piezoelectric properties of MoS_2, increased surface roughness, increase in the negative surface potential, and increase in the charge density because of the enhanced dielectric constant of the resulting nanocomposite thin films [4, 30, 33, 74].

Further to check the practical application of hybrid nanogenerator, we have charged the three different capacitors of 1 μF, 2 μF and 10 μF which are charged upto ~9.1 V, ~9.2 V and ~9.5 V, respectively. Figure 4.12(e) shows the charging of these capacitors with different time

taken by the capacitors in charging. We have also simultaneously lit 21 LEDs connected in series at a tapping frequency of 7 Hz by hybrid output and the glowing LEDs are shown in inset of Figure 4.12(e). We have also used the generated voltage to drive the scientific calculator and the digital wrist watch as shown in Figure 4.12(d).

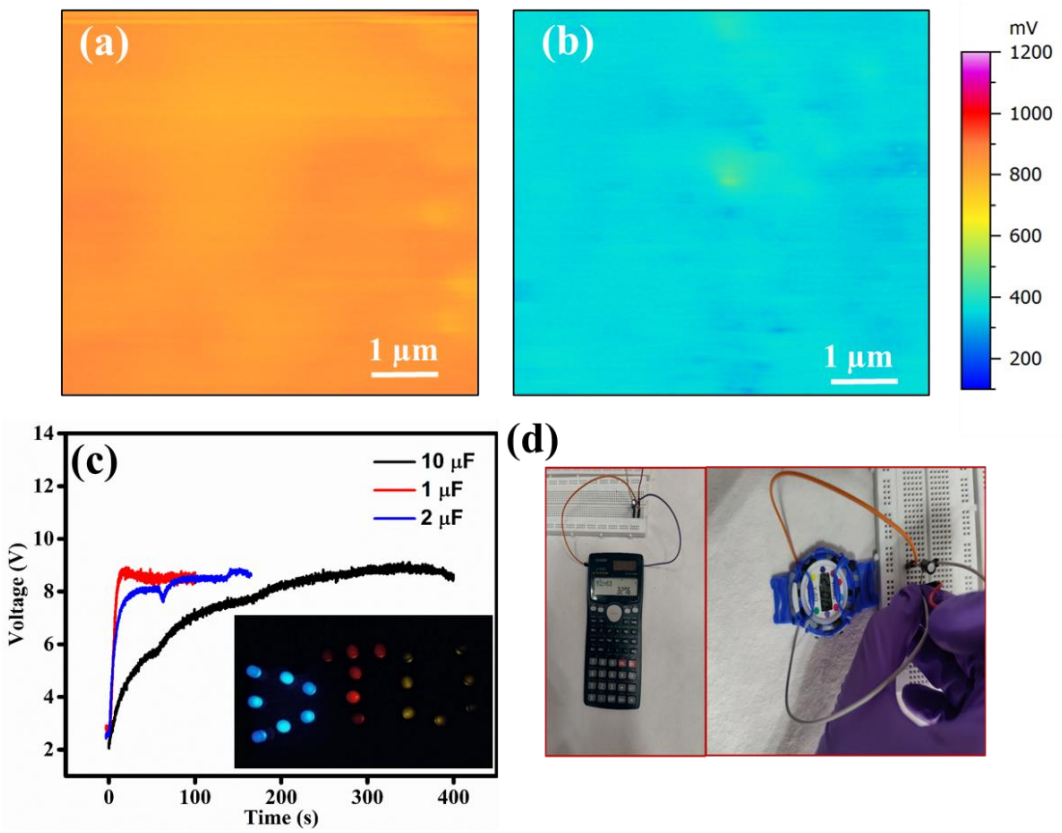

Figure 4.12. KPFM images showing the surface potentials of (a) PMS0, (b) PMS7 thin films, (c) Charging profile for 1 µF, 2 µ F and 10 µ F capacitors and inset shows the lighten up of LEDs and (d) Pictural representation of the devices (scientific calculator and the digital wrist watch) derived by PMS7 based hybrid nanogenerator.

In addition to the above measurements, the effect of load resistance variation on the output voltage and power density was also analyzed for both PMS0 and PMS7 based hybrid nanogenerators. The output voltage and power density were compared for piezoelectric, triboelectric and hybrid output under various load resistances for both the devices which is shown in Figure 4.13(a) and (b) for PMS0 and Figure 4.13(c) and (d) for PMS7. The maximum power is observed for the hybrid output for both PMS0 and PMS7 which are ~88 µW/cm^2 and ~220 µW/cm^2 respectively at a load resistance of 1 MΩ.

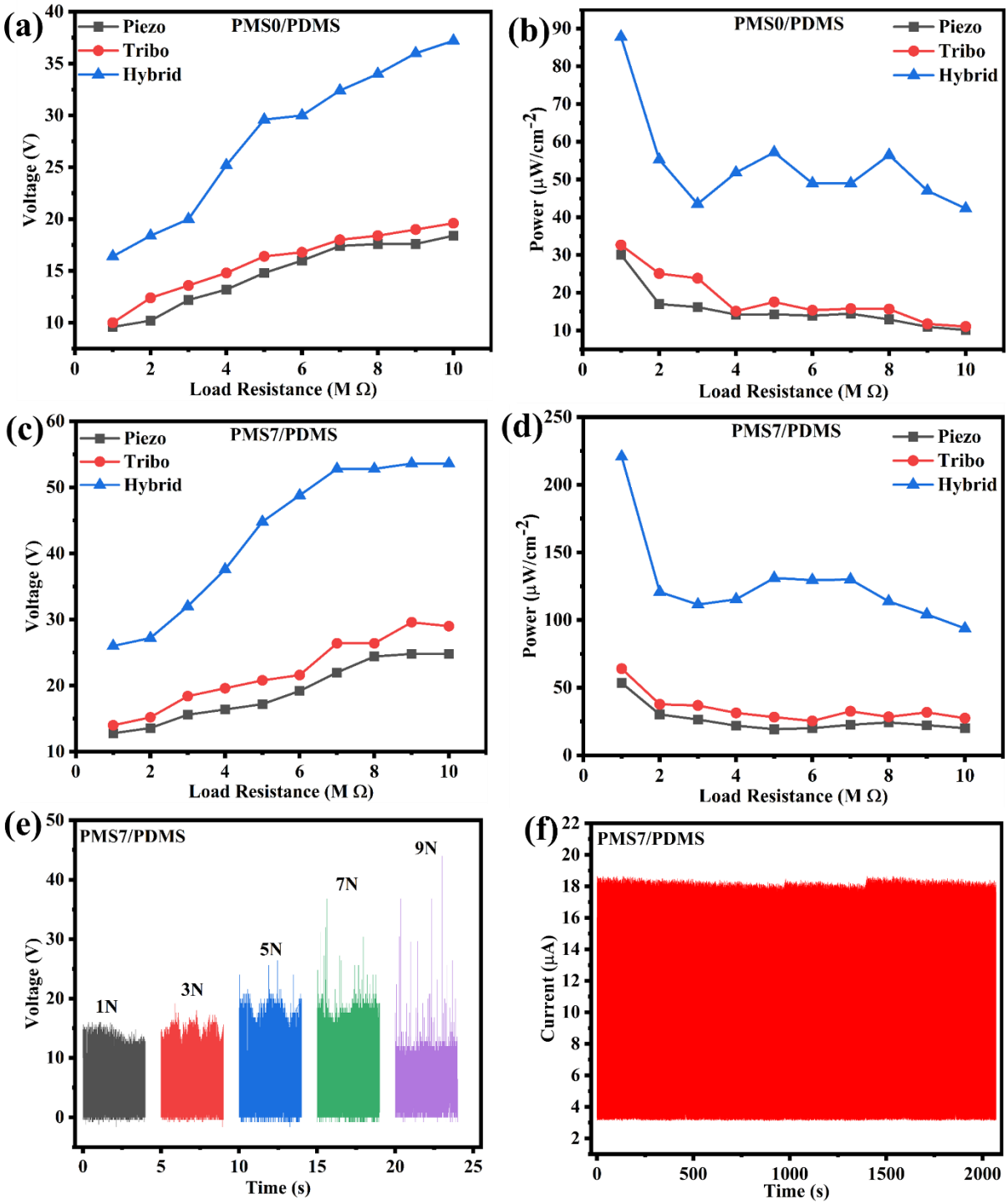

Figure 4.13. (a) Output voltage, (b) power density as a function of load resistance for piezo, tribo and hybrid output of PMS0 based nanogenerator, (c) Output voltage, (d) power density as a function of load resistance for piezo, tribo and hybrid output of PMS7 based nanogenerator, (e) effect of tapping force on the output voltage, and (f) current showing the long-term stability of PMS7/PDMS based HNG.

We have also studied the effect of tapping force on the hybrid output voltage of PMS7 based nanogenerator which is shown in Figure 4.13(e). It was observed that with the increase in the tapping force from 1 N to 9 N, the output voltage was also increased from ~16 V to ~45 V. The increment in the output voltage with the tapping force may be attributed to the elastic properties of polymeric materials; the effective contact area of HNG is improved with a rise in tapping force, which results in the generation of more charges and a higher power output.

Further, to ensure the stability and durability of the fabricated nanogenerator, more than 2000 cycles of mechanical stimulus were given to the HNG nanogenerator. The resulting current output without any serious degradation is shown in Figure 4.13(f). The present study therefore proposes an environmentally friendly ubiquitously available nanogenerator device capable of fulfilling the rising demand of smart and wearable electronic industry, which is growing at very faster rate to assist our living style.

4.4 Conclusion

In the present work, we have fabricated a piezo-tribo hybrid nanogenerator for harvesting waste mechanical energy for useful conversion into electricity. The HNG is composed of MoS_2 filled PVDF and PDMS films. The output voltage and current performance of the HNG is compared with its individual piezo and tribo components showing an enhancement in its performance which may be contributed to the synergistic effect of piezoelectricity and triboelectricity. Initially, the piezoelectric and triboelectric performance of MoS_2 filled PVDF films were compared with bare PVDF and it was observed that 7 wt% of MoS_2 is the optimal level of doping for mechanical energy harvesting. Above 7 wt% of MoS_2 the performance of the nanogenerator abruptly declined due to the agglomeration of MoS_2 in the PVDF matrix. Therefore, the pure piezoelectric nanogenerator having 7 wt % of MoS_2 shows maximum output voltage of 18.3 V, rectified short circuit current of 14.6 μA at a tapping frequency of 7 Hz and power density of 53.4 μWcm^{-2}. The triboelectric nanogenerator with 7 wt% MoS_2 exhibits a maximum power density of 104.5 μWcm^{-2} and a short circuit current of 1.61 μA. The HNG having MoS_2 filled PVDF with PDMS generates a power density of 220 μWcm^{-2} and rectified current of 20.8 μA just by finger tapping. Our study reveals that inclusion of MoS_2 in the PVDF matrix stimulates the generation of β-phase and also the intrinsic piezoelectric properties which contributes in the overall enhancement of the piezoelectric output of PVDF. In addition to enhanced β-phase, the distribution of MoS_2 increase the surface roughness which increases the contact area and also boosts the surface potential and dielectric constant thereby

increasing the triboelectric output of the device. Each of these factors combine to significantly increase the performance of the hybrid nanogenerator. As a result, the present study suggests a feasible, economical approach to fabricate a high performance hybrid nanogenerator by combining both the piezoelectric and triboelectric effects which may be utilized to drive the wearable electronic devices.

References

[1] X. Hu, L. Xu, X. Lin, M. Pecht, Joule, 4 (2020) 310-346.

[2] Q. Jiang, B. Chen, K. Zhang, Y. Yang, ACS applied materials & interfaces, 9 (2017) 43716-43723.

[3] K. Zhao, Y. Yang, X. Liu, Z.L. Wang, Advanced Energy Materials, 7 (2017) 1700103.

[4] V. Singh, D. Meena, H. Sharma, A. Trivedi, B. Singh, Energy, 239 (2022) 122125.

[5] T. Chen, L. Qiu, Z. Yang, Z. Cai, J. Ren, H. Li, H. Lin, X. Sun, H. Peng, Angewandte Chemie International Edition, 51 (2012) 11977-11980.

[6] J.P. Rojas, D. Conchouso, A. Arevalo, D. Singh, I.G. Foulds, M.M. Hussain, Nano Energy, 31 (2017) 296-301.

[7] X. Yang, W.A. Daoud, Advanced Functional Materials, 26 (2016) 8194-8201.

[8] J. Briscoe, S. Dunn, Nano Energy, 14 (2015) 15-29.

[9] S. Rana, V. Singh, B. Singh, iScience, 25 (2022) 103748.

[10] L. Lu, W. Ding, J. Liu, B. Yang, Nano Energy, 78 (2020) 105251.

[11] U. Yaqoob, A.S.M.I. Uddin, G.-S. Chung, Applied Surface Science, 405 (2017) 420-426.

[12] H.H. Singh, S. Singh, N. Khare, Composites Science and Technology, 149 (2017) 127-133.

[13] P. Fakhri, B. Amini, R. Bagherzadeh, M. Kashfi, M. Latifi, N. Yavari, S.A. Kani, L. Kong, RSC advances, 9 (2019) 10117-10123.

[14] M. Zeyrek Ongun, S. Oguzlar, E.C. Doluel, U. Kartal, M. Yurddaskal, Journal of Materials Science: Materials in Electronics, 31 (2020) 1960-1968.

[15] S. Niu, Z.L. Wang, Nano Energy, 14 (2015) 161-192.

[16] Y.S. Zhou, Y. Liu, G. Zhu, Z.-H. Lin, C. Pan, Q. Jing, Z.L. Wang, Nano letters, 13 (2013) 2771-2776.

[17] H. Zhang, Y. Yang, Y. Su, J. Chen, C. Hu, Z. Wu, Y. Liu, C.P. Wong, Y. Bando, Z.L. Wang, Nano Energy, 2 (2013) 693-701.

[18] M. Sahu, S. Hajra, S. Panda, M. Rajaitha, B.K. Panigrahi, H.-G. Rubahn, Y.K. Mishra, H.J. Kim, Nano Energy, 97 (2022) 107208.

[19] N. Lim, D. Hong, J. Jeong, H.W. Lee, K.-H. Kwon, Journal of Nanoscience and Nanotechnology, 17 (2017) 3328-3332.

[20] H.Y. Li, L. Su, S.Y. Kuang, C.F. Pan, G. Zhu, Z.L. Wang, Advanced Functional Materials, 25 (2015) 5691-5697.

[21] B. Mahanty, S.K. Ghosh, S. Garain, D. Mandal, Materials Chemistry and Physics, 186 (2017) 327-332.

[22] K.Y. Lee, M.K. Gupta, S.-W. Kim, Nano Energy, 14 (2015) 139-160.

[23] X. Chen, M. Han, H. Chen, X. Cheng, Y. Song, Z. Su, Y. Jiang, H. Zhang, Nanoscale, 9 (2017) 1263-1270.

[24] X. Wang, B. Yang, J. Liu, C. Yang, Journal of Materials Chemistry A, 5 (2017) 1176-1183.

[25] S. Hajra, A.M. Padhan, M. Sahu, P. Alagarsamy, K. Lee, H.J. Kim, Nano Energy, 89 (2021) 106316.

[26] M. Sahu, V. Vivekananthan, S. Hajra, A. K S, N.P. Maria Joseph Raj, S.-J. Kim, Journal of Materials Chemistry A, 8 (2020) 22257-22268.

[27] M. Sahu, V. Vivekananthan, S. Hajra, D.K. Khatua, S.-J. Kim, Applied Materials Today, 22 (2021) 100900.

[28] X. Cao, J. Ma, X. Shi, Z. Ren, Applied Surface Science, 253 (2006) 2003-2010.

[29] S.S. Nardekar, K. Krishnamoorthy, P. Pazhamalai, S. Sahoo, S. Jae Kim, Nano Energy, 93 (2022) 106869.

[30] L. Shi, H. Jin, S. Dong, S. Huang, H. Kuang, H. Xu, J. Chen, W. Xuan, S. Zhang, S. Li, X. Wang, J. Luo, Nano Energy, 80 (2021) 105599.

[31] V. Singh, B. Singh, Materials Today: Proceedings, 28 (2020) 282-285.

[32] H.H. Singh, S. Singh, N. Khare, Polymers for Advanced Technologies, 29 (2018) 143-150.

[33] H.H. Singh, N. Khare, Nano Energy, 51 (2018) 216-222.

[34] B. Hedau, B.-C. Kang, T.-J. Ha, ACS Nano, (2022).

[35] C. Wu, T.W. Kim, J.H. Park, H. An, J. Shao, X. Chen, Z.L. Wang, ACS Nano, 11 (2017) 8356-8363.

[36] M. Kim, D. Park, M.M. Alam, S. Lee, P. Park, J. Nah, ACS Nano, 13 (2019) 4640-4646.

[37] M.P. Kim, D.-S. Um, Y.-E. Shin, H. Ko, Nanoscale Research Letters, 16 (2021) 1-14.

[38] A. Sasmal, A. Patra, A. Arockiarajan, Applied Physics Letters, 121 (2022) 133902.

[39] F. Xue, L. Chen, L. Wang, Y. Pang, J. Chen, C. Zhang, Z.L. Wang, Advanced Functional Materials, 26 (2016) 2104-2109.

[40] J. Xiong, P. Cui, X. Chen, J. Wang, K. Parida, M.-F. Lin, P.S. Lee, Nature communications, 9 (2018) 1-9.

[41] S. Tu, Q. Jiang, X. Zhang, H.N. Alshareef, ACS Nano, 12 (2018) 3369-3377.

[42] A. Yu, Y. Zhu, W. Wang, J. Zhai, Advanced Functional Materials, 29 (2019) 1900098.

[43] P. Cui, K. Parida, M.-F. Lin, J. Xiong, G. Cai, P.S. Lee, Advanced Materials Interfaces, 4 (2017) 1700651.

[44] Y. Zhang, W. Zeng, Y. Li, Journal of Alloys and Compounds, 749 (2018) 355-362.

[45] W. Ding, L. Hu, J. Dai, X. Tang, R. Wei, Z. Sheng, C. Liang, D. Shao, W. Song, Q. Liu, M. Chen, X. Zhu, S. Chou, X. Zhu, Q. Chen, Y. Sun, S.X. Dou, ACS Nano, 13 (2019) 1694-1702.

[46] N. Chaudhary, M. Khanuja, Abid, S.S. Islam, Sensors and Actuators A: Physical, 277 (2018) 190-198.

[47] B. Jaleh, A. Jabbari, Applied Surface Science, 320 (2014) 339-347.

[48] P.I. Devi, K. Ramachandran, Journal of Experimental Nanoscience, 6 (2011) 281-293.

[49] S. Sarkar, S. Garain, D. Mandal, K.K. Chattopadhyay, RSC Advances, 4 (2014) 48220-48227.

[50] P. Martins, A.C. Lopes, S. Lanceros-Mendez, Progress in polymer science, 39 (2014) 683-706.

[51] N. Soin, D. Boyer, K. Prashanthi, S. Sharma, A.A. Narasimulu, J. Luo, T.H. Shah, E. Siores, T. Thundat, Chemical Communications, 51 (2015) 8257-8260.

[52] J.S. Lee, K.-Y. Shin, O.J. Cheong, J.H. Kim, J. Jang, Sci Rep, 5 (2015) 1-8.

[53] D. Sengupta, A.G.P. Kottapalli, S.H. Chen, J.M. Miao, C.Y. Kwok, M.S. Triantafyllou, M.E. Warkiani, M. Asadnia, AIP Advances, 7 (2017) 105205.

[54] P. Thakur, A. Kool, B. Bagchi, S. Das, P. Nandy, Physical Chemistry Chemical Physics, 17 (2015) 1368-1378.

[55] P. Biswas, N.A. Hoque, P. Thakur, M.M. Saikh, S. Roy, F. Khatun, B. Bagchi, S. Das, ACS Sustainable Chemistry & Engineering, 7 (2019) 4801-4813.

[56] C. Zhang, L. Zhou, P. Cheng, X. Yin, D. Liu, X. Li, H. Guo, Z.L. Wang, J. Wang, Applied Materials Today, 18 (2020) 100496.

[57] K. Maity, B. Mahanty, T.K. Sinha, S. Garain, A. Biswas, S.K. Ghosh, S. Manna, S.K. Ray, D. Mandal, Energy Technology, 5 (2017) 234-243.

[58] K.-A.N. Duerloo, M.T. Ong, E.J. Reed, The Journal of Physical Chemistry Letters, 3 (2012) 2871-2876.

[59] M.N. Blonsky, H.L. Zhuang, A.K. Singh, R.G. Hennig, ACS Nano, 9 (2015) 9885-9891.

[60] K. Maity, B. Mahanty, T.K. Sinha, S. Garain, A. Biswas, S.K. Ghosh, S. Manna, S.K. Ray, D. Mandal, Energy Technology, 5 (2017) 234-243.

[61] D. Bhattacharya, S. Bayan, R.K. Mitra, S.K. Ray, Nanoscale, 13 (2021) 15819-15829.

[62] W. Qin, P. Zhou, X. Xu, M.S. Irshad, Y. Qi, T. Zhang, Sensors and Actuators A: Physical, 333 (2022) 113307.

[63] K. Shi, B. Chai, H. Zou, P. Shen, B. Sun, P. Jiang, Z. Shi, X. Huang, Nano Energy, 80 (2021) 105515.

[64] S.M.S. Rana, M.T. Rahman, M. Salauddin, S. Sharma, P. Maharjan, T. Bhatta, H. Cho, C. Park, J.Y. Park, ACS Applied Materials & Interfaces, 13 (2021) 4955-4967.

[65] Y. Dong, S.S.K. Mallineni, K. Maleski, H. Behlow, V.N. Mochalin, A.M. Rao, Y. Gogotsi, R. Podila, Nano Energy, 44 (2018) 103-110.

[66] T. Bhatta, P. Maharjan, H. Cho, C. Park, S.H. Yoon, S. Sharma, M. Salauddin, M.T. Rahman, S.M.S. Rana, J.Y. Park, Nano Energy, 81 (2021) 105670.

[67] V. Harnchana, H.V. Ngoc, W. He, A. Rasheed, H. Park, V. Amornkitbamrung, D.J. Kang, ACS applied materials & interfaces, 10 (2018) 25263-25272.

[68] S. Niu, S. Wang, L. Lin, Y. Liu, Y.S. Zhou, Y. Hu, Z.L. Wang, Energy & Environmental Science, 6 (2013) 3576-3583.

[69] M. Faraz, H.H. Singh, N. Khare, Journal of Alloys and Compounds, 890 (2022) 161840.

[70] S. Cao, H. Zou, B. Jiang, M. Li, Q. Yuan, Nano Energy, (2022) 107635.

[71] S.P. Muduli, S. Veeralingam, S. Badhulika, ACS Applied Energy Materials, 4 (2021) 12593-12603.

[72] J. Zhu, X. Hou, X. Niu, X. Guo, J. Zhang, J. He, T. Guo, X. Chou, C. Xue, W. Zhang, Sensors and Actuators A: Physical, 263 (2017) 317-325.

[73] F.-R. Fan, L. Lin, G. Zhu, W. Wu, R. Zhang, Z.L. Wang, Nano letters, 12 (2012) 3109-3114.

[74] T. Hisakado, Wear, 28 (1974) 217-234.

[75] M. Kanik, M.G. Say, B. Daglar, A.F. Yavuz, M.H. Dolas, M.M. El-Ashry, M. Bayindir, Advanced Materials, 27 (2015) 2367-2376.

CHAPTER 5

Energy harvesting performance of PVDF-$MoSe_2$ electrospun fiber based flexible nanogenerator for generating green hydrogen.

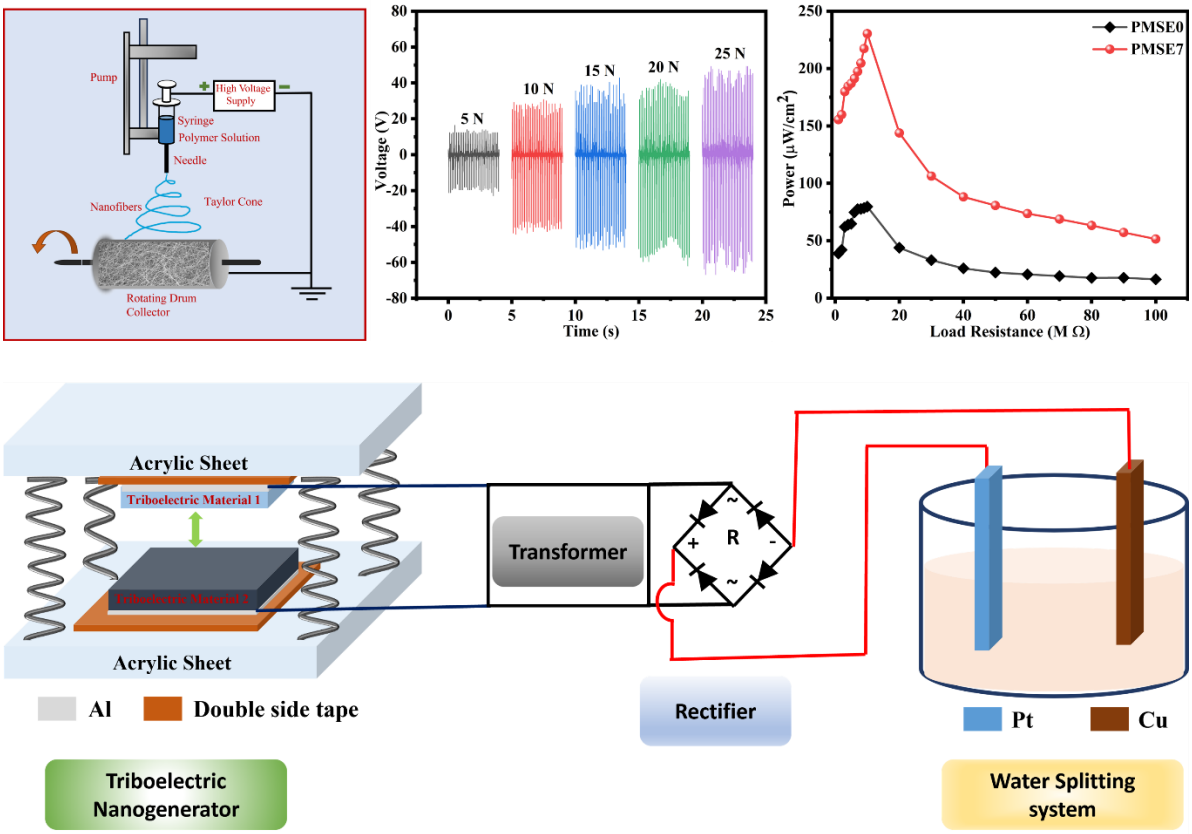

In the present chapter, electrospinning technique is used to prepare nanofiber thin films of PVDF-$MoSe_2$ with different wt% of $MoSe_2$ (0 wt%, 3 wt%, 5 wt%, 7 wt% and 10 wt%) for improving the nanogenerator performance. Here, hybrid triboelectric nanogenerator coupling both the piezoelectric and triboelectric effects have been fabricated to drive the environment friendly approach for splitting the water for hydrogen production. Here, electrospun PVDF-$MoSe_2$ fiber deposited over aluminum foil as triboelectric negative and Nylon fiber film as tribopositive material, have been used for the designing of hybrid TENG device. The PVDF-$MoSe_2$/Nylon based HNG exhibits remarkable peak to peak open-circuit voltage of 113.6 V and 26.5 μA of short-circuit current. Moreover, it exhibits a high-power density of 230.4 μWcm^{-2} under piezo-tribo coupling, which is even superior than the majority of previously fabricated similar type of devices.

5.1. Introduction

The entire human race is facing two major challenge which are related to energy and the current environmental pollution [1]. The rapid depletion of fossil reservoirs and the rising world population have increased fears about an impending energy crisis. In addition, the increasing greenhouse gas emissions to meet the energy requirement of the current population have further played a role in increased global warming and climate change around the world [2]. At this stage, producing sustainable energy supplies is the most popular topic of discussion all over the world [3, 4]. In this way, the hydrogen because of its large energy capacity of 143 MJ/kg and environmental friendliness with H_2O as the distinctive oxidation product, can be considered as an excellent substitute for the fossil fuels [5, 6]. However, presently, the generation of H_2 is primarily derived from the products based on fossil fuels [7] and is still very difficult to create a highly efficient technique for producing H_2 from renewable energy that is also economically competitive and environmentally friendly [8]. The scientific community has been doing continuous efforts of getting hydrogen by water splitting from available renewable energy sources, due to its carbon free byproducts, thereby supporting the mission of world's green hydrogen production [9].

A potential solution to the problem involves gathering available energy from the environment, which may then be used directly for electrolysis of water without the need for an external power source [9, 10]. Recently, the mechanical energy harvesting using piezoelectric and triboelectric nanogenerators have been demonstrated to be a successful mechanism for converting ubiquitously mechanical energy into electricity and attracted great attention because of its cost-effectiveness, resilience and high efficiency [11-14]. The working mechanism of piezoelectric nanogenerators is based on the polarization of material and charge separation caused because of external vibration [15, 16], while the triboelectric nanogenerator works on the triboelectric phenomenon, generally known as contact electrification [17]. The opposite charges are made to flow through the external circuit because of the developed potential difference during piezoelectric and triboelectric processes, allowing the nanogenerator device to be used as a power source [18].

Polyvinylidene fluoride (PVDF) which is a ferroelectric polymer with different crystallite polymorphs, among which the β-phase of PVDF is widely explored for piezoelectric nanogenerators due to its flexibility, outstanding stability, and promising piezoelectric coefficient [19-21]. PVDF, on the other hand, has a strong electron affinity as well as great spontaneous polarisation, making it a suitable triboelectric material for TENGs [22, 23].

Several approaches have been explored to improve the β-phase, such as electric poling and thermal treatment [24, 25]. Researchers have also explored the inclusion of different nanofillers into the PVDF matrix for improving its polar β-phase content, charge trapping capabilities, dielectric properties and surface potential [26, 27]. Furthermore, 2D nanomaterials with an extraordinarily thin layer of crystalline structure are employed as fillers to improve the β-phase and dielectric characteristics of PVDF [28-30]. The inherent piezoelectric properties of 2D materials are responsible for the enhanced piezoelectric output of the nanogenerator [31, 32]. While, TENGs output performance is improved by the maximising surface charges generated by high surface to volume ratio and the ultrathin structure of 2D nanomaterials [33, 34]. To improve the output performance of PVDF based PENGs and TENGs, recent works have referenced 2D materials as fillers such as MoS_2, $MoSe_2$, black phosphorus [28, 35, 36]. However, there are limited studies on the effect of filler weight percentage on the PVDF matrix. The concentration of nanofiller in the PVDF solution has found to impact the device output performance and therefore drive the current piece of research work.

Electrospinning is one of the method capable of producing nanofibers with diameters in nanometer range (5-500 nm) which are useful in variety of fields, such as, healthcare, defence and security, biomedical, environmental engineering, and energy generation [37-40]. In fact, by decreasing the fiber diameter from microscale to nanoscale, remarkable features such as flexibility, extraordinarily large surface and improved mechanical performance have been obtained [41-43]. Therefore, electrospinning is regarded as one of the most beneficial techniques for the production of PVDF nanofiber films because the high voltage supplied during synthesis aids in obtaining the required crystalline β-phase [44]. The piezoelectric characteristics of the synthesized fibers would improve further as a result of mechanical stretching by polymer jet elongation [44, 45]. As a result, electrospun PVDF films exhibit increased piezoelectric characteristics without the post-poling step commonly utilised in other production processes.

In the present chapter, we have studied the effect of varying $MoSe_2$ wt% on the piezoelectric output of PVDF-$MoSe_2$ nanofiber based piezoelectric nanogenerator. The PVDF-$MoSe_2$ nanofibers were synthesized via electrospinning technique with different wt% of $MoSe_2$ (0, 3, 5, 7 and 10 wt%). Pure PENG device having 7 wt% $MoSe_2$ generates maximum piezoelectric output, with an output voltage of 64.8 V and 13.4 μA of short circuit current. Further, hybrid TENG device was fabricated in the vertical contact-separation mode based on PVDF-$MoSe_2$ nanofibers with 7wt% of $MoSe_2$ having highest piezo performance as one of the

layer and the Nylon nanofibers as another triboelectric layer. The TENG with PVDF-$MoSe_2$ produces a remarkable output voltage and short circuit current of 113.6 V and 26.5 μA respectively. The resulting hybrid TENG nanogenerator produces a maximum power density of 230.4 $\mu W/cm^2$, which is 2.9 times higher than that of bare PVDF nanofiber based TENG which produces a power density of 79.7 $\mu W/cm^2$. Further, the outcome of different tapping force and frequency was also analysed on the PVDF-$MoSe_2$ based triboelectric nanogenerator and at a contact force of 25 N it produces a maximum output voltage of 116 V. It has shown that the considerable improvement in triboelectric output of PVDF-$MoSe_2$ nanofiber-based hybrid triboelectric nanogenerator is mostly due to the addition of $MoSe_2$, which promotes the creation of electroactive β-phase in PVDF and improves the triboelectric performance. Furthermore, the $MoSe_2$ nanosheets embedded into PVDF matrix may be used as charge trapping regions, improving the triboelectric charge density and hence increasing its triboelectric output. Further based on hybrid TENG output voltage an entirely self-powered water splitting system for generation of hydrogen has been described where instead of using an external power source, the electricity that is produced is used for splitting water in order to make H_2 by harvesting ambient mechanical energy. This type of self-powered water splitting technology pave the way for future energy alternatives.

5.2. Experimental Section

5.2.1 Synthesis of PVDF-$MoSe_2$ Nanofibers and Nylon Nanofibers.

Simple hydrothermal process was used for the synthesis of $MoSe_2$ nanosheets which has been previously described in chapter 3 [28]. To prepare the solution for the electrospinning, 1 g of PVDF powder has been dissolved in DMF and stirred continuously for 1 hour at 60°C. Further, various amounts of $MoSe_2$ sheets were then dissolved into the above solution to obtain the PVDF-$MoSe_2$ hybrid solution with different wt % of $MoSe_2$, and the solution was stirred for next 2 hrs to get the homogeneous solution. Following that, the resulting solution was added into 10 mL syringe with varied $MoSe_2$ wt% of 0, 3, 5, 7, and 10 wt% for electrospinning, which was done using an electrospinning machine at a high voltage of 12 kV with 1 mL h^{-1} flow rate. The fibers were collected on Al foil which is rolled over the drum collector and kept at a distance of 12 cm from needle. The hybrid films of PVDF-$MoSe_2$ nanofibers with a thickness of ~50 μm were formed after constantly collecting for about 5 hrs and drying for 12 hrs at 60 °C in an oven, and has been named as PMSE0, PMSE3, PMSE5, PMSE7 and PMSE10 for $MoSe_2$ wt% of 0%, 3%, 5%, 7% and 10%, respectively. The synthesis of nanofiber films is illustrated in Figure 5.1.

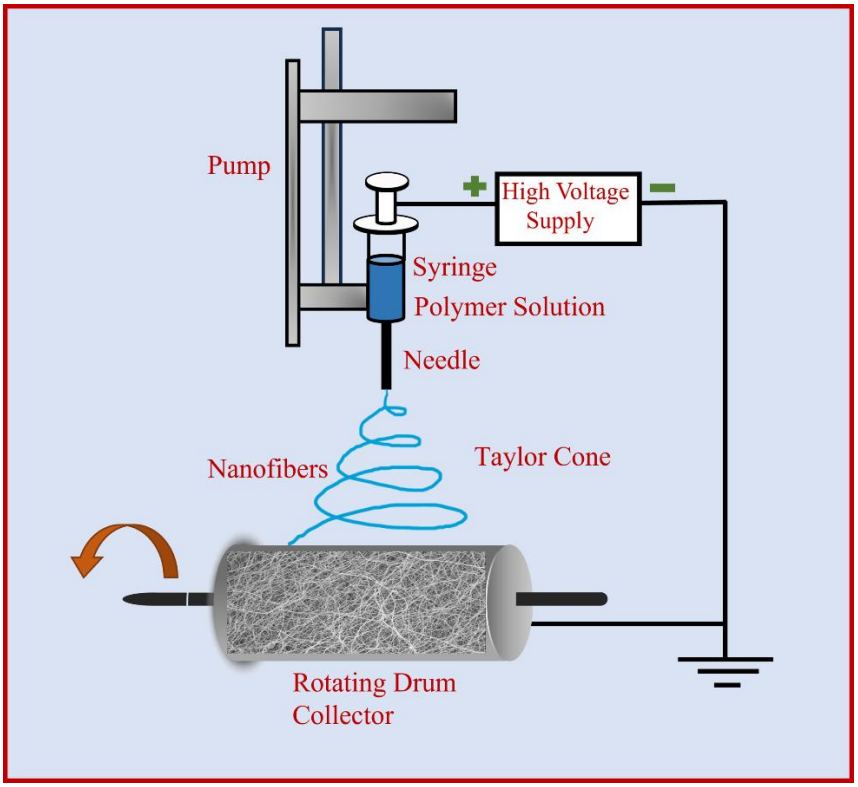

Figure 5.1 Schematic diagram showing the synthesis of nanofibers using electrospinning technique.

For the synthesis of Nylon nanofibers, 20 wt% solution of Nylon was prepared in formic acid. The prepared solution was homogeneously mixed by continuous stirring at 70°C for three hours using a magnetic stirrer. The solution was loaded into a 5 ml syringe for electrospinning, which was done at a flow rate of 1 mL h^{-1} at a voltage of 20 kV. The Nylon fibers were also deposited over an Al foil using the same drum collector.

5.2.2 Fabrication of Nanogenerators

To analyse the effect of wt% on piezoelectric performance, PVDF and PVDF-$MoSe_2$ nanofiber based piezoelectric nanogenerators were fabricated by sandwiching the nanofiber films of 1.75 cm x 1.75 cm between two aluminium electrodes. The copper wires were then used to connect the PENG with the external circuit.

Further, PVDF and PVDF-$MoSe_2$ with 7 wt% of $MoSe_2$ were used for the fabrication of hybrid TENG in vertical contact-separation mode. PVDF or PVDF-$MoSe_2$ nanofiber films were coupled with Nylon nanofiber film, which will act as second triboelectric layer. Both the layers have aluminium electrode at one side and copper wires were used to make the electrical connections. To arrange the TENG, both the films of 1.75 cm x 1.75 cm were pasted on acrylic sheets using a double-sided tape.

5.2.3 Characterizations and Energy Harvesting Performance

Bruker D8-Advance X-ray diffractometer with X-ray source of Cu K_α (λ= 1.54 Å) has been utilized to analyze the crystallinity of the synthesised thin films. PerkinElmer spectrum-II instrument was used for the fourier transform infrared spectroscopy (FTIR) studies of the synthesized films. The synthesized films morphology was examined using a field-emission scanning electron microscope (FESEM, Zeiss Gemini SEM 500) at a 15 kV accelerating voltage. The dielectric measurements were performed using an LCR metre (Agilent E4980A) with in the 20 Hz-10^4 Hz frequency range. For examining the piezoelectric and triboelectric performance of devices, a dynamic shaker (Micron MEV-0025) was used to manage the continuous contact-separation motions between the triboelectric layers by adjusting its operating parameters, which included tapping frequency and contact force. The open circuit voltages for PENG and TENG were determined using an oscilloscope (Tektronix MDO34). Short circuit current and the charge measurements were performed using an electrometer (Keysight B2985B). The measurement of triboelectric output in a typical contact separation mode includes regulating the movement of negative layer of TENG (PVDF or PVDF-$MoSe_2$) to make connection with the positive layer of TENG (Nylon).

5.3. Results and Discussion

5.3.1 Structural and Morphological Analysis of PVDF-$MoSe_2$ Nanofibers

XRD and Fourier-transform infrared spectroscopy (FTIR) investigations were carried out to confirm the different phases of fluoropolymer PVDF. These techniques were used to determine the presence of electroactive β-phase and non-electroactive α-phase in fabricated thin films of PVDF. Figure 5.2(a) illustrates the XRD spectra of the thin films composed of different synthesized nanofibers, incorporating varying wt% of $MoSe_2$ into the PVDF matrix. $MoSe_2$ peaks are indicated by the symbol "#" in the XRD spectra of synthesised nanofiber-based films, while the PVDF peaks are designated by the symbol "α" and “β” respectively. The non-polar α-phase in PVDF is represented by the diffraction peak observed at 18.3°, while the electroactive β-phase is represented by the peak at 20.2° [28, 46-50]. According to the XRD spectra, the β-phase increases significantly after the addition of $MoSe_2$, because the peak intensity corresponding to the non-electroactive α-phase decreases whereas the peak intensity indicating the electroactive β-phase increases. As a result, XRD spectra shows that $MoSe_2$ filled PVDF nanofiber films were successfully synthesised with increased electroactive β-phase. FTIR spectral analysis was carried out as well to better define the polar crystalline phase

present in the PVDF-$MoSe_2$ nanofiber based thin films. As depicted in Figure 5.2(b), for β-phase, characteristic vibrational bands at 840 cm^{-1}, 1276 cm^{-1} and 1402 cm^{-1} are observed, while the α-phase is confirmed by characteristic vibrational bands at 614 cm^{-1}, 762 cm^{-1} and 796 cm^{-1}.

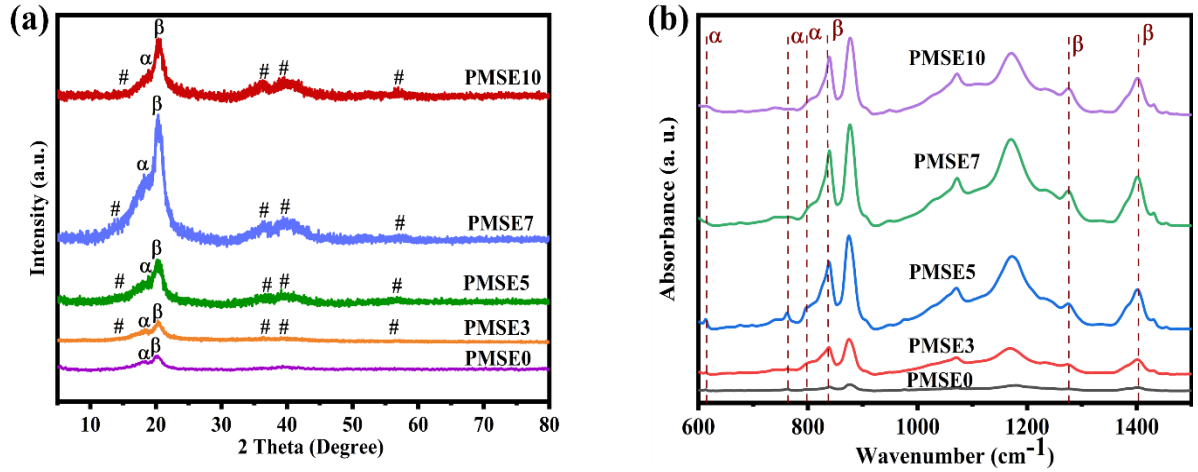

Figure 5.2 Structural characterization of PVDF-$MoSe_2$ composite nanofiber films (a) XRD spectra (b) FTIR spectra of PMSE0, PMSE3, PMSE5, PMSE7 and PMSE10, respectively.

It can be concluded from FTIR spectra that the nanofibers are made up of both α and β-phases [47, 48, 51-53]. More precisely, following the Lambert-Beer law, the absorption vibrational bands at 762 cm^{-1} and 840 cm^{-1} were quantified in order to calculate the percentage of β-phase in different PVDF-$MoSe_2$ based nanofibers [52, 54]. The percentage composition of β-phase in bare PVDF nanofiber film is 66.50 %, while in PVDF-$MoSe_2$ nanofiber films its value is 73.20 %, 77.05, 85.55 % and 83.10 % for 3, 5, 7 and 10 wt% of $MoSe_2$, respectively. The percentage composition of β-phase is increased from 66.50 % to 85.55 %, for $MoSe_2$ nanosheet concentration increased from 0 to 7 wt % and further decreases on increasing the $MoSe_2$ concentration 10 %. When $MoSe_2$ is introduced into the PVDF solution, the negative surface of the $MoSe_2$ interacts strongly with the positive CH_2 dipoles of the PVDF chain, resulting in the formation of stable longer trans-trans-trans (TTTT) configuration [19, 28, 54, 55]. On further increasing the $MoSe_2$ wt % from 7 to 10 in the PVDF matrix the electroactive phase intensity reduces, which can be attributed to [19, 55, 56]. The electroactive β-phase concentration is directly related to the piezoelectric performance and hence the $MoSe_2$ insertion greatly enhances the output voltage of the fabricated PENG. Not only the piezoelectric properties, the enhanced β-phase composition also has a significant impact on triboelectric output capabilities of PVDF.

Further, to understand the increased device performance as a function of $MoSe_2$ nanofiller, surface morphology of fabricated PVDF-$MoSe_2$ nanofiber films were also studied. Fibrous networks with few beads without nanosheet aggregation are observed in electrospun PVDF-$MoSe_2$ nanofiber films, as illustrated in Figure 5.3 (i-iv), when the $MoSe_2$ concentration increases from 0 to 7 wt%. After 7 wt% the agglomeration of $MoSe_2$ into the PVDF matrix is observed and is shown in Figure 5.3 (v). The average diameters of these nanofibers are nearly identical, indicating that $MoSe_2$ nanosheets have little impact on the morphology and microstructure of electrospun PVDF-$MoSe_2$ nanofiber films. Morphological image of Nylon fibers is shown in Figure 5.3 (vi), where well organized bead free fibrous network was observed.

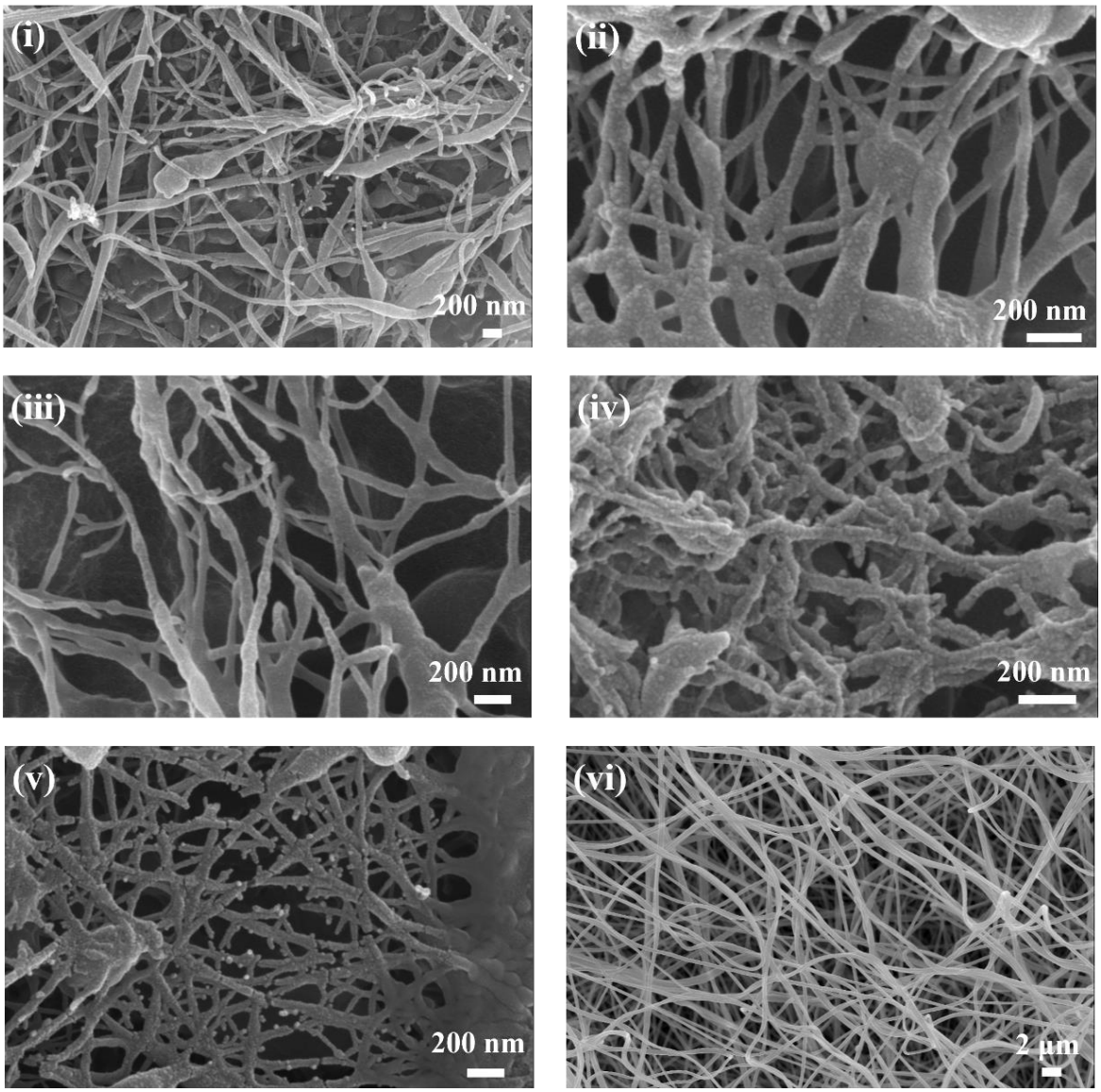

Figure 5.3 FESEM image of (i) PVDF, (ii-v) PVDF-$MoSe_2$ composite and (vi) Nylon nanofiber films.

5.3.2 Dielectric Property Analysis of Different PVDF-$MoSe_2$ Thin Films.

It has been observed in various studies that dielectric constant of triboelectric materials is one of the critical parameter for selecting the TENG material. Therefore by improving the dielectric constant of the selected material, the triboelectric output performance of the device can be enhanced [57]. Figure 5.4 shows the dielectric constant of the nanofiber-based films as a function of frequency where increasing $MoSe_2$ wt % (0, 3, 5, 7, and 10%), enhanced the dielectric constant from 8.3 to 10.8, 14.5, 17.6 and 11.7, respectively. As a result, the inclusion of 7% $MoSe_2$ to the PVDF matrix produced highest dielectric constant nanofiber film. The dielectric constant rapidly decreases as the $MoSe_2$ concentration was raised further, up to 10 wt% due to the percolation limit for the PVDF-$MoSe_2$ composite [57, 58].

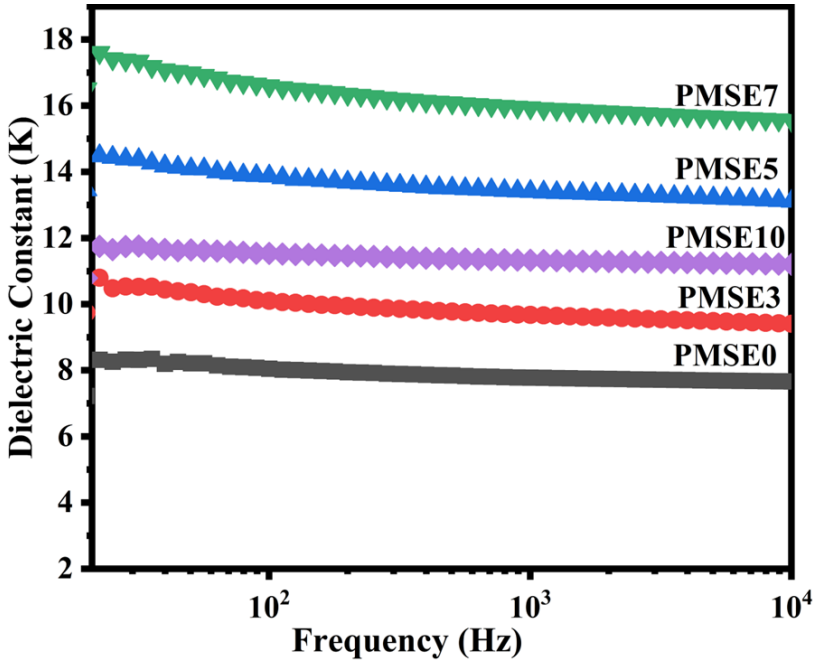

Figure 5.4 Dielectric constant of PVDF-$MoSe_2$ composite nanofiber films for PMSE0, PMSE3, PMSE5, PMSE7 and PMSE10, respectively.

PVDF became more polarizable as a result of the dipolar contribution of the $MoSe_2$, which enhanced the value of the dielectric constant [19, 57]. The dielectric studies complemented the FTIR results which states that PVDF-$MoSe_2$ film with 7 wt% $MoSe_2$ has the maximum percentage of β-phase. According to the FTIR spectra, the incorporation of $MoSe_2$ into PVDF matrix increases the concentration of β-phase, implying that the inclusion of $MoSe_2$ results in dipolar polarisation resulting into the increased dielectric constant. This also confirms that the piezoelectric response of the nanofiber film will also enhances with the inclusion of $MoSe_2$. As reported the transmitted charge density is determined by the dielectric

property of the thin film, and has substantial impact on the triboelectric output efficiency of a triboelectric nanogenerator [57, 59]. The increased dielectric constant with the addition of $MoSe_2$ enhances the surface charge density of the triboelectric layer material which is attributed to the increased capacitance that is directly related to the dielectric constant of the synthesized material [57, 60, 61].

5.3.3 Output Performance Analysis of Fabricated PENGs

To further investigate the influence of weight percentage of $MoSe_2$ (0, 3, 5, 7, and 10 wt%) on piezoelectric performance, PVDF and PVDF-$MoSe_2$ nanofiber film based nanogenerators were fabricated by sandwiching the composite thin films between aluminium electrodes and electrical measurements were performed. The fabricated nanogenerators were constantly tapped by finger to check their piezoelectric output performances. The piezoelectric output voltage and current of the $MoSe_2$ filled PVDF nanofibers are shown in Figure 5.5 (a) and (b), respectively in order to compare their piezoelectric energy harvesting capabilities. Pure PVDF nanofiber based nanogenerator has generated peak to peak open circuit output voltage of 19.2 V, while PVDF-$MoSe_2$ composite nanofiber based nanogenerators have generated the output voltages of 37.6 V, 41.6 V, 64.8 V, and 40.0 V for PMSE3, PMSE5, PMSE7, and PMSE10, respectively. The piezoelectric performance of $MoSe_2$ filled PVDF nanofibers based PENGs grows progressively as the $MoSe_2$ wt% increases. The PMSE7 film based nanogenerator produces the highest output voltage, which is three times more than that of the open circuit voltage generated by bare PVDF, demonstrating the greatest improvement in energy harvesting properties.

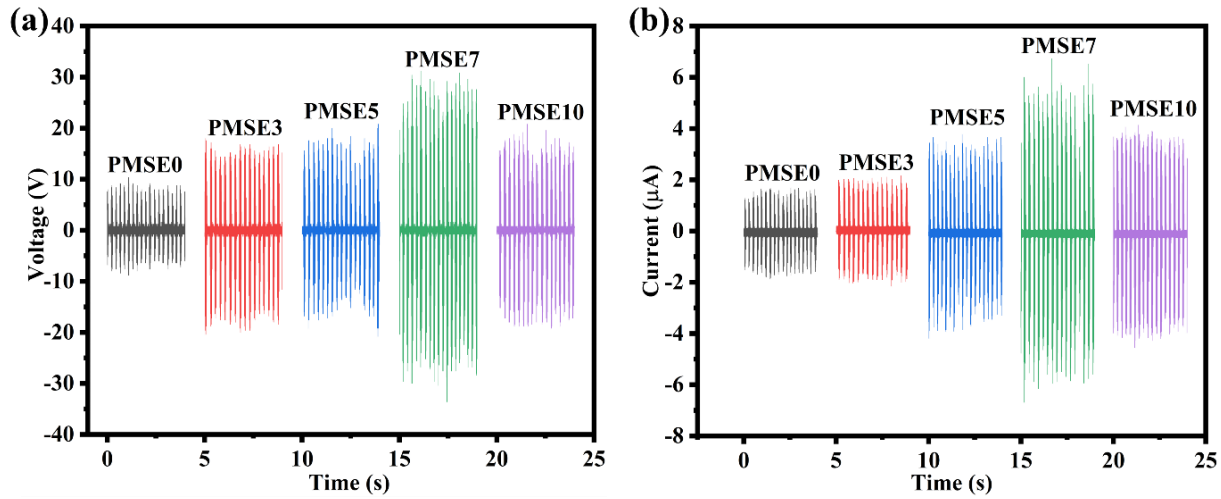

Figure 5.5 Effect of $MoSe_2$ wt% on the piezoelectric (a) open circuit voltage and (b) short circuit current of PVDF-$MoSe_2$ nanofiber based PENGs.

Under identical conditions, the short circuit current of PENGs for various weight percentage of $MoSe_2$ is shown in Figure 5.5 (b). Bare PVDF nanofiber-based PENG generates a short circuit current of 3.6 μA, while PVDF-$MoSe_2$ based nanogenerators with 3, 5, 7, and 10 wt % of $MoSe_2$ generate a short circuit current of 4.3 μA, 7.9 μA, 13.4 μA, and 7.9 μA, respectively. The short circuit current for all the nanogenerators also followed the similar trend as the voltage output. The increase in the piezoelectric performance of PVDF nanofiber based PENGs following the addition of $MoSe_2$ into the PVDF matrix can be attributed to two reasons: (i) an additional contribution of the intrinsic piezoelectric capabilities of $MoSe_2$ to the overall output of the nanogenerator [31, 32] and (ii) an increase in the β-phase content of PVDF [21, 28]. Based on the piezoelectric output performance, the 7 wt% $MoSe_2$ loaded PVDF is best for effective harvesting of mechanical energy. The rapid drop in output performance above 7 wt% of $MoSe_2$ is credited to $MoSe_2$ agglomeration in the PVDF matrix and low surface qualities, as shown in the FESEM image in Figure 5.3. These findings are also consistent with previously reported research indicating that the inclusion of nanofillers improves the piezoelectric characteristics of PVDF and its copolymers [28, 62-65].

5.3.4 Output Performance Analysis of Fabricated TENGs

To further improve the efficiency of electrical energy generation from mechanical energy harvesting, we have fabricated a hybrid triboelectric nanogenerator in the vertical contact-separation mode, where PMSE7 based nanofiber film with highest piezoelectric output is used as one of the triboelectric layer and Nylon nanofiber film as the second triboelectric layer. After the fabrication of TENGs, the electrical measurements were performed to study the triboelectric properties of PVDF-$MoSe_2$ hybrid films based TENG in comparison to the bare PVDF film based TENG. An electrodynamic shaker was used to continuously stress both TENGs in contact separation mode. It was observed that the triboelectric output voltage was increased from 54.8 V to 113.6 V after the inclusion of $MoSe_2$ into the PVDF matrix, whereas the associated short-circuit current rises from 6.0 μA to 26.5 μA as shown in Figure 5.6(a) and (b). Furthermore, as shown in Figure 5.6(c), the transmitted surface charge of the PVDF-$MoSe_2$/Nylon TENG increases from 6.9 nC for pristine PVDF based TENG to 20.1 nC for PVDF-$MoSe_2$ TENG with 7 wt% $MoSe_2$. It appears that just the addition of $MoSe_2$ nanosheets have a considerable impact on the triboelectric characteristics of PVDF nanofiber films.

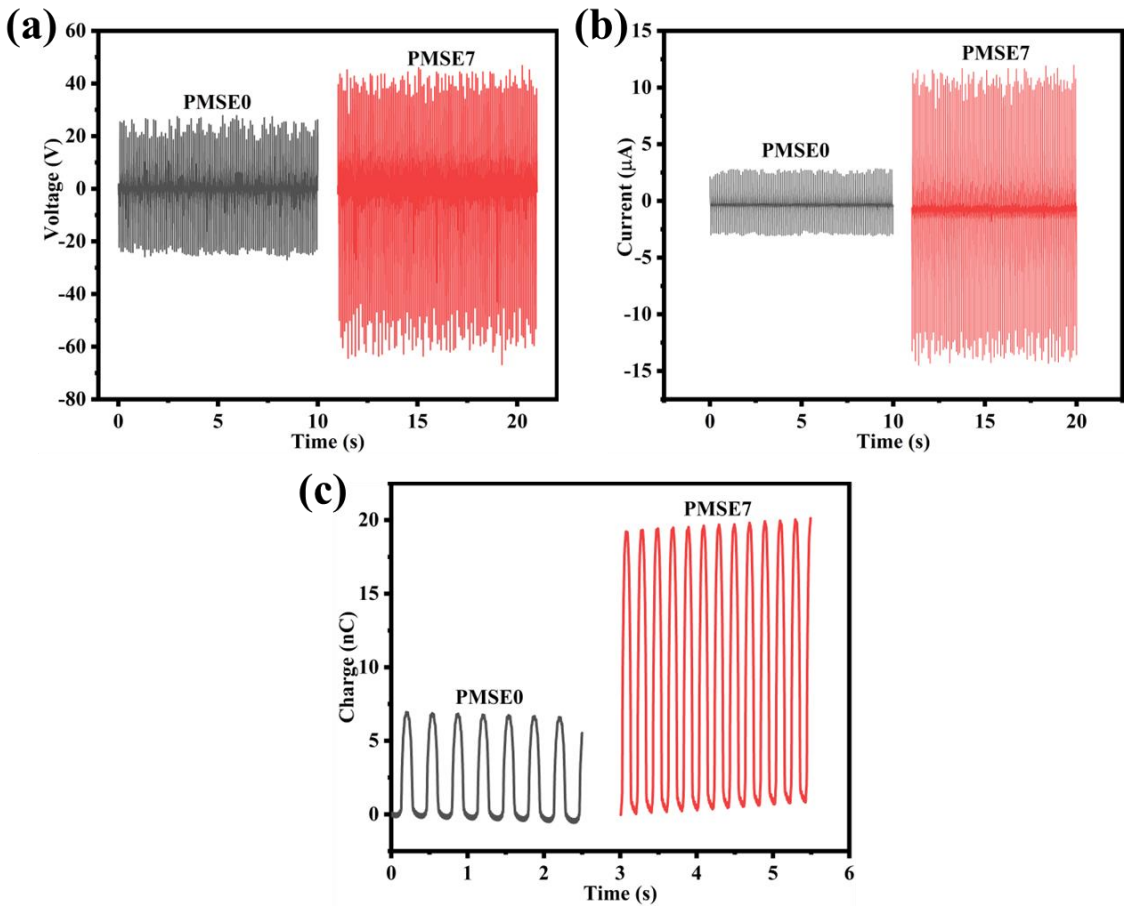

Figure 5.6 Triboelectric output performance of PMSE0/Nylon and PMSE7/Nylon based TENGs (a) open circuit voltage, (b) short circuit current, (c) charge transfer.

For both TENGs, the influence of load resistance on their generated voltage and power density has been investigated as well and are illustrated in Figure 5.7 (a) and (b). For all load resistances, the output voltage and power density of the PVDF-$MoSe_2$/Nylon TENG is higher in comparison to pure PVDF based TENG. The triboelectric voltage for TENGs first rises with rise in the value of load resistance and then become almost saturated. The PVDF-$MoSe_2$/Nylon has produced a maximum power density of 230.4 $\mu W/cm^2$, while the PVDF/Nylon TENG generated power density of 79.7 $\mu W/cm^2$ at a load resistance of 10 MΩ. Being an attractive source of power for electronic devices the triboelectric performance investigation of PVDF-$MoSe_2$/Nylon under various operating situations is also important. Thus, the impact of contact force and tapping frequency on the output performance of the hybrid TENG has been examined. To investigate the influence of tapping frequency on the triboelectric performance of the TENG, an electrodynamic shaker is used to tap the nanogenerator with 7 wt% $MoSe_2$. The impact of tapping frequency on the triboelectric performance with varied frequencies ranging from 2 Hz to 10 Hz is depicted in Figure 5.7(c). The generated output voltage grows

with frequency and is reached up to ~110 V at 10 Hz. As illustrated in Figure 5.7(d), the generated short circuit current shows a similar pattern as the tapping frequency increases. Since there is faster charge transfer at higher contact frequencies, the short-circuit current of PVDF-$MoSe_2$/Nylon TENG rises with working frequency [33].

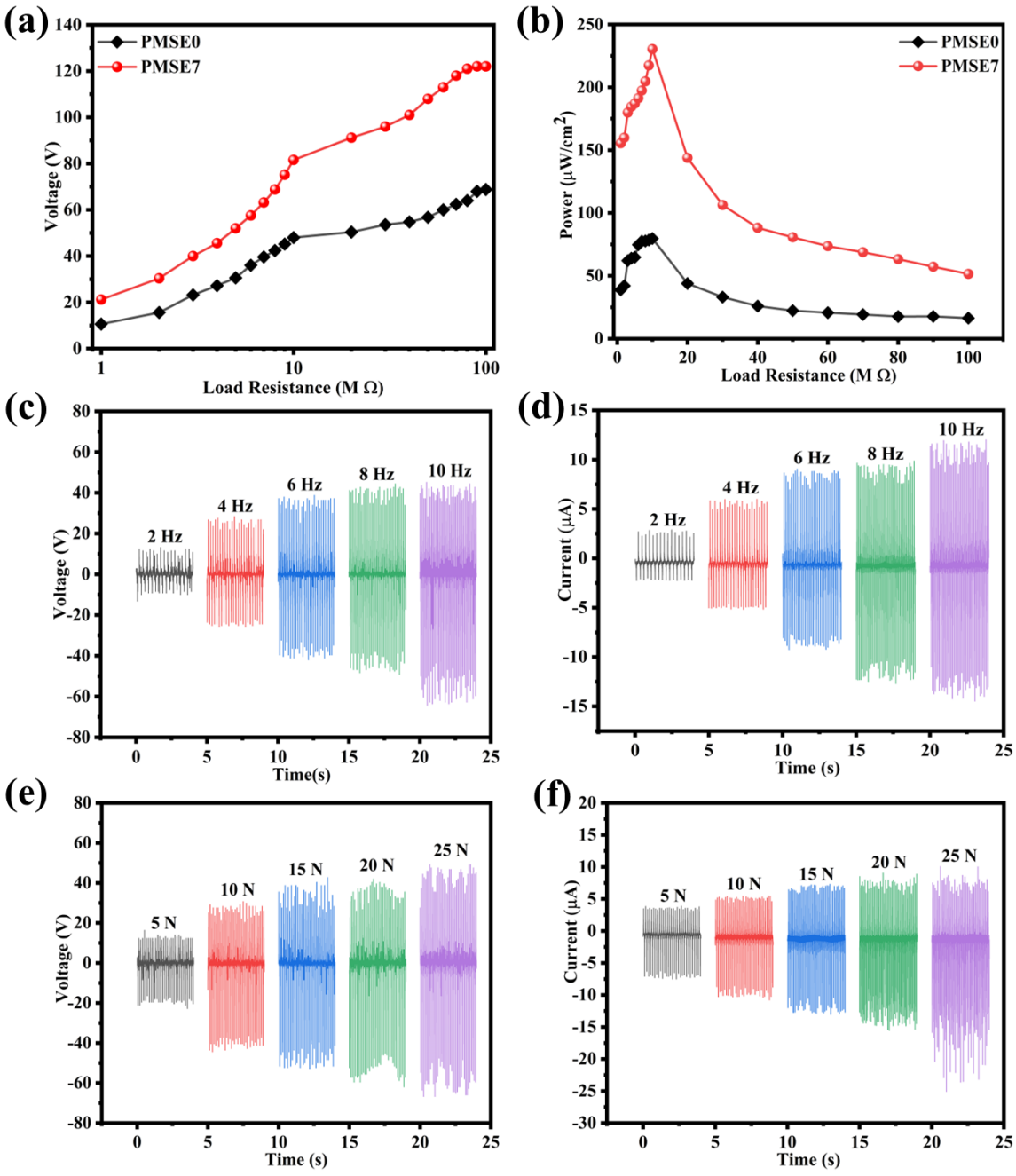

Figure 5.7 Triboelectric output performance of PMSE0/Nylon and PMSE7/Nylon based TENGs (a) output voltage with different load resistance, (b) power per unit area with different load resistance at a tapping frequency of 9 Hz and effect of (c-d) tapping frequency and (e-f) contact force on triboelectric performance of PMSE7 based TENG.

Figure 5.7(e) and (f) illustrate the reliance of triboelectric output on impact force, when the PVDF-$MoSe_2$/Nylon TENG operated under various impact forces ranging from 5 N to 25 N with a fixed operating frequency of 8 Hz. As shown in Figure 5.7(e), the output voltage gradually rises from 19 V to 100 V when the contact force rises from 5 N to 20 N, finally achieving 116 V of output voltage at an impact force of 25 N. At the same time, the associated short-circuit current of the TENG exhibit a similar trend, increasing from 11.4 µA to 35.1 µA when the contact force was raised from 5 N to 25 N. As a result, an impact force has a considerable role in the generation of triboelectric output. This may be attributed to the elastic characteristic of polymeric triboelectric materials, which on increasing the impact force, increases the effective area of contact of TENG, resulting in more triboelectric charges being created for increased power generation. The elastic deformation of the PVDF-$MoSe_2$ and Nylon nanofiber film increases as contact force increases, resulting in larger TENG capacitance, which is advantageous for storing triboelectric charges and attaining greater triboelectric output [17, 33].

The output performance of the fabricated TENG with the previously reported TENGs has been compared in the table 5.1. To check the stability and durability of the fabricated TENG device, we have measured the output current of the TENG for 3500 cycles and no degradation is observed during the measurement as shown in Figure 5.8.

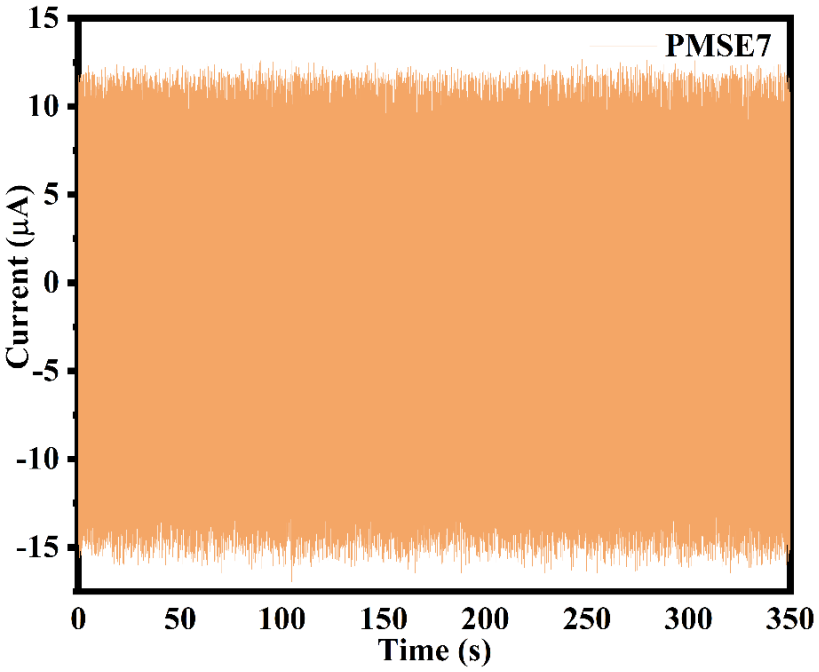

Figure 5.8 Short circuit current for 3500 cycles showing the durability of PMSE7 based TENG.

Table 5.1. Comparison of TENG output generated by PVDF-$MoSe_2$/Nylon with previously reported TENGs.

Device Structure	V_{oc}	I_{sc}	Power Density	Synthesis	Reference
PVDF-MWCNT/Nylon	14 V	0.7 μA	0.065 mW/m^2	Electrospinning	[66]
3D-MXene/PDMS-Nylon	45 V	0.6 μA	-		[67]
PVDF/TOML	52 V	5.69 μA/cm^2	0.37 W (Only power)	Solution casting,	[68]
ZnO-PVDF/PTFE	119 V	1.6 μA	10.6 μW/cm^2	Solution Casting	[69]
P3HT/PVDF-HFP	78 V	7 μA	0.55 mW (Only power)	Electrospinning	[70]
ZnO-PVDF/PTFE	90 V	7.4 μA/cm^2	0.13 W/m^2	Electrospinning	[71]
PVDF-$MoSe_2$/Nylon	116 V	35.1 μA	230.4 μW/cm^2 (2.304 W/ m^2)	Electrospinning	**This work**

5.3.5 Underlying Operating Mechanism of TENGs

The operating mechanism of PVDF-$MoSe_2$/Nylon nanofiber based TENG is depicted in Figure 5.9. Since no charge exits prior to the contact between the layers of TENG, resulting in zero potential difference between the layers (Figure 5.9(a)). Using a dynamic shaker, both triboelectric layers are pushed into contact, leading electrons to move from Nylon surface towards the PVDF-$MoSe_2$ surface via contact electrification. As a result, the Nylon surface charges positively, whereas the PVDF-$MoSe_2$ surface charges negatively. (Figure 5.9(b)). Because of the polymer films insulating nature, these charges will not flow away or be neutralised quickly. When these layers are separated, an electrical potential difference among their associated electrodes is created, causing electrons to travel via an external circuit, leading to an electrical signal (Figure 5.9(c)). Once the separation distance is maximised, the electric potential difference between the electrodes is entirely neutralised by electron transfer, and in the external circuit no electrical signal is produced (Figure 5.9(d)). When the TENG is compressed again, an opposite electrical signal is produced due to back-flow of electron (Figure 5.9(e)). As a result, despite being repeatedly driven by an external force, TENG could generate a continuous alternating electrical output.

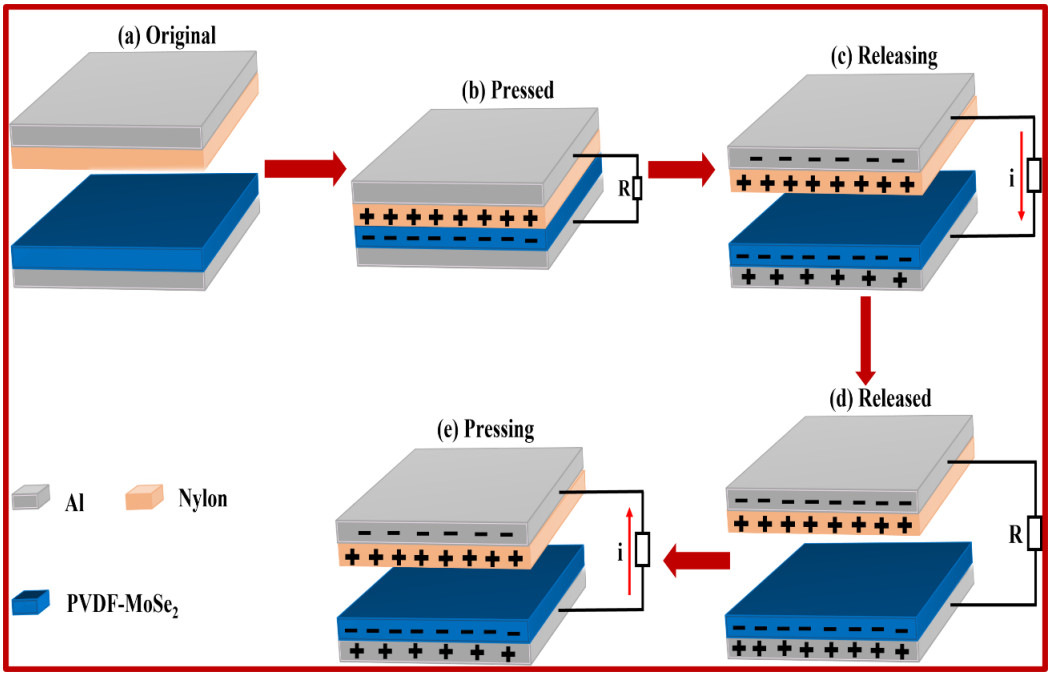

Figure 5.9 Schematic illustrating the operating mechanism of PVDF-$MoSe_2$/Nylon based TENG device.

5.3.6 Surface Potential Analysis using COMSOL Simulations

Furthermore, the simulated surface potential distribution between the two contacting layers of PVDF/Nylon and PVDF-$MoSe_2$/Nylon based TENG device was calculated by a finite element model via COMSOL software. Figure 5.10 illustrates the potential difference between Nylon and PVDF-$MoSe_2$ is more than the potential difference generated for Nylon and bare PVDF films.

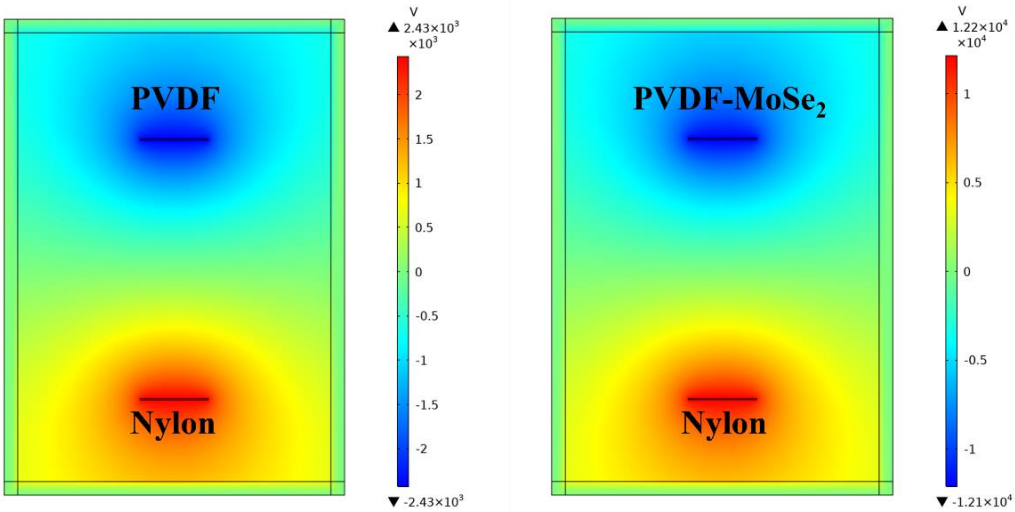

Figure 5.10 COMSOL simulated distribution of surface potential for PVDF and PVDF-$MoSe_2$ in comparison to Nylon.

As a result of the increased potential difference between the surface of PVDF-$MoSe_2$/Nylon TENG more charges are transferred between both the surfaces. Increased charge transfer for PVDF-$MoSe_2$/Nylon TENG as compared to PVDF/Nylon TENG results in the enhanced output performance. These results also support the above-mentioned experimental investigations where the triboelectric output of the TENG is improved after the addition of $MoSe_2$. More is the potential difference between the triboelectric layers, more charges are transferred between layers, resulting in enhanced triboelectric output [22, 33, 59].

5.3.7 Self Powered Water Splitting System

In order to show the practical applicability of our current work, we utilised the produced output for powering the water splitting system, thereby eliminating the requirement for an external power source. The circuit diagram of the self-powered water splitting system for the generation of H_2 is shown in Figure 5.11.

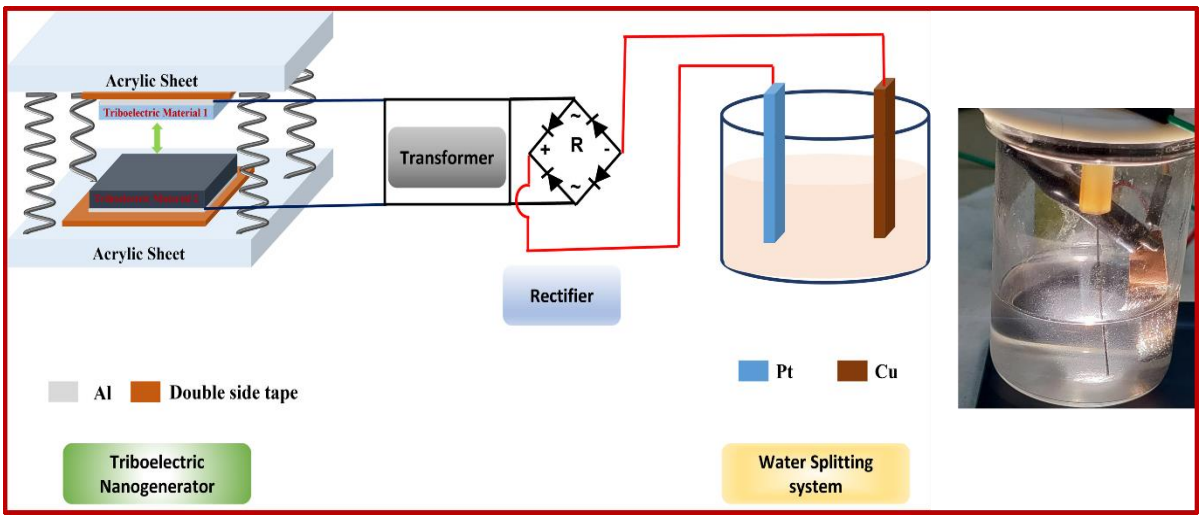

Figure 5.11 Schematic showing the mechanism for water splitting system with the real optical image.

To create a self-power water splitting system, the TENG has been attached to an electrolytic cell, then the generated voltage is transformed and rectified before providing the generated power to the electrolytic cell. In the electrolytic cell, Pt wire and copper sheet were used as electrodes and 1 M KOH solution was used as the electrolyte. Overall splitting of water often depends on two half reactions of HER and OER on the cathode and anode, respectively, where hydrogen is produced at cathode, while the oxygen is at anode as shown below [3, 6].

$$2H_2O = O_2 + 4H^+ + 4e^-(\text{anode}) \quad (5.1)$$

$$4H^+ + 4e^- = 2H_2\ (\text{cathode}) \quad (5.2)$$

TENG may viewed as a source of current with a high output impedance, resulting in a serious mismatch in impedance when the output is directly used for water splitting because of the low resistance of the electrolyte. To enhance the output current at the cost of output voltage, a transformer was utilised to modify the output impedance of the TENG, thereby increasing the current output.

5.4. Conclusion

In summary, we have developed a self-powered system for the splitting of water for generation of hydrogen as a source of green energy by converting mechanical energy into electrical energy with the use of hybrid triboelectric nanogenerator. We have shown that incorporation of $MoSe_2$ nanosheets can considerably improve the piezoelectric and triboelectric performance of PVDF. At first, the comparison between the piezoelectric efficiency of different PVDF-$MoSe_2$ nanofiber based films as a function of $MoSe_2$ wt% was carried out, and it has been discovered that 7 wt % of $MoSe_2$ is the ideal concentration for piezoelectric energy harvesting. The output efficiency of the PENG was suddenly dropped after 7 wt% of $MoSe_2$, because of the agglomeration of $MoSe_2$ in the PVDF matrix. As a result, the PENG with 7 wt% of $MoSe_2$ has generated maximum piezo output voltage of 64.8 V and a short circuit current of 13.4 μA. Furthermore, TENG based on PVDF-$MoSe_2$ having highest piezo output as a negative triboelectric material and Nylon as tribopositive materials has been successfully designed. The TENG with 7 wt% of $MoSe_2$ exhibits excellent triboelectric performance as well by generating an output voltage of 113.6 V and a short-circuit current of 26.5 μA. The maximum power density produced by the PVDF-$MoSe_2$ based nanogenerator is 230.4 $\mu W/cm^2$, that is approximately 2.9 times greater than the maximum power density produced by pure PVDF based TENG. The impact of contact force and tapping frequency on the triboelectric performance of the TENG has also been examined. The output performance of the TENG has been found to improve with increasing frequency since charges transfers more quickly at higher frequencies. As the contact force grows, so does capacitance and the effective area of the TENG, resulting in an increase in the performance of TENG. PVDF-$MoSe_2$/Nylon TENG with 7 wt% of $MoSe_2$ generates a maximum triboelectric voltage of 116 V and short circuit current of 35.1 μA at an impact force of 25 N. Additional studies have demonstrated that the addition of $MoSe_2$ improves the content of the polar crystalline β-phase and dielectric constant, which results in the enhanced piezoelectric performance. Furthermore, the distributed $MoSe_2$ nanosheets in PVDF boosts its surface potential to improve charge transfer density. All of this contributes greatly to the enhanced triboelectric output of the PVDF-$MoSe_2$/Nylon TENG.

Finally, a self-sustaining water splitting system utilising TENG as the power supply resource for hydrogen production was established. As a result, the current study proposes a feasible, low-cost way for creating a high-performance triboelectric nanogenerator for the application of clean and sustainable energy.

References

[1] S. Chu, A. Majumdar, Opportunities and challenges for a sustainable energy future, Nature, 488,(2012), 294-303

[2] P.M. Cox, R.A. Betts, C.D. Jones, S.A. Spall, I.J. Totterdell, Acceleration of global warming due to carbon-cycle feedbacks in a coupled climate model, Nature, 408,(2000), 184-187

[3] J.A. Turner, Sustainable hydrogen production, Science, 305,(2004), 972-974

[4] J.A. Turner, A realizable renewable energy future, Science, 285,(1999), 687-689

[5] X. Zhu, T. Zhang, Z. Sun, H. Chen, J. Guan, X. Chen, H. Ji, P. Du, S. Yang, Black phosphorus revisited: a missing metal-free elemental photocatalyst for visible light hydrogen evolution, Advanced Materials, 29,(2017), 1605776

[6] X. Ren, H. Fan, C. Wang, J. Ma, H. Li, M. Zhang, S. Lei, W. Wang, Wind energy harvester based on coaxial rotatory freestanding triboelectric nanogenerators for self-powered water splitting, Nano Energy, 50,(2018), 562-570

[7] W. Wang, X. Xu, W. Zhou, Z. Shao, Recent progress in metal-organic frameworks for applications in electrocatalytic and photocatalytic water splitting, Advanced science, 4,(2017), 1600371

[8] S.Y. Tee, K.Y. Win, W.S. Teo, L.D. Koh, S. Liu, C.P. Teng, M.Y. Han, Recent progress in energy-driven water splitting, Advanced science, 4,(2017), 1600337

[9] J. Tang, T. Liu, S. Miao, Y. Cho, Catalysts2021.

[10] H. You, Z. Wu, L. Zhang, Y. Ying, Y. Liu, L. Fei, X. Chen, Y. Jia, Y. Wang, F. Wang, Harvesting the vibration energy of BiFeO3 nanosheets for hydrogen evolution, Angewandte Chemie, 131,(2019), 11905-11910

[11] K.-S. Hong, H. Xu, H. Konishi, X. Li, Direct water splitting through vibrating piezoelectric microfibers in water, The journal of physical chemistry letters, 1,(2010), 997-1002

[12] M.B. Starr, X. Wang, Coupling of piezoelectric effect with electrochemical processes, Nano Energy, 14,(2015), 296-311

[13] A. Wei, X. Xie, Z. Wen, H. Zheng, H. Lan, H. Shao, X. Sun, J. Zhong, S.-T. Lee, Triboelectric nanogenerator driven self-powered photoelectrochemical water splitting based on hematite photoanodes, ACS nano, 12,(2018), 8625-8632

[14] T. Li, Y. Xu, F. Xing, X. Cao, J. Bian, N. Wang, Z.L. Wang, Boosting photoelectrochemical water splitting by TENG-charged Li-ion battery, Advanced Energy Materials, 7,(2017), 1700124

[15] A. Bhatt, V. Singh, P. Bamola, D. Aswal, S. Rawat, S. Rana, C. Dwivedi, B. Singh, H. Sharma, Enhanced Piezoelectric Response Using TiO2/MoS2 Heterostructure Nanofillers in PVDF Based Nanogenerators, Journal of Alloys and Compounds,(2023), 170664

[16] J. Briscoe, S. Dunn, Piezoelectric nanogenerators–a review of nanostructured piezoelectric energy harvesters, Nano Energy, 14,(2015), 15-29

[17] V. Singh, B. Singh, PDMS/PVDF-MoS2 based flexible triboelectric nanogenerator for mechanical energy harvesting, Polymer, 274,(2023), 125910

[18] S. Rana, V. Singh, B. Singh, Tailoring the Output Performance of PVDF-Based Piezo–Tribo Hybridized Nanogenerators via B, N-Codoped Reduced Graphene Oxide, ACS Applied Electronic Materials, 4,(2022), 5893-5904

[19] S.S. Nardekar, K. Krishnamoorthy, P. Pazhamalai, S. Sahoo, S.J. Kim, MoS2 quantum sheets-PVDF nanocomposite film based self-poled piezoelectric nanogenerators and photovoltaically self-charging power cell, Nano Energy, 93,(2022), 106869

[20] V. Singh, B. Singh, Fabrication of PVDF-transition metal dichalcogenides based flexible piezoelectric Nanogenerator for energy harvesting applications, Materials Today: Proceedings, 28,(2020), 282-285

[21] H.H. Singh, S. Singh, N. Khare, Enhanced β-phase in PVDF polymer nanocomposite and its application for nanogenerator, Polymers for Advanced Technologies, 29,(2018), 143-150

[22] V. Singh, B. Singh, MoS2-PVDF/PDMS Based Flexible Hybrid Piezo-Triboelectric Nanogenerator for Harvesting Mechanical Energy, Journal of Alloys and Compounds,(2023), 168850

[23] L. Shi, H. Jin, S. Dong, S. Huang, H. Kuang, H. Xu, J. Chen, W. Xuan, S. Zhang, S. Li, X. Wang, J. Luo, High-performance triboelectric nanogenerator based on electrospun PVDF-graphene nanosheet composite nanofibers for energy harvesting, Nano Energy, 80,(2021), 105599

[24] M. Satthiyaraju, T. Ramesh, Effect of annealing treatment on PVDF nanofibers for mechanical energy harvesting applications, Materials Research Express, 6,(2019), 105366

[25] H. Pan, B. Na, R. Lv, C. Li, J. Zhu, Z. Yu, Polar phase formation in poly (vinylidene fluoride) induced by melt annealing, Journal of Polymer Science Part B: Polymer Physics, 50,(2012), 1433-1437

[26] X. Pu, J.-W. Zha, C.-L. Zhao, S.-B. Gong, J.-F. Gao, R.K.Y. Li, Flexible PVDF/nylon-11 electrospun fibrous membranes with aligned ZnO nanowires as potential triboelectric nanogenerators, Chemical Engineering Journal, 398,(2020), 125526

[27] W. Yang, S. Yu, R. Sun, R. Du, Nano-and microsize effect of CCTO fillers on the dielectric behavior of CCTO/PVDF composites, Acta Materialia, 59,(2011), 5593-5602

[28] V. Singh, D. Meena, H. Sharma, A. Trivedi, B. Singh, Investigating the role of chalcogen atom in the piezoelectric performance of PVDF/TMDCs based flexible nanogenerator, Energy, 239,(2022), 122125

[29] S. Rana, V. Singh, B. Singh, Recent trends in 2D materials and their polymer composites for effectively harnessing mechanical energy, Iscience,(2022), 103748

[30] L. Lu, W. Ding, J. Liu, B. Yang, Flexible PVDF based piezoelectric nanogenerators, Nano Energy, 78,(2020), 105251

[31] K.-A.N. Duerloo, M.T. Ong, E.J. Reed, Intrinsic piezoelectricity in two-dimensional materials, The Journal of Physical Chemistry Letters, 3,(2012), 2871-2876

[32] M.N. Blonsky, H.L. Zhuang, A.K. Singh, R.G. Hennig, Ab initio prediction of piezoelectricity in two-dimensional materials, ACS nano, 9,(2015), 9885-9891

[33] L. Shi, H. Jin, S. Dong, S. Huang, H. Kuang, H. Xu, J. Chen, W. Xuan, S. Zhang, S. Li, High-performance triboelectric nanogenerator based on electrospun PVDF-graphene nanosheet composite nanofibers for energy harvesting, Nano Energy, 80,(2021), 105599

[34] S. Tu, Q. Jiang, X. Zhang, H.N. Alshareef, Large dielectric constant enhancement in MXene percolative polymer composites, ACS nano, 12,(2018), 3369-3377

[35] P. Cui, K. Parida, M.F. Lin, J. Xiong, G. Cai, P.S. Lee, Transparent, flexible cellulose nanofibril–phosphorene hybrid paper as triboelectric nanogenerator, Advanced Materials Interfaces, 4,(2017), 1700651

[36] C. Wu, T.W. Kim, J.H. Park, H. An, J. Shao, X. Chen, Z.L. Wang, Enhanced triboelectric nanogenerators based on MoS2 monolayer nanocomposites acting as electron-acceptor layers, ACS nano, 11,(2017), 8356-8363

[37] E.S. Cozza, O. Monticelli, E. Marsano, P. Cebe, On the electrospinning of PVDF: influence of the experimental conditions on the nanofiber properties, Polymer International, 62,(2013), 41-48

[38] S. Agarwal, J.H. Wendorff, A. Greiner, Use of electrospinning technique for biomedical applications, Polymer, 49,(2008), 5603-5621

[39] W.-E. Teo, S. Ramakrishna, Electrospun nanofibers as a platform for multifunctional, hierarchically organized nanocomposite, Composites Science and Technology, 69,(2009), 1804-1817

[40] S. Ramakrishna, K. Fujihara, W.-E. Teo, T. Yong, Z. Ma, R. Ramaseshan, Electrospun nanofibers: solving global issues, Materials Today, 9,(2006), 40-50

[41] V. Beachley, X. Wen, Effect of electrospinning parameters on the nanofiber diameter and length, Materials Science and Engineering: C, 29,(2009), 663-668

[42] C.J. Thompson, G.G. Chase, A.L. Yarin, D.H. Reneker, Effects of parameters on nanofiber diameter determined from electrospinning model, Polymer, 48,(2007), 6913-6922

[43] S.H. Tan, R. Inai, M. Kotaki, S. Ramakrishna, Systematic parameter study for ultra-fine fiber fabrication via electrospinning process, Polymer, 46,(2005), 6128-6134

[44] G. Kalimuldina, N. Turdakyn, I. Abay, A. Medeubayev, A. Nurpeissova, D. Adair, Z. Bakenov, Sensors2020.

[45] Y. Xin, J. Zhu, H. Sun, Y. Xu, T. Liu, C. Qian, A brief review on piezoelectric PVDF nanofibers prepared by electrospinning, Ferroelectrics, 526,(2018), 140-151

[46] H.H. Singh, S. Singh, N. Khare, Design of flexible PVDF/NaNbO3/RGO nanogenerator and understanding the role of nanofillers in the output voltage signal, Composites Science and Technology, 149,(2017), 127-133

[47] B. Jaleh, A. Jabbari, Evaluation of reduced graphene oxide/ZnO effect on properties of PVDF nanocomposite films, Applied Surface Science, 320,(2014), 339-347

[48] S. Sarkar, S. Garain, D. Mandal, K.K. Chattopadhyay, Electro-active phase formation in PVDF–BiVO 4 flexible nanocomposite films for high energy density storage application, RSC Advances, 4,(2014), 48220-48227

[49] Z. Wang, H.Y. Yue, Z.M. Yu, F. Yao, X. Gao, E.H. Guan, H.J. Zhang, W.Q. Wang, S.S. Song, One-pot hydrothermal synthesis of MoSe 2 nanosheets spheres-reduced graphene oxide composites and application for high-performance supercapacitor, Journal of Materials Science: Materials in Electronics, 30,(2019), 8537-8545

[50] Y. Peng, Z. Meng, C. Zhong, J. Lu, W. Yu, Y. Jia, Y. Qian, Hydrothermal synthesis and characterization of single-molecular-layer MoS2 and MoSe2, Chemistry Letters, 30,(2001), 772-773

[51] P.I. Devi, K. Ramachandran, Dielectric studies on hybridised PVDF–ZnO nanocomposites, Journal of Experimental Nanoscience, 6,(2011), 281-293

[52] P. Martins, A.C. Lopes, S. Lanceros-Mendez, Electroactive phases of poly (vinylidene fluoride): Determination, processing and applications, Progress in polymer science, 39,(2014), 683-706

[53] N. Soin, D. Boyer, K. Prashanthi, S. Sharma, A.A. Narasimulu, J. Luo, T.H. Shah, E. Siores, T. Thundat, Exclusive self-aligned β-phase PVDF films with abnormal piezoelectric coefficient prepared via phase inversion, Chemical Communications, 51,(2015), 8257-8260

[54] J.S. Lee, K.-Y. Shin, O.J. Cheong, J.H. Kim, J. Jang, Highly sensitive and multifunctional tactile sensor using free-standing ZnO/PVDF thin film with graphene electrodes for pressure and temperature monitoring, Sci Rep, 5,(2015), 7887

[55] P. Thakur, A. Kool, B. Bagchi, S. Das, P. Nandy, Effect of in situ synthesized Fe 2 O 3 and Co 3 O 4 nanoparticles on electroactive β phase crystallization and dielectric properties of poly (vinylidene fluoride) thin films, Physical Chemistry Chemical Physics, 17,(2015), 1368-1378

[56] P. Biswas, N.A. Hoque, P. Thakur, M.M. Saikh, S. Roy, F. Khatun, B. Bagchi, S. Das, Highly efficient and durable piezoelectric nanogenerator and photo-power cell based on CTAB modified montmorillonite incorporated PVDF film, ACS Sustainable Chemistry & Engineering, 7,(2019), 4801-4813

[57] S.M.S. Rana, M.T. Rahman, M. Salauddin, S. Sharma, P. Maharjan, T. Bhatta, H. Cho, C. Park, J.Y. Park, Electrospun PVDF-TrFE/MXene nanofiber mat-based triboelectric nanogenerator for smart home appliances, ACS applied materials & interfaces, 13,(2021), 4955-4967

[58] Y. Dong, S.S.K. Mallineni, K. Maleski, H. Behlow, V.N. Mochalin, A.M. Rao, Y. Gogotsi, R. Podila, Metallic MXenes: a new family of materials for flexible triboelectric nanogenerators, Nano Energy, 44,(2018), 103-110

[59] T. Bhatta, P. Maharjan, H. Cho, C. Park, S.H. Yoon, S. Sharma, M. Salauddin, M.T. Rahman, S.M.S. Rana, J.Y. Park, High-performance triboelectric nanogenerator based on MXene functionalized polyvinylidene fluoride composite nanofibers, Nano Energy, 81,(2021), 105670

[60] V. Harnchana, H.V. Ngoc, W. He, A. Rasheed, H. Park, V. Amornkitbamrung, D.J. Kang, Enhanced power output of a triboelectric nanogenerator using poly (dimethylsiloxane) modified with graphene oxide and sodium dodecyl sulfate, ACS applied materials & interfaces, 10,(2018), 25263-25272

[61] S. Niu, S. Wang, L. Lin, Y. Liu, Y.S. Zhou, Y. Hu, Z.L. Wang, Theoretical study of contact-mode triboelectric nanogenerators as an effective power source, Energy & Environmental Science, 6,(2013), 3576-3583

[62] K. Maity, B. Mahanty, T.K. Sinha, S. Garain, A. Biswas, S.K. Ghosh, S. Manna, S.K. Ray, D. Mandal, Two-Dimensional piezoelectric MoS2-modulated nanogenerator and nanosensor made of poly (vinlydine Fluoride) nanofiber webs for self-powered electronics and robotics, Energy Technology, 5,(2017), 234-243

[63] D. Bhattacharya, S. Bayan, R.K. Mitra, S.K. Ray, 2D WS 2 embedded PVDF nanocomposites for photosensitive piezoelectric nanogenerators with a colossal energy conversion efficiency of~ 25.6%, Nanoscale, 13,(2021), 15819-15829

[64] W. Qin, P. Zhou, X. Xu, M.S. Irshad, Y. Qi, T. Zhang, Enhanced output performance of piezoelectric energy harvester based on hierarchical Bi3. 15Nd0. 85Ti3O12 microspheres/PVDF-HFP composite, Sensors and Actuators A: Physical, 333,(2022), 113307

[65] K. Shi, B. Chai, H. Zou, P. Shen, B. Sun, P. Jiang, Z. Shi, X. Huang, Interface induced performance enhancement in flexible BaTiO3/PVDF-TrFE based piezoelectric nanogenerators, Nano Energy, 80,(2021), 105515

[66] M.O. Shaikh, Y.-B. Huang, C.-C. Wang, C.-H. Chuang, Micromachines2019.

[67] D. Wang, Y. Lin, D. Hu, P. Jiang, X. Huang, Multifunctional 3D-MXene/PDMS nanocomposites for electrical, thermal and triboelectric applications, Composites Part A: Applied Science and Manufacturing, 130,(2020), 105754

[68] R. Wen, J. Guo, A. Yu, K. Zhang, J. Kou, Y. Zhu, Y. Zhang, B.-W. Li, J. Zhai, Remarkably enhanced triboelectric nanogenerator based on flexible and transparent monolayer titania nanocomposite, Nano Energy, 50,(2018), 140-147

[69] H.H. Singh, N. Khare, Improved performance of ferroelectric nanocomposite flexible film based triboelectric nanogenerator by controlling surface morphology, polarizability, and hydrophobicity, Energy, 178,(2019), 765-771

[70] M.-F. Lin, K.-W. Chang, C.-H. Lee, X.-X. Wu, Y.-C. Huang, Electrospun P3HT/PVDF-HFP semiconductive nanofibers for triboelectric nanogenerators, Sci Rep, 12,(2022), 14842

[71] Y. Song, J. Bao, Y. Hu, H. Cai, C. Xiong, Q. Yang, H. Tian, Z. Shi, Forward polarization enhanced all-polymer based sustainable triboelectric nanogenerator from oriented electrospinning PVDF/cellulose nanofibers for energy harvesting, Sustainable Energy & Fuels, 6,(2022), 2377-2386

CHAPTER 6

Effect of variation of triboelectric layer material on output performance of the PVDF-$MoSe_2$ based flexible triboelectric nanogenerator.

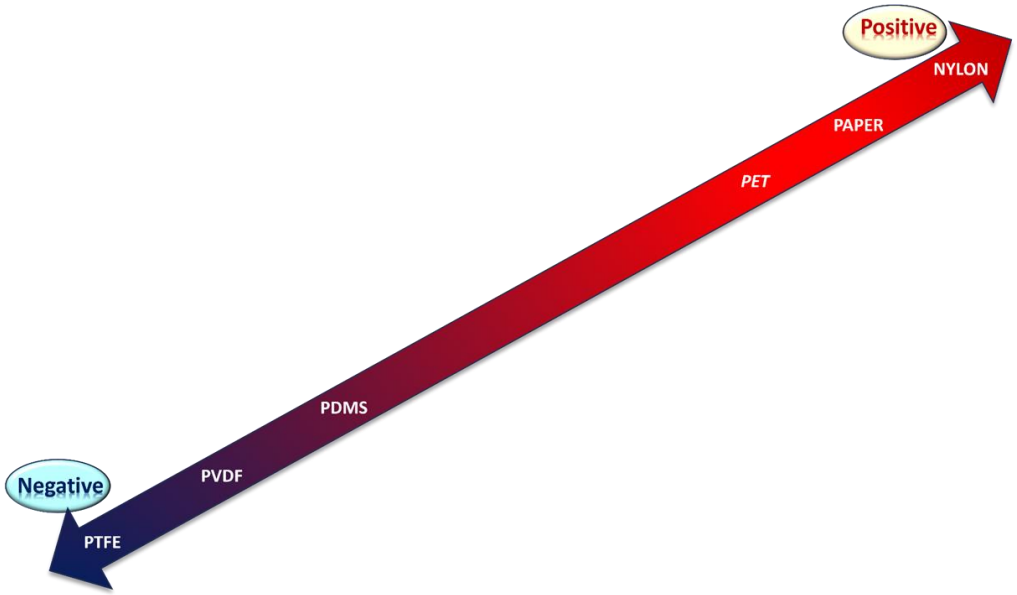

In the present chapter, the effect of triboelectric layer material on the output performance of the TENG device will be investigated. For this, PVDF-$MoSe_2$ nanofiber film has been fixed as one of the triboelectric layers, whereas the second layer material has been varied including PTFE, PDMS, PET, Paper and Nylon. The TENG consisting of Nylon as second triboelectric material demonstrates the maximum power density of ~231 μWcm^{-2}. The effect of tapping frequency and force on the triboelectric output of PVDF-$MoSe_2$/Nylon was also studied and an increasing trend of output voltage and current is observed with increasing force and frequency thereby producing a maximum voltage of ~206 V. The increase in output performance of the TENG with increase in frequency is attributed to faster charge transfers process, when the contact frequency is higher. With the rise in contact force, the effective area and capacitance of the TENG also increases which further results in the enhancement of triboelectric output of the nanogenerator. This study proposes an effective approach for enhancing the performance of triboelectric nanogenerator just by selecting the suitable material.

6.1 Introduction

Triboelectrification has long been studied as a phenomenon characterised by the creation of static electricity when different materials come into contact [1, 2]. While several static electricity harnessing devices have been created, triboelectrification is widely seen as an unwanted occurrence in our daily lives, industrial operations, and transportation networks. As a result, there has been little scholarly attention on investigating the possible good uses of triboelectrification. A dramatic shift in this approach has happened since 2012, with the advent of triboelectric nanogenerators (TENGs), which are based on principle of triboelectrification. These TENGs have garnered significant scientific interest as a cutting-edge technology with diverse applications, including mechanical energy harvesting, self-powered sensing, high-voltage generation, and the field of tribotronics [3-7].

The fundamental operating basis of a Triboelectric Nanogenerator (TENG) is the use of a pair of triboelectric materials with differing charge affinities [8]. In theory, a significant difference in the charge affinities of the two materials is beneficial to improve charge generation or obtain improved TENG output [1]. Practical reasons, on the other hand, frequently lead to the selection of materials that do not necessarily demonstrate the biggest discrepancy in charge affinity. This variation from theoretical expectations occurs because the phenomena of triboelectrification is dependent not only on the chemical compositions of the materials but also on a variety of physical properties such as elasticity, frictional properties, and surface topographical structure [9]. Furthermore, the selection of triboelectric materials is dependent on the individual application requirements. Different applications demand different material qualities in addition to excellent triboelectric capabilities. As a result, it would be unjust to directly compare the merits and drawbacks of various triboelectric materials without considering their intended applications [10-13].

Researchers often examine the triboelectric effects of materials by measuring the surface charge density after a triboelectrification process with a reference material [14]. Contact and separation or sliding between materials can occur during this process [15, 16]. It's worth noting that different triboelectrification procedures can result in varied surface charge densities for the same material. They have distinct affinities for positive and negative charges due to the underlying chemical compositions of materials, assuming perfectly flat atomic surfaces [11]. To comprehensively categorise these charge densities and affinities, researchers developed a triboelectric series of materials based on the resultant charge densities after

triboelectrification operations [1, 14]. Triboelectrification is the process by which electrons are transferred between two materials when they come into physical contact [13]. The difference in electron affinities between the two materials involved in the triboelectrification process determines the direction of this electron transfer [17]. Specifically, the material possessing a higher electron affinity tends to attract electrons from the other, earning it the designation of an electron acceptor. Conversely, the material losing electrons assumes the role of an electron donor in this interaction [18]. Typically, the identity of the donor and acceptor materials can be determined by their respective positions within the triboelectric series [17-19].

In our study, we have investigated the electrification properties PVDF-$MoSe_2$ nanofibers by combining it with different polymers, such as, Polytetrafluoroethylene (PTFE), Polydimethylsiloxane (PDMS), Polyethylene terephthalate (PET), Paper and Nylon to fabricate a high performance Triboelectric Nanogenerators (TENG). The synthesis of PVDF-$MoSe_2$ nanofibers was carried out through the electrospinning technique. Furthermore, we used the vertical contact-separation mode of TENG device, where one layer of PVDF-$MoSe_2$ nanofibers was fixed, while the other layer was varied with different materials included PTFE, PDMS, PET, Paper and Nylon nanofibers. Notably, our results show that the triboelectric nanogenerator device containing PVDF-$MoSe_2$ with Nylon as second triboelectric layer achieves the maximum triboelectric output, with a 144.2 V output voltage and a 32.7 μA short-circuit current. The TENG nanogenerator with Nylon as second layer produced a maximum power density of 231.1 $\mu W/cm^2$, demonstrating a significant ~4.5 fold improvement over the PTFE based TENG, which produced a power density of 51.9 $\mu W/cm^2$. We also investigated the effect of different tapping forces and frequencies on the performance of the PVDF-$MoSe_2$/Nylon based triboelectric nanogenerator. Significantly, this nanogenerator achieved a peak output voltage of 206 V at a tapping frequency of 10 Hz. Furthermore, we harnessed the output voltage from the TENG to drive LEDs to show its practical application. This novel technology uses ambient mechanical energy as the only source of energy for driving LEDs, paving the way for future sustainable energy alternatives.

6.2 Experimental Section

6.2.1 Synthesis of PVDF-$MoSe_2$ Nanofibers, Nylon Nanofibers and PDMS Films

The synthesis of $MoSe_2$ nanosheets followed a straightforward hydrothermal process, as detailed in chapter 3 [20]. In the preparation of the electrospinning solution, 1 gram of PVDF powder was immersed in N, N-Dimethylformamide (DMF) and continuously stirred at 60°C for one hour. Subsequently, $MoSe_2$ sheets were introduced into the aforementioned solution to

achieve PVDF-$MoSe_2$ composite solution. This mixture was further stirred for an additional two hours to ensure homogeneity. Following this, the resultant solution was put into a 10 mL syringe for electrospinning process. Electrospinning was carried out using an electrospinning machine, applying a high voltage of 12 kV and a flow rate of 1 mL per hour. The resulting fibers were collected onto aluminium foil, which was positioned on a rotating drum collector at a distance of 12 cm from the needle. After roughly 5 hours of continuous collection, PVDF-$MoSe_2$ composite nanofibers based thin film with an approximate thickness of 50 μm were synthesised. These films were then oven dried for 12 hours at 60°C in order to ensure complete solvent elimination.

To synthesize Nylon nanofibers, we initially prepared a solution containing 20 weight percent (wt%) of Nylon dissolved in formic acid. The homogeneity of the solution was achieved by supplying it to three hours of continuous stirring at 70°C using a magnetic stirrer. Subsequently, the prepared solution was loaded into a 5 mL syringe, and the electrospinning process was carried out at a flow rate of 1 mL per hour, utilizing a voltage of 20 kV. The Nylon fibres were deposited onto aluminium foil during the electrospinning process, using the identical drum collector arrangement as previously reported.

A PDMS thin film was synthesized by blending the base resin and curing agent (Sylgard 184, Dow Corning Co.) in a weight ratio of 10:1. To ensure the removal of air bubbles, the resulting solution underwent a vacuum-assisted degassing process. Following that, the solution was spin-coated onto a glass substrate and oven-dried to remove any leftover moisture.

PET (SKNMT, India) and PTFE (Sigma Aldrich) were directly used as commercially available.

6.2.2 Fabrication of TENG

To investigate the influence of different materials as second triboelectric layer on the triboelectric performance of PVDF-$MoSe_2$ nanofiber based TENG, we have fabricated a TENG in vertical contact-separation mode. We utilized PVDF-$MoSe_2$ nanofiber based film as one triboelectric layer for all TENGs and used different materials (PTFE, PDMS, PET, Paper and Nylon) serving as the second triboelectric layer. Each of these layers consisted of an aluminium electrode, and the electrical connections were made using copper wires. To assemble the TENG, both films, measuring 2 cm x 2 cm, were securely affixed to acrylic sheets using double-sided tape.

6.2.3 Characterizations and Energy Harvesting Performance

To assess the crystallinity of the PVDF-$MoSe_2$ nanofiber, X-ray diffraction analyses were conducted using a Cu K_α X-ray source (Bruker D8-Advance) with a wavelength of 1.54 Å. Fourier transform infrared spectroscopy (FTIR) was employed to examine the PVDF-$MoSe_2$ nanofiber films, utilizing a PerkinElmer Spectrum-II instrument. To investigate the morphology of the synthesized nanofibers, field-emission scanning electron microscopy (FESEM) was employed, utilizing a Zeiss Gemini SEM 500 microscope at an accelerating voltage of 15 kV. For the evaluation of the triboelectric performance of the devices, a dynamic shaker (Micron MEV-0025) was employed. The shaker facilitated continuous contact-separation motions between the triboelectric layers, with the ability to adjust operational parameters, including tapping frequency and contact force. The open circuit voltages of the Triboelectric Nanogenerators (TENGs) were measured using an oscilloscope (Tektronix MDO34). Additionally, short circuit current and charge measurements were conducted using an electrometer (Keysight B2985B). In typical contact-separation mode measurements, the triboelectric output involved the controlled movement of the one triboelectric layer of TENG (PVDF-$MoSe_2$) to establish contact with the second layer of the TENG (PTFE, PDMS, PET, Paper and Nylon).

6.3 Results and Discussion

6.3.1 Structural and Morphological Analysis of PVDF-$MoSe_2$ Nanofibers

X-ray diffraction (XRD) and Fourier-transform infrared spectroscopy (FTIR) were employed to confirm the distinct phases of the fluoropolymer PVDF, distinguishing between the electroactive β-phase and the non-electroactive α-phase. In Figure 6.1(a), we present the XRD spectra of thin film composed of nanofibers of PVDF-$MoSe_2$. Notably, the $MoSe_2$ peaks are denoted by "#" in the XRD spectra of the synthesized nanofiber-based films, while the PVDF peaks are labelled as "α" and “β” correspondingly. The non-polar α-phase in PVDF is represented by the diffraction peak observed at 18.3°, whereas the electroactive β-phase is indicated by the peak at 20.2° [20-25]. As a result, the XRD spectra confirms the successful incorporation of $MoSe_2$ into PVDF nanofibers. Concurrently, FTIR spectral analysis was conducted to elucidate the presence of the polar crystalline phase within the PVDF-$MoSe_2$ nanofiber based thin film. As illustrated in Figure 6.1(b), characteristic vibrational bands at 840 cm^{-1}, 1276 cm^{-1}, and 1402 cm^{-1} confirm the presence of the β-phase, while vibrational bands at 614 cm^{-1}, 762 cm^{-1}, and 796 cm^{-1} are indicative of the α-phase [22, 23, 26-28]. Specifically, in line with the Lambert-Beer law, we quantified the absorption vibrational bands

at 762 cm^{-1} and 840 cm^{-1} to calculate the percentage of β-phase in PVDF-$MoSe_2$ based nanofibers [27, 29]. The results show that the percentage composition of β-phase in the PVDF-$MoSe_2$ nanofiber film is ~86%. The better β-phase composition not only influences the piezoelectric properties but also significantly impacts the triboelectric output capabilities of PVDF [30].

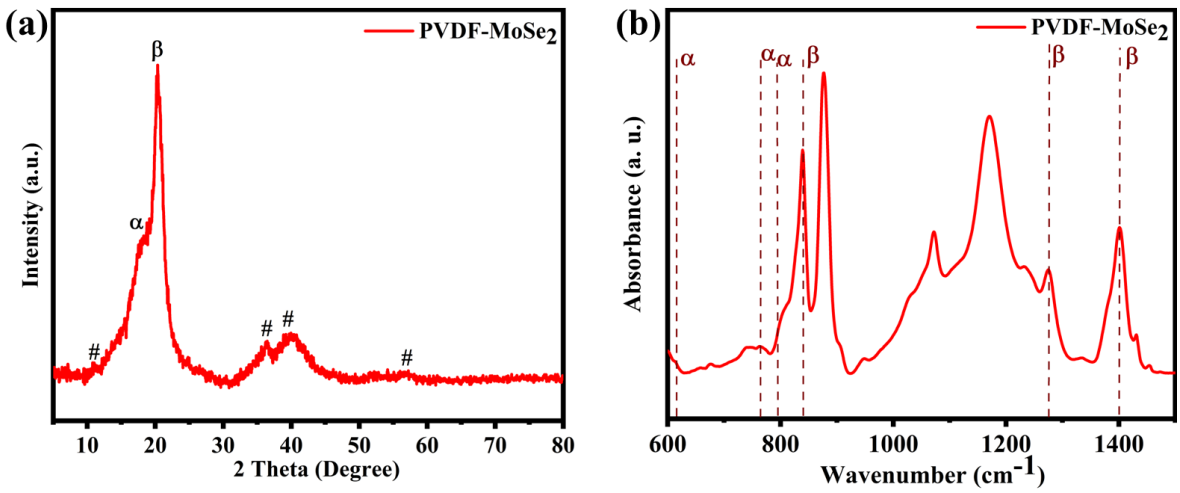

Figure 6.1 Structural characterization of PVDF-$MoSe_2$ composite nanofiber films (a) XRD spectra (b) FTIR spectra.

Furthermore, we have also studied the surface morphology of the fabricated PVDF-$MoSe_2$ nanofiber film. The film exhibited fibrous networks with minimal bead formation and absence of nanosheet aggregation, as depicted in Figure 6.2(a). Additionally, we provide a morphological image of Nylon fibers in Figure 6.2(b), where a well-organized, bead-free fibrous network was observed for Nylon.

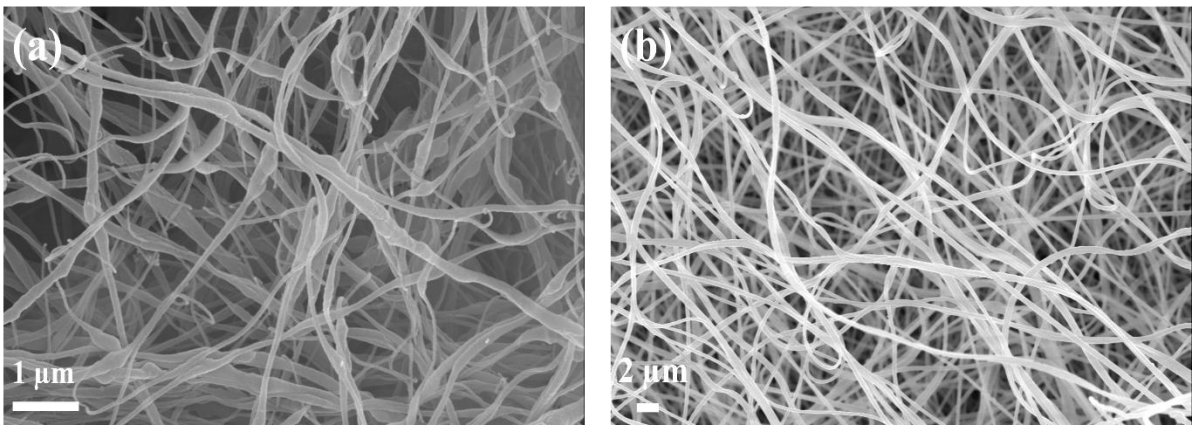

Figure 6.2 FESEM images showing the morphology of (a) PVDF-$MoSe_2$ and (b) Nylon nanofibers.

6.3.2 Output Performance Analysis of Fabricated TENGs

To investigate the impact of various materials on the triboelectric performance of PVDF-$MoSe_2$ nanofiber film based nanogenerators, we designed a hybrid triboelectric nanogenerator operating in the vertical contact-separation mode. In this configuration, PVDF-$MoSe_2$ nanofiber-based film was fixed as one of the triboelectric layers for all the TENGs, chosen for its exceptional piezoelectric output, while the second triboelectric layer was varied for all the TENGs and is made of PTFE, PDMS, PET, Paper and Nylon, respectively. Following the fabrication of these TENGs, we conducted electrical measurements to compare the triboelectric properties of PVDF-$MoSe_2$ nanofiber films based TENG as a function of varying second layer of TENG. To facilitate controlled and continuous mechanical stress in the contact-separation mode, we employed an electrodynamic shaker, subjecting all TENGs to the required operating conditions for comprehensive performance evaluation. The operational mechanism of the PVDF-$MoSe_2$/Nylon nanofiber-based Triboelectric Nanogenerator (TENG) has already been discussed in chapter 5.

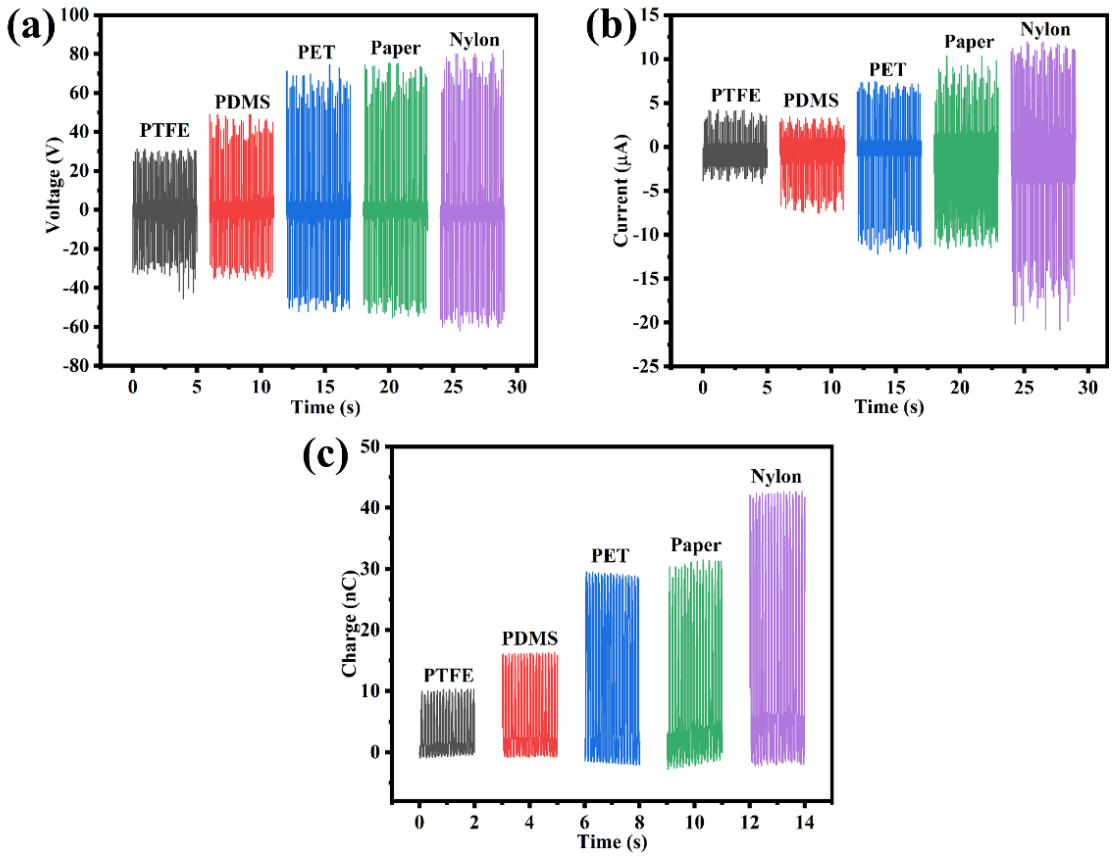

Figure 6.3 Triboelectric output performance of PVDF-$MoSe_2$ based TENGs (a) open circuit voltage, (b) short circuit current, (c) charge transfer for varying second layer.

The resulting triboelectric output voltage and current of PVDF-$MoSe_2$ nanofiber film based TENGs are shown in Figure 6.3(a) and (b), respectively, allowing for a comparative analysis of their energy harvesting efficiencies. In this comparison, it was observed that the TENG with PVDF-$MoSe_2$/Nylon has generated maximum peak-to-peak open-circuit output voltage of 144.2 V. In contrast, the other TENGs with PVDF-$MoSe_2$ composite nanofiber exhibited output voltages, with values of 76.8 V, 87.2 V, 126.0 V and 134.0 V for PTFE, PDMS, PET and Paper, respectively as second triboelectric layers. The TENG with PTFE as second tribo layer shows the minimum output voltage. This trend indicates that the triboelectric performance of a TENG is significantly affected by the choice of the contacting materials. Similarly, under identical conditions, the short-circuit current characteristics of the TENGs with different tribo layers are depicted in Figure 6.3(b). The PVDF-$MoSe_2$/Nylon based TENG yielded maximum short-circuit current of 32.7 µA. In contrast, the other PVDF-$MoSe_2$ based nanogenerators, with PTFE, PDMS, PET and Paper as second tribo layers, generated short-circuit currents of 8.5 µA, 10.8 µA, 19.7 µA, and 21.9 µA, respectively. These short-circuit current values followed a similar trend as the voltage output, highlighting that the PVDF-$MoSe_2$ and Nylon are the most suitable combination for a TENG as compared to other fabricated TENGs. Furthermore, as depicted in Figure 6.3(c), the transmitted surface charge of the PVDF-MoSe/Nylon Triboelectric Nanogenerator (TENG) is 42.6 nC which is again maximum when compared with other TENGs, having the value of surface charge densities are 10.2 nC, 16.1 nC, 29.2 nC, and 31.3 nC for PTFE, PDMS, PET and Paper, respectively.

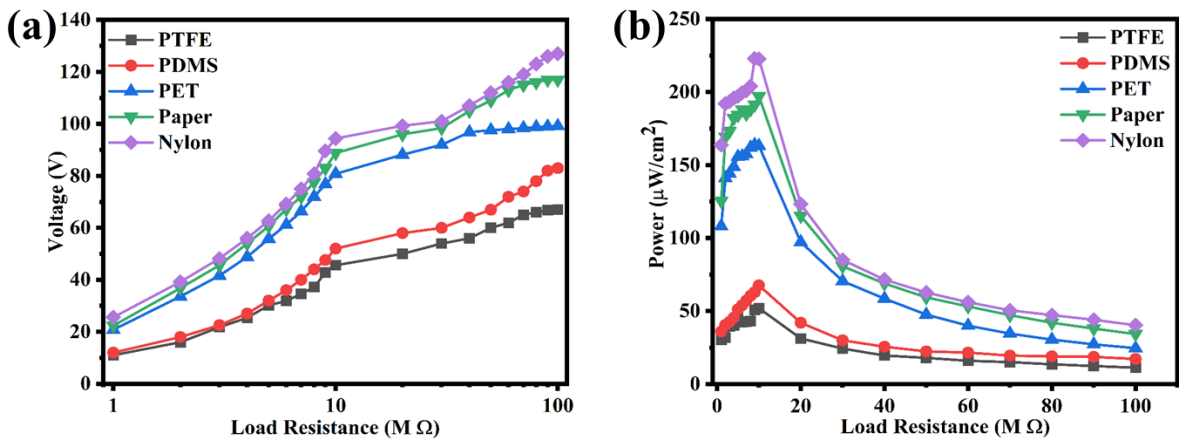

Figure 6.4 Effect of load resistance on (a) output voltage, (b) power per unit area for PVDF-$MoSe_2$ based TENGs at a tapping frequency of 9 Hz as a function of varying the tribo layer.

Additionally, the impact of load resistance on the generated voltage and power density of all TENGs was investigated and is presented in Figure 6.4(a) and (b). It is noteworthy that

the triboelectric voltage for all TENGs initially increased with higher load resistance values before reaching a saturation point. All TENGs also shows similar trend for power density and at a load resistance of 10 MΩ all TENGs generated the maximum power density. Across all load resistances, the PVDF-$MoSe_2$/Nylon Triboelectric Nanogenerator (TENG) consistently exhibited superior performance in terms of both output voltage and power density when compared to the all other fabricated TENGs. Specifically, the PVDF-$MoSe_2$/Nylon TENG achieved a maximum power density of 231.1 μW/cm^2, whereas the PVDF-$MoSe_2$/PTFE, PVDF-$MoSe_2$/PDMS, PVDF-$MoSe_2$/PET and PVDF-$MoSe_2$/Paper TENG generated power density of 51.9 μW/cm^2, 67.6 μW/cm^2, 163.2 μW/cm^2 and 197.6 μW/cm^2 at load resistance of 10 MΩ.

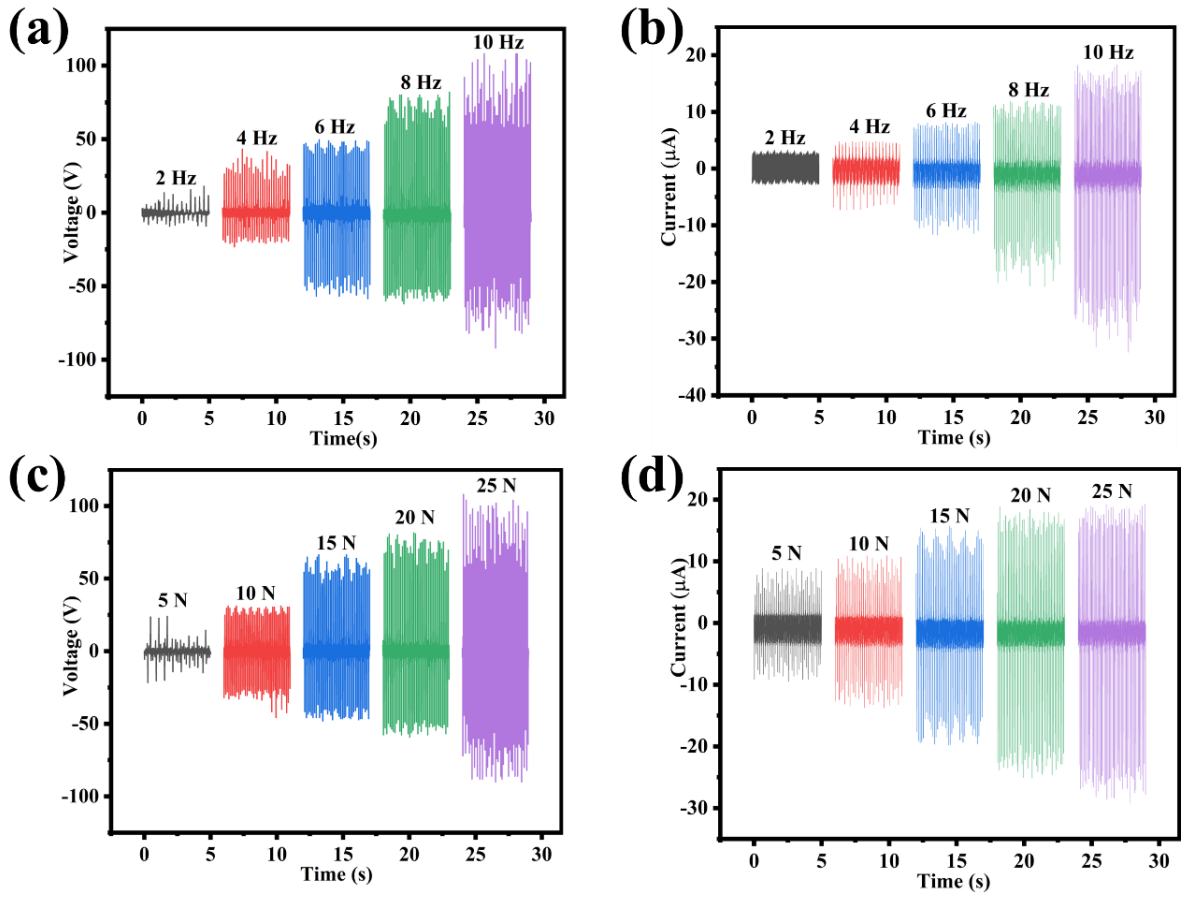

Figure 6.5 Effect of tapping frequency on (a) open circuit voltage, (b) short circuit current and contact force on (c) open circuit voltage, (d) short circuit current on triboelectric performance of PVDF-$MoSe_2$ /Nylon based TENG.

The investigation of the triboelectric performance of the PVDF-$MoSe_2$/Nylon TENG under various operational conditions is crucial due to its potential as an attractive power source for electronic devices. Therefore, we conducted an examination of the output performance of

TENG in response to varying contact force and tapping frequency. To investigate the effect of tapping frequency on the triboelectric performance of the TENG, we used an electrodynamic shaker to tap the nanogenerator with varying frequencies. The results, depicted in Figure 6.5(a), indicate that the generated output voltage increases with frequency, reaching approximately 206 V at a frequency of 10 Hz. Figure 6.5(b) illustrates a similar pattern for the generated short-circuit current, which increases with higher tapping frequencies. This phenomenon can be attributed to the enhanced charge transfer occurring at higher contact frequencies, leading to an increase in the short-circuit current of the PVDF-$MoSe_2$/Nylon TENG [30, 31]. Furthermore, Figure 6.5(c) and (d) showcase the influence of impact force on the triboelectric performance of TENG. The TENG was operated under various impact forces ranging from 5 N to 25 N, with a fixed operating frequency of 8 Hz. As illustrated in Figure 6.5(c), the output voltage gradually rises from 45.2 V to 140.8 V as the contact force increases from 5 N to 20 N, eventually reaching an output voltage of 198.0 V at an impact force of 25 N. Similarly, the associated short-circuit current of the TENG exhibits a parallel trend, increasing from 18.4 µA to 48.44 µA as the contact force is raised from 5 N to 25 N. This observation underscores the significant role of impact force in triboelectric output generation. The elastic properties of polymeric triboelectric materials are important in this phenomenon because they increase the effective contact area of the TENG, leading in the creation of additional triboelectric charges for increased power generation. The elastic deformation of the PVDF-$MoSe_2$ and Nylon nanofiber film rises with increasing contact force, resulting in a greater TENG capacitance [30, 31]. This is advantageous for storing triboelectric charges and achieving greater triboelectric output.

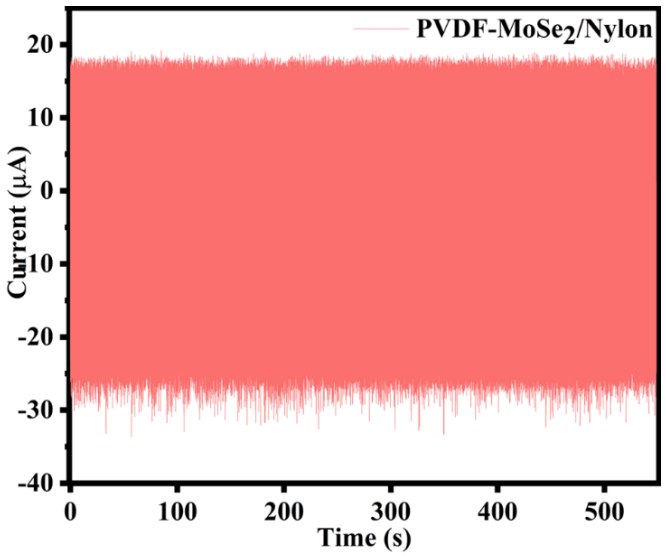

Figure 6.6 Graph showing the stability of PVDF-$MoSe_2$/Nylon based TENG.

In addition, we measured the output current for 5000 cycles to determine the stability and endurance of the manufactured TENG device. As shown in the Figure 6.6, no evidence of degradation was found throughout this measurement.

6.3.3 Surface Potential Analysis using COMSOL Simulations

Moreover, we employed a finite element model in COMSOL software to simulate the surface potential distribution between the layers of the Triboelectric Nanogenerator with PVDF-$MoSe_2$ as one layer fixed.

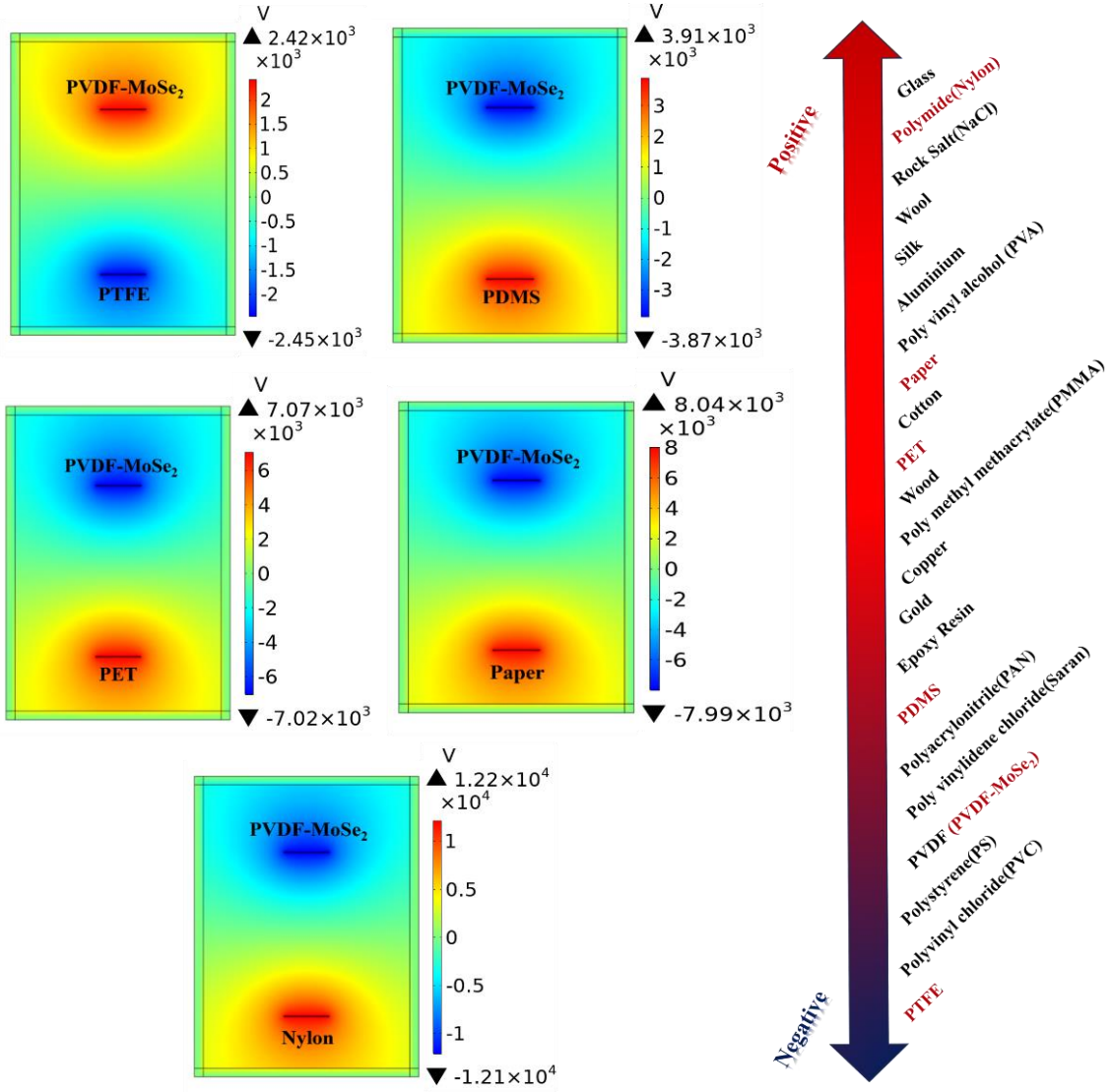

Figure 6.7 COMSOL simulated distribution of surface potential for PVDF-$MoSe_2$ in comparison to PTFE, PDMS, PET, Paper, and Nylon with the theoretical triboelectric series.

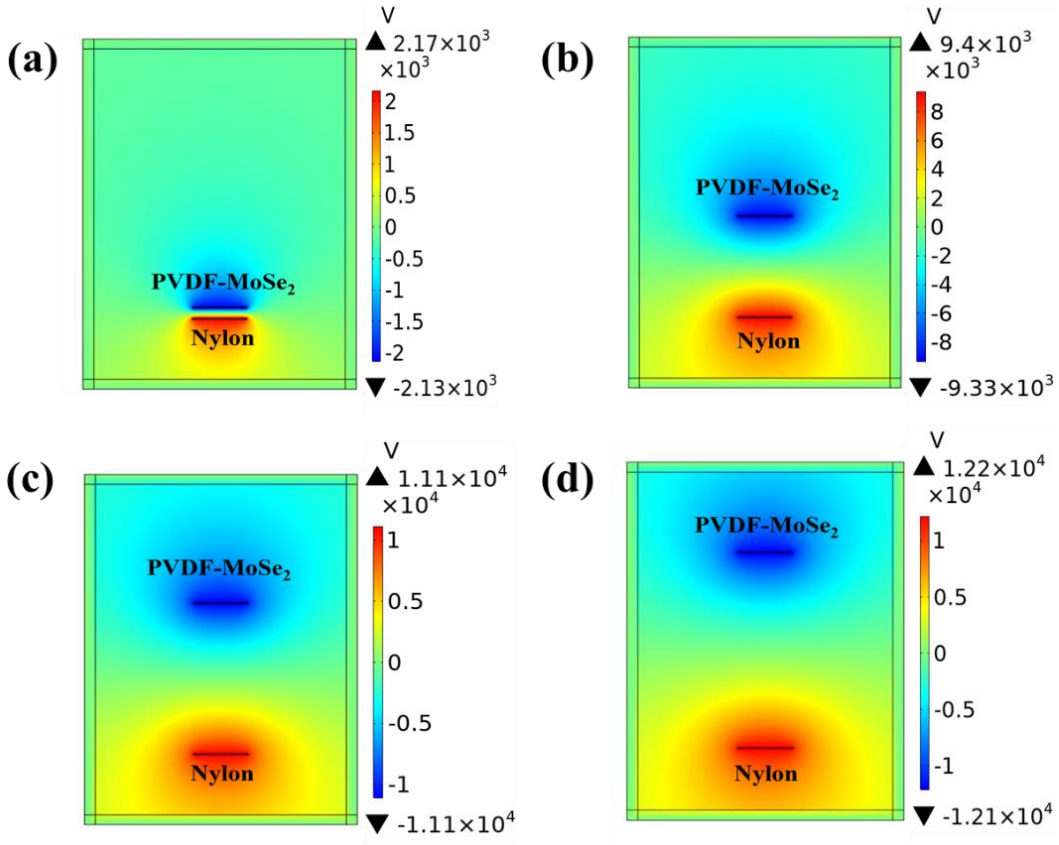

Figure 6.8 COMSOL simulated distribution of surface potential for PVDF-$MoSe_2$/Nylon TENG showing the effect of separation distance between two tribo layers in vertical contact separation mode (a) 0.5 mm, (b) 1 mm, (c) 1.5 mm and (d) 2 mm.

Figure 6.7 illustrates the potential difference between PVDF-$MoSe_2$ and other selected tribolayer materials for different fabricated TENGs. We have observed from these simulations that in case of PVDF-$MoSe_2$/PTFE based TENG, PVDF-$MoSe_2$ is acting as a positive triboelectric material. While for all other TENGs PVDF-$MoSe_2$ is acting as a negative triboelectric material thereby accepting electrons from other materials. The difference between the surface potential of PVDF-$MoSe_2$ and Nylon is notably maximum when compared to the potential difference generated between the layers of all other fabricated TENGs. This increased potential difference between the surfaces of the PVDF-$MoSe_2$/Nylon TENG leads to a greater transfer of charges between the two surfaces. The enhanced charge transfer observed in the PVDF-$MoSe_2$/Nylon TENG, in contrast to the all other TENGs, directly contributes to its improved output performance. These findings provide further support for the earlier investigations, demonstrating that the triboelectric output of the TENG was significantly enhanced when the two tribo layers have large difference between their electron affinities. Essentially, a greater potential difference between the triboelectric layers results in an increased

transfer of charges between the layers, ultimately leading to enhanced triboelectric output [31-33]. Based on these results we have made a triboelectric series for PVDF-$MoSe_2$ in comparison to PTFE, PDMS, PET, Paper and Nylon as shown in Figure 6.7. We have found from the above results that PVDF-$MoSe_2$ will be at the negative side of the triboelectric series, therefore for fabricating a high performance TENG with PVDF-$MoSe_2$ as one triboelectric layer one need to use a positive material such as Nylon for the second triboelectric layer in contact separation mode. Additionally, we have also investigated the effect of separation distance between the two tribo layers in a triboelectric nanogenerator via using the COMSOL simulations. The value of surface potential between PVDF-$MoSe_2$ and Nylon layers as a function of separation distance is depicted in Figure 6.8. It can be seen from the simulated results that greater the separation between the layers, more will be the surface potential generated during contact separation mode of TENG, which further results in the enhanced charge transfer between the layers of TENG [31, 34].

6.4 Conclusion

In brief, we have studied the effect of different triboelectric materials on the output performance of PVDF-$MoSe_2$ nanofiber based hybrid triboelectric nanogenerator (TENG). We have focused on enhancing the performance of PVDF-$MoSe_2$ based TENG by changing the second triboelectric layers such as PTFE, PDMS, PET, Paper and Nylon. Initially, we fabricated different TENGs by taking PVDF-$MoSe_2$ nanofibers as one layer in all TENGs and varying the second layer in order to investigated the triboelectric output performance of all fabricated TENGs. Our studies demonstrated that the TENG with PVDF-$MoSe_2$ and Nylon as two triboelectric layers generates the maximum triboelectric output by producing an output voltage of 144.2 V and a short-circuit current of 32.7 μA. Notably, the maximum power density achieved by the PVDF-$MoSe_2$/Nylon based hybrid triboelectric nanogenerator reached 231.1 $\mu W/cm^2$, while the power density generated by other TENGs with triboelectric layers of PTFE, PDMS, PET, and Paper are 51.9 $\mu W/cm^2$, 67.6 $\mu W/cm^2$, 163.2 $\mu W/cm^2$ and 197.6 $\mu W/cm^2$, respectively. We have also studied the effect of contact force and tapping frequency on the triboelectric performance of the PVDF-$MoSe_2$/Nylon based TENG. Higher frequencies have been found to improve output performance through more efficient charge transfer. Increasing contact force resulted in increased capacitance and a larger effective area, which improved TENG performance even more. The PVDF-$MoSe_2$/Nylon TENG achieved a maximum triboelectric voltage of 206 V and a short-circuit current of ~50 μA under a tapping frequency of 10 Hz. Our COMSOL simulations reveals that in the case of the PVDF-$MoSe_2$/PTFE TENG

PVDF-$MoSe_2$ functions as a positive triboelectric material, indicating its propensity to donate electrons during the triboelectric effect. In contrast, in all other TENG setups, PVDF-$MoSe_2$ assumes the role of a negative triboelectric material, implying its electron-accepting nature during contact-separation processes. When compared to the potential difference generated between the layers of all other fabricated TENGs, the difference between PVDF-$MoSe_2$ and Nylon is noticeably greatest. The larger potential difference between the PVDF-$MoSe_2$/Nylon TENG surfaces results in a greater transfer of charges between the two surfaces, therefore, PVDF-$MoSe_2$/Nylon generates the maximum triboelectric output. As a result, while constructing a high-performance TENG with PVDF-$MoSe_2$ as one triboelectric layer, it is critical to couple it with a positive material such as Nylon as the second triboelectric layer in contact-separation mode. Additionally, our simulated results also demonstrate that increasing the separation distance between the layers leads to a higher surface potential generated during the contact-separation mode of the TENG. Consequently, this investigation presents a viable and cost-effective approach for the development of a high-efficiency triboelectric nanogenerator suitable for clean and sustainable energy applications.

References

[1] R. Zhang, H. Olin, Material choices for triboelectric nanogenerators: A critical review, EcoMat, 2,(2020), e12062

[2] K. Wang, Z. Qiu, J. Wang, Y. Liu, R. Chen, H. An, J.H. Park, C.H. Suk, C. Wu, J. Lin, T.W. Kim, Effect of relative humidity on the enhancement of the triboelectrification efficiency utilizing water bridges between triboelectric materials, Nano Energy, 93,(2022), 106880

[3] D. Li, C. Wu, L. Ruan, J. Wang, Z. Qiu, K. Wang, Y. Liu, Y. Zhang, T. Guo, J. Lin, T.W. Kim, Electron-transfer mechanisms for confirmation of contact-electrification in ZnO/polyimide-based triboelectric nanogenerators, Nano Energy, 75,(2020), 104818

[4] Q. Zhou, K. Lee, K.N. Kim, J.G. Park, J. Pan, J. Bae, J.M. Baik, T. Kim, High humidity- and contamination-resistant triboelectric nanogenerator with superhydrophobic interface, Nano Energy, 57,(2019), 903-910

[5] J.-H. Zhang, Y. Li, J. Du, X. Hao, Q. Wang, Bio-inspired hydrophobic/cancellous/hydrophilic Trimurti PVDF mat-based wearable triboelectric nanogenerator designed by self-assembly of electro-pore-creating, Nano Energy, 61,(2019), 486-495

[6] T. Zhao, Y. Fu, Y. Zhao, L. Xing, X. Xue, Ga-doped ZnO nanowire nanogenerator as self-powered/active humidity sensor with high sensitivity and fast response, Journal of Alloys and Compounds, 648,(2015), 571-576

[7] V. Nguyen, R. Zhu, R. Yang, Environmental effects on nanogenerators, Nano Energy, 14,(2015), 49-61

[8] X. Chen, Y. Song, H. Chen, J. Zhang, H. Zhang, An ultrathin stretchable triboelectric nanogenerator with coplanar electrode for energy harvesting and gesture sensing, Journal of materials chemistry A, 5,(2017), 12361-12368

[9] J. Chen, Z.L. Wang, Reviving vibration energy harvesting and self-powered sensing by a triboelectric nanogenerator, Joule, 1,(2017), 480-521

[10] G. Zhu, B. Peng, J. Chen, Q. Jing, Z.L. Wang, Triboelectric nanogenerators as a new energy technology: From fundamentals, devices, to applications, Nano Energy, 14,(2015), 126-138

[11] W.-G. Kim, D.-W. Kim, I.-W. Tcho, J.-K. Kim, M.-S. Kim, Y.-K. Choi, Triboelectric nanogenerator: Structure, mechanism, and applications, Acs Nano, 15,(2021), 258-287

[12] Z.L. Wang, Triboelectric nanogenerator (TENG)—sparking an energy and sensor revolution, Advanced Energy Materials, 10,(2020), 2000137

[13] C. Wu, A.C. Wang, W. Ding, H. Guo, Z.L. Wang, Triboelectric nanogenerator: a foundation of the energy for the new era, Advanced Energy Materials, 9,(2019), 1802906

[14] Z.L. Wang, L. Lin, J. Chen, S. Niu, Y. Zi, Z.L. Wang, L. Lin, J. Chen, S. Niu, Y. Zi, Triboelectrification, Triboelectric Nanogenerators,(2016), 1-19

[15] Z.L. Wang, L. Lin, J. Chen, S. Niu, Y. Zi, Z.L. Wang, L. Lin, J. Chen, S. Niu, Y. Zi, Triboelectric nanogenerator: Vertical contact-separation mode, Triboelectric nanogenerators,(2016), 23-47

[16] Z.L. Wang, L. Lin, J. Chen, S. Niu, Y. Zi, Z.L. Wang, L. Lin, J. Chen, S. Niu, Y. Zi, Triboelectric nanogenerator: lateral sliding mode, Triboelectric nanogenerators,(2016), 49-90

[17] D.M. Gooding, G.K. Kaufman, Tribocharging and the triboelectric series, Encyclopedia of Inorganic and Bioinorganic Chemistry,(2011), 1-14

[18] M. Kanik, M.G. Say, B. Daglar, A.F. Yavuz, M.H. Dolas, M.M. El-Ashry, M. Bayindir, A Motion- and Sound-Activated, 3D-Printed, Chalcogenide-Based Triboelectric Nanogenerator, Advanced Materials, 27,(2015), 2367-2376

[19] H. Zou, Y. Zhang, L. Guo, P. Wang, X. He, G. Dai, H. Zheng, C. Chen, A.C. Wang, C. Xu, Quantifying the triboelectric series, Nature communications, 10,(2019), 1427

[20] V. Singh, D. Meena, H. Sharma, A. Trivedi, B. Singh, Investigating the role of chalcogen atom in the piezoelectric performance of PVDF/TMDCs based flexible nanogenerator, Energy, 239,(2022), 122125

[21] H.H. Singh, S. Singh, N. Khare, Design of flexible PVDF/NaNbO3/RGO nanogenerator and understanding the role of nanofillers in the output voltage signal, Composites Science and Technology, 149,(2017), 127-133

[22] B. Jaleh, A. Jabbari, Evaluation of reduced graphene oxide/ZnO effect on properties of PVDF nanocomposite films, Applied Surface Science, 320,(2014), 339-347

[23] S. Sarkar, S. Garain, D. Mandal, K.K. Chattopadhyay, Electro-active phase formation in PVDF–BiVO 4 flexible nanocomposite films for high energy density storage application, RSC Advances, 4,(2014), 48220-48227

[24] Z. Wang, H.Y. Yue, Z.M. Yu, F. Yao, X. Gao, E.H. Guan, H.J. Zhang, W.Q. Wang, S.S. Song, One-pot hydrothermal synthesis of MoSe 2 nanosheets spheres-reduced graphene oxide composites and application for high-performance supercapacitor, Journal of Materials Science: Materials in Electronics, 30,(2019), 8537-8545

[25] Y. Peng, Z. Meng, C. Zhong, J. Lu, W. Yu, Y. Jia, Y. Qian, Hydrothermal synthesis and characterization of single-molecular-layer MoS2 and MoSe2, Chemistry Letters, 30,(2001), 772-773

[26] P.I. Devi, K. Ramachandran, Dielectric studies on hybridised PVDF–ZnO nanocomposites, Journal of Experimental Nanoscience, 6,(2011), 281-293

[27] P. Martins, A.C. Lopes, S. Lanceros-Mendez, Electroactive phases of poly (vinylidene fluoride): Determination, processing and applications, Progress in polymer science, 39,(2014), 683-706

[28] N. Soin, D. Boyer, K. Prashanthi, S. Sharma, A.A. Narasimulu, J. Luo, T.H. Shah, E. Siores, T. Thundat, Exclusive self-aligned β-phase PVDF films with abnormal piezoelectric coefficient prepared via phase inversion, Chemical Communications, 51,(2015), 8257-8260

[29] J.S. Lee, K.-Y. Shin, O.J. Cheong, J.H. Kim, J. Jang, Highly sensitive and multifunctional tactile sensor using free-standing ZnO/PVDF thin film with graphene electrodes for pressure and temperature monitoring, Sci Rep, 5,(2015), 1-8

[30] V. Singh, B. Singh, PDMS/PVDF-MoS2 based flexible triboelectric nanogenerator for mechanical energy harvesting, Polymer, 274,(2023), 125910

[31] L. Shi, H. Jin, S. Dong, S. Huang, H. Kuang, H. Xu, J. Chen, W. Xuan, S. Zhang, S. Li, High-performance triboelectric nanogenerator based on electrospun PVDF-graphene nanosheet composite nanofibers for energy harvesting, Nano Energy, 80,(2021), 105599

[32] V. Singh, B. Singh, MoS2-PVDF/PDMS Based Flexible Hybrid Piezo-Triboelectric Nanogenerator for Harvesting Mechanical Energy, Journal of Alloys and Compounds,(2023), 168850

[33] T. Bhatta, P. Maharjan, H. Cho, C. Park, S.H. Yoon, S. Sharma, M. Salauddin, M.T. Rahman, S.M.S. Rana, J.Y. Park, High-performance triboelectric nanogenerator based on MXene functionalized polyvinylidene fluoride composite nanofibers, Nano Energy, 81,(2021), 105670

[34] G.-Z. Li, G.-G. Wang, Y.-W. Cai, N. Sun, F. Li, H.-L. Zhou, H.-X. Zhao, X.-N. Zhang, J.-C. Han, Y. Yang, A high-performance transparent and flexible triboelectric nanogenerator based on hydrophobic composite films, Nano Energy, 75,(2020), 104918

CHAPTER 7

Conclusions and future Prospectives

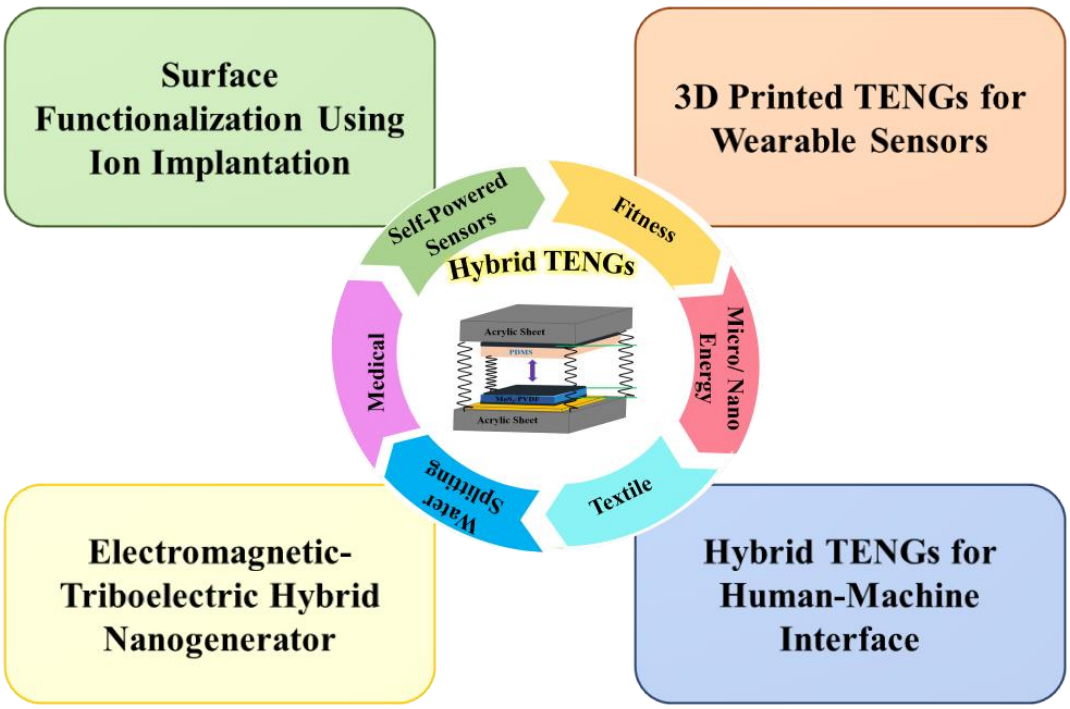

The main aim of this chapter is to summarize the key observations, findings, and conclusions that have emerged during the research. This chapter also includes chapter specific summaries. We will explore the future prospects and directions that have been disclosed as a result of the research in the following section of this chapter, which will be a vital platform for us.

7.1 Conclusions

This present thesis focuses on the synthesis of PVDF (Polyvinylidene fluoride) nanocomposite films and their use in mechanical energy harvesting systems. We have demonstrated the significance of different 2D transition metal dichalcogenides (TMDCs) as nanofillers in improving the performance of PVDF based piezoelectric and triboelectric nanogenerators throughout this work. We have shown that, the adding of these nanostructures to PVDF increases its applicability for harvesting mechanical energy. In this study, we successfully fabricated a hybrid nanogenerator that incorporates both piezoelectric and triboelectric effects for powering small scale electronic devices and for making sustainable water splitting system. When compared to individual impacts, the hybrid systems perform much better. The main results gained from this investigation will be expanded on in the following parts.

1. The hydrothermal technique has been used for the synthesis of various transition metal dichalcogenides (MoS_2, $MoSe_2$, MoSSe). Detailed structural, morphological studies have been investigated using XRD, Raman, FTIR and FESEM techniques.
2. The effect of various synthesized TMDCs (MoS_2, $MoSe_2$, MoSSe). on output performance of PVDF based piezoelectric nanogenerator has been studied. It was found that the piezoresponse of PVDF/TMDCs based nanogenerators was greatly enhanced in comparison to pristine PVDF. The PVDF based piezoelectric device having MoSSe as nanofiller reported the maximum energy harvesting performance with 31.2 V and 1.26 μA as open circuit peak to peak voltage and short circuit current, respectively. Further to mimic the variety of vibration present in the environment, an electrodynamic shaker capable of generating different frequency and force was used. It was observed that 7 Hz is the optimum frequency for generating the maximum output signal. The improved performance of the fabricated PVDF/TMDCs based PENG is due to the combined contribution of nucleation of the electroactive polar β-phase content of the PVDF in the composite films, and inherent piezoelectric property of TMDC (MoS_2, $MoSe_2$) because of their in-plane asymmetry. In addition to the above two reasons, an additional breaking of out-of-plane symmetry for MoSSe in comparison to MoS_2 and $MoSe_2$ increases its piezoelectric properties, thereby generating the highest piezoelectric output for PVDF/MoSSe based PENG. To check the practical applicability of the device, the generated output power was used to glow the commercially available LED.
3. To further understand the ideal concentration of nanofiller, we have fabricated PVDF-MoS_2 based PENG with varying concentration of MoS_2 (0 %, 3%, 5 % , 7 wt %and 10 wt%) in PVDF matrix. The piezoelectric performance of MoS_2 filled PVDF films were compared with bare PVDF and it was observed that 7 wt% of MoS_2 is the optimal level of doping for mechanical

energy harvesting. Above 7 wt% of MoS_2 the performance of the nanogenerator abruptly declined due to the agglomeration of MoS_2 in the PVDF matrix. Therefore, the pure piezoelectric nanogenerator having 7 wt % of MoS_2 shows maximum output voltage of 18.3 V and rectified short circuit current of 14.6 μA at a tapping frequency of 7 Hz.

4. To further explore the mechanical energy harvesting capabilities of PVDF/MoS_2 based composite film, triboelectric nanogenerator based on PDMS as one triboelectric layer and PVDF/MoS_2 (7 wt %) as another layer has been studied. The fabricated TENG with 7 wt% MoS_2 exhibits a maximum output voltage of 189 V and a short circuit current of 1.61 μA. Further a piezo-tribo hybrid nanogenerator (HNG) capable of integrating both piezoelectric and triboelectric effects in a single device is studied. The output voltage and current performance of the HNG is enhanced in comparison to its individual piezo and tribo components. The increased output performance is attributed to the combined effect of β-phase nucleation, increased roughness, enhanced dielectric constant on addition of filler in the PVDF matrix. Each of these factors combine to significantly increase the performance of the hybrid nanogenerator. PVDF-MoS_2/PDMS based piezo-tribo based hybrid nanogenerator (HNG) generated the power density of ~220 μWcm^{-2}. The generated output power was used for powering of electronic stopwatch and scientific calculator. As a result, this study suggests a feasible, economical approach to fabricate a high-performance hybrid nanogenerator by combining both the piezoelectric and triboelectric effects and has been utilized to drive the wearable electronic devices.
5. To further improve the efficiency of the PENG and TENG, the PVDF-$MoSe_2$ nanofibers were synthesized via electrospinning technique with different wt% of $MoSe_2$ (0 wt%, 3 wt%, 5 wt%, 7 wt% and 10 wt%). Here, hybrid triboelectric nanogenerator coupling both the piezoelectric and triboelectric effects have been fabricated to drive the environment friendly approach of splitting the water for hydrogen production. The comparison between the piezoelectric efficiency of different PVDF-$MoSe_2$ nanofiber-based films as a function of $MoSe_2$ wt% was carried out, and it has been discovered that 7 wt % of $MoSe_2$ is the ideal concentration for piezoelectric energy harvesting like the case of PVDF-MoS_2. Furthermore, TENG based on high performance PVDF-$MoSe_2$ as a negative triboelectric material and Nylon as tribopositive materials has been successfully designed. The TENG with 7 wt% of $MoSe_2$ exhibits excellent triboelectric performance with generated maximum power density of 230.4 $\mu W/cm^2$, which is approximately 2.9 times greater than the maximum power density produced by pure PVDF based TENG. Finally, the generated power is utilized for developing a self-powered system for the splitting of water for generation of hydrogen as a source of green energy.

6. To understand the effect of triboelectric layer material on the output performance of the TENG various materials have been investigated including PTFE, PDMS, PET, Paper and Nylon as one layer whereas PVDF-$MoSe_2$ nanofiber film as another triboelectric layer. It was observed that the TENG consisting of PVDF-$MoSe_2$/Nylon in the vertical contact-separation mode demonstrates the maximum power density of ~231 μWcm^{-2}. The effect of tapping frequency and force on the triboelectric output of PVDF-$MoSe_2$/Nylon was also studied and an increasing trend of output voltage and current is observed with increasing force and frequency thereby producing a maximum voltage of ~206 V. The increase in output performance of the TENG with increase in frequency is attributed to faster charge transfers process when the contact frequency is higher. With the rise in contact force, the effective area and capacitance of the TENG also increases which further results in the enhancement of triboelectric output of the nanogenerator. The difference between the surface potential of two contacting materials is very important parameter for the performance of a TENG. The COMSOL software is used to simulate the relationship of the surface potential between the two layers of the TENG. Theoretical analysis of the simulation result is offered, along with a brief description of the simulation procedure.

7.2 Future Prospectives

1. The choice of the material and the geometry of the fabricated TENGs is very important to effectively utilize the generated power for different applications, including, wearable sensors, biomedical, environmental monitoring, robotic, agriculture and smart homes, etc. To meet the specific criteria for a particular application, various critical parameters, such as, power density, stability, flexibility, and sustainability need to be taken care by wisely selecting the triboelectric layer materials, hence required further study.
2. For a TENG device, morphology of the surface of two layers is very important for charge generation. With change in surface morphologies, the number of charges that resides on the surface of triboelectric material during contact separation mode also changes. Greater will be the surface charge density, greater will be the efficiency of a triboelectric nanogenerator. These modifications on the surface of the synthesized thin films can be done via ion irradiation and lithography techniques. Ion irradiation can also change the functional groups and chemical structure of polymer materials used in flexible TENGs, which results in the enhancement of the power generation efficiency of the TENG.
3. In present thesis, we have enhanced the output performance of the mechanical energy harvester by coupling between piezoelectric and triboelectric phenomenon. In future, we can also combine electromagnetic and thermoelectric nanogenerator with hybrid TENG for increasing the overall

power output. Further the hybrid nanogenerator can be integrated with a storage device for driving small scale microelectronic devices.

4. The development of self-powered sensors represents a critical step towards enhancing healthcare. These sensors have the potential to provide real-time data on vital health parameters without the need for constant battery replacements, making them highly suitable for continuous and long-term health monitoring. For this the utilization of 3D printing as an effective means for designing wearable devices is of paramount importance. Furthermore, it may serve as an inspiration for advancements in the domains of artificial intelligence, health monitoring, and electronic skin applications.

Bio-data

Vishal Singh is a research scholar at Delhi Technological University, Delhi pursuing his research in the Applied Physics Department since July 2018. Prior to this, he completed his Master in Physics from Department of Physics, Deenbandhu Chhotu Ram University of Science and Technology, Murthal Sonipat (Haryana) in the year 2017 and Bachelor of Science from Govt. P.G. College Bhiwani, Maharshi Dayanand University Rohtak in the year 2015. He has been awarded the Commendable Research Award for excellence in Research by DTU in year 2023. He has received best poster presentation award in ICMAT 2023, at SUNTEC, Singapore, 26^{th} - 30^{th} June, 2023. His present research interests are in the field of fabrication of piezoelectric and triboelectric nanogenerators for mechanical energy harvesting and their applications in making wearable devices.